Mitteilungen aus dem Institut für Mechanik

Zoran Stankovic

Detection of fatigue crack growth using nondestructive testing methods

Heft Nr. 151

RUHR-UNIVERSITÄT BOCHUM

INSTITUT FÜR MECHANIK
RUHR-UNIVERSITÄT BOCHUM

Zoran Stanković

Detection of fatigue crack growth using nondestructive testing methods

MITTEILUNGEN AUS DEM INSTITUT FÜR MECHANIK NR. 151
April 2009

Herausgeber:

Institut für Mechanik
— Schriftenreihe —
Ruhr-Universität Bochum
D-44780 Bochum

ISBN 978-3-935892-29-2

Printed in Germany

Abstract

In this thesis, experimental and numerical investigations of the damage evolution in cyclic loaded specimens are performed. The fatigue crack growth is observed on two different specimen forms. The fatigue loading is defined as a cyclic loading either as Wöhler or block program experiments. The cyclic loading is applied in tension range, which leads to a high cyclic fatigue and brittle damage. In order to investigate kinked cracks, an additional group of experiments with a load applied in two different directions is performed on one of two specimen geometries. The damage evolution is monitored on measuring the specimen elongation and the applied force and by means of two nondestructive methods – the detection of acoustic emission and the measurement of electrical resistance. Acoustic emission is used for detecting sound waves as a result of the dissipation of elastic strain energy during microcrack and macrocrack growth, as well as for the detection of the origin of crack initiation and propagation. The measurement of the electrical resistance is applied for monitoring the crack length in fatigue research and is used for the quantitative investigation of the crack growth. The measured data obtained during the service life is additionaly used for the parameter identification of a brittle damage material model.

Zusammenfassung

In dieser Arbeit werden experimentelle und numerische Untersuchung der Schädigungsentwicklung in Proben unter zyklischer Belastung durchgeführt. Das Risswachstum wird für zwei verschiedene Probengeometrien beobachtet. Die Ermüdungsbeanspruchung wird als zyklische Belastung entweder als Wöhlervesuche oder Blockprogrammversuche definiert und in einem Zugbereich durchgeführt, in dem die Langzeitfestigkeit hinsichtlich einer spröden Schädigung analysiert werden kann. Um einen abgeknickten Riss zu untersuchen, wird eine zusätzliche Reihe von Experimenten mit Belastungen, die in zwei verschiedene Richtungen angewendet werden, durchgeführt. Die Schädigungsentwicklung wird durch die Messung der Verlängerung der Probe und der angelegten Kraft sowie durch zwei zerstörungsfreie Methoden – die Messung der akustischen Emissionen und die Messung des elektrischen Widerstands – überwacht. Akustische Emissionen werden gemessen, um Schallwellen als das Ergebnis der Dissipation der elastischen Verzerrungsenergie während des Wachstums von Mikro- und Makrorissen zu ermitteln, aber auch, um den Ursprung der Rissbildung und Rissausbreitung zu bestimmen. Die Messung des elektrischen Widerstands erfolgt zur Überwachung der Risslänge und zur quantitativen Ermittlung des Risswachstums in den Ermüdungsuntersuchungen. Die während der Versuche gemessenen Daten werden abschließend zur Parameteridentifikation eines Materialmodells zur Beschreibung spröder Schädigungen eingesetzt.

Vorwort

Die vorliegende Arbeit entstand während meiner Tätigkeit als wissenschaftlicher Mitarbeiter am Institut für Mechanik der Ruhr-Universität Bochum und wurde von der Fakultät für Bau- und Umweltingenieurwissenschaften als Dissertation angenommen. Sie wurde im Rahmen des Sonderforschungsbereiches 398 Lebensdauerorientierte Enwurfskonzepte unter Schädigungs- und Deteriationsaspekte von der Deutschen Forschungsgemeinschaft gefördert.

Mein besonderer Dank gilt Herrn Prof. Dr.-Ing. Otto T. Bruhns für die Anregung zu dieser Arbeit und seine Unterstützung bei ihrer Anfertigung. Herrn Prof. Dr.-Ing. Henning Schütte danke ich für sein Interesse, die Unterstützung und die Übernahme des Koreferates.

Bei allen Mitarbeitern des Lehrstuhls für Technische Mechanik bedanke ich mich für die Hilfsbereitschaft und die angenehme und freundliche Arbeitsatmosphäre. Besonderer Dank gilt hierbei den Herren Dr.-Ing. habil. Claus Oberste-Brandenburg und Dr.-Ing. Patrick Luig für die fruchtbaren Gespräche und Diskussionen. Desweiteren danke ich den technischen Mitarbeitern, ohne die die vorliegende Arbeit nicht in dieser Art und Weise möglich gewesen wäre.

Schließlich danke ich meiner Familie und insbesondere meiner Frau Lidija für ihre Unterstützung und ihren Zuspruch.

Bochum, im April 2009 Zoran Stanković

Referenten: Prof. Dr.-Ing. Otto T. Bruhns
Prof. Dr.-Ing. Henning Schütte

Tag der Einreichung: 12.08.2008
Tag der mündlichen Prüfung: 17.11.2008

Contents

List of Figures

List of Tables

Conventions and Notations

Scalars (italics)

a	Half crack length
A	Area
B	Body
C, C'	Paris' law material parameter
$\mathcal{D}$	Damage variable
$\mathcal{D}^d$	Damage dissipation rate
E	Young's modulus
G	Strain energy release rate
h	Heat flux
I	Electrical current
J	Determinant of the deformation gradient (Jacobian determinant)
J	J-integral
K	Kinetic energy
$\mathrm{K_i}$	Stress intensity factor
k_t	Stress concentration factor
m	Paris' law material parameter
N	Number of load cycles
P_a	Work of external forces
Q	Heat
r	Internal heat source
R	Stress ratio
s	Specific entropy
S	Entropy
t	Time
u	Specific internal energy
U	Internal energy
v	Volume in the current configuration
V	Volume in the reference configuration
V_v	Void volume
W	Total energy
W^d	Damage work
W^e	Elastic strain energy density
W^p	Plastic work
X	Particle

Scalars (Greek characters)

α	Scalar in the current configuration
$\hat{\alpha}$	Scalar in the reference configuration
α_p	Temperature coefficient of specific electrical resistance
α_ϵ	Linear thermal expansions coefficient
β	Crack orientation angle
γ	Surface energy density
$\dot{\gamma}$	Rate of internal entropy production
Γ	Dissipated energy during crack growth
δA	Total area
$\delta \tilde{A}$	Effective remaining area
$\delta A_{\mathcal{D}}$	Damaged area
$\Delta\varepsilon^e$	Elastic strain amplitude
$\Delta\varepsilon^p$	Plastic strain amplitude
η	Paris' law material parameter
λ	Lamé constant
$\dot{\lambda}^d$	Damage multiplier
μ	Lamé constant
ν	Poisson's ratio
θ	Kink angle
Θ	Absolute temperature
ρ	Specific electrical resistance
ρ_0	Mass density in the reference configuration
σ	Uniaxial stress
$\tilde{\sigma}$	Effective uniaxial stress
σ_a	Stress amplitude
σ_e	Endurance limit
σ_{loc}	Local stress
σ_m	Mean stress
σ_{nom}	Nominal stress
σ_u	Ultimate stress
σ_y	Yield stress
$\Delta\sigma$	Stress range
$\bar{\phi}^d$	Damage potential
χ_i	Eigenvalue of the left Cauchy-Green tensor
ψ	Continuity
Ψ	Airy stress function

Vectors (boldface roman)

$\mathbf{b}$	Force per volume in the current configuration
$\mathbf{b_0}$	Force per volume in the reference configuration
$\mathbf{c}$	Translation
$\mathbf{da}$	Area element in the current configuration

$\mathbf{dA}$	Area element in the reference configuration
$\mathbf{dl}$	Force element in the current configuration
$\mathbf{dL}$	Force element in the reference configuration
$\mathbf{dx}$	Line element in the current configuration
$\mathbf{dX}$	Line element in the reference configuration
$\mathbf{n}$	Normal vector in the current configuration
$\mathbf{N}$	Normal vector in the reference configuration
$\mathbf{o}$	Origin in the current configuration
$\mathbf{O}$	Origin in the reference configuration
$\mathbf{q}$	Heat flow in the current configuration
$\mathbf{Q}$	Heat flow in the reference configuration
$\mathbf{e}_i$	Unit vector in the current configuration
$\mathbf{E}_\alpha$	Unit vector in the reference configuration
$\mathbf{t}$	Stress vector
$\mathbf{u}$	Displacement
$\mathbf{v}$	Velocity
$\mathbf{x}$	Position in the current configuration
$\mathbf{X}$	Position in the reference configuration
$\mathbf{o}$	Origin in the current configuration
$\mathbf{O}$	Origin in the reference configuration

Vectors (Greek characters)

$\boldsymbol{\alpha}$	Vector in the current configuration
$\hat{\boldsymbol{\alpha}}$	Vector in the reference configuration
$\boldsymbol{\chi}$	Deformation

Second order tensors (boldface roman)

$\mathbf{1}$	Unit tensor
$\mathbf{A}$	Tensor in the current configuration
$\hat{\mathbf{A}}$	Tensor in the reference configuration
$\tilde{\mathbf{A}}$	Two-point tensor
$\mathbf{B}$	Left Cauchy-Green tensor
$\mathbf{B}_i$	Eigenprojection of the left Cauchy-Green tensor
$\mathbf{C}$	Right Cauchy-Green tensor
$\mathbf{D}$	Stretching tensor
$\boldsymbol{\mathcal{D}}$	Damage tensor
$\mathbf{e}$	Almansi-Euler strain tensor
$\mathbf{E}$	Green-Lagrange strain tensor
$\mathbf{F}$	Deformation gradient
$\mathbf{h}$	Hencky strain in current configuration
$\mathbf{H}$	Hencky strain in reference configuration
$\bar{\mathbf{k}}^d$	Damage driving force
$\mathbf{L}$	Velocity gradient

$\mathbf{M}$	Arbitrary non-singular tensor
$\mathbf{P}$	Nominal stress tensor
$\mathbf{Q}$	Rotation tensor
$\mathbf{R}$	Rotation tensor (polar decomposition)
$\mathbf{R}^{\mathrm{Log}}$	Logarithmic rotation tensor
$\mathbf{S}$	Second Piola Kirchhoff stress tensor
$\mathbf{T}$	First Piola Kirchhoff stress tensor
$\mathbf{U}$	Right stretch tensor
$\mathbf{V}$	Left stretch tensor
$\mathbf{W}$	Spin tensor

Second order tensors (Greek characters)

$\tilde{\boldsymbol{\varepsilon}}$	Effective strain tensor
$\boldsymbol{\sigma}$	Cauchy stress tensor
$\tilde{\boldsymbol{\sigma}}$	Effective stress tensor
$\boldsymbol{\tau}$	Kirchhoff stress tensor
$\boldsymbol{\Omega}$	Spin tensor
$\boldsymbol{\Omega}^{\mathrm{J}}$	Zaremba-Jaumann spin tensor
$\boldsymbol{\Omega}^{\mathrm{R}}$	Green-Naghdi spin tensor
$\boldsymbol{\Omega}^{\mathrm{Log}}$	Logarithmic spin tensor

Fourth order tensors (boldface roman)

$\mathbb{C}$	Elastic stiffness tensor
$\tilde{\mathbb{C}}$	Damaged elastic stiffness tensor
$\mathbb{D}$	Damage tensor
$\mathbb{I}$	Identity tensor
$\mathbb{M}$	Damage effect tensor

Other symbols

$\mathcal{B}$	Current configuration
$\mathcal{B}_0$	Reference configuration
$\mathbb{E}$	Euclidean vector space
$\mathcal{E}$	Euclidean point space
$\mathcal{O}$	Observer

Special symbols & functions

det	Determinant
Δ	Laplace operator
div	Divergence with respect to $\mathbf{x}$
Div	Divergence with respect to $\mathbf{X}$
grad	Gradient with respect to $\mathbf{x}$
Grad	Gradient with respect to $\mathbf{X}$

$\mathcal{L}$	Lie derivative
$\mathrm{skw}(\cdot)$	Skew-symmetric part of a tensor
$\mathrm{sym}(\cdot)$	Symmetric part of a tensor
$(\cdot)^T$	Transpose of a tensor
$(\cdot)^{-1}$	Inverse of a tensor
$\dot{(\cdot)}$	Material time derivative
$\overset{\circ}{(\cdot)}^{\log}$	Logarithmic time rate
$\cdot$	Scalar product
:	Double contraction
$\times$	Vector product
$\otimes$	Dyadic product

Superscripts

$(\cdot)^{\mathrm{e}}$	Elastic
$(\cdot)^{\mathrm{p}}$	Plastic
$(\cdot)^{\mathrm{d}}$	Damage

Subscripts

$(\cdot)_0$	Quantity associated with reference configuration
$(\cdot)_c$	Critical value
$(\cdot)_{th}$	Threshold value

1 Introduction

1.1 Motivation

Analysis of stress and displacement fields in conjunction with a postulate predicting the event of failure are usually involved in the mechanical design of engineering structures. In order to obtain accurate knowledge of the stress state, a detailed theoretical analyses based on the simplifying assumption regarding material behaviour and structural geometry can be performed. However, experimental and numerical methods are a preferred choice in the case of complicated structures or loading situations. After the stress analysis is performed, a suitable failure criterion for an evaluation of the strength and integrity of structural component can be applied. Conventional failure criteria are developed to explain strength failures of loaded structures which can be roughly classified as ductile or brittle. In the case of a ductile failure, breakage of a structure is preceded by a large deformation that occurs over relatively long time period. A small deformation and a sudden failure are usually characteristics of a brittle failure. Some of the most popular failure criteria were proposed by Tresca (1872), Mohr (1900), von Mises (1913) and Drucker & Prager (1952). These failure criteria have been used in design of engineering structures, and they describe the onset of yield in materials with ductile behaviour, or the fracture in materials with brittle behaviour. The theoretical strength, as determined by the properties of the internal structure of the material, is defined as the highest stress level that the material can withstand. All these criteria are based on the assumption of static single load. However, many structures in engineering practice are loaded with the variable loading and some of them fail although the real stress state is significantly below the highest stress level.

In order to overcome these difficulties, other failure criteria which describe the material behaviour under cyclic loading were proposed. First systematic investigations of fatigue failure in railroad axles given by Wöhler (1858) lead to a conclusion that the strength of steel axles subjected to the cyclic loads is significantly lower than their static strength. Based on these investigations, the characterisation of fatigue behaviour in terms of stress amplitude-life (S-N) curves and the concept of fatigue endurance limit were defined. To determine an approximate shape of S-N curve, experiments with constant loading amplitude are performed. These curves are given for constant mean stress or constant stress ratio. However, engineering structures and components are subjected to different cyclic stress amplitudes, mean stresses, stress ratios and loading frequencies. Therefore, a criterion for the estimation of fatigue damage of structures known

as linear cumulative damage rule was proposed by Palmgren (1924) and Miner (1945). This criterion estimates the fatigue damage induced by a certain block of constant amplitude cyclic stresses in a loading sequence consisting of various blocks of different stress amplitudes. The damage state is introduced as a sum of fractions of expended fatigue life which are represented as a ratio between the number of stress cycles applied to a component and the total number of stress cycles of same amplitude necessary for causing failure. The total number of stress cycles is determined from S-N curve. Based on the linear damage accumulation rule, many other rules are defined to take into account other characteristics of applied loading.

All these damage accumulation rules for cyclic loading are defined to indicate failure of structures or components in the moment of appearance of a macrocrack. However, a structure can show considerable remaining service life during the stable propagation of dominant macrocrack. The behaviour of structures during the stable macrocrack propagation is described using fatigue fracture mechanics. Different evolution laws for describing stable macrocrack growth were proposed by Paris (1962), Forman et al. (1967) and Wheeler (1972). The main task of fatigue crack propagation laws is to determine the number of loading cycles required for a crack to grow from a certain initial crack size a_0 to the maximum permissible crack size a_c, and to describe the form of this increase in function of loading cycles. In this manner, the fatigue failure criterion can be defined as a moment of complete structure failure, or as a moment when the macrocrack length reaches a critical value and remaining load capacity drops below a certain value.

All these approaches cannot give an answer about the material behaviour before the macrocrack initiation. In order to describe the mechanisms involved in deterioration of materials under loading prior to the macrocrack initiation, continuum damage mechanics is implemented. Initiation of damage mechanics can be attributed to Kachanov (1958) and his proposition to characterise a gradual deterioration process of a microstructure by a scalar ψ, which is called continuity. The concept of effective stress introduced by Rabotnov (1968) combined with the work of Kachanov represents the basis of the continuum damage mechanics. After that, many different concepts of damage variables were proposed to describe the existence of distributed microscopic voids, cavities or cracks of the size of crystal grains in the material.

In the present work, the experiments with the cyclic fatigue loading are performed in order to obtain a database of different measurements which can be used for the identification of material parameters in brittle damage material model. The experiments are conducted with the cyclic loading in the range that leads to the high cycle fatigue and the brittle damage. The evolution of the brittle damage is investigated on two types of specimens with different geometry. The experiments are performed as Wöhler experiments or block program experiments.

Two nondestructive measurement methods, measurement of acoustic emission

and measurement of electrical resistance, are used for the detection of damage evolution during the fatigue loading. Additionally, the measurement of the force and the elongation of the specimen is used for the calculation of global stiffness of the specimen. The results derived from nondestructive methods are coupled with the global evolution of the stiffness of damaged specimen.

1.2 Outline

This thesis is structured in eight chapters. Subsequent to this introduction, the basic principles concerning the continuum mechanics and thermodynamics framework are presented. Different strain and stress measures are derived. The concept of work conjugate pairs of stress and strain, as well as the notion of objectivity and some objective rates are introduced. Additionally, the fundamental balance laws and conservation equations are presented.
Chapter 3 begins with the fundamentals of continuum damage mechanics. Basic notions of different scale levels, the classification of fatigue damage, different types of damage variables and damage equivalence principles are presented in this chapter. This is followed by the introduction to fracture mechanics. In this part, the physical mechanisms of fracture and three approaches to the definition of the theory of crack growth in the case of linear elastic fracture mechanics are subsequently presented. Approaches suitable for the fatigue crack growth are briefly explained. The material law proposed by Schütte (2001) used for the parameter identification of the brittle fatigue damage, is also presented. The last part of this chapter deals with the fundamentals of fatigue analysis. After the basics of experimental fatigue analysis, the concept of cumulative damage, as well as the concept of strain life approach in fatigue calculation are introduced. The influence of mean stress and strain on fatigue life is elaborated at the end of this section.
Two nondestructive testing methods are introduced in Chapter 4. The measurement of acoustic emission is introduced in the first part of this chapter. After the description of the acoustic emission phenomenon, the sources of acoustic emission and the Kaiser effect are presented. This is followed by the theoretical background for the localisation of acoustic emission sources in one and two dimensional problems. Furthermore, characteristic parameters and application of acoustic emission are given. In the second part of this chapter, the measurement of electrical resistance, as the second nondestructive testing method used in this work, is introduced.
The experimental setup is presented in Chapter 5. A description of the specimen material and geometry is given at the beginning of the chapter, followed by a detailed description of the clamping procedures for two types of specimen geometries. Special attention is then given to the design of different loading programmes. The measurement of acoustic emission, electrical resistance and temperature is described, together with a presentation of the methods for data acquisition and documentation of macrocrack growth.

Chapter 6 summarises the experimental results. The calibration of the experimental equipment applied in this work is introduced in the first part of the chapter. This is followed by the representation of procedures for the evaluation of measured data. Thereafter, the evaluated experimental results of the measurement of global specimen stiffness, different characteristics of acoustic emission and measurement of electrical resistance are presented. All results are given for the plain specimen with a hole, plain specimen with both side notches and for the circular specimen. At the end of this chapter the thorough documentation of the macroscopic crack growth is presented.
Numerical analysis of experimental data is the topic of Chapter 7. Connection between the evolution of electrical resistance and the crack growth during service life of the specimen is introduced. The material parameters are identified on the basis of an appropriate material model. Consequently, for the identified material parameters, the experiments are recalculated and results of the numerical analysis and experiments are compared.
The thesis is concluded by a summary of the main results of this work. At the end, a few remarks concerning possible further improvements of the experimental database are given.

2 Continuum mechanics and thermodynamics

This chapter is a short overview of some basic principles of continuum mechanics and thermodynamics, and is conceived to introduce a consistent nomenclature and to give the basic assumptions and laws needed in the following parts of this work.
A more detailed overview of these subjects can be found in the works of Ogden (1997); Marsden & Hughes (1983); Truesdell & Noll (2003); Stein & Barthold (1996); Malvern (1969); Xiao et al. (2007).

2.1 Continuum mechanics

2.1.1 Kinematics

Continuum kinematics describes the geometry of a body, its motion in space and the deformation of this body during the motion. A basis for this description is the consideration of a body B as an ensemble of material points or particles which can be put into one-to-one correspondence with some region $\mathcal{B}$ of the Euclidean point space $\mathcal{E}$. The body is said to occupy region $\mathcal{B}$ and as the body moves the region it occupies in $\mathcal{E}$ changes continuously.
A generic particle of body B is labelled by X. In general, different configurations of the body may exist. In a fixed referential configuration $\mathcal{B}_0$, which could coincide with the initial configuration of the body, each generic particle X of the body B is defined by a position vector $\mathbf{X}$ in the Euclidean vector space $\mathbb{E}$ relative to the fixed origin $\mathbf{O}$ in $\mathcal{E}$. In this manner, a mapping of the particle onto its position in the Euclidean (reference) point space is realized and the material point can be identified by the local position in the reference configuration. Similarly, the position of the generic particle X in the current configuration $\mathcal{B}$ is defined by position vector $\mathbf{x}$ in $\mathbb{E}$ relative to the fixed origin $\mathbf{o}$ in $\mathcal{E}$. Hence, it is possible to choose different coordinate systems with different origins for reference and current configuration. The body B with the particle X is depicted in its reference and current configuration in Figure 2.1 (see Ogden 1997).
The current place $\mathbf{x}$ of the particle X with position $\mathbf{X}$ in the reference configuration is

$$\mathbf{x} = \boldsymbol{\chi}(\mathbf{X}, t)\,. \tag{2.1}$$

By (2.1) the distinction between the particle X and the place $\mathbf{X}$ used to identify it for practical purpose is ignored. Definition of $\boldsymbol{\chi}$, which is regarded as a mapping from the reference configuration $\mathcal{B}_0$ to the current configuration $\mathcal{B}$,

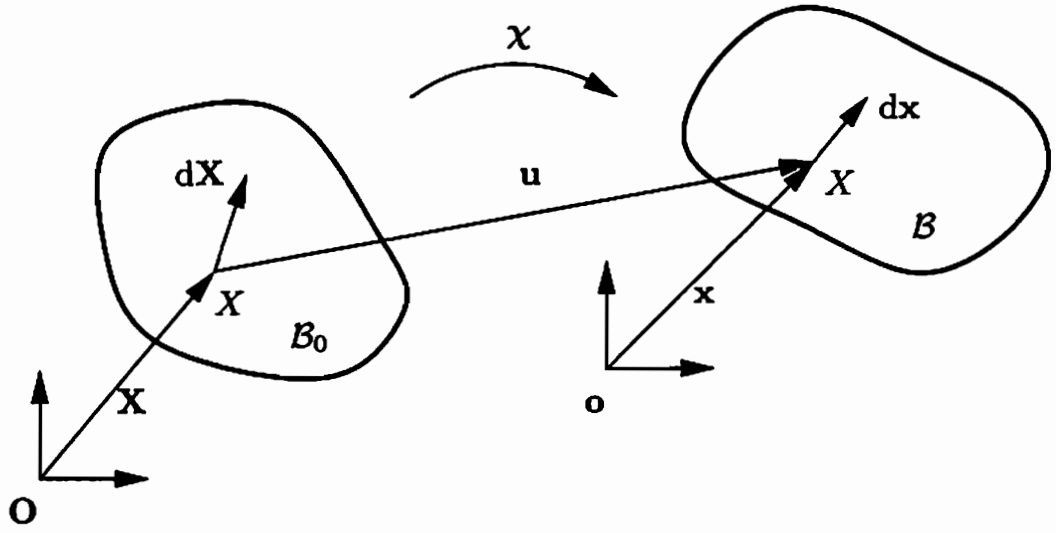

Figure 2.1: A body and a particle in the reference and the current configuration

depends implicitly on the choice of the reference configuration. For any fixed time t, χ is called a deformation from the reference to the current configuration, and for an arbitrary time t (2.1) specifies a one-parameter family of such deformation. It is clear, that a deformation can be defined only for a given reference configuration. While different observers are at liberty to choose a different reference configuration, any choice of a reference configuration is independent of an observer.
Consequently, physical phenomena associated with the deformation (2.1) of a body B can be expressed using fields defined over $\mathcal{B}_0$ in the *Lagrangian* (or material) description, or using fields defined over $\mathcal{B}$ in the *Eulerian* (or spatial) description.
Because the comparison of reference and current configuration does not require knowledge of the intermediate stages in the motion, the time dependence in (2.1) is not needed. Therefore, an explicit dependence on t is omitted and (2.1) is replaced by

$$\mathbf{x} = \chi(\mathbf{X}) . \tag{2.2}$$

The deformation from $\mathcal{B}_0$ to $\mathcal{B}$ in component form may be written as

$$x_i = \chi_i(X_\alpha) \tag{2.3}$$

with respect to origins $\mathbf{O}$ and $\mathbf{o}$ and an orthogonal Cartesian basis $\{\mathbf{E}_\alpha\}$ and $\{\mathbf{e}_i\}$ chosen by observer $\mathcal{O}$ in the reference and current configuration, respectively.
In order to analyse the deformation in a neighbourhood of a material particle X, the derivatives $\partial x_i / \partial X_\alpha$ are continuous and the differential of (2.3) is

$$\mathrm{d}x_i = \frac{\partial x_i}{\partial X_\alpha} \mathrm{d}X_\alpha \tag{2.4}$$

or in tensorial notation

$$\mathrm{d}\mathbf{x} = \mathbf{F}\,\mathrm{d}\mathbf{X}\,, \tag{2.5}$$

where $\mathbf{F}$ is a second-order tensor which is called the *deformation gradient*. In order to calculate $\mathbf{F}$ the following equation is used

$$\mathbf{F} = \mathrm{Grad}\,\mathbf{x} \quad \text{with} \quad \mathrm{Grad} = \frac{\partial}{\partial \mathbf{X}}\,. \tag{2.6}$$

Since the deformation gradient is set partially in the reference configuration and partially in the current configuration, it is often referred to as a *mixed Eulerian-Lagrangian* (or *two-point*) tensor, with one index in each configuration. The deformation gradient is given with respect to the bases $\{\mathbf{E}_\alpha\}$ and $\{\mathbf{e}_i\}$ as

$$\mathbf{F} = \frac{\partial x_i}{\partial X_\alpha}\,\mathbf{e}_i \otimes \mathbf{E}_\alpha\,. \tag{2.7}$$

According to (2.5), the deformation gradient maps a material line element $\mathrm{d}\mathbf{X}$ at the point $\mathbf{X}$ in the reference configuration onto the corresponding line element $\mathrm{d}\mathbf{x}$ at the point $\mathbf{x}$ in the current configuration. Additionally, $\mathbf{F}$ is required to be a non-singular tensor, in order to rule out the physically unrealistic case where the deformation reduces the length of line element of the material in the reference configuration to zero. This is possible if its determinant satisfies the inequality

$$J = \det \mathbf{F} > 0\,. \tag{2.8}$$

Following (2.8) the inverse of the deformation gradient exist and may be used to invert (2.5)

$$\mathrm{d}\mathbf{X} = \mathbf{F}^{-1}\,\mathrm{d}\mathbf{x} \quad \text{where} \quad \mathbf{F}^{-1} = \mathrm{grad}\,\mathbf{X} \quad \text{with} \quad \mathrm{grad} = \frac{\partial}{\partial \mathbf{x}}\,. \tag{2.9}$$

J is called the *Jacobian determinant* and can be interpreted as the local ratio of current to reference volume of a material volume element, or using conservation of mass in Section 2.2.1 as the ratio of the mass densities in the reference and current configuration

$$J = \frac{\mathrm{d}v}{\mathrm{d}V} = \frac{\rho_0}{\rho}\,. \tag{2.10}$$

If the current and reference configuration coincide or if the deformation is a rigid rotation, $J = 1$. Also, if the volume does not change locally during the deformation then

$$J = \det \mathbf{F} = 1 \tag{2.11}$$

at $\mathbf{X}$, and the deformation is said to be *isochoric* or volume preserving at $\mathbf{X}$. The deformation gradient is not practical for describing the distortion of the body, because it includes the total motion of the body between reference and

current configuration, According to the polar decomposition theorem, for any non-singular second order tensor $\mathbf{M}$ there exist unique positive definite symmetric second-order tensors $\mathbf{U}$ and $\mathbf{V}$, and an orthogonal second-order tensors $\mathbf{R}$ such that (cf. Ogden 1997 and Malvern 1969)

$$\mathbf{M} = \mathbf{RU} = \mathbf{VR}. \tag{2.12}$$

Since the deformation gradient $\mathbf{F}$ satisfies the prerequisite of the polar decomposition theorem, $\mathbf{F}$ may be decomposed into its right and left multiplicative decompositions

$$\mathbf{F} = \mathbf{RU} = \mathbf{VR}, \tag{2.13}$$

where the rotation tensor $\mathbf{R}$ is *proper* orthogonal

$$\mathbf{R}^{\mathrm{T}}\mathbf{R} = \mathbf{R}\mathbf{R}^{\mathrm{T}} = \mathbf{1} \quad \text{with} \quad \det \mathbf{R} = 1, \tag{2.14}$$

and the positive definite symmetric second-order tensors $\mathbf{U}$ and $\mathbf{V}$ are called the *right* and *left stretch* tensors, respectively. Here $\mathbf{1}$ is the second order unit (or identity) tensor. From (2.14) it follows that

$$\det \mathbf{F} = \det \mathbf{U} = \det \mathbf{V}. \tag{2.15}$$

It is possible to obtain the left stretch tensor $\mathbf{V}$ from the right stretch tensor $\mathbf{U}$ by forward-rotating with $\mathbf{R}$, and $\mathbf{U}$ from $\mathbf{V}$ by backward-rotating with $\mathbf{R}$

$$\mathbf{V} = \mathbf{RUR}^{\mathrm{T}}, \qquad \mathbf{U} = \mathbf{R}^{\mathrm{T}}\mathbf{VR}. \tag{2.16}$$

The deformation gradient $\mathbf{F}$ represents a pure strain if and only if $\mathbf{R} = \mathbf{1}$ and $\mathbf{F} = \mathbf{U} = \mathbf{V}$. For $\mathbf{U} = \mathbf{V} = \mathbf{1}$ and $\mathbf{R} \neq \mathbf{1}$, the deformation is said to be a rigid rotation. In general, it is possible to decompose the deformation into a stretch $\mathbf{U}$ followed by a rotation $\mathbf{R}$ (right polar decomposition), or using left polar decomposition, into a rotation $\mathbf{R}$ succeeded by a stretch $\mathbf{V}$.
The tensors $\mathbf{F}^{\mathrm{T}}\mathbf{F}$ and $\mathbf{F}\mathbf{F}^{\mathrm{T}}$ are called the *right* and *left Cauchy-Green* deformations tensors, respectively

$$\mathbf{C} = \mathbf{U}^2 = \mathbf{F}^{\mathrm{T}}\mathbf{F}, \qquad \mathbf{B} = \mathbf{V}^2 = \mathbf{F}\mathbf{F}^{\mathrm{T}}. \tag{2.17}$$

The tensors $\mathbf{C}$ and $\mathbf{B}$ are symmetric and positive definite. Similar as in (2.16) the following rotated relation between the Lagrangian tensor $\mathbf{C}$ and the Eulerian tensor $\mathbf{C}$ holds

$$\mathbf{B} = \mathbf{RCR}^{\mathrm{T}}, \qquad \mathbf{C} = \mathbf{R}^{\mathrm{T}}\mathbf{BR}. \tag{2.18}$$

In the solutions of special problems, it is usually better to use $\mathbf{C}$ and $\mathbf{B}$ rather then $\mathbf{U}$ and $\mathbf{V}$ as measures of strain, since the components of $\mathbf{U}$ and $\mathbf{V}$ are complicated irrational functions of the components of $\mathbf{F}$. However, for general considerations, $\mathbf{U}$ and $\mathbf{V}$ are often more suitable, see Truesdell & Noll (2003).

The deformation of an arbitrary line element $\mathrm{d}\mathbf{X}$ at the point $\mathbf{X}$ defines the notion of *strain*. The difference between squared lengths of the line element in the current and reference configuration can be calculated from (2.5)

$$|\mathrm{d}\mathbf{x}|^2 - |\mathrm{d}\mathbf{X}|^2 = \mathrm{d}\mathbf{X}(\mathbf{F}^{\mathrm{T}}\mathbf{F} - \mathbf{1})\mathrm{d}\mathbf{X}\,. \tag{2.19}$$

The material is *unstrained* at $\mathbf{X}$ if the length of the line element is unchanged after deformation and the right-hand side of (2.19) vanishes for arbitrary $\mathrm{d}\mathbf{X}$. In this case, the tensorial restriction

$$\mathbf{F}^{\mathrm{T}}\mathbf{F} = \mathbf{1} \tag{2.20}$$

must hold true.
The material is said to be *strained* at $\mathbf{X}$ if (2.20) is not satisfied at $\mathbf{X}$, and the tensor $\mathbf{F}^{\mathrm{T}}\mathbf{F} - \mathbf{1}$ can be regarded as a *strain tensor*. The strain tensor is then a measure of the change in length of an arbitrary line element of material. It is possible to write (2.19) in terms of $\mathrm{d}\mathbf{x}$ in the current configuration as

$$|\mathrm{d}\mathbf{x}|^2 - |\mathrm{d}\mathbf{X}|^2 = \mathrm{d}\mathbf{x}(\mathbf{1} - (\mathbf{F}\mathbf{F}^{\mathrm{T}})^{-1})\mathrm{d}\mathbf{x}\,, \tag{2.21}$$

and in this case the strain tensor has a form $\mathbf{1} - (\mathbf{F}\mathbf{F}^{\mathrm{T}})^{-1}$.
Set of general strain measures based on $\mathbf{U}$ or $\mathbf{V}$ can be established following the fact that the strain vanishes if and only if $\mathbf{U} = \mathbf{V} = \mathbf{1}$. The different second-order tensors defined in (2.22) are suitable measures of strain.

	Lagrange	Euler
$m \neq 0$	$\frac{1}{m}(\mathbf{U}^m - \mathbf{I})$	$\frac{1}{m}(\mathbf{V}^m - \mathbf{I})$
$m = 0$	$\ln \mathbf{U}$	$\ln \mathbf{V}$

(2.22)

In (2.22) m is an integer. In the cases $m = 2$ and $m = -2$ the *Green-Lagrange* strain tensor $\mathbf{E}$ defined over $\mathcal{B}_0$ and *Almansi-Euler* strain tensor $\mathbf{e}$ defined over $\mathcal{B}$ (cf. Ogden 1997)

$$\mathbf{E} = \frac{1}{2}(\mathbf{U}^2 - 1) \quad \text{and} \quad \mathbf{e} = \frac{1}{2}(1 - \mathbf{V}^{-2}) \tag{2.23}$$

are obtained. For $m = 0$, Hencky's logarithmic strain measures can be introduced

$$\mathbf{H} = \frac{1}{2}\ln(\mathbf{C}) \quad \text{and} \quad \mathbf{h} = \frac{1}{2}\ln(\mathbf{B})\,. \tag{2.24}$$

The logarithmic strains $\mathbf{H}$ and $\mathbf{h}$ posses some intrinsic features in contrast to other measures of strain, i.e. they can be additively decomposed in two parts which are associated with the change of the shape and the change of the volume of the body.

The velocity gradient $\mathbf{L}$ represents an important kinematic tensor in analysing strain velocities and can be obtained as

$$\mathbf{L} = \frac{\partial \dot{\mathbf{x}}}{\partial \mathbf{x}} = \dot{\mathbf{F}}\mathbf{F}^{-1}. \tag{2.25}$$

$\mathbf{L}$ can be interpreted as spatial gradient of the velocity $\dot{\mathbf{x}}$ and may be used to relate an Eulerian line element $\mathrm{d}\mathbf{x}$ to its material time derivative $\mathrm{d}\dot{\mathbf{x}}$

$$\mathrm{d}\dot{\mathbf{x}} = \mathbf{L}\mathrm{d}\mathbf{x}. \tag{2.26}$$

As a second-order tensor the velocity gradient $\mathbf{L}$ can be presented in the form

$$\mathbf{L} = \mathrm{sym}\mathbf{L} + \mathrm{skw}\mathbf{L} = \mathbf{D} + \mathbf{W}, \tag{2.27}$$

i.e. as a sum of a symmetric tensor

$$\mathbf{D} = \frac{1}{2}\left(\mathbf{L} + \mathbf{L}^{\mathrm{T}}\right) = \mathbf{D}^{\mathrm{T}} \tag{2.28}$$

called the *stretching* tensor or *Eulerian deformation rate* tensor and a skew-symmetric tensor

$$\mathbf{W} = \frac{1}{2}\left(\mathbf{L} - \mathbf{L}^{\mathrm{T}}\right) = -\mathbf{W}^{\mathrm{T}} \tag{2.29}$$

called *spin* or *vorticity* tensor. A measure of the rate at which line elements of material are changing their length is described by stretching tensor $\mathbf{D}$, and the vorticity tensor $\mathbf{W}$ contributes a rigid-body spin to the motion.

2.1.2 Kinetics

The action of the outside world on a body in motion and the interaction between the different parts of the body can be described using the concept of force. According to the *Cauchy's fundamental postulate*, it is assumed that the stress vector $\mathbf{t}$ at a position $\mathbf{x}$ depends on the surface only through the unit outward normal vector $\mathbf{n}$ to the considered surface at $\mathbf{x}$. In this case $\mathbf{t}$ has the same value for all surfaces through $\mathbf{x}$ which have a normal in the direction $\mathbf{n}$ at $\mathbf{x}$. As a result from Cauchy's fundamental postulate, it is possible to say that the stress vectors on two opposite cut surfaces of the body are equal but oppositely oriented

$$\mathbf{t}(\mathbf{x}, -\mathbf{n}) = -\mathbf{t}(\mathbf{x}, \mathbf{n}). \tag{2.30}$$

Additionally according to the *Cauchy's theorem*, if the stress vector $\mathbf{t}$ is continuous in $\mathbf{x}$, then the dependence on $\mathbf{n}$ is linear, i.e. there exists a second-order tensor $\boldsymbol{\sigma}$ independent of $\mathbf{n}$ such that

$$\mathbf{t}(\mathbf{x}, \mathbf{n}) = \boldsymbol{\sigma}(\mathbf{x})\mathbf{n}. \tag{2.31}$$

The tensor $\boldsymbol{\sigma}$ is called *Cauchy* or *true stress* tensor and it is a symmetric Eulerian stress measure.
Taking into account remarks concerning strain measures, different Lagrangian, two point and Eulerian stress measures may be established. Using Nanson's formula

$$\mathrm{d}\mathbf{a} = J\mathbf{F}^{-\mathrm{T}}\mathrm{d}\mathbf{A} \tag{2.32}$$

which relates current and reference elements of a surface area, it is possible to calculate the resultant contact force on the boundary $\partial\mathcal{B}$ of the current configuration $\mathcal{B}$ in terms of the force on the reference boundary $\partial\mathcal{B}_0$ of $\mathcal{B}_0$ as follows

$$\int_{\partial\mathcal{B}} \boldsymbol{\sigma}\mathbf{n}\mathrm{d}a = \int_{\partial\mathcal{B}_0} J\boldsymbol{\sigma}\mathbf{F}^{-\mathrm{T}}\mathbf{N}\mathrm{d}A \tag{2.33}$$

where $\mathbf{N}$ and $\mathbf{n}$ are outward unit normals on the boundary $\partial\mathcal{B}_0$ and $\partial\mathcal{B}$, respectively, and $\mathrm{d}A$ and $\mathrm{d}a$ are area elements of surface in $\mathcal{B}_0$ and $\mathcal{B}$, respectively.
By use of (2.33) the *first Piola Kirchhoff stress* tensor $\mathbf{T}$ can be calculated as

$$\mathbf{T} = J\boldsymbol{\sigma}\mathbf{F}^{-\mathrm{T}}\,. \tag{2.34}$$

The first Piola Kirchhoff stress tensor is a two-point tensor, which is in general an unsymmetric tensor. The transpose of $\mathbf{T}$ is called the *nominal stress* tensor $\mathbf{P}$

$$\mathbf{P} = \mathbf{T}^{\mathrm{T}} = J\mathbf{F}^{-1}\boldsymbol{\sigma}\,. \tag{2.35}$$

Locally, the Eulerian load vector $\mathrm{d}\mathbf{l} = \mathbf{t}\mathrm{d}a$ on an element of surface $\mathrm{d}a$ in the current configuration $\mathcal{B}$ may be expressed as

$$\mathrm{d}\mathbf{l} = \boldsymbol{\sigma}\mathrm{d}\mathbf{a} = \mathbf{T}\mathrm{d}\mathbf{A}\,. \tag{2.36}$$

A Lagrangian stress measure may be derived from (2.36) by multiplying with $\mathbf{F}^{-1}$, which leads to a Lagrangian load vector $\mathrm{d}\mathbf{L}$

$$\mathrm{d}\mathbf{L} = \mathbf{F}^{-1}\mathrm{d}\mathbf{l} = \mathbf{F}^{-1}\mathbf{T}\mathrm{d}\mathbf{A} = \mathbf{S}\mathrm{d}\mathbf{A}\,. \tag{2.37}$$

The second order Lagrangian tensor $\mathbf{S}$ is called the *second Piola Kirchhoff stress* tensor. Tensor $\mathbf{S}$ is a symmetric tensor, which has no physical meaning and is only used for calculation purposes

$$\mathbf{S} = J\mathbf{F}^{-1}\boldsymbol{\sigma}\mathbf{F}^{-\mathrm{T}} = \mathbf{F}^{-1}\mathbf{T} = \mathbf{P}\mathbf{F}^{-\mathrm{T}}\,. \tag{2.38}$$

An additional stress measure is frequently used in the description of different problems in continuum mechanics. It is the *Kirchhoff stress* $\boldsymbol{\tau}$, which is the Cauchy stress scaled by the Jacobian determinant

$$\boldsymbol{\tau} = J\boldsymbol{\sigma}\,. \tag{2.39}$$

The Kirchhoff stress is also called *weighted* Cauchy stress, and for isochoric motion it is identical to the Cauchy stress.
The so-called energy conjugate stress and strain variables play important role in the formulation of the internal energy of deformable bodies. All stress measures introduced above can be used to describe the internal energy of a body. However, if a decision is made about the use of a certain strain measure, the stress variable to be used in combination with this strain measure cannot be selected arbitrarily. Strain and stress variables with the property that each stress tensor is related through the *rate of the stresses* on the body (or *stress power*) to a well defined strain tensor, are referred to as *energy conjugate*. The stress power $\dot{w}$ is to be calculated using following energy conjugate stress-strain rate pairs (cf. Hill (1968))

$$\dot{w} = J\boldsymbol{\sigma} : \mathbf{D} = \boldsymbol{\tau} : \mathbf{D} = \mathbf{T} : \dot{\mathbf{F}} = \mathbf{S} : \dot{\mathbf{E}} . \tag{2.40}$$

2.1.3 Objectivity

Distances and time-intervals are fundamental measurable quantities of classical kinematics. Only if a frame of reference, or observer, is given, the position of an event can be specified. For example, different values to the speed of a moving point will be measured from two observers in relative motion. However, physical phenomena do not depend on the choice of observer in contrast to their kinematic descriptions, and therefor the mathematical formulation of physical laws must reflect this independence.
If an arbitrary origin in space is chosen, and the points with their position vectors are identified, it is possible to express a change of observer by the formula

$$\mathbf{x}^* = \mathbf{c}(t) + \mathbf{Q}(t)\mathbf{x} \quad \text{and} \quad t^* = t - a, \tag{2.41}$$

where $\mathbf{c}(t)$ and $\mathbf{Q}(t)$ are the relative translation and the rotation of two observers, and a is a time shift. The tensor $\mathbf{Q}(t)$ introduced above is a time dependent second-order proper orthogonal tensor which is uniquely determined by the choice of observer, but the vector $\mathbf{c}(t)$ depends also on the choice of the origin.
A choice of observer induces transformations, for each time t, on scalars, vectors and tensors. The quantities, which are independent of the choice of observer, are termed objective. Following Ogden (1997), it is to be distinguished between the transformation rules for Lagrangian and Eulerian quantities and two-point tensors. The transformation rules for Lagrangian and Eulerian quantities are given in Table 2.1. The objectivity criterion for a second-order two-point tensor is defined as follows

$$\tilde{\mathbf{A}}^*(\mathbf{X}, t^*) = \mathbf{Q}(t)\tilde{\mathbf{A}}^*(\mathbf{X}, t) . \tag{2.42}$$

According to these transformation rules, objectivity of introduced kinematic quantities can be analysed. It is possible to see, that the tensors $\mathbf{U}$, $\mathbf{C}$, $\mathbf{E}$ and

	Lagrangian configuration	Eulerian configuration
Scalar	$\hat{\alpha}^*(\mathbf{X}, t^*) = \hat{\alpha}^*(\mathbf{X}, t)$	$\alpha^*(\mathbf{x}^*, t^*) = \alpha(\mathbf{X}, t)$
Vector	$\hat{\boldsymbol{\alpha}}^*(\mathbf{X}, t^*) = \hat{\boldsymbol{\alpha}}^*(\mathbf{X}, t)$	$\boldsymbol{\alpha}^*(\mathbf{x}^*, t^*) = \mathbf{Q}(t)\boldsymbol{\alpha}(\mathbf{X}, t)$
Tensor	$\hat{\mathbf{A}}^*(\mathbf{X}, t^*) = \hat{\mathbf{A}}^*(\mathbf{X}, t)$	$\mathbf{A}^*(\mathbf{x}^*, t^*) = \mathbf{Q}(t)\mathbf{A}(\mathbf{X}, t)\mathbf{Q}(t)^{\mathrm{T}}$

Table 2.1: Transformation rules for different objective quantities depending on the configuration

$\mathbf{S}$ are objective Lagrangian tensors, the tensors $\mathbf{V}$, $\mathbf{B}$, $\mathbf{D}$, $\boldsymbol{\sigma}$ and $\boldsymbol{\tau}$ are objective Eulerian tensors, and the tensors $\mathbf{F}$, $\mathbf{R}$ and $\mathbf{T}$ are objective two-point tensor. Investigation of objectivity of material time derivatives is a further important question. In the case of a Lagrangian tensor, the material time derivative is an objective measure. On the other hand, material time derivatives of Eulerian tensors are not an objective measures. As an example, the material time derivative of an objective Eulerian stress tensor $\mathbf{A}$ is given

$$\dot{\mathbf{A}}^* = \dot{\overline{\mathbf{Q}\mathbf{A}\mathbf{Q}^{\mathrm{T}}}} = \dot{\mathbf{Q}}\mathbf{A}\mathbf{Q}^{\mathrm{T}} + \mathbf{Q}\dot{\mathbf{A}}\mathbf{Q}^{\mathrm{T}} + \mathbf{Q}\mathbf{A}\dot{\mathbf{Q}}^{\mathrm{T}}. \tag{2.43}$$

Although tensor $\mathbf{A}$ is an objective Eulerian second-order tensor, the material time derivative of $\mathbf{A}$ is not objective. If the time-dependent skew-symmetric Eulerian spin tensor $\boldsymbol{\Omega}^* = \dot{\mathbf{Q}}^{\mathrm{T}}\mathbf{Q} = -\mathbf{Q}^{\mathrm{T}}\dot{\mathbf{Q}}$ is used, (2.43) becomes

$$\dot{\mathbf{A}}^* = \dot{\overline{\mathbf{Q}\mathbf{A}\mathbf{Q}^{\mathrm{T}}}} = \mathbf{Q}\overset{\circ}{\mathbf{A}}{}^*\mathbf{Q}^{\mathrm{T}}, \tag{2.44}$$

where

$$\overset{\circ}{\mathbf{A}}{}^* = \dot{\mathbf{A}} + \mathbf{A}\boldsymbol{\Omega}^* - \boldsymbol{\Omega}^*\mathbf{A} \tag{2.45}$$

is the corotational rate of the tensor $\mathbf{A}$ defined by spin $\boldsymbol{\Omega}^*$. It is evident that there is an infinite number of different corotational rates, but not all of them are objective. The commonly known examples of objective corotational rates are Zaremba-Jaumann, Green-Naghdi and logarithmic rate with $\boldsymbol{\Omega}^{\mathrm{J}} = \mathbf{W}$ for the Zaremba-Jaumann rate, $\boldsymbol{\Omega}^{\mathrm{R}} = \dot{\mathbf{R}}\mathbf{R}^{\mathrm{T}}$ for the Green-Naghdi rate and $\boldsymbol{\Omega}^{\mathrm{Log}}$ given in (2.48) for the logarithmic rate. Well known non-corotational objective rates are Oldroyd rate, Cotter-Rivlin rate and Truesdell rate (cf. Xiao et al. 2000a). Besides represented corotational and non-corotational objective rates, one more possibility is the concept of Lie derivatives which provides a mathematically consistent method for defining objective time derivatives of tensors. The Lie derivative is essentially the set of operations which transforms an Eulerian measure from the current to the reference configuration (pull-back transformation),

produces a material time derivative of this measure in the reference configuration and transforms the derived measure from the reference to the current configuration (push-forward transformation).
As can be seen, many different objective material time derivatives are introduced, but most of them cannot satisfy the requirement that the stretching tensor $\mathbf{D}$ can be written as a direct flux of a strain measure. Up to now, only the logarithmic rate of the Eulerian Hencky strain $\mathbf{h}$ and the Lie derivative of Almansi-Euler strain tensor $\mathbf{e}$ with the deformation gradient $\mathbf{F}$ in the transformation rule are proven to satisfy this requirement

$$\mathbf{D} = \overset{\circ}{\mathbf{h}}^{\mathrm{Log}} = \dot{\mathbf{h}} + \mathbf{h}\,\boldsymbol{\Omega}^{\mathrm{Log}} - \boldsymbol{\Omega}^{\mathrm{Log}}\mathbf{h} \quad \text{and} \tag{2.46}$$

$$\mathbf{D} = \mathcal{L}_{\mathbf{F}}\mathbf{e} = \mathbf{F}^{-\mathrm{T}}(\overline{\mathbf{F}^{\mathrm{T}}\mathbf{e}\mathbf{F}})\mathbf{F}^{-1}\,, \tag{2.47}$$

where $\boldsymbol{\Omega}^{\mathrm{Log}}$ is the logarithmic spin tensor defined as

$$\boldsymbol{\Omega}^{\mathrm{Log}} = \mathbf{W} + \sum_{\sigma\neq\tau}^{n}\left(\frac{1+(\chi_\sigma/\chi_\tau)}{1-(\chi_\sigma/\chi_\tau)} + \frac{2}{\ln(\chi_\sigma/\chi_\tau)}\right)\mathbf{B}_\sigma\mathbf{D}\mathbf{B}_\tau\,, \tag{2.48}$$

and χ_i and $\mathbf{B}_i$ are eigenvalues and eigenprojections of the left Cauchy-Green tensor $\mathbf{B}$. The proper orthogonal tensor $\mathbf{R}^{\mathrm{Log}}$, called *logarithmic rotation* tensor, defines a rotating frame whose spin is the logarithmic spin $\boldsymbol{\Omega}^{\mathrm{Log}}$, and is derived from the tensor differential equation (see Bruhns et al.(1999, 2003) Xiao et al.(1997a, 1997b, 2000b, 2006))

$$\dot{\mathbf{R}}^{\mathrm{Log}} = -\mathbf{R}^{\mathrm{Log}}\boldsymbol{\Omega}^{\mathrm{Log}} \quad \text{and} \quad (\mathbf{R}^{\mathrm{Log}})|_{t=0} = \mathbf{1}\,. \tag{2.49}$$

2.2 Balance laws

In this section the principle of conservation of mass, linear and angular momentum, as well as the first and the second law of thermodynamics are presented. Only basic concepts and results of those laws are showed in this section, based on the works of Ogden (1997); Marsden & Hughes (1983); Truesdell & Noll (2003); Belytschko et al. (2000).

2.2.1 Conservation of mass

Observing the body B in the current configuration $\mathcal{B}$, the mass $m(B)$ in the considered current state is

$$m(B) = \int_{\mathcal{B}} \rho(\mathbf{x},t)\mathrm{d}v\,, \tag{2.50}$$

where $\rho(\mathbf{x},t)$ is the mass density and $\mathrm{d}v$ is the volume element for $\mathcal{B}$. The law of conservation of mass requires that the mass of a body remains constant during

deformation, which means that the mass cannot disappear or be created within the body, and that a mass transfer throughout the surface of the body does not exist. This leads to

$$\int_{\mathcal{B}} \rho \, \mathrm{d}v = \int_{\mathcal{B}_0} \rho_0 \, \mathrm{d}V \,. \tag{2.51}$$

Applying (2.51) to an arbitrary body, and using the continuity of ρ and (2.10) it follows that densities ρ_0 and ρ are related by

$$\rho = J^{-1} \rho_0 \,. \tag{2.52}$$

Equation (2.52) represents the *first local form of conservation of mass.* Since ρ is a smooth function, the material time derivative of (2.51) leads to

$$\dot{\rho} + \rho \, \mathrm{div}\mathbf{v} = 0 \,, \tag{2.53}$$

where $\dot{\mathbf{x}} = \mathbf{v}$ is the velocity field. Equation (2.53) is known as the *continuity condition* or the *second local form of conservation of mass.*

2.2.2 Conservation of linear momentum

The *linear momentum* of the body B in $\mathcal{B}$ at a arbitrary time t of the motion is defined by

$$\int_{\mathcal{B}} \rho \mathbf{v} \, \mathrm{d}v \,. \tag{2.54}$$

Further, it is supposed that the body B in $\mathcal{B}$ with boundary $\partial\mathcal{B}$ is subjected to *body forces* and the *contact forces*

$$\int_{\mathcal{B}} \rho \mathbf{b} \, \mathrm{d}v + \int_{\partial\mathcal{B}} \mathbf{t} \, \mathrm{d}a \,, \tag{2.55}$$

where $\mathbf{b}$ is the *body-force density* acting over $\mathcal{B}$ and represents the force per unit mass, and $\mathbf{t}$ is the *contact-force density* acting over boundary surface $\partial\mathcal{B}$ and is a force per unit area.
The *law of conservation of linear momentum* states that the rate of change of the linear momentum given in (2.54) is equal to the resultant external forces (2.55)

$$\frac{\mathrm{d}}{\mathrm{d}t} \int_{\mathcal{B}} \rho \mathbf{v} \, \mathrm{d}v = \int_{\mathcal{B}} \rho \mathbf{b} \, \mathrm{d}v + \int_{\partial\mathcal{B}} \mathbf{t} \, \mathrm{d}a \,. \tag{2.56}$$

Applying Cauchy's theorem (2.31) and the divergence theorem to the surface integral in (2.56) leads to the local form known as *Cauchy's first law of motion*

$$\rho \dot{\mathbf{v}} = \mathrm{div}\, \boldsymbol{\sigma} + \rho \mathbf{b} \,. \tag{2.57}$$

2.2.3 Conservation of angular momentum

The *angular momentum* (or *moment of momentum*) of the body B in $\mathcal{B}$ with respect to a point x_0 is defined as

$$\int_{\mathcal{B}} \rho\,(\mathbf{x}-\mathbf{x_0}) \times \mathbf{v}\,\mathrm{d}v\,. \tag{2.58}$$

The point $\mathbf{x_0}$ is an arbitrary point in $\mathcal{E}$ which needs not be a point of $\mathcal{B}$, but the value of the angular momentum depends on the choice of $\mathbf{x_0}$. The resultant moment of the applied external forces about point $\mathbf{x_0}$ is

$$\int_{\mathcal{B}} \rho\,(\mathbf{x}-\mathbf{x_0}) \times \mathbf{b}\,\mathrm{d}v + \int_{\partial\mathcal{B}} (\mathbf{x}-\mathbf{x_0}) \times \mathbf{t}\,\mathrm{d}a\,. \tag{2.59}$$

The *law of conservation of angular momentum* states that the rate of the change of angular momentum of the body is equal to the resultant moment of body- and surface-forces acting on the deformed body

$$\frac{\mathrm{d}}{\mathrm{d}t}\int_{\mathcal{B}} \rho\,(\mathbf{x}-\mathbf{x_0}) \times \mathbf{v}\,\mathrm{d}v = \int_{\mathcal{B}} \rho\,(\mathbf{x}-\mathbf{x_0}) \times \mathbf{b}\,\mathrm{d}v + \int_{\partial\mathcal{B}} (\mathbf{x}-\mathbf{x_0}) \times \mathbf{t}\,\mathrm{d}a\,. \tag{2.60}$$

Substitution of (2.57) and applying divergence theorem to the surface integral in (2.60) leads to *Cauchy's second law of motion*

$$\boldsymbol{\sigma}^{\mathrm{T}} = \boldsymbol{\sigma}\,, \tag{2.61}$$

which shows that the Cauchy stress tensor is a symmetric tensor if the angular momentum balance exists.

2.2.4 Conservation of energy

The *work of external forces* P_a done by body forces and surface tractions is defined by

$$P_a = \int_{\mathcal{B}} \rho\,\mathbf{b}\cdot\mathbf{v}\,\mathrm{d}v + \int_{\partial\mathcal{B}} \mathbf{t}\cdot\mathbf{v}\,\mathrm{d}a\,. \tag{2.62}$$

The *heat input* Q due to the *heat flux* h and the *internal heat source* r is defined by

$$Q = \int_{\mathcal{B}} \rho\,r\,\mathrm{d}v + \int_{\partial\mathcal{B}} h\,\mathrm{d}a\,, \tag{2.63}$$

where the heat flux is obtained by

$$h = -\mathbf{q}\cdot\mathbf{n}\,. \tag{2.64}$$

Here, $\mathbf{n}$ is the unit outward vector normal to the boundary surface element $\mathrm{d}\mathbf{a}$ and $\mathbf{q}$ is the *heat flux vector*. The negative sign of the first integral means that $\mathbf{q} \cdot \mathbf{n}$ expresses the positive heat flux out of the body.
The *total energy* W of the system consists of two parts, the *kinetic energy* K obtained by integration of the square of the body velocity over $\mathcal{B}$ and the *internal energy* U corresponding to the integral of the specific internal energy u over the mass of the body

$$W = K + U = \frac{1}{2} \int_{\mathcal{B}} \rho \mathbf{v} \cdot \mathbf{v} \, \mathrm{d}v + \int_{\mathcal{B}} \rho u \, \mathrm{d}v \,. \tag{2.65}$$

The *first law of thermodynamics* states that the rate of change of total energy W is equal to the sum of the work of external forces P_a and the heat input Q so that

$$\dot{W} = P_a + Q \,. \tag{2.66}$$

The weak form of the first law of thermodynamics is defined as

$$\int_{\mathcal{B}} \rho \dot{u} \, \mathrm{d}v = \int_{\mathcal{B}} (\boldsymbol{\sigma} : \mathbf{D} - \operatorname{div} \mathbf{q} + \rho r) \, \mathrm{d}v \,. \tag{2.67}$$

Last equation holds for an arbitrary domain, and the partial differential equation of energy conservation is given by

$$\rho \dot{u} = \boldsymbol{\sigma} : \mathbf{D} - \operatorname{div} \mathbf{q} + \rho r \,. \tag{2.68}$$

The Lagrangian description of the weak form of the first law of thermodynamics is defined as

$$\int_{\mathcal{B}_0} \rho_0 \dot{u} \, \mathrm{d}V = \int_{\mathcal{B}_0} (\mathbf{S} : \dot{E} - \operatorname{Div} \mathbf{Q} + \rho_0 r) \, \mathrm{d}V \,, \tag{2.69}$$

and the Lagrangian counterpart to (2.68) is

$$\rho_0 \dot{u} = \mathbf{S} : \dot{E} - \operatorname{Div} \mathbf{Q} + \rho_0 r \,, \tag{2.70}$$

where

$$\mathbf{Q} = J \mathbf{F}^{-1} \mathbf{q} \,. \tag{2.71}$$

2.2.5 Conservation of entropy

If the *specific entropy* of the body is denoted by s, then the *entropy* S of the body B is obtained by integration of s over $\mathcal{B}$

$$S = \int_{\mathcal{B}} \rho s \, \mathrm{d}v \,. \tag{2.72}$$

The *second law of thermodynamics* states that the total rate of increase of entropy in the body is greater than or equal to the entropy input supplied to the body from outside

$$\frac{\mathrm{d}}{\mathrm{d}t} \int_{\mathcal{B}} \rho s \, \mathrm{d}v \geq \int_{\mathcal{B}} \frac{\rho r}{\Theta} \, \mathrm{d}v - \int_{\partial \mathcal{B}} \frac{\mathbf{q} \cdot \mathbf{n}}{\Theta} \, \mathrm{d}a \,, \tag{2.73}$$

where Θ is the *absolute temperature*, and r/Θ is the specific rate of entropy production. Taking into account that the inequality is valid for arbitrary volumes and applying the divergence theorem to the surface integral gives

$$\rho \dot{s} - \frac{\rho r}{\Theta} + \mathrm{div} \frac{\mathbf{q}}{\Theta} \geq 0 \,. \tag{2.74}$$

Inequality (2.74) is known as *Clausius-Duhem inequality*. Let the *rate of internal entropy production* per unit mass $\dot{\gamma}$ be defined as

$$\rho \dot{\gamma} = \rho \dot{s} - \frac{\rho r}{\Theta} + \mathrm{div} \frac{\mathbf{q}}{\Theta} \,. \tag{2.75}$$

Hence, the Clausius-Duhem inequality is written as

$$\dot{\gamma} \geq 0 \,, \tag{2.76}$$

which means that the internal entropy production is always nonnegative. The *specific Helmholtz free energy* ψ is defined as

$$\psi = u - \Theta s \,. \tag{2.77}$$

Applying the first law of thermodynamics (2.68) in Clausius-Duhem inequality (2.74) to eliminate the internal heat source r and using the time derivative of the specific Helmholtz free energy leads to

$$\Theta \rho \dot{\gamma} = \boldsymbol{\sigma} : \mathbf{D} - \rho (\dot{\psi} + s \dot{\Theta}) - \frac{1}{\Theta} \mathbf{q} \cdot \mathrm{grad} \Theta \geq 0 \,. \tag{2.78}$$

Inequality (2.78) is called *reduced dissipation inequality*. In the Lagrangian formulation, inequalities (2.73), (2.74), (2.78) are given as

$$\frac{\mathrm{d}}{\mathrm{d}t} \int_{\mathcal{B}_0} \rho_0 s \, \mathrm{d}V \geq \int_{\mathcal{B}_0} \frac{\rho_0 r}{\Theta} \, \mathrm{d}V - \int_{\partial \mathcal{B}_0} \frac{\mathbf{Q} \cdot \mathbf{N}}{\Theta} \, \mathrm{d}A \,, \tag{2.79}$$

$$\rho_0 \dot{s} - \frac{\rho_0 r}{\Theta} + \mathrm{Div} \frac{\mathbf{Q}}{\Theta} \geq 0 \,, \tag{2.80}$$

$$\Theta \rho_0 \dot{\gamma} = \mathbf{S} : \dot{\mathbf{E}} - \rho_0 (\dot{\psi} + s \dot{\Theta}) - \frac{1}{\Theta} \mathbf{Q} \cdot \mathrm{Grad} \Theta \geq 0 \,. \tag{2.81}$$

3 Damage and fracture mechanics

First section of this chapter gives the basic notions in the damage mechanics. After that, the introduction of the fracture mechanics with emphasis on linear elastic fracture mechanics is presented. As one part of this work is concerned with the identification of material parameters, a suitable material model is presented in the third part of this chapter. The material model is developed by Schütte (2001) and it describes brittle damage behaviour. The last section introduces fundamentals of experimental fatigue analysis and concepts for the determination of the fatigue life. Since the purpose of this chapter is a brief introduction to the field of damage and fracture mechanics, the reader is referred to the cited literature for a more detailed investigation.

3.1 Damage mechanics

The damage in solid materials is an accumulation of many small defects inside the material by which they weaken. The mechanics of damage is the study of the mechanisms involved in this deterioration of materials when the materials are subjected to loading. According to Chaboche (1988) and Skrzypek & Ganczarski (1999), the *material damage* is the existence of distributed microscopic voids, cavities, or cracks of the size of crystal grains, and *damage evolution* is the process of void nucleation, growth and coalescence, which initiates the macrocracks and causes progressive material degradation through the strength and stiffness reduction.

3.1.1 Scale levels

It is possible to define different defects and damage models associate with them by using different scale levels. With respect to their scale, damage models may be referred to the macroscale (continuum mechanics), the mesoscale, the microscale (micromechanics) and the atomic scale (molecular dynamics). The graphical representation of these scale levels is given in Figure 3.1.
At the macroscale level, a defect is the growth of the crack. On this scale, the discontinuous and heterogeneous solid which suffers damage evolution is approximated by ideal pseudo undamaged continuum using the couples of *effective state variables* in the state and dissipation potential instead of classical state variables for the true (damaged) solid. The definition of the effective state variables can be based on so-called *damage equivalence principles* introduced in (3.1.4), where

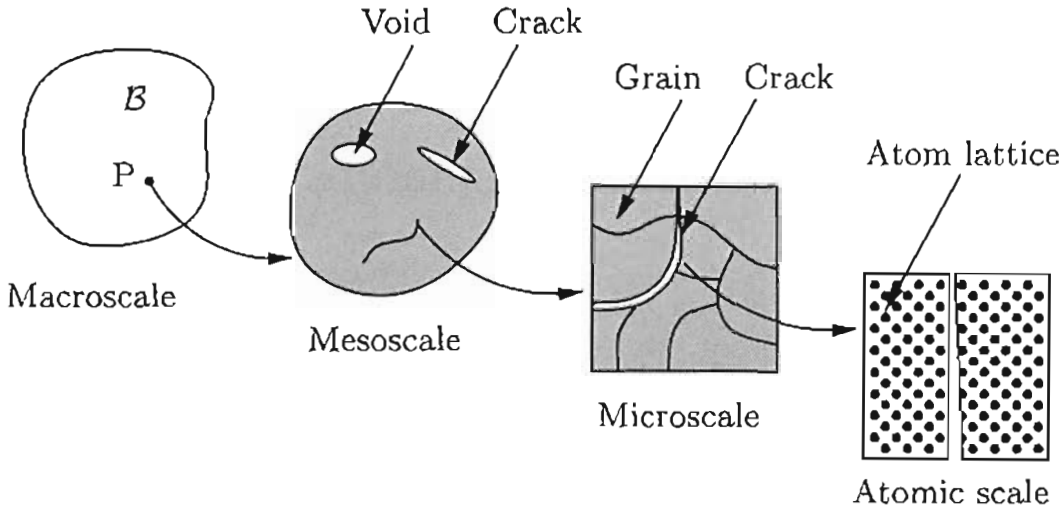

Figure 3.1: Representation of different scale levels

the effective state variables associated with the pseudo undamaged state are defined in such a way that the strains, the stresses, the elastic energy or the total energy in the damaged (true) and undamaged states are the same.

At the mesoscale level, defects of the representative volume element are represented as the growth and coalescence of microcracks or microvoids which initiate a single crack together.

The accumulation of microstresses in the neighbourhood of defects or interfaces and the breaking of bonds, which both damage the material, are characteristic for the microscale level. Single grains are visible in this scale, and they are described using continuum mechanic laws (Asaro & Rice 1977; Le et al. 1998). In general, the microscale and mesoscale level may be studied by means of damage variables of the mechanics of continuous media defined at the mesoscale level (see Lemaitre 1996).

At the atomic scale, at which the material structure is represented by a configuration of atoms in the order of crystal lattice or molecular chains bonded by interatomic forces, the material damage is determined by the configuration of atomic bonds, and the damage evolution is defined by breaking and re-establishing of atomic bonds. Continuum mechanics is not valid anymore on this scale and the connections between atoms and molecules must be determined.

In the continuum damage mechanics, it is assumed that the state of the damage of a volume element in a material is determined by the amount, dimensions and arrangement of the voids, cavities and cracks. It is possible to homogenise for the macroscale the true distribution of the interatomic bonds, dislocations and vacancies (atomic scale), or individual microvoids and microcracks (microscale) through a selection of the properly defined internal variables that characterise the damage state. These internal variables are called *damage variables.*

	Number of cycles to failure	Stress range σ	Strain ratio $\Delta\varepsilon^p/\Delta\varepsilon^e$	Energy ratio $\Delta W^p/\Delta W^e$
High cycle fatigue HCF	$> 10^5$	$< \sigma_y$	$\cong 0$	$\cong 0$
Low cycle fatigue LCF	10^2 to 10^4	σ_y to σ_u	1 to 10	1 to 10
Very low cycle fatigue VLCF	1 to 20	close to σ_u	10 to 100	10 to 100

Table 3.1: Classification of fatigue

3.1.2 Classification of fatigue damage

Fatigue damage is a damage of the material which appears under cyclic load and can manifest itself in various ways depending upon the nature of the material, the type of loading and the temperature. A useful classification according to Dufailly & Lemaitre (1995) and depending on the stress range and the number-of-cycles-to-failure range is given in Table (3.1). The following nomenclature is used: σ_y is the yield stress, σ_u is the ultimate stress, $\Delta\varepsilon^e$ and $\Delta\varepsilon^p$ are elastic and plastic strain amplitudes, ΔW^e and ΔW^p are elastic and plastic energies per cycles.

3.1.2.1 High cycle fatigue damage

When a material is loaded by the stress level σ which is below the yield stress ($\sigma < \sigma_y$), the plastic strain is very small and occurs only around microscopic defects. Consequently, the dissipative energy ΔW^p can be disregarded when compared to the reversible elastic energy ΔW^e. The number of cycles to failure is assumed to be larger than 10^5, and this case of fatigue is called the *high cycle fatigue* (HCF). Damage in HCF tests is a strongly localised phenomenon with high stress and damage concentration and has all characteristics of brittle damage. This strong localisation of the damage is not always compatible with continuum mechanics for which the damage is "uniformly" distributed in a volume element of a "finite" size. Even in the case of a uniform stress distribution, the HCF microcracks always start from the surface boundary of the body along the length of one or two crystals in a direction of about $\pi/4$ with respect to the direction of the maximum principle stress. Later, microcracks grow perpendicular to this direction and the development of a single crack is represented by the coalescence of several microcracks.
In Figure 3.2 stress-strain response for the strain loaded material under HCF is

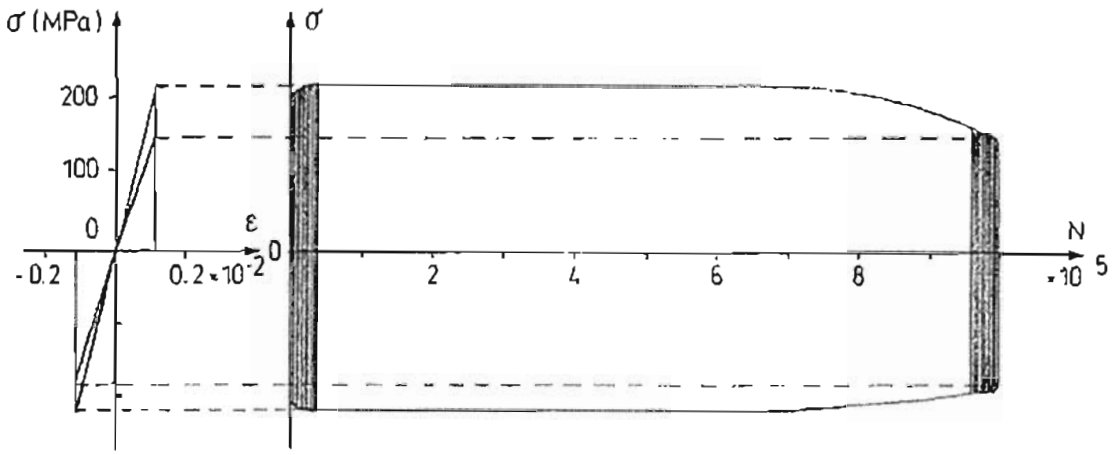

Figure 3.2: Cyclic tension-compression curves for high cycle fatigue of A 316 stainless steel (after J. Dufailly)

given. It is possible to see stress-strain loops corresponding to the stabilised cycle and stress-strain loops corresponding to the cycle close to the rupture. In the case of brittle damage and HCF damage, space localisation induces microplastic and damage zones much smaller than those of the specimen. This is the reason why a stress-strain curve obtained from a classical tension-compression test at the mesoscale usually does not represent the "true" behaviour for strain and damage.

3.1.2.2 Low cycle fatigue damage

In the case when the stress level σ is larger than the yield stress ($\sigma > \sigma_y$), the continuum damage develops together with the cyclic plastic strain after the incubation period and preceding the phases of nucleation and propagation of microcracks. The mechanism of the ductile damage is manifested through the transgranular slipbands fields of plasticity developed in the large size grains. Because of the high values of the stress, the number of cycles to failure is between 10^2 and 10^4 and it is the *low cycle fatigue* (LCF). In the case of LCF the dissipative energy ΔW^p is of the same order as the elastic energy ΔW^e. In other words, a large volume of the specimen with weak localisation is concerned for the plasticity damage field in LCF tests. The stress-strain response for the strain loaded material under LCF is given in Figure 3.3. It is possible to see that the drop of stress at the mesolevel for an experiment similar to that of Figure 3.2 occurs earlier.

In the case when the number of cycles is between 10^4 and 10^5, the success of both the high cycle fatigue model and low cycle fatigue model depends on the material and the loading.

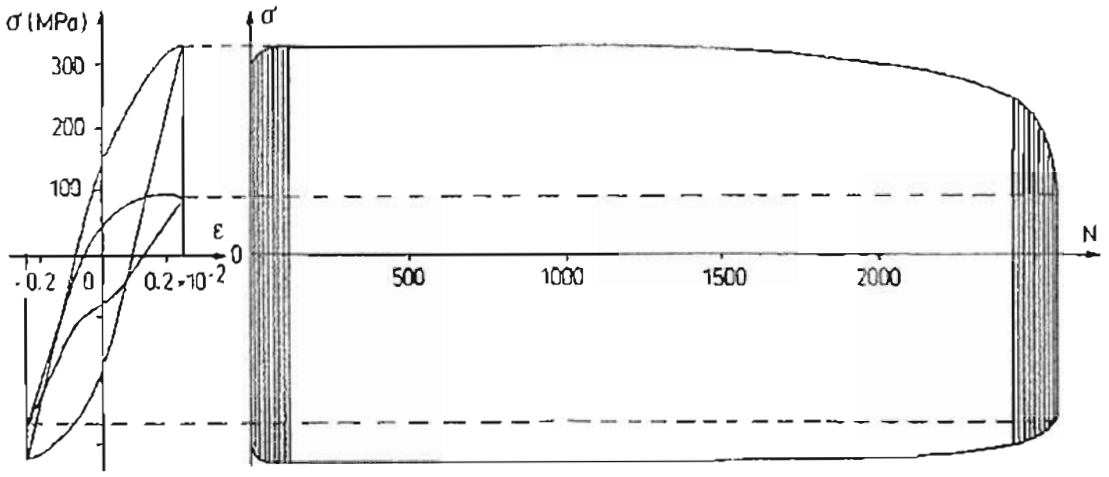

Figure 3.3: Cyclic tension-compression curves for low cycle fatigue of A 316 L stainless steel (after J. Dufailly)

3.1.2.3 Very low cycle fatigue damage

In the case when the stress level σ is close to the ultimate stress σ_u, the plastic strain $\Delta\varepsilon^p$ or the dissipative energy ΔW^p are much larger then the elastic strain $\Delta\varepsilon^e$ or the elastic energy ΔW^e, and the number of cycles to failure is of the order of 10. This state is called the *very low cycle fatigue* (VLCF). The main feature of VLCF is its high dependence on plasticity. The cyclic damage mechanism is governed by the slipbands of plasticity in the grains in the vicinity of the surface. They are oriented roughly at 45° to the main stress. In the transgranular mode a rapid crack growth in the slip planes is the reason why the influence of the grain size on the fatigue strength is large. In VLCF the number of sites with microcracks initiation is large enough to allow damage homogenisation. Since the damage evolution starts during or just after the first cycle no damage threshold is needed (cf. Dufailly & Lemaitre 1995).

3.1.3 Damage variables

The proper and accurate modelling of material damage represents the crucial problem of continuum damage mechanics. It is possible to homogenise the true distribution of damage in a quasicontinuum by using properly defined internal variables that characterise damage. Damage variables can be scalars, vectors, second-, fourth- or eight-order tensors. A scalar damage variable is sufficient to model isotropic damage processes, but modelling of anisotropic damage processes requires tensor valued damage variables. The review of damage variables used to describe damage process is given in Skrzypek & Ganczarski (1999).

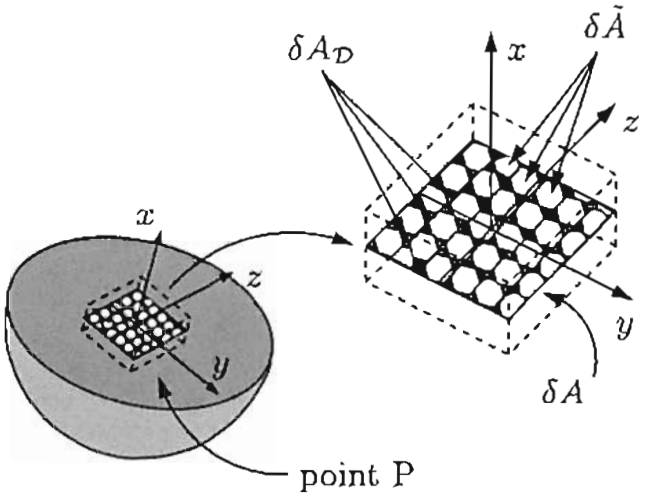

Figure 3.4: Surface damage measure - continuity definition by Kachanov

3.1.3.1 Scalar damage variables

In a pioneering paper, Kachanov (1958) proposed to characterise a gradual deterioration process of a microstructure by a scalar ψ, which is called *continuity*. For a completely undamaged material $\psi = 1$ and for a completely damaged material with no remaining load carrying capacity $\psi = 0$. According to Kachanov, the rate of the change of continuity is given by

$$\frac{\mathrm{d}\psi}{\mathrm{d}t} = -A\left(\frac{\sigma}{\psi}\right)^n , \tag{3.1}$$

where $A > 0$ and $n \geq 0$ are some material constants, and σ is the nominal stress. The quantity σ/ψ can be interpreted as a certain effective stress, and in this case, for an intersection surface area with normal $\mathbf{n}$ of the representative volume element (RVE) at the point P continuity ψ can be defined as

$$\psi = \frac{\delta\tilde{A}}{\delta A}, \quad \psi \in [0,1], \tag{3.2}$$

where $\delta\tilde{A}$ is the effective remaining area, which is deteriorated via microcrack and microvoid nucleation and evolution, and δA is the total undamaged area (Figure 3.4).
Later damage models introduce a *damage variable* $\mathcal{D}$, which in contrast to continuity ψ, represents the ratio between the area $\mathcal{D}$ of the intersection of all microcracks and microvoids with the plane δA and the total undamaged area δA. Obviously, $\mathcal{D}$ depends on the position (x) and orientation ($\mathbf{n}$) of the intersection area in RVE. It is given as

$$\mathcal{D}(P,\mathbf{n}) = \max_x \mathcal{D}(P,\mathbf{n},x) = \frac{\delta A_{\mathcal{D}}}{\delta A}, \quad \mathcal{D} \in [0,1], \quad \delta A = \delta\tilde{A} + \delta A_{\mathcal{D}}. \tag{3.3}$$

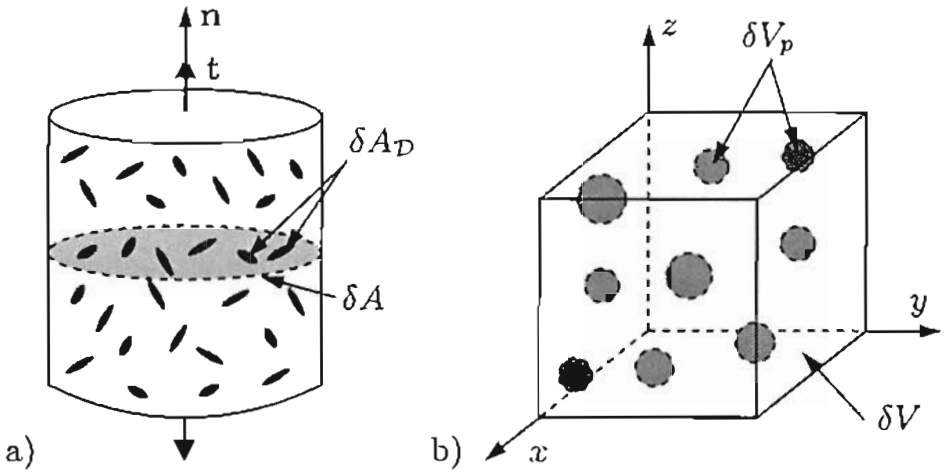

Figure 3.5: Representation of damage measure: a) damaged volume element (Rabatnov), b) void volume fraction in the RVE (Gurson)

Here $\mathcal{D}=1-\psi=0$ corresponds to the undamaged state of the considered surface element, and $\mathcal{D}=1$ to the completely damaged element. In fact, the failure occurs for $\mathcal{D}<1$ through a process of instability.
Another scalar valued damage variable is introduced by Rabotnov (1968). He considers a one-dimensional damaged volume element loaded by a tension force $\mathbf{t}=\mathbf{n}t$. The uniaxial stress for the undamaged material is given as

$$\sigma = \frac{t}{\delta A}\,. \tag{3.4}$$

For the case that all defects are open in a such way that no microforces are acting on the surfaces of microcracks, it is possible to introduce the stress $\tilde{\sigma}$ related to the surface that effectively resists the load

$$\tilde{\sigma} = \frac{t}{\delta A - \delta A_{\mathcal{D}}} = \frac{\sigma}{1-\mathcal{D}}\,, \tag{3.5}$$

where the damage variable $\mathcal{D}$ is defined by (3.3), and $\tilde{\sigma}$ is the *effective uniaxial stress* in the material in tension (Figure 3.5a). The damage remains unchanged in the case of compression, but some defects close and the surface that effectively resists the load is larger than $\delta A-\delta A_{\mathcal{D}}$. Therefore, the effective stress in compression is between σ and $\tilde{\sigma}$ for tension. This problem with the calculation of the effective damage area $\delta A_{\mathcal{D}}$ in compression can be overcome by the introduction of a crack closure parameter which depends on the material and the loading (see Lemaitre (1996) for more details).
Another possibility for the determination of a damage variable is given by Gurson (1977). It takes into account the nucleation and the growth of voids in the case of ductile fracture in metals (Figure 3.5b). The current void volume fraction f

in a RVE is defined as a ratio between the void volume δV_v and the volume of the undamaged RVE δV

$$f = \frac{\delta V_v}{\delta V} . \tag{3.6}$$

Considering an idealised case when a single spherical cavity is nucleated within a spherical RVE and assuming no density change of the solid constituent RVE, the relation between the void volume fraction f and the surface damage parameter $\mathcal{D}$ is given by

$$\mathcal{D} = f^{2/3} . \tag{3.7}$$

3.1.3.2 Second-order damage tensors

It is possible to see from (3.3) that the damage variable $\mathcal{D}$ depends on the position and orientation of the intersection area in the RVE. In the direction of the normal $\mathbf{n}$, the scalar equation is given as

$$\delta\tilde{A} = (1 - \mathcal{D}(\mathbf{n}))\delta A . \tag{3.8}$$

According to Murakami & Ohno (1981), (3.8) can be extended to a three dimensional case using normals $\mathbf{n}_1$, $\mathbf{n}_2$ and $\mathbf{n}_3$ for three orthogonal directions

$$\delta\tilde{A}_i = (1 - \mathcal{D}_i)\delta A_i , \quad i = 1, 2, 3 . \tag{3.9}$$

In case of arbitrary coordinate system, (3.9) is given as

$$\delta\tilde{\mathbf{A}} = \tilde{\mathbf{n}}\delta\tilde{A} = (\mathbf{1} - \boldsymbol{\mathcal{D}})\mathbf{n}\delta A = (\mathbf{1} - \boldsymbol{\mathcal{D}})\delta\mathbf{A} , \tag{3.10}$$

where $\boldsymbol{\mathcal{D}}$ is a symmetric second-order damage tensor

$$\boldsymbol{\mathcal{D}} = \sum_{i=1}^{3} \mathcal{D}_i \mathbf{n}_i \otimes \mathbf{n}_i , \tag{3.11}$$

and $\mathcal{D}_i$ and $\mathbf{n}_i$ are the principal values and the unit vectors of principal directions of the damage tensor $\boldsymbol{\mathcal{D}}$. Using Cauchy's theorem (2.31), the stress vector $\mathbf{t}$ for either an undamaged surface element or a damaged surface element can be defined by

$$\mathbf{t} = \boldsymbol{\sigma}\delta\mathbf{A} = \tilde{\boldsymbol{\sigma}}\delta\tilde{\mathbf{A}} . \tag{3.12}$$

Applying (3.10) in (3.12) leads to the effective stress tensor

$$\tilde{\boldsymbol{\sigma}} = \boldsymbol{\sigma}(\mathbf{1} - \boldsymbol{\mathcal{D}})^{-1} , \tag{3.13}$$

which is in general an unsymmetric tensor.
Using a symmetric second order damage tensor $\boldsymbol{\mathcal{D}}$ gives the possibility to represent damage induced by anisotropy through the orthotropy with three orthogonal

symmetry planes. In the case of isotropic damage, the mechanical behaviour of microcracks or microvoids is independent of their orientation and depends only on a scalar damage variable $\mathcal{D}$. Accordingly, second-order damage tensor $\boldsymbol{\mathcal{D}}$ is given as volumetric tensor $\boldsymbol{\mathcal{D}} = \mathcal{D}\mathbf{1}$.
Various authors proposed stress concepts with a symmetric effective stress tensor $\tilde{\boldsymbol{\sigma}}$ (cf. Zheng & Betten 1996)

- $\tilde{\boldsymbol{\sigma}} = (\mathbf{1} - \boldsymbol{\mathcal{D}})^{-1/2} : \boldsymbol{\sigma} : (\mathbf{1} - \boldsymbol{\mathcal{D}})^{-1/2}$ (Cordebois & Sidoroff 1982),
- $\tilde{\boldsymbol{\sigma}} = (\mathbf{1} - \boldsymbol{\mathcal{D}})^{-1} : \boldsymbol{\sigma} : (\mathbf{1} - \boldsymbol{\mathcal{D}})^{-1}$ (Betten 1986),
- $\tilde{\boldsymbol{\sigma}} = \frac{1}{2}(\boldsymbol{\sigma}(\mathbf{1} - \boldsymbol{\mathcal{D}})^{-1} + (\mathbf{1} - \boldsymbol{\mathcal{D}})^{-1}\boldsymbol{\sigma})$ (Murakami 1988).

3.1.3.3 Fourth-order damage tensors

In order to model arbitrary anisotropic damage processes Chaboche (1981), Simo & Ju (1987), Chow & Wang (1987), Leckie & Onat (1981) and other authors proposed to expand the second-order damage tensor $\boldsymbol{\mathcal{D}}$ in (3.13) to the fourth-order damage tensor $\mathbb{D}$

$$\tilde{\boldsymbol{\sigma}} = (\mathbb{I} - \mathbb{D})^{-1} : \boldsymbol{\sigma} = \mathbb{M} : \boldsymbol{\sigma}\,, \tag{3.14}$$

where $\mathbb{I}$ is a fourth-order *identity* tensor, $\mathbb{D}$ is the fourth-order *damage* tensor, and $\mathbb{M}$ is a linear symmetric operator represented as a fourth-order *damage effect* tensor.
$\mathbb{M}$ characterises the state of the damage and transforms the Cauchy stress tensor $\boldsymbol{\sigma}$ in a damaged configuration into the effective stress tensor $\tilde{\boldsymbol{\sigma}}$ in an equivalent pseudo undamaged solid. In the case of isotropic damage fourth-order damage effect tensor $\mathbb{M}$ will simply reduce to $\mathbb{M} = (1 - \mathcal{D})\mathbb{I}$.

3.1.4 Damage equivalence principles

The mechanical state of a damaged solid in a current configuration is defined through the external and internal variables $(\boldsymbol{\sigma}, \boldsymbol{\varepsilon}, \mathbb{D})$, where $\boldsymbol{\sigma}$ is the Cauchy stress tensor, $\boldsymbol{\varepsilon}$ is the linear strain tensor and $\mathbb{D}$ is the damage tensor. In order to use the simplicity of the undamaged solid, a fictive pseudo undamaged configuration is introduced. In this configuration the mechanical state can be characterised by

$$(\boldsymbol{\sigma}, \boldsymbol{\varepsilon}, \mathbb{D}) \equiv (\tilde{\boldsymbol{\sigma}}, \tilde{\boldsymbol{\varepsilon}}, \mathbb{D} = 0) \equiv (\tilde{\boldsymbol{\sigma}}, \tilde{\boldsymbol{\varepsilon}})\,, \tag{3.15}$$

where $\tilde{\boldsymbol{\sigma}}$ is the effective stress, and $\tilde{\boldsymbol{\varepsilon}}$ is the effective strain. In the pseudo undamaged configuration all material parameters and constitutive laws for the undamaged state must hold. Then it is possible to calculate the damage effect tensor by assuming that one variable stays unchanged under damage. This assumption is incorporated in various damage equivalence principles.

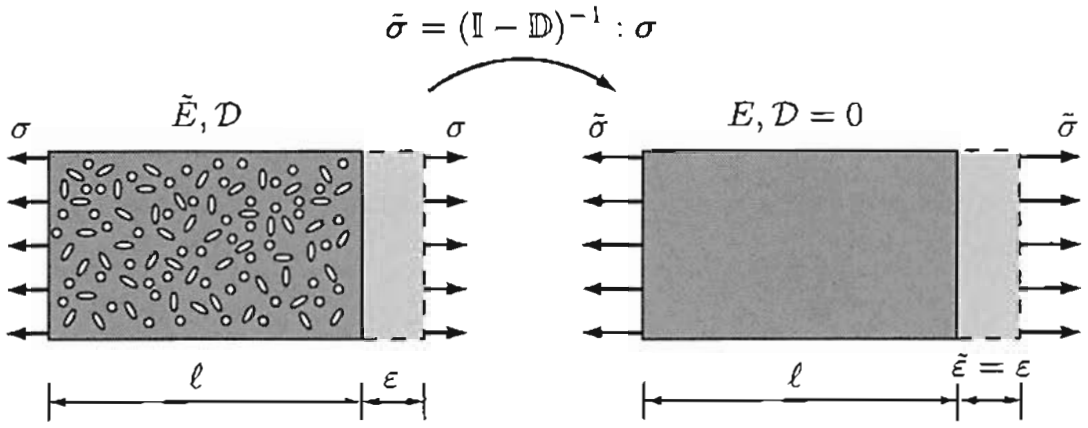

Figure 3.6: One-dimensional representation of strain equivalence concept

3.1.4.1 Principle of strain equivalence

The *principle of strain equivalence* is also known as *the effective stress concept.* It states that the strain associated with a damaged state under the applied stress σ is equivalent to the strain associated with the undamaged state under the effective stress $\tilde{\sigma}$ (Chaboche 1984, Lemaitre 1996) (see Figure 3.6):

$$\tilde{\varepsilon}(\tilde{\sigma}, 0) = \varepsilon(\sigma, \mathbb{D}) . \tag{3.16}$$

In the general case, the stress-strain relation in the undamaged linear elastic material is represented by Hooke's law

$$\sigma = \mathbb{C} : \varepsilon , \tag{3.17}$$

where $\mathbb{C}$ is the fourth-order *elastic stiffness* tensor. In the case of damaged material Hooke's law has a form

$$\sigma = \tilde{\mathbb{C}} : \varepsilon , \tag{3.18}$$

where $\tilde{\mathbb{C}}$ is the fourth-order *damaged elastic stiffness* tensor. Based on the principle of strain equivalence (3.16), and on (3.18), the stress-strain relation in the undamaged configuration with undamaged elastic stiffness tensor reads

$$\tilde{\sigma} = \mathbb{C} : \tilde{\varepsilon} = \mathbb{C} : \varepsilon = \mathbb{C} : \tilde{\mathbb{C}}^{-1} : \sigma . \tag{3.19}$$

Applying the definition of damage effect tensor (3.14) the damage tensor $\mathbb{D}$ and damaged elastic stiffness tensor $\tilde{\mathbb{C}}$ are given as

$$\mathbb{D} = \mathbb{I} - \tilde{\mathbb{C}} : \mathbb{C}^{-1} \quad \text{and} \quad \tilde{\mathbb{C}} = (\mathbb{I} - \mathbb{D}) : \mathbb{C} . \tag{3.20}$$

It should be pointed out, that the principle of strain equivalence leads to the restrictive conclusion that the Poisson ratio is not affected by damage. It would be mean that the material is damaged only in the direction of the tensile stresses

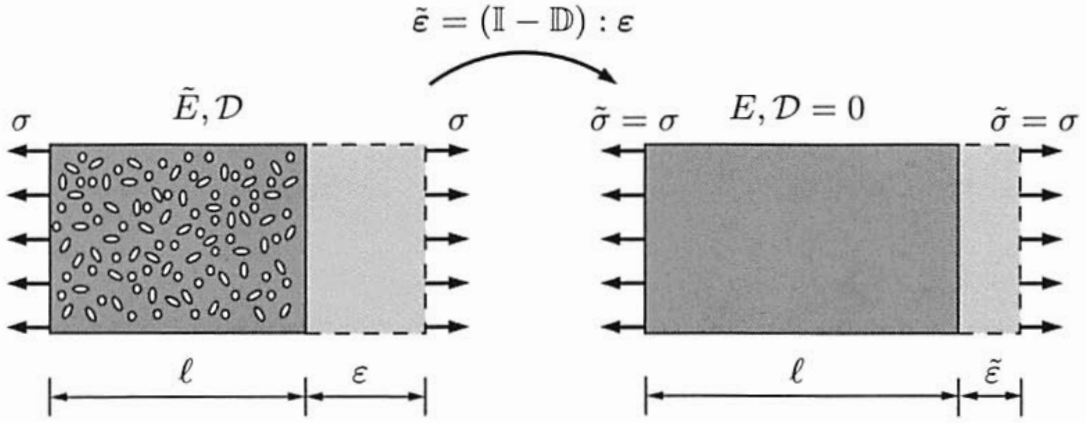

Figure 3.7: One-dimensional representation of stress equivalence concept

in a uniaxial tension test. For most materials this assumption is questionable since the nucleation and the growth of microcracks and microvoids results in a stress redistribution due to the cross-sectional area reduction and the decrease of stiffness in the material (cf. Chow & Lu 1992).

3.1.4.2 Principle of stress equivalence

The *principle of stress equivalence* is also known as *the effective strain concept.* It states that the stress associated with a damaged state under the applied strain $\boldsymbol{\varepsilon}$ is equivalent to the stress associated with the undamaged state under the effective strain $\tilde{\boldsymbol{\varepsilon}}$ (Cordebois & Sidoroff 1979, Simo & Ju 1987) (see Figure 3.7):

$$\tilde{\boldsymbol{\sigma}}(\tilde{\boldsymbol{\varepsilon}}, 0) = \boldsymbol{\sigma}(\boldsymbol{\varepsilon}, \mathbb{D}) \,. \tag{3.21}$$

If the analogy with the principle of strain equivalence is used, it is possible to define damaged elastic stiffness tensor and damage tensor. Consideration of the inverse stress-strain relation for damaged and fictive undamaged linear elastic material

$$\boldsymbol{\varepsilon} = \tilde{\mathbb{C}}^{-1} : \boldsymbol{\sigma} \quad \text{and} \quad \tilde{\boldsymbol{\varepsilon}} = \mathbb{C}^{-1} : \tilde{\boldsymbol{\sigma}} \,, \tag{3.22}$$

and the principle of stress equivalence (3.7) gives

$$\tilde{\boldsymbol{\varepsilon}} = \mathbb{C}^{-1} : \boldsymbol{\sigma} = \mathbb{C}^{-1} : \tilde{\mathbb{C}} : \boldsymbol{\varepsilon} \,. \tag{3.23}$$

Equivalent to the definition of damage effect tensor (3.14)

$$\tilde{\boldsymbol{\varepsilon}} = (\mathbb{I} - \mathbb{D}) : \boldsymbol{\varepsilon} \,. \tag{3.24}$$

The damage tensor $\mathbb{D}$ and the damaged elastic stiffness tensor $\tilde{\mathbb{C}}$ are given as

$$\mathbb{D} = \mathbb{I} - \mathbb{C}^{-1} : \tilde{\mathbb{C}} \quad \text{and} \quad \tilde{\mathbb{C}} = \mathbb{C} : (\mathbb{I} - \mathbb{D}) \,. \tag{3.25}$$

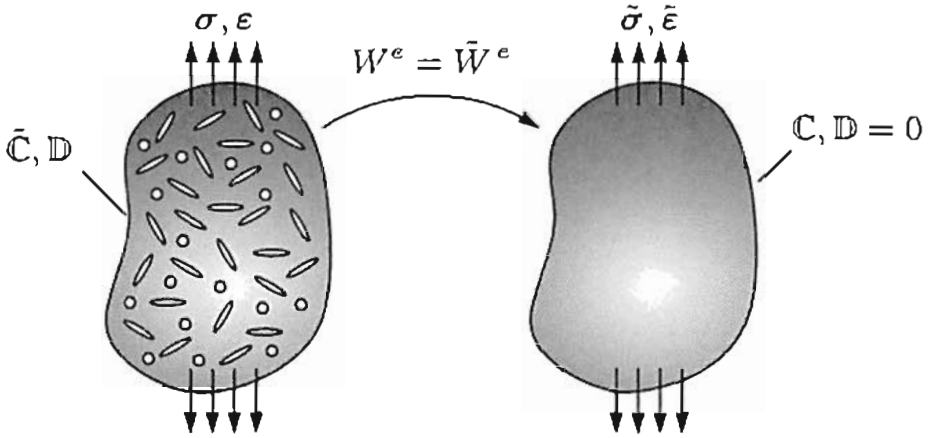

Figure 3.8: Three-dimensional representation of principle of complementary elastic energy equivalence

3.1.4.3 Principle of complementary elastic energy equivalence

In the principles presented in 3.1.4.1 and 3.1.4.2, the effective stress or effective strain distribution is affected by the stiffness reduction due to microcracks or microvoids growth, contrarily to the strain or stress tensor. According to Skrzypek & Ganczarski 1999, real irreversible thermodynamic material degradation processes are not properly described through these two principles. In order to define the fictive pseudo undamaged equivalent configuration and corresponding effective variables $\tilde{\sigma}$ and $\tilde{\varepsilon}$, Cordebois & Sidoroff (1979) introduce the *principle of complementary elastic energy equivalence*. It states that the elastic energy associated with a damaged state under the applied stress $\boldsymbol{\sigma}$ and corresponding strain $\boldsymbol{\varepsilon}$ is equivalent to the elastic energy associated with the undamaged state, if the effective stress $\tilde{\sigma}$ and the effective strain $\tilde{\varepsilon}$ are used in the elastic potential (see Figure 3.8):

$$W^e(\boldsymbol{\sigma}, \boldsymbol{\varepsilon}, \mathcal{D}) = \tilde{W}^e(\tilde{\boldsymbol{\sigma}}, \tilde{\boldsymbol{\varepsilon}}, 0)\,. \tag{3.26}$$

where W^e is the elastic energy associated with a damaged state, and $\tilde{W}^e$ is elastic energy associated with the undamaged state:

$$W^e = \frac{1}{2}(\boldsymbol{\sigma} : \boldsymbol{\varepsilon}) = \frac{1}{2}(\boldsymbol{\sigma} : \tilde{\mathbb{C}}^{-1} : \boldsymbol{\sigma})\,, \tag{3.27}$$

$$\tilde{W}^e = \frac{1}{2}(\tilde{\boldsymbol{\sigma}} : \tilde{\boldsymbol{\varepsilon}}) = \frac{1}{2}(\tilde{\boldsymbol{\sigma}} : \mathbb{C}^{-1} : \tilde{\boldsymbol{\sigma}})\,. \tag{3.28}$$

If the principle of complementary elastic energy equivalence (3.26) is used in (3.27) and (3.28), the effective stress and strain tensors are given as

$$\tilde{\boldsymbol{\sigma}} = (\mathbb{I} - \mathbb{D})^{-1} : \boldsymbol{\sigma}\,, \quad \tilde{\boldsymbol{\varepsilon}} = (\mathbb{I} - \mathbb{D}) : \boldsymbol{\varepsilon}\,, \tag{3.29}$$

and the fourth-order damage tensor $\mathbb{D}$ is defined as

$$\mathbb{D} = \mathbb{I} - \tilde{\mathbb{C}}^{1/2} : \mathbb{C}^{1/2} . \tag{3.30}$$

Opposite to the principles of strain and stress equivalence where the local stiffness drop results exclusively in a local stress decrease or a local strain increase, the microcrack or microvoid growth influences both the stress and the strain distribution in the energy based damage equivalence model.

3.1.4.4 Principle of total energy equivalence

The principle of complementary elastic energy equivalence, which is limited to the cases of damage coupled elasticity, is extended by Chow & Lu (1992) for the description of inelastic material response affected by anisotropic damage. For a material undergoing progressive deterioration and using conditions of infinitesimal deformation, quasistatic damage growth and negligible thermal effects, the first law of thermodynamics requires that

$$\mathrm{d}W = \mathrm{d}W^e + \mathrm{d}W^d + \mathrm{d}W^p , \tag{3.31}$$

where $\mathrm{d}W = \int \boldsymbol{\sigma} : \mathrm{d}\boldsymbol{\varepsilon}$ is the work of the applied forces, $W^e = (1/2)\boldsymbol{\sigma} : \boldsymbol{\varepsilon}^e$ represents the elastic energy, W^p is the plastic work, and W^d is the work due to damage nucleation and propagation.

$$\mathrm{d}W = \boldsymbol{\sigma} : \mathrm{d}\boldsymbol{\varepsilon} , \quad \mathrm{d}W^e = \frac{1}{2}(\boldsymbol{\sigma} : \mathrm{d}\boldsymbol{\varepsilon}^e + \mathrm{d}\boldsymbol{\sigma} : \boldsymbol{\varepsilon}^e) , \quad \mathrm{d}W^p = \boldsymbol{\sigma} : \mathrm{d}\boldsymbol{\varepsilon}^p . \tag{3.32}$$

The *principle of total energy equivalence* states the existence of a pseudo undamaged solid made of virgin material, in the sense that the total work done by external tractions during the same load history as that for the real, damaged material, is not changed (cf. Chow & Lu 1992) (see Figure 3.9).

$$\mathrm{d}W(\boldsymbol{\sigma}, \boldsymbol{\varepsilon}, \mathcal{D}) = \mathrm{d}\tilde{W}(\tilde{\boldsymbol{\sigma}}, \tilde{\boldsymbol{\varepsilon}}, 0) , \tag{3.33}$$

or

$$\mathrm{d}W^e + \mathrm{d}W^d = \mathrm{d}\tilde{W}^e \quad \text{and} \quad \mathrm{d}W^p = \mathrm{d}\tilde{W}^p , \tag{3.34}$$

where

$$\mathrm{d}\tilde{W} = \tilde{\boldsymbol{\sigma}} : \mathrm{d}\tilde{\boldsymbol{\varepsilon}} , \quad \mathrm{d}\tilde{W}^e = \frac{1}{2}(\tilde{\boldsymbol{\sigma}} : \mathrm{d}\tilde{\boldsymbol{\varepsilon}}^e + \mathrm{d}\tilde{\boldsymbol{\sigma}} : \tilde{\boldsymbol{\varepsilon}}^e) , \quad \mathrm{d}\tilde{W}^e = \tilde{\boldsymbol{\sigma}} : \mathrm{d}\tilde{\boldsymbol{\varepsilon}}^p . \tag{3.35}$$

Using the equivalent form of (3.33)-(3.35) leads to

$$\begin{aligned} &\boldsymbol{\sigma} : \mathrm{d}\boldsymbol{\varepsilon} = \tilde{\boldsymbol{\sigma}} : \mathrm{d}\tilde{\boldsymbol{\varepsilon}} , \\ &\frac{1}{2}(\boldsymbol{\sigma} : \mathrm{d}\boldsymbol{\varepsilon}^e + \mathrm{d}\boldsymbol{\sigma} : \boldsymbol{\varepsilon}^e) = \frac{1}{2}(\tilde{\boldsymbol{\sigma}} : \mathrm{d}\tilde{\boldsymbol{\varepsilon}}^e + \mathrm{d}\tilde{\boldsymbol{\sigma}} : \tilde{\boldsymbol{\varepsilon}}^e) , \\ &\boldsymbol{\sigma} : \mathrm{d}\boldsymbol{\varepsilon}^p = \tilde{\boldsymbol{\sigma}} : \mathrm{d}\tilde{\boldsymbol{\varepsilon}}^p , \end{aligned} \tag{3.36}$$

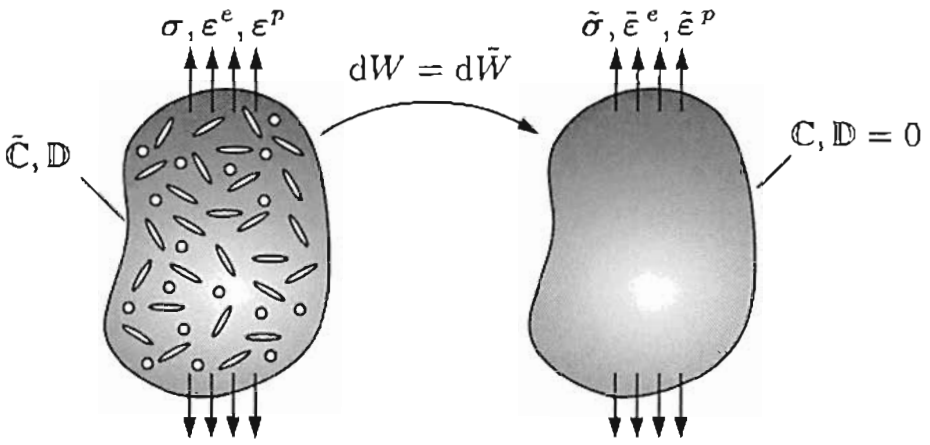

Figure 3.9: Three-dimensional representation of principle of total energy equivalence

where the state variables on the left-hand side of (3.36) refer to the physical (damaged) configuration, and the effective state variables on the right-hand side refer to the energy equivalent fictive (pseudo undamaged) configuration.
As proposed by Chow & Lu (1992), the effective state variables obtained from the principle of total energy equivalence are given as

$$\tilde{\sigma} = \mathbb{M}(\mathcal{D}) : \sigma\,, \quad \tilde{\varepsilon}^{\,e} = \mathbb{M}^{-1}(\mathcal{D}) : \varepsilon^{\,e}\,, \quad \mathrm{d}\tilde{\varepsilon}^{\,p} = \mathbb{M}^{-1}(\mathcal{D}) : \mathrm{d}\varepsilon^{\,p}\,, \tag{3.37}$$

where the elements of a fourth-order damage effect tensor $\mathbb{M}(\mathcal{D})$ are dependent on the anisotropic damage representation by the second-order $\mathbf{D}$ or fourth-order $\mathbb{D}$ damage tensor components.

3.2 Fracture mechanics

The behaviour of solids and structures with macroscopic discontinuities at the structural scale is described by fracture mechanics. These discontinuities can be line discontinuities in a two-dimensional media (e.g. in plates and shells) and surface discontinuities in a three-dimensional media. In contrast to damage mechanics, which is used to predict the initiation of a macroscopic crack, fracture mechanics is used to predict the evolution of the crack until the final failure of the structure. These discontinuities modify the stress, strain and displacement fields on such a scale that the assumption of a homogeneous medium would no longer be meaningful and they must be taken into account in structural analysis. The failure of a brittle elastic medium could be characterised by a variable, whose critical value is independent of the structure geometry and is characteristic of material, as introduced by Griffith (1921). This variable is called the *energy release rate*. This approach, called *global approach*, shows that the essential phenomena occur in the vicinity of the crack front and that it is possible to

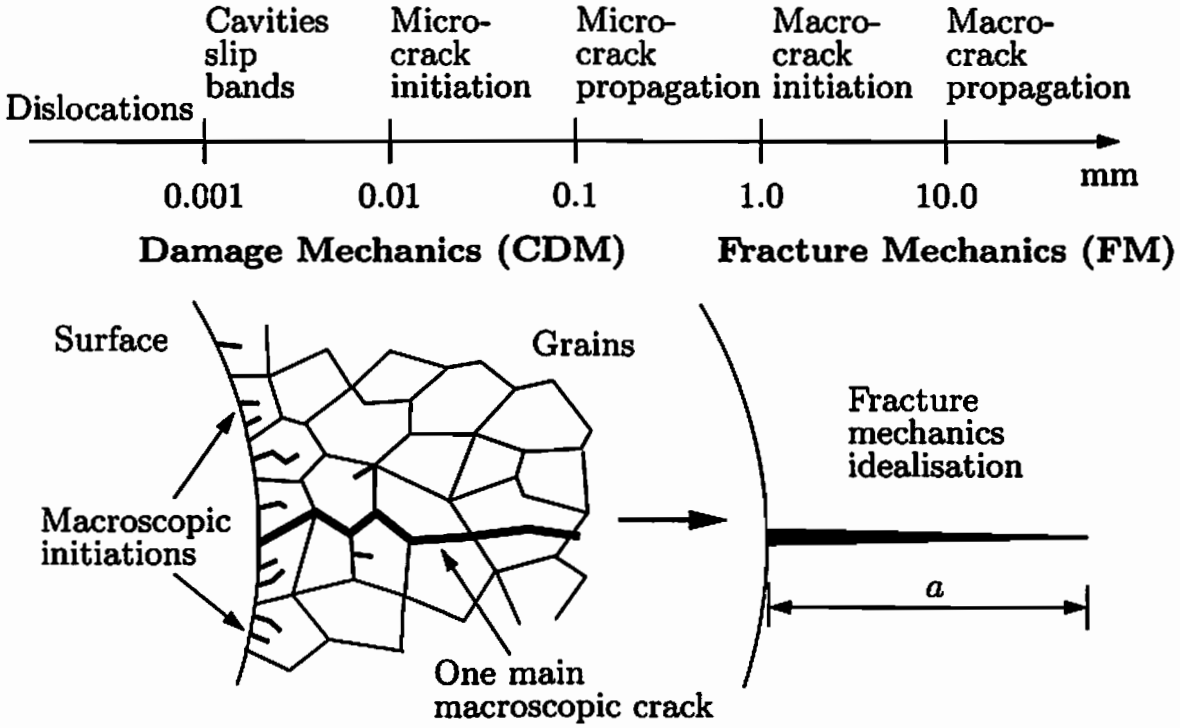

Figure 3.10: Schematic illustration of a macroscopic crack initiation concept (after Chaboche)

study the macroscopically cracked medium with the help of intrinsic variables. This behaviour is due to the high stress concentration present at the crack tip, which, in the case of linear elasticity and the HRR-field of exponential hardening plasticity (Hutchinson (1968), Rice & Rosengren (1968)), can be represented by the singularity of the stress field.
Using the concept of the strength of stress singularities at crack tips, Irwin (1957) has introduced *stress intensity factors* corresponding to the particular kinematics of the crack propagation. Both Irwin (1957) and Williams (1957) have obtained the form of the elastic stress distribution in the vicinity of a crack tip in extensional problems using crack solutions given by Westergaard (1939). This approach is known as the *semilocal approach.*
Between the global and semilocal approach there exist the contour integrals of Rice (1968b) which characterise the singularity from an energy point of view. He introduced the two-dimensional version of the conservation law as a path independent line integral, known as *J-integral.*

3.2.1 Physical mechanisms of fracture

Elastic and plastic deformations, which take place at atomic and crystalline levels respectively, maintain the cohesion of the matter. By definition, fracture is degradation of this cohesion by creating surface or volume discontinuities within

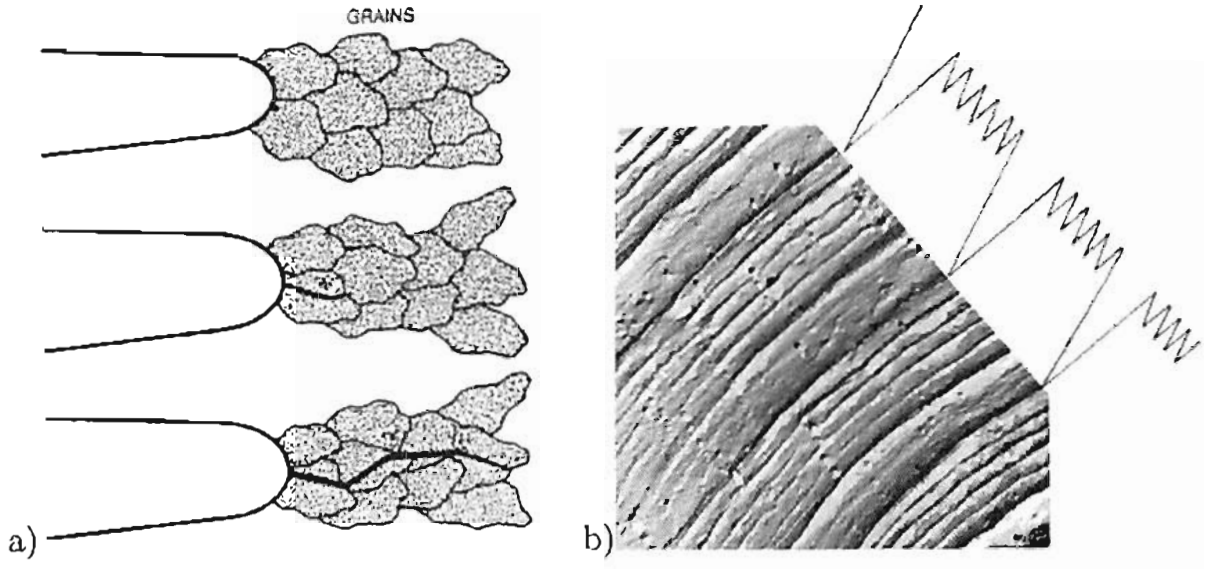

Figure 3.11: a) cleavage fracture starting at crack tip, b) fatigue striations on crack surface of aluminium alloy (after Broek)

the material. According to Lemaitre & Chaboche (1990), fracture happens at a larger scale of crystals: microcracks and cavities have a size in microns or hundredths of a millimetre, macrocracks have the order of a millimetre, and cracks, which occur at the scale of a mechanical structure, can be measurable in centimetres or decimetres. A schematic illustration of these measurements and concepts of continuum damage mechanics and fracture mechanics is given in Figure 3.10 (see Chaboche 1981).

A brittle fracture by cleavage and a ductile fracture by large localised plastic deformations, are two of the main basic mechanisms of local fracture.

Brittle fracture is characterised by the fracture of interatomic bonds, without noticeable overall plastic deformations. This fracture is a result of equalising the local strain energy due to external loads and the energy necessary to pull the atom layers apart. Accidental geometrical imperfections or lattice defects lead to a stress concentration, and therefore they play on important role in the initiation of the fracture process. Brittle fracture by cleavage represents a direct separation of particular crystallographic planes. Several parallel surfaces of cleavage can develop in a crystal, which join perpendicularly in the form of steps. In order to follow the crystallographic cleavage planes of the next crystal, the cleavage surfaces change direction at grain boundaries. A cleavage that follows the grain boundaries is known as intergranular fracture. It occurs in form of brittle fracture itself at low temperature and due to creep, observed mostly at average and high temperatures (see Figure 3.12).

The instability which is a result of a very large local deformation in the vicinity of crystalline defects leads to ductile fracture. A material which shows signs

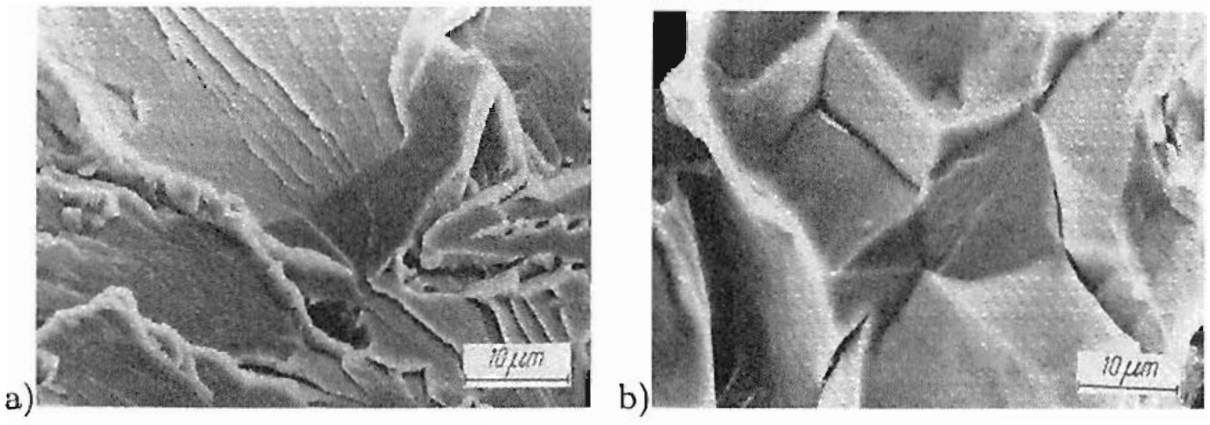

Figure 3.12: Brittle fracture: a) transgranular, b) intergranular (after Blumenauer & Pusch)

of ductile fracture can have either a ductile or brittle global behaviour depending on the density of crystalline defects and the resulting overall macroscopic deformation may or may not be significant. Particles of added elements in alloys, inclusions, piling up of dislocations, grain boundaries and triple points are defects responsible for initiating ductile fracture.
The external loads which lead to large plastic deformations in the vicinity of the defects create stress concentrations. A particle or a foreign defect can produce an instability which results in the decohesion at the interface or in fracture due to cleavage and thus initiating a microcrack or a cavity. The growth of cavities takes place through plastic slips with local strains, and further coalescence of the cavities leads to the final fracture (see Figure 3.13).
However, different interacting mechanisms are involved in the fracture of an element under service conditions. Fatigue failure under cyclic loads clearly distinguishes different stages of such fracture. In the case of a polycrystal subjected to a periodic load, the stages of fracture are nucleation and initiation of microcracks, growth of microcracks, and growth of macrocracks.

3.2.1.1 Nucleation and initiation of microcracks

Even in the case when the maximum load is under the usual elastic limit, the stress concentrations in the vicinity of the defects create locally cyclic plastic microdeformations, which block further slip by virtue of multiplication of dislocation nodes. Local rise in temperature produced by this dissipative mechanism can induce the relaxation of microstresses. Depending on whether hardening or relaxation is predominant in the material, a hardening or softening of the material takes place. Slip bands formed during this phase result in steps form on the surface of the sample. Depending on the material and the load level the initiation of microcracks can be influenced by several mechanisms, such as

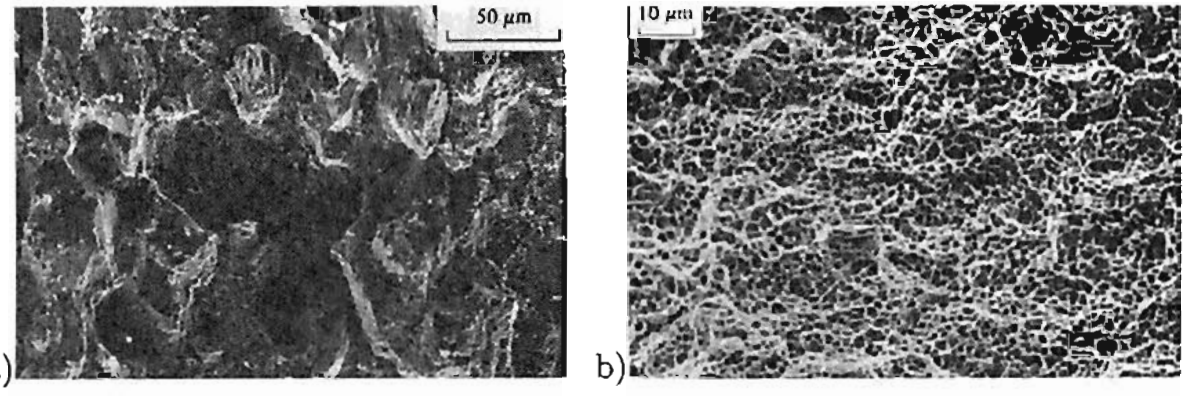

Figure 3.13: Ductile fracture: a) intergranular - in a Nickel based Inconel 718 alloy, b) transgranular in a 0.30 C-1 Cr-0.25 Mo steel (after Pineau)

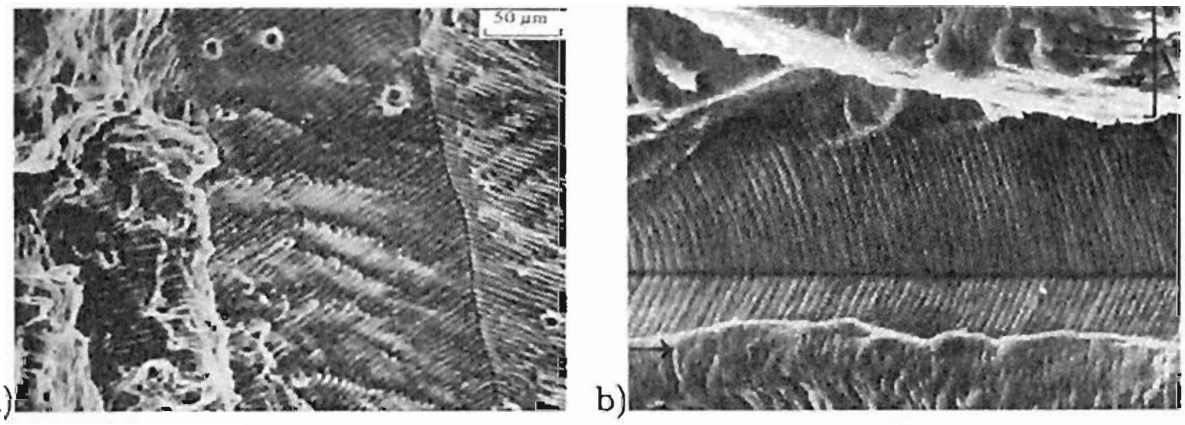

Figure 3.14: Fatigue striation: a) stainless austenitic steel, b) Inconel 718 alloy (after Pineau)

dislocation climbs in connection with the formation of voids, the formation of permanent slip bands and decohesion, and intrusion-extrusion mechanisms. In this initiation phase, the defects are in the planes which have inclination of $\pm 45°$ to the direction of the largest principle stress. The microcracks usually have a length in the range of the grains of the polycrystal.

3.2.1.2 Microcracks growth

Growth of microcracks represents important phase in the fatigue failure. The beginning of this phase is the moment when a microcrack crosses the first grain. Thereafter, microcracks move through the successive grains or along the grain boundaries. In this moment the microcracks have tendency to orient themselves perpendicular to the direction of the maximum principle stress. When one mi-

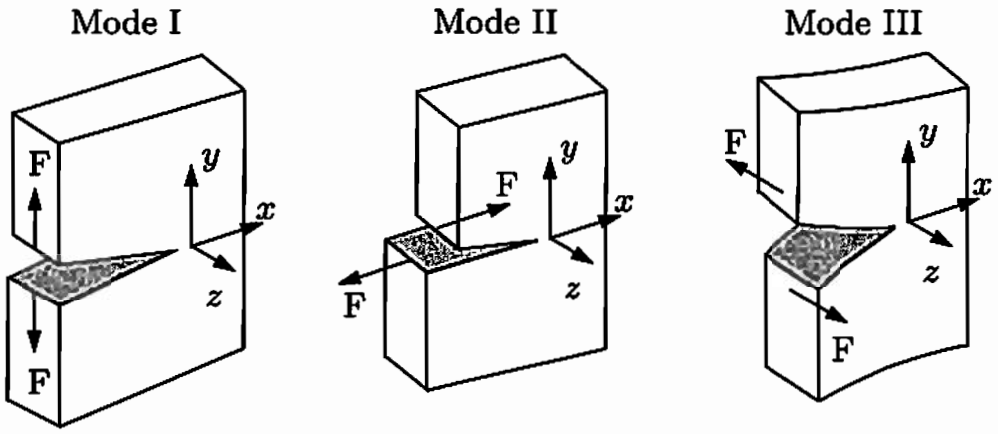

Figure 3.15: The loading modes: Mode I - opening mode, Mode II - shear mode, Mode III - tearing mode

crocrack becomes significant in size and obtains a well-defined direction, it grows further in a preferential way. This leads to the partial unloading of other microcracks and a high stress concentration at the front of microcrack is generated (see Figure 3.11a). A macroscopic initiation takes place and after that point the material cannot be considered as a homogeneous macroscopic medium.

3.2.1.3 Macrocracks growth

The growth of macrocracks is based on the same principles as the growth of microcracks. The stress concentration at the crack tip results in the local plastic deformation which leads to the separation of the material at the crack tip. The fractured surface reveals a succession of striations which often permits a measurement of the crack tip progress in each cycle (see Figures 3.11b and 3.14). After the crack reaches a critical size, the cracked part becomes unstable, and the crack propagates rapidly, breaking the structural element into two or more pieces.

3.2.2 Linear elastic fracture mechanics

Linear elastic fracture mechanics (LEFM) analyses materials with relatively low fracture resistance which fail below their collapse strength, using an elastic analysis of the stress field for small strains. Such materials are brittle-elastic materials like high-strength steel, cold worked stainless steel, glass, concrete, etc. The basic problem in fracture mechanics is the analysis of the stress distribution in plane, linear elastic, cracked media.
A plane crack extending through the thickness of a flat plate is considered. The crack plane occupies the plane xz and the crack front is parallel to the z-axis. The origin of the coordinate system $Oxyz$ is situated at the midpoint of the

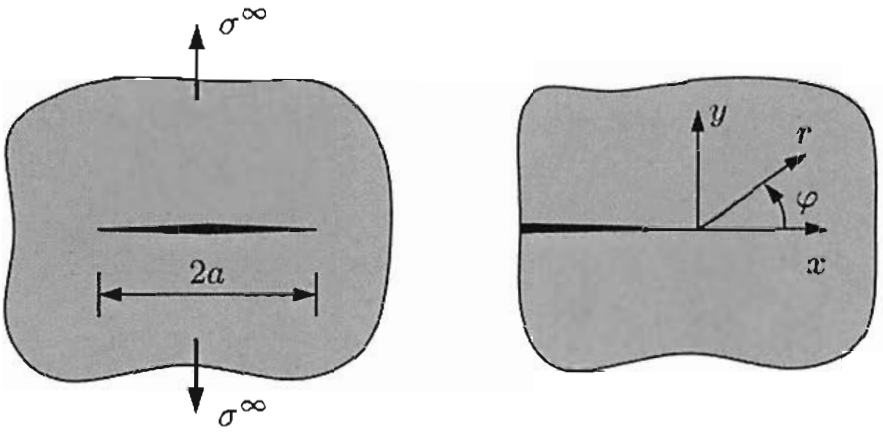

Figure 3.16: A crack in an infinite plate subjected to a uniform stress at infinity

crack front. Depending on the direction of the load with respect to the direction of the crack, three independent relative movements of the upper and lower crack surfaces exist. Figure 3.15 illustrates these three basic modes. A superposition of these basic modes can give any deformation of the crack surface. Three loading modes are defined as follows:

- *Opening mode* or mode I: crack surfaces separate symmetrically with respect to the planes xy and xz.
- *Sliding mode* or mode II: crack surfaces slide relative to each other symmetrically with respect to the plane xy and skew-symmetrically with respect to the plane xz.
- *Tearing mode* or mode III: crack surfaces slide relative to each other skew-symmetrically with respect to both xy and xz planes.

Next, three different possibilities for the definition of the theory of crack growth are presented. Those three approaches are the stress intensity factors approach, the strain energy release rate approach and J-integral approach. Section 3.2.2.4 presents approaches suitable for the fatigue crack growth.

3.2.2.1 Stress intensity factors

The stress and the deformation fields associated with each of these three loading modes will be determined for the cases of plane strain and plane stress using the solution for asymptotic problem in the vicinity of a two-dimensional crack in the infinite plate proposed by Williams (1957). The solution of this problem is obtained using Airy stress function Ψ which satisfies biharmonic equation for plane strain and plane stress problem

$$\Delta\Delta\Psi = 0\,. \tag{3.38}$$

In the case of polar coordinates, Laplace operator Δ is defined as

$$\Delta = \frac{\partial^2}{\partial r^2} + \frac{1}{r}\frac{\partial}{\partial r} + \frac{1}{r^2}\frac{\partial^2}{\partial^2 \varphi}\,. \tag{3.39}$$

The stress components as function of Airy stress function are given as

$$\begin{aligned}
\sigma_{rr} &= \frac{1}{r}\frac{\partial \Psi}{\partial r} + \frac{1}{r^2}\frac{\partial^2 \Psi}{\partial \varphi^2} \\
\sigma_{\varphi\varphi} &= \frac{\partial^2 \Psi}{\partial r^2} \\
\sigma_{r\varphi} &= \frac{1}{r^2}\frac{\partial \Psi}{\partial \varphi} - \frac{1}{r}\frac{\partial^2 \Psi}{\partial r \partial \varphi}\,.
\end{aligned} \tag{3.40}$$

Here, r and φ are polar coordinates with the origin at the crack front (see Figure 3.16). In order to satisfy (3.38), stress function is chosen in the form

$$\Psi(r, \varphi, \lambda) = R(r, \lambda) F(\varphi, \lambda) = r^{\lambda+1} F(\varphi, \lambda)\,, \quad \lambda > 0\,. \tag{3.41}$$

The general solution of the biharmonic equation (3.38) is given in the form

$$\begin{aligned}
\Psi = r^{\lambda+1}[&C_1 \sin(\lambda+1)\varphi + C_2 \cos(\lambda+1)\varphi + \\
&C_3 \sin(\lambda-1)\varphi + C_4 \cos(\lambda-1)\varphi]\,,
\end{aligned} \tag{3.42}$$

where C_i $(i = 1..4)$ are unknown solution constants, to be determined from boundary conditions. The boundary conditions for the stress free crack edge are given as

$$\sigma_{\varphi\varphi}(\pm\pi) = \sigma_{r\varphi}(\pm\pi) = 0. \tag{3.43}$$

Applying the boundary conditions in (3.40) leads to a system of algebraic equations for the four unknown constants

$$\begin{pmatrix}
(\lambda+1)\sin\lambda\pi & -(\lambda+1)\cos\lambda\pi & (\lambda+1)\sin\lambda\pi & -(\lambda+1)\cos\lambda\pi \\
-(\lambda+1)\sin\lambda\pi & -(\lambda+1)\cos\lambda\pi & -(\lambda+1)\sin\lambda\pi & -(\lambda+1)\cos\lambda\pi \\
(\lambda+1)\cos\lambda\pi & (\lambda+1)\sin\lambda\pi & (\lambda-1)\cos\lambda\pi & (\lambda-1)\sin\lambda\pi \\
(\lambda+1)\cos\lambda\pi & -(\lambda+1)\sin\lambda\pi & (\lambda-1)\cos\lambda\pi & -(\lambda-1)\sin\lambda\pi
\end{pmatrix}
\begin{pmatrix} C_1 \\ C_2 \\ C_3 \\ C_4 \end{pmatrix}
=
\begin{pmatrix} 0 \\ 0 \\ 0 \\ 0 \end{pmatrix}. \tag{3.44}$$

A nontrivial solution for the system of equations (3.44) requires that the determinant of the coefficient matrix is singular

$$4r^{4(\lambda-1)}\lambda^4(\lambda+1)^2 \sin^2(2\pi\lambda) = 0\,. \tag{3.45}$$

Equation (3.45) has admissible solutions

$$\lambda = \frac{n}{2}\,, \quad n = 1, 2, 3....\,. \tag{3.46}$$

The solution $\lambda = 1/2$ leads to singular stresses at the crack tip. Applying this solution in the coefficient matrix (3.44) eliminates two constants and the asymptotic stress and displacement fields in the vicinity of the crack tip in Cartesian coordinates for mode I and II are:

$$\sigma_{xx} = \frac{\mathrm{K_I}}{\sqrt{2\pi r}} \cos\frac{\varphi}{2}\left(1 - \sin\frac{\varphi}{2}\sin\frac{3\varphi}{2}\right) - \frac{\mathrm{K_{II}}}{\sqrt{2\pi r}} \sin\frac{\varphi}{2}\left(2 + \cos\frac{\varphi}{2}\cos\frac{3\varphi}{2}\right) + O(1)\,, \tag{3.47}$$

$$\sigma_{yy} = \frac{\mathrm{K_I}}{\sqrt{2\pi r}} \cos\frac{\varphi}{2}\left(1 + \sin\frac{\varphi}{2}\sin\frac{3\varphi}{2}\right) + \frac{\mathrm{K_{II}}}{\sqrt{2\pi r}} \sin\frac{\varphi}{2}\cos\frac{\varphi}{2}\cos\frac{3\varphi}{2} + O(\sqrt{r})\,, \tag{3.48}$$

$$\sigma_{xy} = \frac{\mathrm{K_I}}{\sqrt{2\pi r}} \sin\frac{\varphi}{2}\cos\frac{\varphi}{2}\cos\frac{3\varphi}{2} + \frac{\mathrm{K_{II}}}{\sqrt{2\pi r}} \cos\frac{\varphi}{2}\left(1 - \sin\frac{\varphi}{2}\sin\frac{3\varphi}{2}\right) + O(\sqrt{r})\,, \tag{3.49}$$

$$u_x = \frac{\mathrm{K_I}}{2\mu}\sqrt{\frac{r}{2\pi}} \cos\frac{\varphi}{2}\,(k - \cos\varphi) + \frac{\mathrm{K_{II}}}{2\mu}\sqrt{\frac{r}{2\pi}} \sin\frac{\varphi}{2}\,(k + 2 + \cos\varphi) + O(r)\,, \tag{3.50}$$

$$u_y = \frac{\mathrm{K_I}}{2\mu}\sqrt{\frac{r}{2\pi}} \sin\frac{\varphi}{2}\,(k - \cos\varphi) + \frac{\mathrm{K_{II}}}{2\mu}\sqrt{\frac{r}{2\pi}} \cos\frac{\varphi}{2}\,(k - 2 + \cos\varphi) + O(r)\,, \tag{3.51}$$

where

$$\begin{array}{lll} \text{for plane strain:} & k = 3 - 4\nu\,, & \sigma_{zz} = \nu(\sigma_{xx} + \sigma_{yy})\,, \\ \text{for plane stress:} & k = (3-\nu)/(1+\nu)\,, & \sigma_{zz} = 0\,, \end{array} \tag{3.52}$$

and $\mu = \frac{\mathrm{E}}{2(1+\nu)}$. E and ν are Young's modulus and Poisson's ratio respectively. In the case of mode III, the asymptotic stress and displacement fields in the vicinity of the crack tip in Cartesian coordinates are

$$\sigma_{xz} = -\frac{\mathrm{K_{III}}}{\sqrt{2\pi r}} \sin\frac{\varphi}{2}\,, \quad \sigma_{yz} = \frac{\mathrm{K_{III}}}{\sqrt{2\pi r}} \cos\frac{\varphi}{2}\,, \tag{3.53}$$

$$u_z = \frac{K_{III}}{\nu}\sqrt{\frac{r}{2\pi}}\sin\frac{\varphi}{2}. \tag{3.54}$$

It can be seen from the above that the stresses at the crack tip are singular in $r^{-1/2}$ and the crack-opening displacement tends to zero as $r^{1/2}$ tends to zero. The coefficients K_I, K_{II}, K_{III} are the so-called *stress intensity factors* introduced by Irwin (1957). They express the strength of the singular elastic stress field at the crack tip and they are proportional to the discontinuity in the displacement of the crack surfaces. Subscripts I, II and III indicate that the stress intensity factors correspond to the appropriate loading modes defined in Figure 3.15. In this manner, it is possible to completely determine the stress and the displacement field in a cracked structure which is assumed to behave elastically if the stress intensity factors are known.
Since the stresses in a real material cannot be infinite, a plastic deformation with the length in micrometer range occurs at the crack tip even in highly brittle materials. However, if the region of plastic deformation at the crack tip is sufficiently small compared to the dominant region of the singular solution at the crack tip, the singular stress field governed by the stress intensity factors forms a useful approximation to the elastic field in the whole region at the crack tip. In that case the linear elastic fracture mechanics stays valid (cf. Rice 1974).

3.2.2.2 Strain energy release rate

Another possibility to develop the theory of crack growth is based on the global energy balance of the entire system. This approach is proposed by Griffith (1921, 1924), and represents the earliest attempt to formulate a linear elastic theory of crack propagation.
Consider a deformable continuum subjected to arbitrary loading with a crack. The crack has the area A. Applying the law of conservation of energy 2.2.4 to the whole solid leads

$$\dot{W} = \dot{K} + \dot{U} + \dot{\Gamma}, \tag{3.55}$$

where $\dot{W}$, $\dot{K}$ and $\dot{U}$ are rates of total, kinetic and internal energy respectively, and additional term $\dot{\Gamma}$ is the rate of energy spent in increasing the crack area. Additionally, the internal energy can be given as a sum of the elastic strain energy W^e and the plastic work W^p

$$U = W^e + W^p. \tag{3.56}$$

Under the assumption that all applied loads are time independent and that the crack grows slowly, the kinetic term is negligible. Since all changes with respect to time are caused by changes in crack size, (3.55) becomes

$$\frac{\partial W}{\partial A} = \frac{\partial W^e}{\partial A} + \frac{\partial W^p}{\partial A} + \frac{\partial \Gamma}{\partial A}. \tag{3.57}$$

For an ideally brittle material, the energy dissipated in plastic deformation is negligible and (3.57) can be rewritten in the form

$$G = \frac{\partial W}{\partial A} - \frac{\partial W^e}{\partial A} = \frac{\partial \Gamma}{\partial A} = 2\gamma\,, \tag{3.58}$$

where γ represents the energy required to form a unit of new material surface and it is a characteristic constant of the material. The factor 2 refers to two new material surfaces formed during the crack growth. Symbol G is given in honour of Griffith and represents the energy available for the crack growth. G is often referred to as the *crack driving force*. The right-hand side of (3.58) represents the resistance of the material which must be overcame in order for the crack to grow.

If the surface of a continuum on which the loads are applied is assumed to remain stationary during crack growth and if the work of body forces is ignored, the work performed by the applied forces vanishes and (3.58) has the form

$$G = -\frac{\partial W^e}{\partial A} = 2\gamma \quad \text{where} \quad \frac{\partial W^e}{\partial A} < 0\,. \tag{3.59}$$

This loading is known as *fixed-grips* loading.

On the other hand, it can be assumed that the applied loads on the surface of the solid are kept constant during crack growth. Using (3.58) and Clapeyron's theorem of linear elastostatics, which states that the work performed by constant applied loads is two times bigger as the increase of elastic strain energy, leads to

$$G = \frac{\partial W^e}{\partial A} = 2\gamma\,. \tag{3.60}$$

This loading is known as *dead-load*. The graphical representation of the fixed-grips and dead-load is given in Figure 3.17.

In the fixed-grip case, the energy required for crack growth is supplied by the existing elastic energy of the solid. In the dead-load case, the energy required for crack growth is supplied by the work performed by the external loads. It is clear from (3.59) and (3.60) that the deliverable energy is always equal to the change of the elastic strain energy regardless of its sign. Therefore, the absolute change of elastic strain energy can be used in the fracture criterion for crack growth (3.58). In the case of a plate with the constant thickness t, the change of the crack area is $\mathrm{d}A = t\mathrm{d}a$. The fracture occurs if the released elastic energy is sufficient for the extension of the crack $\mathrm{d}a$

$$G = \frac{\mathrm{d}\,W^e}{t\mathrm{d}a} = \frac{\mathrm{d}\,\Gamma}{t\mathrm{d}a} = 2\gamma\,. \tag{3.61}$$

Here, the crack driving force G can be understood as the *elastic strain energy release rate*. If an infinite plate subjected to a uniform stress σ perpendicular to

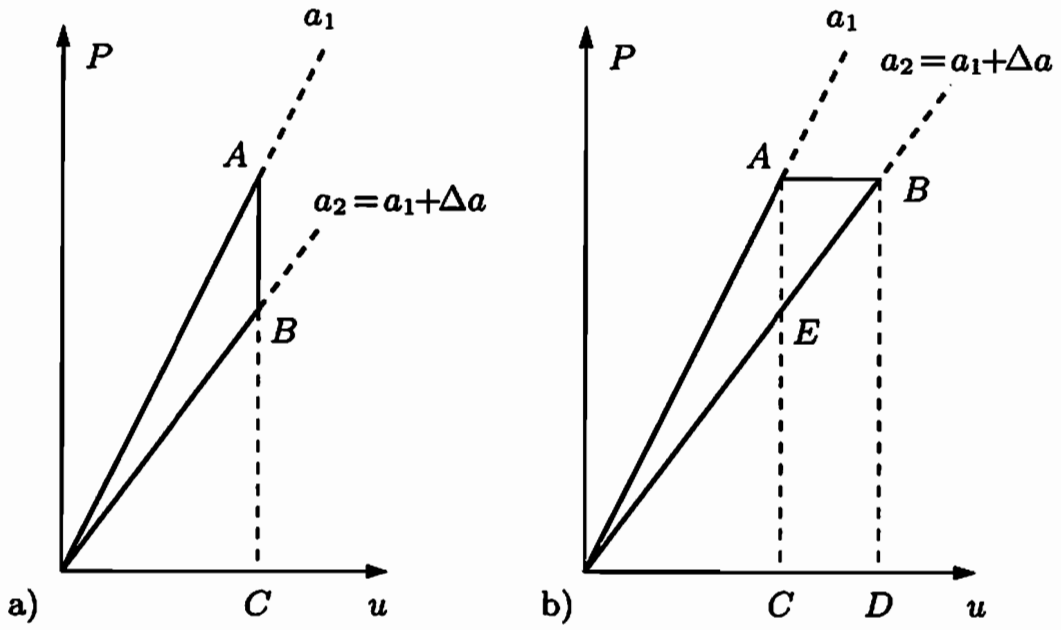

Figure 3.17: Load-displacement response of a cracked plate to a propagation of a crack from length a_1 to a_2: a) fixed-grips condition, b) under dead-load

the line crack of length $2a$ is considered, the change in elastic strain energy due to the presence of a crack is given by Griffith (1921, 1924)

$$W^e = \frac{\pi a^2 \sigma^2}{8\mu}(k+1) \quad \Rightarrow \quad G = 2\frac{\pi a \sigma^2}{8\mu}(k+1)\,, \tag{3.62}$$

where k is defined by (3.52).
According to Westergaard (1939) and Irwin (1957) the stress intensity factor for an infinite plate and mode I loading is

$$\mathrm{K_I} = \sigma\sqrt{\pi a}\,. \tag{3.63}$$

Applying (3.63) in the equation for G in (3.62) and taking into account that the elastic strain energy release rate G for one crack tip is exactly one half of the change of strain energy given in (3.62) leads to

$$G_\mathrm{I} = \frac{k+1}{8\mu}\mathrm{K_I^2}\,. \tag{3.64}$$

Using definitions for k for plane strain and plane stress leads to

$$\begin{aligned} &\text{for plane strain:} \quad G_\mathrm{I} = \frac{(1-\nu^2)\mathrm{K_I^2}}{E}\,, \\ &\text{for plane stress:} \quad G_\mathrm{I} = \frac{\mathrm{K_I^2}}{E}\,. \end{aligned} \tag{3.65}$$

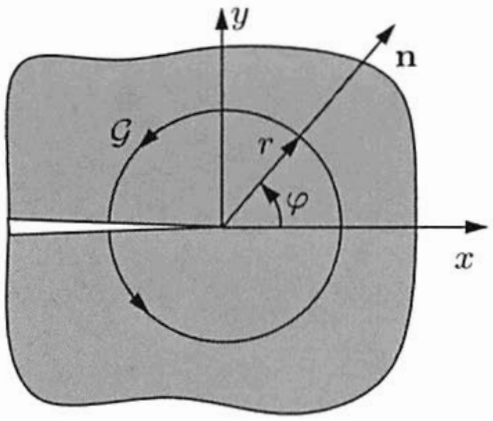

Figure 3.18: Representation of J-integral along a path $\mathcal{G}$

Similarly, the connection between the elastic strain energy release rate and the stress intensity factors approach in fracture mechanics for mode II and III is given by

$$G_{\mathrm{II}} = \frac{k+1}{8\mu}\mathrm{K}_{\mathrm{II}}^2 \quad \text{and} \quad G_{\mathrm{III}} = \frac{\mathrm{K}_{\mathrm{III}}^2}{2\mu}\,. \tag{3.66}$$

Equations (3.64) and (3.66) form the basis for the critical stress intensity factor fracture criterion, which in the case of mode I is

$$\begin{array}{lll} \mathrm{K_I} < \mathrm{K_{Ic}} & \rightarrow & \text{crack in equilibrium}\,, \\ \mathrm{K_I} = \mathrm{K_{Ic}} & \rightarrow & \text{unstable crack growth}\,. \end{array} \tag{3.67}$$

Here, $\mathrm{K_{Ic}}$ is the critical stress intensity factor. In the case of plane strain, $\mathrm{K_{Ic}}$ is the characteristic toughness of the material. In the case of plane stress, $\mathrm{K_{Ic}}$ depends on the thickness of the plate.

3.2.2.3 Contour integrals - J-integral

Yet another way of characterising the singularity of the stress field in the vicinity of the crack tip is a special mathematical formulation of the elastostatic conservation laws. In this approach, they assume a form of path independent integrals of some functionals of the elastic field over the bounding surface of a closed region. The two-dimensional version of the conservation law as a path independent integral for notch problems is introduced by Rice (1968b), and is known as *J-integral*. For a homogeneous body of linear or nonlinear elastic material with a notch subjected to a two-dimensional deformation field, the integral J is defined by

$$\mathrm{J} = \int_{\mathcal{G}} \left(W^e \mathrm{d}y - \mathbf{t} \cdot \frac{\partial \mathbf{u}}{\partial x}\,\mathrm{d}s \right) = \int_{\mathcal{G}} \left(W^e \mathrm{d}y - \mathbf{n} \cdot \boldsymbol{\sigma} \cdot \frac{\partial \mathbf{u}}{\partial x}\,\mathrm{d}s \right)\,, \tag{3.68}$$

where W^e is the elastic strain energy density, $\mathcal{G}$ is a curve surrounding the notch tip, $\mathbf{n}$ is the outward normal to $\mathcal{G}$, $\mathbf{u}$ is the displacement vector, and $\mathbf{t}$ and σ are defined by (2.31). The integral is evaluated in a counterclockwise sense starting from the lower flat notch surface and continuing along the path $\mathcal{G}$ to the upper flat surface (see Figure 3.18).
For the case of small scale yielding, Rice (1968b) has defined the relationship between the J-integral and the stress intensity factor for mode I loading as

$$\mathrm{J} = \frac{\eta}{E}\mathrm{K_I^2}\,. \tag{3.69}$$

For all three loading modes, this relation has a form

$$\mathrm{J} = \frac{\eta}{E}(\mathrm{K_I^2} + \mathrm{K_{II}^2}) + \frac{1+\nu}{E}\mathrm{K_{III}^2}\,, \tag{3.70}$$

where $\eta = 1-\nu^2$ for plane strain and $\eta = 1$ for plane stress. If (3.69) and (3.70) are compared to (3.65) and (3.66), it is clear that the J-integral is equal to the elastic strain energy release rate G

$$\mathrm{J} = G\,. \tag{3.71}$$

The last equation holds only for self-similar crack growth. However, a crack under mixed-mode loading and mode II loading does not extend along its own plane and therefor the value of the strain energy release rate G given in (3.71) is physically unrealistic. In order to get a better representation of the crack growth in a body, a variational principle of fracture mechanics can be used. For more information about the variational principle see Schütte (2001) and citations therein.

3.2.2.4 Fatigue crack growth

If an engineering component subjected to a cyclic load is considered, the failure of material during fatigue life may be represented through three stages (see Figure 3.19). In stage I the initiation of the macrocrack occurs. Slow stable crack propagation until the crack reaches a critical size corresponding to the onset of global stability is characteristic of stage II. In stage III or fracture, the crack growth rate increases rapidly as global instability is approached, which leads to the final failure of the component in two or more pieces. The first two stages are identified in 3.2.1 as fatigue. The stage of macroscopic crack initiation is additionally divided into the initiation of microcracks and the microcracks growth.
The change in crack length is usually recorded as a function of loading cycles. One possibility to analyse fatigue crack propagation results is using the stress intensity factor as a correlation parameter. The representation of experimental results is usually given as a logarithmic diagram of the range of stress intensity factor $\Delta\mathrm{K}$ versus the crack propagation rate $\mathrm{d}a/\mathrm{d}N$. A plot of the characteristic

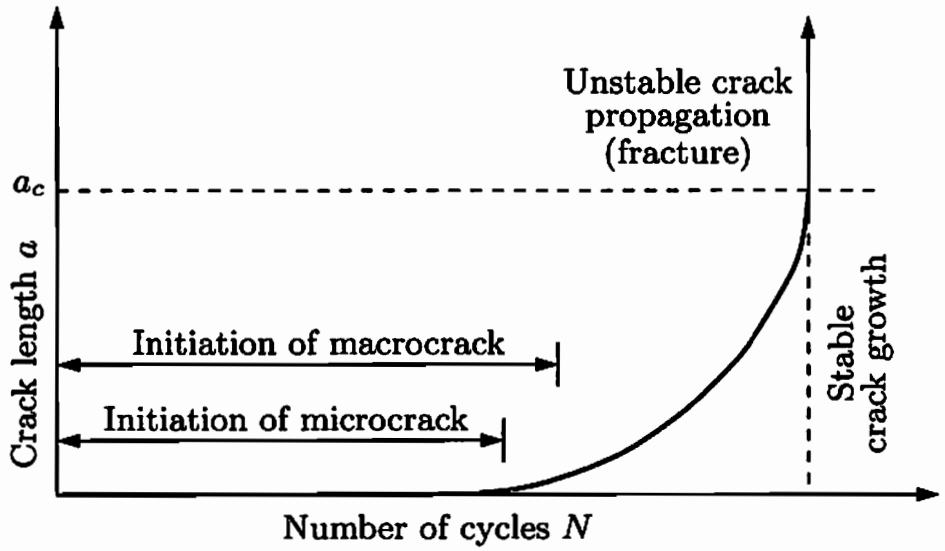

Figure 3.19: Diagram of crack size versus number of cycles: a curve for constant amplitude loading

sigmoidal variation of logarithmic growth rate with logarithmic ΔK is given in Figure 3.20 and can be characterised in terms of different primary fracture mechanisms (cf. Ritchie 1977, 1999). Three regimes which represent three primary fracture mechanisms are given in Figure 3.20.

In regime A, da/dN decreases rapidly to a vanishingly small level, and for some materials there exist a threshold value of the stress intensity amplitude ΔK_{th}, below which crack propagation cannot be detected. At these low growth rates a strong influence of the mean stress and the microstructure on growth rates is observed, together with an increased sensitivity to environmental effects and stress history.

In region B, a linear relation between $\log(\Delta K)$ and $\log(da/dN)$ is observed. In this regime, the influence of the mean stress and the microstructure on the crack growth is small, and failure generally occurs by a transgranular ductile striation mechanism.

In regime C, the maximum stress intensity factor ΔK_{max} in the fatigue cycle becomes equal to the critical stress intensity factor ΔK_c, and the crack growth rate curve rises leading to a catastrophic failure. Here, crack growth rates are extremely sensitive to the mean stress and the microstructure due to a departure from striation growth to static fracture modes, such as cleavage and intergranular and fibrous fracture.

To describe all these phenomena number of different quantitative continuum mechanics models of fatigue crack propagation are proposed. One of the most widely used fatigue crack propagation laws is proposed by Paris (1962), Paris et al. (1961) and Paris & Erdogan (1963). It is known in the literature as *Paris'*

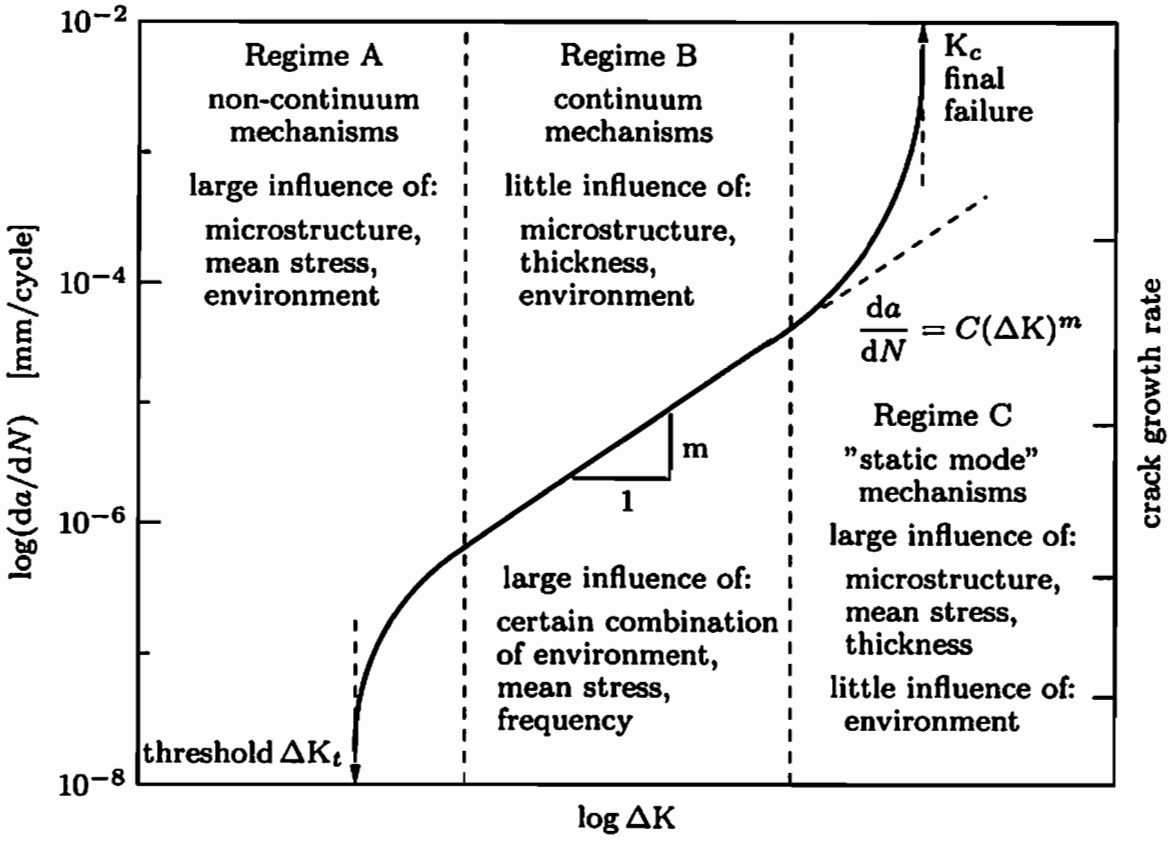

Figure 3.20: Representation of the typical variation in fatigue crack propagation rate ($\mathrm{d}a/\mathrm{d}N$) with applied stress intensity range ($\Delta\mathrm{K}$)

law

$$\frac{\mathrm{d}a}{\mathrm{d}N} = C(\Delta\mathrm{K})^m \quad \text{and} \quad \Delta\mathrm{K} = \mathrm{K_{max}} - \mathrm{K_{min}}\,, \tag{3.72}$$

where $\mathrm{K_{max}}$ and $\mathrm{K_{min}}$ refer to the maximum and minimum values of the stress intensity factors in the load cycle, and C and m are material parameters determined from a $\log(\Delta\mathrm{K})$–$\log(\mathrm{d}a/\mathrm{d}N)$ plot. Paris' law represents linear a relationship between $\log(\Delta\mathrm{K})$ and $\log(\mathrm{d}a/\mathrm{d}N)$ and it is used to describe fatigue crack propagation behaviour in regime B in Figure 3.20. The effect of the specimen geometry, the loading and the mean stress is included in the constant C. Further on, integrating the fatigue crack propagation law (3.72) gives

$$N - N_0 = \int_{a_0}^{a} \frac{\mathrm{d}a}{C(\Delta\mathrm{K})^m}\,, \tag{3.73}$$

where N_0 is the number of load cycles corresponding to the half crack length a_0, and N is the number of load cycles corresponding to the current half crack length a.

However, in the case of low and high levels of ΔK, the correlation between experimental and calculated results, given by Paris' law, is not satisfying. For the case of high ΔK, when K_{max} is close to the critical level K_c (regime C in Figure 3.20), Forman et al. (1967) proposed the relation

$$\frac{da}{dN} = \frac{C(\Delta K)^n}{(1-R)K_c - \Delta K}, \tag{3.74}$$

where $R = K_{min}/K_{max}$, and C and n are material constants. In the regime A, when low values of ΔK exist, it is possible to introduce threshold levels of the stress intensity below which crack does not propagate. In this case, Donahue et al. (1972) suggested the relation

$$\frac{da}{dN} = A((\Delta K_a)^m - (\Delta K_{at})^m), \tag{3.75}$$

where ΔK_{at} denotes the threshold value of ΔK_a, A and m are material constants, and $\Delta K_a = (K_{max} - K_{min})/2$ is the amplitude of the stress intensity factor. According to Klesnil & Lukaš (1972), ΔK_{at} is given by

$$\Delta K_{at} = (\Delta K_{atb})^{1-n}(\Delta K_a)^n, \tag{3.76}$$

where n is a material constant and ΔK_{atb} is the basic threshold value of ΔK_a, which is also a material constant. Erdogan & Ratwani (1970) proposed a generalised fatigue crack propagation law, which can describe the sigmoidal response given in Figure 3.20

$$\frac{da}{dN} = \frac{C(1+\beta)^m(\Delta K_a - \Delta K_{at})^n}{K_c - (1+\beta)\Delta K_a} \quad \text{and} \quad \beta = \frac{K_{max} + K_{min}}{K_{max} - K_{min}}, \tag{3.77}$$

and C, m, n are empirical material constants.
In the desire to formulate more a realistic fatigue crack propagation law, many authors proposed a propagation law using the thermodynamics of the irreversible process of crack growth, strain energy release rate or driving force instead of stress intensity factors. Using a complete analogy to the Paris' law, Sutton (1974) and Dowling & Begley (1976) proposed two fatigue crack propagation laws based on the strain energy release rate and J-integral respectively

$$\frac{da}{dN} = C(\Delta G)^m \quad \text{and} \quad \frac{da}{dN} = C(\Delta J)^m. \tag{3.78}$$

As in the case of Paris' law, different extensions of the laws given in the (3.78) are proposed, in order to achieve better congruence between experimental and calculated results. Woo & Chow (1984) and Chow & Lu (1990) formulated two laws based on the (3.78) using a critical fracture toughness (G_c) and critical value of the J-integral (J_c) respectively

$$\frac{da}{dN} = C\frac{(\Delta G)^m}{G_c - G_{max}} \quad \text{and} \quad \frac{da}{dN} = C\frac{(\Delta J)^m}{J_c - J_{max}}. \tag{3.79}$$

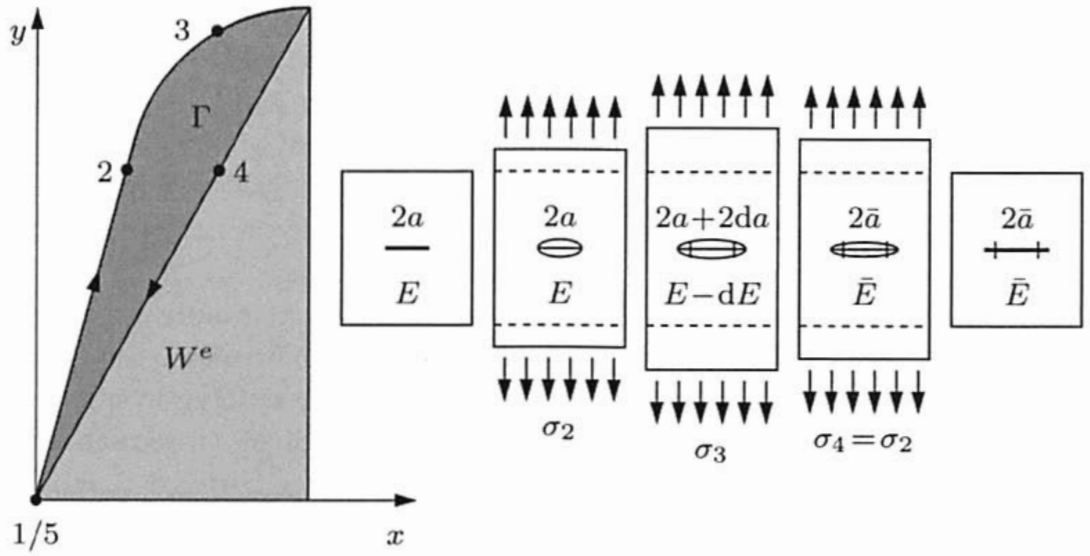

Figure 3.21: Crack growth in a unit cell

Lemaitre & Chaboche (1990) proposed another fatigue crack propagation law using a threshold value of the elastic strain energy release rate (G_0)

$$\frac{\mathrm{d}a}{\mathrm{d}N} = \frac{1}{C^{\eta/2}} \left(\sqrt{G_{\max}} - \sqrt{G_0} \right)^{\eta} . \tag{3.80}$$

Schütte (2001) extended (3.80) for the case of the kinked crack using a variational principle of a cracked body in the equilibrium

$$\frac{\mathrm{d}a}{\mathrm{d}N} = \frac{1}{C^{\eta/2}} \left(\sqrt{G^*_{\max}} - \sqrt{G^*_0} \right)^{\eta} , \tag{3.81}$$

where $G^*_{\max}$ is the maximum value of the strain energy release rate at the kinked crack tip, and C, η are material constants.

3.3 Material law for description brittle damage

Since one part of this work is the identification of material parameters, the appropriate material law is presented in this section. The material law which is used for the parameter identification of the brittle fatigue damage is developed by Schütte (2001) and it is given in Schütte & Bruhns (2002a, 2002b). The finite deformation framework is based on the multiplicative decomposition of the deformation gradient $\mathbf{F}$ in an elastically recoverable part and a damage part whose energy is dissipated.

3.3.1 Material model for finite elasto-damage

It is assumed that the damage of a material occurs by microcracks activated by elastic stress, and therefore the material is without macroscopic plasticity.

A body with growing microcracks, which is deformed by a total deformation $\mathbf{F}$ is considered. One part of this deformation is elastically recoverable, and the rest is unrecoverable part induced by damage. In contrast to plasticity, the body has no permanent deformation after the release of the loads. However, the state of body can be changed. The growth of microcracks can reduce the elastic stiffness of the body. In the case when no further damaging occurs, the total deformation consists only of the elastic part and starts from a state with changed elastic properties. The micromechanics for a continuum point and the corresponding macro-stresses and strains are given in Figure 3.21. The starting point is an unstressed body with a crack length $2a$ and resulting average elastic stiffness E. The load increases and up to a threshold load the crack will not grow but it will open. After the threshold level has been reached, the crack grows and the average stiffness decreases. After the body is unloaded, the crack is closed without any further crack growth. No permanent deformation is left in this state, but the average stiffness is less than its initial value. Due to the reduced stiffness, the same stress leads to a greater strain. The elastic strain energy W^e stored at the end of the process and the energy dissipated by the crack growth Γ are shown in Figure 3.21.
The base of the presented material model is the multiplicative decomposition of the deformation gradient. Similar to the multiplicative decomposition used in finite elastoplasticity, it can be described as

$$\mathbf{F} = \mathbf{F}^e \mathbf{F}^d \,, \tag{3.82}$$

where $\mathbf{F}^e$ is the elastic part of deformation gradient, and $\mathbf{F}^d$ is the damage part of deformation gradient. In contrast to finite elastoplasticity, where the plastic part of deformation is determined by unloading the body to an unstressed state, a crack tends to close in unloaded damaged body leaving no remaining deformation. For this reason, the split of the deformation is based on the energy principle. $\mathbf{F}^e$ represents the part of the deformation corresponding to the elastically recoverable energy, and $\mathbf{F}^d$ represents the part of the deformation due to energy which is dissipated by growth of microcracks. Three configurations induced by multiplicative decomposition are given in Figure 3.22. Those are the undamaged reference configuration $\mathcal{B}_0$, the damaged unloaded intermediate configuration $\mathcal{B}_d$ and the damaged loaded current configuration $\mathcal{B}$. If the concept of push- and pull-operations is used, it is possible to connect all quantities defined in these three configuration (see Marsden & Hughes 1983; Stumpf & Hoppe 1997).

3.3.2 Variational principle of fracture mechanics

In order to evaluate the evolution of damage in a unit cell with a single crack, the direction of the crack growth must be known. If a suitable micro-macro transition is used, a relationship between the damage evolution and the micromechanics of

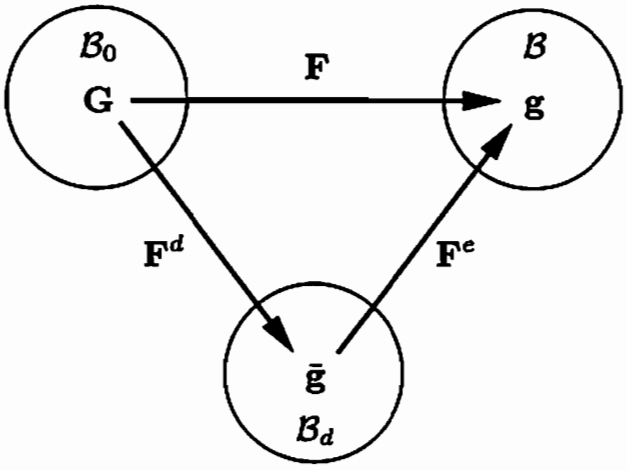

Figure 3.22: Multiplicative decomposition of the deformation gradient $\mathbf{F}$

a crack is established. A framework of linear elastic fracture mechanics is chosen according to the described class of materials.

Since the material law should describe the anisotropic properties of a damaged body with cracks, the evolution of mixed mode cracks is used. In the case of mixed-mode loading conditions the crack can grow in directions which are not situated in the tangent plane to the initial crack surface. As pointed out earlier, the calculation of strain energy release rate becomes complicated and cannot be performed using methods given in 3.2.2.2 and 3.2.2.3 in the case of non-tangential crack propagation. The calculation of the strain energy release rate requires a comparison of energy stored in the body prior to the crack extension with the energy stored in the body containing the kinked crack. The singular stress and displacement fields in the vicinity of the crack tip have a strong influence on the change in energy for small crack extensions. If the kink's length tends to zero, the stress intensity factors do not tend to those prior to crack extension (see Bilby & Cardew 1975; Wu 1978a, 1978b; Amestoy & Leblond 1992; Leblond 1993). This fact is the main difficulty in calculating the energy release rate of the kinked crack.

What follows is a brief representation of results proposed by Le et al. (1998) and Le et al. (1999), who derived a formulation based on Irwin's formula, which contains the limiting stress intensity factor after kinking of the two modes by using the variational principle by Le (1989) in combination with results of Wu (1978a) and Leblond (1993). The proposed variational formulation gives a criterion of maximum energy release rate.

A linear elastic body, which occupies the region $\mathcal{B}_S = \mathcal{B} \setminus \bar{\mathcal{S}}$ of the three-dimensional Euclidean space with the interior boundary $\bar{\mathcal{S}} = \mathcal{S} \cup \partial\mathcal{S}$ and the exterior boundary $\partial\mathcal{B}$ is considered, where $\mathcal{S}$ is a crack surface in its initial configuration. The loaded body has the displacement field $\mathbf{w}$ with the associated stress $\boldsymbol{\sigma}$. The loading conditions are considered in such a way that the crack

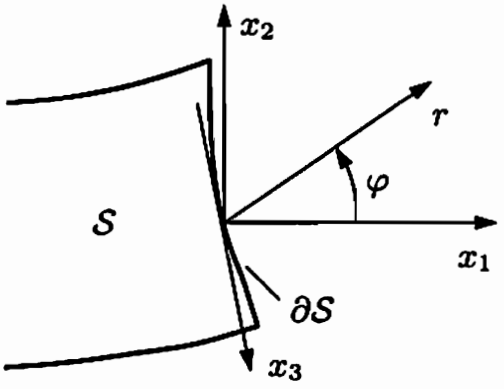

Figure 3.23: The local coordinate system and the initial crack

faces are stress free. On two sides of the crack surface the boundary conditions are given by

$$\sigma^{\pm} \cdot \mathbf{n} = 0 \quad \text{on} \quad \partial\mathcal{S}, \tag{3.83}$$

where indices + and − indicate limit values of quantities on the two sides of $\mathcal{S}$, and $\mathbf{n}$ is the normal vector pointing in the direction +. Before the crack extension, the singular stress and displacement field near the crack front are given as

$$\sigma_{ij} = K_\alpha \frac{f_{ij}^\alpha(\varphi)}{\sqrt{2\pi r}} + O(1), \quad w_i = K_\alpha \sqrt{\frac{r}{2\pi}} v_i^\alpha(\varphi) + O(r), \tag{3.84}$$

where r and φ are local polar coordinates in the plane perpendicular to the crack front (see Figure 3.23), α represents one of a three crack loading modes, K_α are stress intensity factors before the crack extension, and f and v are functions which define the stress and the displacement field, respectively. It is assumed that the crack surface $\mathcal{S}$ extends to the new surface $\mathcal{S}_\varepsilon$, which is expected to be smooth at the points of $\partial\mathcal{S}$ (see Figure 3.24). In this case, the singular stress and displacement fields near the extended crack front $\partial\mathcal{S}_\varepsilon$ are given by

$$\sigma'_{i'j'} = K'_\alpha \frac{f_{i'j'}^\alpha(\varphi')}{\sqrt{2\pi r'}} + O(1), \quad w'_i = K'_\alpha \sqrt{\frac{r'}{2\pi}} v_{i'}^\alpha(\varphi') + O(r'), \tag{3.85}$$

where r' and φ' are the local polar coordinates of the shifted and rotated coordinate system, and prime indices denote the projections onto the corresponding rotated coordinate axes (see Figure 3.24). Equation (3.85) is applied on a domain with the radius of a order smaller than ε and tending to zero together with ε. The limiting values of stress intensity factor $K_\alpha^\star$ when ε tends to zero are given by

$$K_\alpha^\star = F_{\alpha\beta}(\theta) K_\beta, \tag{3.86}$$

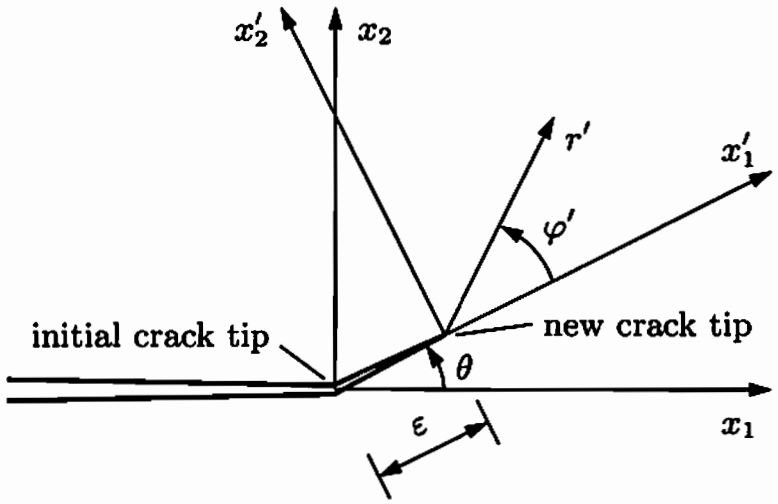

Figure 3.24: The shifted and the rotated coordinate system and crack growth

where $F_{\alpha\beta}(\theta)$ is a matrix, whose elements are functions of θ given by Amestoy & Leblond (1992), and θ is the kink angle.
Consider $\Sigma \supseteq S$, which is a virtually extended crack surface, and let $\mathcal{B}_\Sigma = \mathcal{B} \setminus \bar{\Sigma}$. Then, for an arbitrary field $\mathbf{u}$ the total energy functional is given as

$$I[\mathbf{u}] = \int_{\mathcal{B}_\Sigma} W^e(\varepsilon_{ij}(u_i))\mathrm{d}v - \int_{\partial\mathcal{B}_t} t_i u_i \mathrm{d}a + \int_{\Sigma} 2\gamma \mathrm{d}a\,. \tag{3.87}$$

Here $W^e(\varepsilon_{ij})$ is the elastic strain energy density, ε_{ij} is the strain field and t_i are the external tractions

$$W^e(\varepsilon_{ij}) = \frac{1}{2}\lambda\varepsilon_{ii}^2 + \mu\varepsilon_{ij}\varepsilon_{ij} \quad \text{and} \quad \varepsilon_{ij} = \frac{1}{2}(u_{i,j} + u_{j,i})\,. \tag{3.88}$$

The second integral in (3.87) represents the work done by the external traction and the third integral roughly represents the energy of the crack. Factor 2 signifies two crack surfaces, and γ is the so-called surface energy density.
The variational principle of fracture mechanics states that the body with a crack can be in stable equilibrium only if the variation of its total energy functional is not negative for all families of admissible displacement fields (cf. Le 1990, Le et al. 1999).
The variation of the total energy functional (3.87) is given by

$$\delta I = \frac{\mathrm{d}}{\mathrm{d}\epsilon} I[\mathbf{u}(\varepsilon)]\Big|_{\epsilon=0} \geq 0\,. \tag{3.89}$$

According to Le et al. (1999), the variational principle (3.88) is given in the local rotated coordinate system x_i' with axes which coincide with the vectors ν_i, η_i,

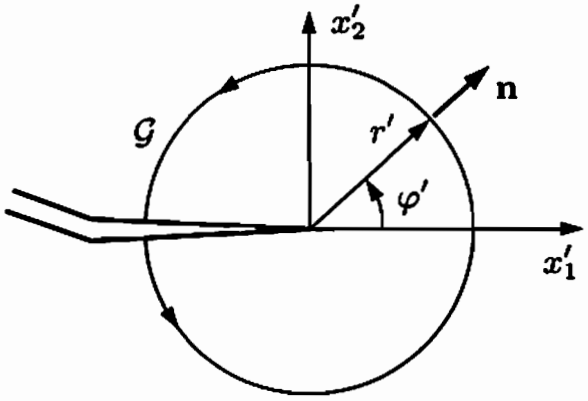

Figure 3.25: The kinked crack with the local coordinate system

τ_i by

$$\delta I = \int_{\partial S} \left(2\gamma - \lim_{\varepsilon \to 0} \mathrm{J}_{1'}'\right) \delta y \mathrm{d}s \geq 0\,, \tag{3.90}$$

after some transformations. Here, δy is virtual crack extension, and $J_{1'}'$ represents the corresponding component of the J-integral vector defined by

$$\mathrm{J}_{i'}'(\theta) = \int_{\mathcal{G}} \left(W^{e\prime} n_{i'} - \sigma_{k'j'}' u_{k',i'}' n_{j'}\right) \mathrm{d}s\,. \tag{3.91}$$

Here, $u_{k',i'}'$ is the displacement gradient, $\mathcal{G}$ is the contour with radius $h = \varepsilon/2$ surrounding the point of ∂S, and $n_{i'}$ is the unit normal vector on $\mathcal{G}$ (see Figure 3.25). In the given coordinate system, the magnitude of the driving force is defined as

$$G_\theta = \lim_{\varepsilon \to 0} \mathrm{J}_{1'}' = \lim_{\varepsilon \to 0} \int_{\mathcal{G}} \left(W^{e\prime} n_{1'} - \sigma_{k'j'}' u_{k',1'}' n_{j'}\right) \mathrm{d}s\,, \tag{3.92}$$

and is called the energy release rate for the non-tangential crack extension. Using (3.85), where the functions $f_{i'j'}^{\alpha}(\varphi')$ and $v_{i'}^{\alpha}(\varphi')$ describe the angular distributions of the stress and displacement fields respectively (see Rice 1968a), leads to

$$G_\theta = \frac{1-\nu^2}{E}\left[(K_{\mathrm{I}}^{\star})^2 + (K_{\mathrm{II}}^{\star})^2 + \frac{1}{1-\nu}(K_{\mathrm{III}}^{\star})^2\right]. \tag{3.93}$$

Taking into account the variational inequality (3.90) and $\delta y \geq 0$, the body with the crack S can be in the state of stable equilibrium if and only if

$$G^{\star} = \max_{\theta} G_\theta \leq 2\gamma\,. \tag{3.94}$$

The last equation represents the criterion of the maximum energy release rate.

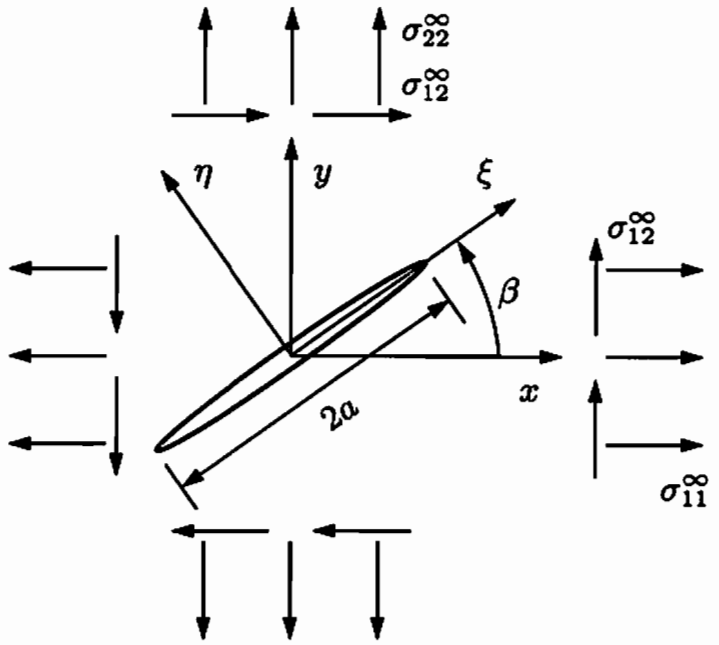

Figure 3.26: Inclined crack in the infinite plane

3.3.3 Two-dimensional planar crack growth

In the case of plane problems, a unit cell with a single crack is considered. The single crack fulfils the above presented law of crack propagation (see Figure 3.26). For an infinite plate with an inclined crack, the stress intensity factors prior to crack kinking are given by Irwin (1957)

$$K_{\mathrm{I}} = \sqrt{\pi a}\sigma_{\eta\eta}\,, \quad K_{\mathrm{II}} = \sqrt{\pi a}\sigma_{\eta\xi}\,, \tag{3.95}$$

where $\sigma_{\eta\eta}$ and $\sigma_{\eta\xi}$ are the far-field stresses resolved on the crack plane

$$\sigma_{\eta\eta} = \sigma_{11}^{\infty}\sin^2\beta + \sigma_{22}^{\infty}\cos^2\beta - \sigma_{12}^{\infty}\sin 2\beta\,, \tag{3.96}$$

$$\sigma_{\eta\xi} = \frac{1}{2}(\sigma_{22}^{\infty} - \sigma_{11}^{\infty})\sin 2\beta + \sigma_{12}^{\infty}\cos 2\beta\,. \tag{3.97}$$

Here, the mode mixity factor λ represents the relationship between stress intensity factors for Mode I and Mode II loading, and it is given by

$$\lambda = \frac{|K_{\mathrm{II}}|}{K_{\mathrm{I}} + |K_{\mathrm{II}}|}\,, \tag{3.98}$$

where the absolute value of K_{II} includes cracks with shear loading in both directions. With this in mind, the kinking angle can be expressed using the maximum energy release rate principle by the function

$$\begin{aligned}\theta_{\max} = \operatorname{sgn}(K_{\mathrm{II}})[&0.70966\lambda^3 - 0.097725\sin^2(3.9174\lambda) \\ &- 13.1588\tanh(0.15199\lambda)]\,.\end{aligned} \tag{3.99}$$

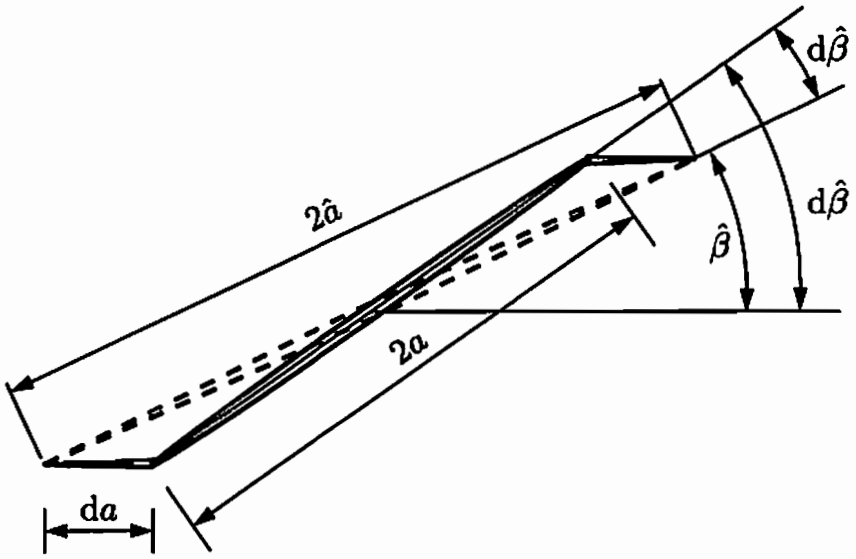

Figure 3.27: Kinked crack and its equivalent replacement crack

Same as in (3.98), the signum function is used to allow for both kinking directions.
According to (3.93), the maximum energy release rate for the plane problem is defined by

$$G^\star = \max_\theta G_\theta = \frac{1-\nu^2}{E}\left[(K_{\mathrm{I}}^\star)^2 + (K_{\mathrm{II}}^\star)^2\right] . \tag{3.100}$$

For a given unit cell under a known stress state, the direction of crack propagation is known. This information is however not sufficient to calculate the whole trajectory of the crack growth, since the analytical expressions for the stress intensity factors at the newly developed crack tips are unknown after the first kinking steps. In order to solve this problem, a computationally expensive method of finite element simulation of the unit cell containing a crack can be used. The second possibility is introduced in Schütte (2001) and represents the replacement of kinked crack by an equivalent straight crack in each infinitesimal step of the crack propagation. Equivalence between the kinked and the replacing crack can be introduced using a number of criteria, such as the equivalence of stress intensity factors, mode mixity factor, J-integral or rate of crack growth. In this work, the thermodynamic equivalence is used, which means that the amount of energy dissipated by the original and the equivalent crack growth remains the same. This follows directly from the correlation between the driving force and the dissipation rate. The kinked and the replacement crack are given in Figure 3.27.
The total work required to create the crack in the current stress field is introduced as the crack potential ψ. All values corresponding to the equivalent replacement crack have the superimposed hat. The crack potential required for the growing

of a straight crack with self-similar crack growth is given by

$$\hat{\psi} = 2\int_0^{\hat{a}} \hat{\mathrm{J}}_1 \mathrm{d}\hat{a}\,, \quad \hat{\mathrm{J}}_1 = \frac{1-\nu^2}{E}\left(\hat{K}_{\mathrm{I}}^2 + \hat{K}_{\mathrm{II}}^2\right)\,, \tag{3.101}$$

where a is the crack length, J_1 is the first component of the J-integral vector, and 2 represents two crack tips. Stress intensity factors can be determined using equations (3.95)÷(3.97). Based on the thermodynamic equivalence, the change of the crack potential for the kinked crack has to be the same as the change of the crack potential for the replacement crack

$$\mathrm{d}\psi = \mathrm{d}\hat{\psi}\,. \tag{3.102}$$

The change in the potential of the kinked crack is defined by

$$\mathrm{d}\psi = 2G^{\star}\mathrm{d}a\,. \tag{3.103}$$

As the potential of the replaced crack is a function of the crack length $\hat{a}$ and inclination angle $\hat{\beta}$, the change of the potential for the replacement crack is given by

$$\mathrm{d}\hat{\psi} = \frac{\partial\hat{\psi}}{\partial\hat{a}}\,\mathrm{d}\hat{a} + \frac{\partial\hat{\psi}}{\partial\hat{\beta}}\,\mathrm{d}\hat{\beta}\,. \tag{3.104}$$

In addition, the crack growth rates for the kinked and the replaced crack shall be the same and the starting point of the infinitesimal rotation $\mathrm{d}\hat{\beta}$ is the straight part of the kinking crack

$$\mathrm{d}a = \mathrm{d}\hat{a} \quad \text{and} \quad \hat{\beta}|_{\mathrm{d}a=0} = \beta\,. \tag{3.105}$$

This leads to the evolution equation for the rotation of the replaced crack in terms of the crack growth

$$\frac{\mathrm{d}\hat{\beta}}{\mathrm{d}a} = 2(G^{\star} - \hat{\mathrm{J}}_1) \Big/ \frac{\partial\hat{\psi}}{\partial\hat{\beta}}\,. \tag{3.106}$$

3.3.4 Damage evolution law

In order to develop a damage evolution law, the material is divided into unit cells with the thickness t and area A. A representative unit cell contains a single straight crack with a length a, inclined to the x-axis at an angle β. It is assumed that the cracks in the neighbouring unit cells are not interacting. According to Kachanov (1992) and Mauge & Kachanov (1994), this assumption gives good results even for high crack density assuming random positions.
In the intermediate configuration, the damage evolution law can be given in the form

$$\bar{\mathbf{D}}^d = \dot{\lambda}^d \frac{\partial\bar{\phi}^d}{\partial\bar{\mathbf{k}}^d}\,, \tag{3.107}$$

where $\bar{\mathbf{D}}^d$ is the damage part of the Eulerian strain tensor, $\dot{\lambda}^d$ is the damage multiplier, $\bar{\phi}^d$ is the damage potential, and $\bar{\mathbf{k}}^d$ is the damage driving force. Furthermore, the equivalence between macroscopic damage dissipation rate $\mathcal{D}^d$ and the microscopic change of the crack potential can be introduced by

$$\mathcal{D}^d = \bar{\mathbf{k}}^d : \bar{\mathbf{D}}^d = \frac{\dot{\psi}}{A} = \frac{2G^* \dot{a}}{A} . \tag{3.108}$$

The assumption that the change of the strain due to damage is orthogonal to the new opening crack surfaces leads to non-vanishing components of the damage stretching tensor, which are orthogonal to the current direction of the crack propagation

$$\bar{\mathbf{D}}^d = \bar{D}^d_{n^* n^*} (\mathbf{n}^* \otimes \mathbf{n}^*) , \tag{3.109}$$

where $\mathbf{n}^*$ is the normal vector onto the new developing crack surfaces. Applying the last equation in (3.108) leads to

$$\bar{k}^d_{n^* n^*} \cdot \bar{D}^d_{n^* n^*} = \frac{2G^* \dot{a}}{A} . \tag{3.110}$$

Using the assumption that driving forces for the crack propagation and the damage are equal

$$\bar{k}^d_{n^* n^*} = -\frac{2G^* t}{A} , \tag{3.111}$$

leads to the damage evolution law

$$\bar{\mathbf{D}}^d = -\frac{\dot{a}}{t} (\mathbf{n}^* \otimes \mathbf{n}^*) , \tag{3.112}$$

where minus sign shows that an increase in the crack length leads to a decrease in the stiffness. With the help of a damage multiplier

$$\dot{\lambda}^d = -\frac{\dot{a}}{t} , \tag{3.113}$$

the damage potential $\bar{\phi}^d$ is defined as

$$\bar{\phi}^d = |\bar{k}^d_{n^* n^*}| - \bar{h}^*_0 , \tag{3.114}$$

where $\bar{h}^*_0$ is a threshold value for damage.
The evolution equation for the fatigue crack growth is derived from a threshold function for a crack propagation proposed by Lemaitre & Chaboche (1990)

$$f_{crack} = \tilde{G}^* - H^* , \quad \text{with} \quad \tilde{G}^* = \left(\sqrt{G^*} - \sqrt{G^*_0} \right) , \tag{3.115}$$

where H^* is a variable which corresponds to the critical value of $\tilde{G}^*$

$$H^* = C' h^{2/\eta} , \tag{3.116}$$

and $G_0^\star$ is the initial value of the fracture threshold. C' and η in (3.116) are coefficients similar to two coefficients from the Paris' law (Paris 1962). The evolution equations for a and h are

$$\dot{a} = \dot{\lambda}^a \frac{\partial f_{crack}}{\partial \tilde{G}^\star} = \dot{\lambda}^a , \quad \dot{h} = -\dot{\lambda}^a \frac{\partial f_{crack}}{\partial H^\star} = \dot{\lambda}^a , \tag{3.117}$$

and the consistency equation $\dot{f}_{crack} = 0$ leads to the evolution law for fatigue crack growth

$$\dot{a} = \frac{\eta}{2C'} \left(\frac{\tilde{G}^\star}{C'} \right)^{\eta/2-1} \left\langle \dot{\tilde{G}}^\star \right\rangle , \tag{3.118}$$

where $\langle\,\rangle$ are Macaulay brackets defined as $\langle a \rangle = (a + |a|)/2$. Integration of (3.118) over a cycle of length Δt leads to the expression of the evolution law in terms of the number of cycles N

$$\begin{aligned} \frac{\mathrm{d}a}{\mathrm{d}N} &= \int_t^{t+\Delta t} \dot{a}\mathrm{d}t = \int_{\tilde{G}^\star_{\min}}^{\tilde{G}^\star_{\max}} \frac{\eta}{2C'} \left(\frac{\tilde{G}^\star}{C'} \right)^{\eta/2-1} \mathrm{d}\tilde{G}^\star \\ &= \frac{1}{C'^{\eta/2}} \left(\tilde{G}^{\star\eta/2}_{\max} - \tilde{G}^{\star\eta/2}_{\min} \right) , \end{aligned} \tag{3.119}$$

where $\tilde{G}^\star_{\max}$ and $\tilde{G}^\star_{\min}$ are functions of maximum and minimum values of $G^\star$ defined as

$$\tilde{G}^\star_{\max} = \left\langle \sqrt{G^\star_{\max}} - \sqrt{G^\star_0} \right\rangle^2 , \quad \tilde{G}^\star_{\min} = \left\langle \sqrt{G^\star_{\min}} - \sqrt{G^\star_0} \right\rangle^2 . \tag{3.120}$$

When $G^\star_{\min}$ is smaller than the threshold $G^\star_0$, the exact Paris' law can be derived from (3.119). For a Mode I loading and a self-similar crack growth, the Paris' law is given by

$$\frac{\mathrm{d}a}{\mathrm{d}N} = \frac{1}{C'^{\eta/2}} \left\langle \sqrt{G^\star_{\max}} - \sqrt{G^\star_0} \right\rangle^\eta = C(K_{\mathrm{I}\max} - K_0)^\eta , \tag{3.121}$$

with

$$C' = \left(C \cdot \sqrt{E'^\eta} \right)^{-2/\eta} , \tag{3.122}$$

and

$$E' = \begin{cases} \dfrac{E}{1-\nu^2} & \text{for plane strain}, \\ E & \text{for plain stress}. \end{cases} \tag{3.123}$$

Computation of the evolution of damage (3.112) requires the momentaneous direction of crack propagation, which can be calculated from Figure 3.28 as

$$\mathbf{n}^\star = \begin{pmatrix} -\sin(\beta + \theta_{\max}) \\ \cos(\beta + \theta_{\max}) \end{pmatrix} . \tag{3.124}$$

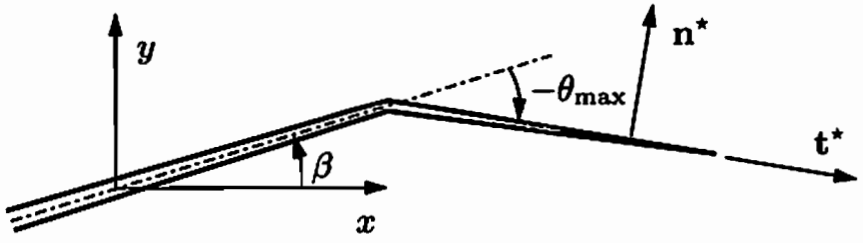

Figure 3.28: A crack tip with normal vector $\mathbf{n}^*$ and crack growth in direction $\mathbf{t}^*$

The evolution of damage is primarily governed by the evolution of the cracks length

$$\dot{a} = \hat{g}(\tilde{G}^*)\dot{\tilde{G}}^* . \tag{3.125}$$

Since G^* is a functional depending on the remote stress tensor $\boldsymbol{\sigma}^\infty$, the crack length a and the inclination angle β as

$$G^* = G^*(\boldsymbol{\sigma}^\infty, a, \beta) , \tag{3.126}$$

its time derivative is given as

$$\dot{G}^* = \frac{\partial G^*}{\partial a}\,\dot{a} + \frac{\partial G^*}{\partial \beta}\dot{\beta} + \frac{\partial G^*}{\partial \boldsymbol{\sigma}^\infty} : \dot{\boldsymbol{\sigma}}^\infty . \tag{3.127}$$

After some transformations, the evolution of the crack length is derived as

$$\dot{a} = \frac{\hat{g}(\tilde{G}^*) \cdot \dfrac{\partial G^*}{\partial \boldsymbol{\sigma}^\infty}}{1 - \hat{g}(\tilde{G}^*) \cdot \left(\dfrac{G^*}{a} + \dfrac{\partial G^*}{\partial \beta}\dfrac{\partial \beta}{\partial a} \right)} : \dot{\boldsymbol{\sigma}}^\infty . \tag{3.128}$$

Applying the definition for the remote stress tensor and its rate

$$\boldsymbol{\sigma}^\infty = \bar{\mathbb{C}}^e : \bar{\mathbf{e}} , \quad \dot{\boldsymbol{\sigma}}^\infty = \bar{\mathbb{C}}^e : \bar{\mathbf{D}} \tag{3.129}$$

in (3.128) and rearranging (3.112) leads to the definition of the damage evolution

$$\bar{\mathbf{D}}^d = -\frac{1}{t} \frac{\hat{g}(\tilde{G}^*) \cdot \left((\mathbf{n}^* \otimes \mathbf{n}^*) \otimes \dfrac{\partial G^*}{\partial \boldsymbol{\sigma}^\infty} : \bar{\mathbb{C}}^e \right)}{1 - \hat{g}(\tilde{G}^*) \cdot \left(\dfrac{G^*}{a} + \dfrac{\partial G^*}{\partial \beta}\dfrac{\partial \beta}{\partial a} \right)} : \bar{\mathbf{D}} = \mathbb{A} : \bar{\mathbf{D}} . \tag{3.130}$$

The rate of the remote stress tensor follows the statement that the material time derivative in the microscopic unit cell corresponds to the material time derivative with respect to the intermediate configuration of the macroscopic framework. The fourth-order tensor $\bar{\mathbb{C}}^e$ is called the damaged tensor of elastic moduli.

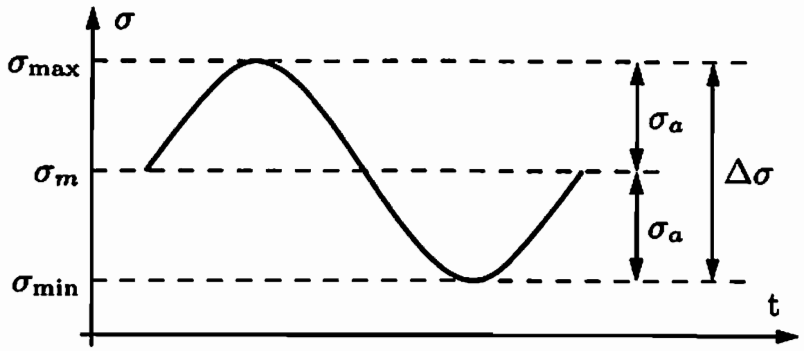

Figure 3.29: Nomenclature for the characterisation of cyclic loads

3.4 Fundamentals of fatigue analysis

Phenomenological continuum approaches are widely used to characterise the total fatigue life as a function of variables such as the applied stress range, the strain range, the mean stress and the environment. These stress- and strain-procedures represent the damage evolution, the crack nucleation and the crack growth stages of fatigue and lead to a single, experimentally characterisable continuum formulation. In these approaches, the fatigue life of a component is defined as the total number of cycles or the time necessary to induce damage and to initiate a dominant fatigue flaw which is propagated to final failure.

3.4.1 Fundamentals of experimental fatigue analysis

The development of load spectra, which represent the stresses and strains actually experienced during service life, is one of the most important tasks in the design of fatigue loaded structural components in engineering structures. These service spectra are estimated under typical operating conditions, by monitoring for example the output of strain gauges mounted of different critical parts of the component. The appropriate service spectra to which the component is subjected are edited and/or simplified for the purpose of life prediction.

3.4.1.1 Wöhler experiments

First characterisation of a fatigue life in terms of nominal stress amplitudes using experimental data obtained from rotating bend experiments on smooth specimens is introduced in the work of Wöhler on fatigue of railroad axles. In stress life approach, smooth test specimens are machined to provide a waisted cylindrical gauge length. After that, fatigue is tested under plane bending, rotating bending, uniaxial tension-compression or tension-tension cyclic loading. The load is usually given as a periodical function. A typical fatigue cycle of sinusoidal waveform is given in Figure 3.29. Here, σ_{max} and σ_{min} represent the maximum and the minimum stress during one cycle, σ_m is the mean stress, $\Delta\sigma$

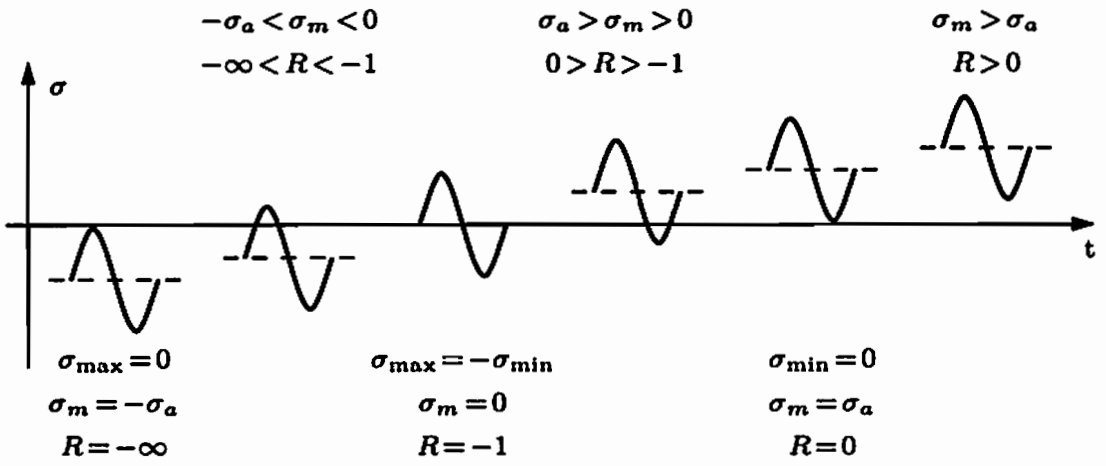

Figure 3.30: Different cyclic loading forms according to Haibach

is the stress range, σ_a is the stress amplitude, R is the stress ratio and A is the amplitude ratio. These parameters are related by equations

$$\begin{aligned} \sigma_m &= \frac{\sigma_{max} + \sigma_{min}}{2}, \quad \Delta\sigma = \sigma_{max} - \sigma_{min}, \\ \sigma_a &= \frac{\sigma_{max} - \sigma_{min}}{2}, \quad R = \frac{\sigma_{min}}{\sigma_{max}}, \\ A &= \frac{\sigma_a}{\sigma_m} = \frac{1-R}{1+R}. \end{aligned} \tag{3.131}$$

It is possible to distinguish different loading forms for different values of the stress ratio and the mean stress (see Figure 3.30). It is zero-compression fatigue for $R = -\infty$, at values $-\infty < \sigma < -1$ there is an alternating loading with negative mean stress, and for fully reversed loading $R = -1$. At values $-1 < R < 0$ there is an alternating loading with positive mean stress, for zero-tension fatigue $R = 0$, and for alternating loading in tension region $0 < R < 1$. Case $R = 1$ leads to the pure static load (tension or compression). In the case of uniaxial tension-compression test, it is possible to represent the loading in terms of strain, force or moment instead of normal stress. In the case of multiaxial stress state, it is possible to use equivalent or maximum stress according to appropriate strength criteria.

It is necessary to load specimens with cyclic loading under constant amplitude loading conditions in order to determine the approximate shape of Wöhler curve. A schematic representation of test results is shown in Figure 3.31 on a type of graph called *stress-life plot* (or S-N curve, or Wöhler curve), which shows the relationship between the amplitude (or maximum value, or mean value) of the applied stress and number of cycles N for fracture. Usually, the abscissa is the logarithm of the number of cycles N, while the vertical axis may be either the stress amplitude σ_a (or stress σ) or the logarithm of σ_a (or logarithm of σ).

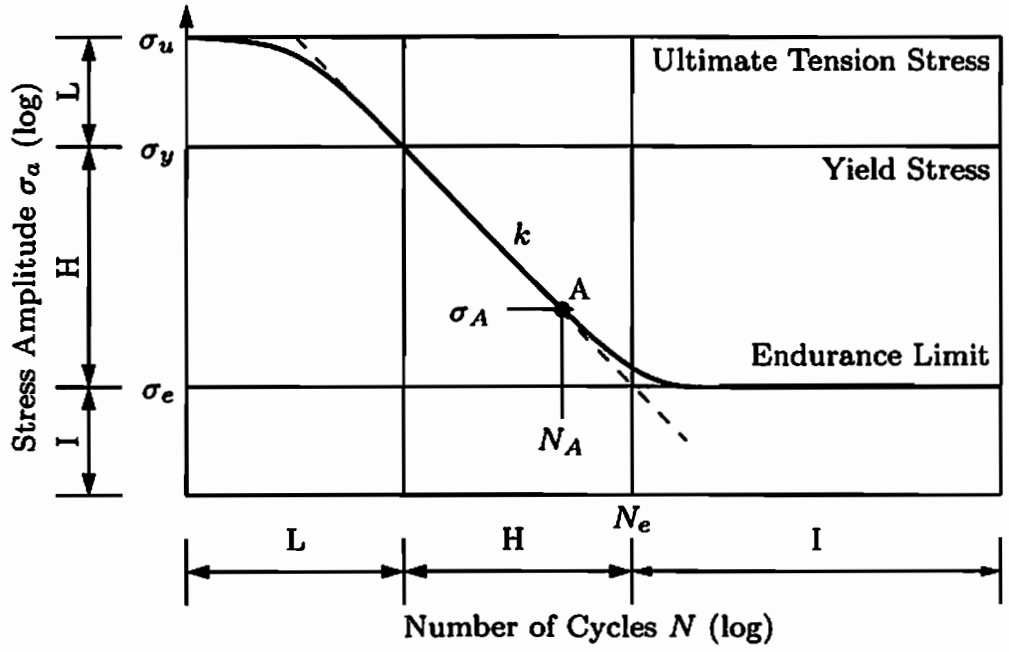

Figure 3.31: Typical Wöhler curve with characteristic values: L - Low Cycle Fatigue, H - High Cycle fatigue, I - Infinite Life (Haibach)

Under constant amplitude loading conditions most of steels and steel alloys exhibit a plateau in the stress-life plot. This plateau typically occurs beyond 10^6 fatigue cycles. When the load is below the plateau level, the specimen may be cycled indefinitely without causing failure. The according stress amplitude is called *endurance limit* or *fatigue limit* σ_e, and for most steels and copper alloys it is between 35% and 50% of the ultimate tensile strength σ_u. On the other hand, most aluminium alloys and some high strength steels which have been case-hardened by carburising do not generally exhibit a fatigue limit. For these materials, the stress amplitude decreases continuously with increasing number of cycles. For such cases, the stress amplitude which the specimen can support for at least 10^7 fatigue cycles represents an endurance limit.

Since a great scattering of endurance values at a certain value of the loading amplitude can be observed (see Figure 3.32), the statistical processing of endurance probability is required. Hence, a large number of tests must be performed. For this reason, Wöhler curve usually represents a characteristic curve of 90% of probability of failure.

If the S-N curve is drawn on a log – log scale, with the stress amplitude plotted as a function of the number of fatigue cycles or load reversals[1], a linear relationship is commonly observed in the high cycle fatigue. Many authors propose different

[1] A constant amplitude fatigue cycle is composed of two reversals. The use of the number of reversals, instead of the number of fatigue cycles, is useful for analysing variable amplitude fatigue.

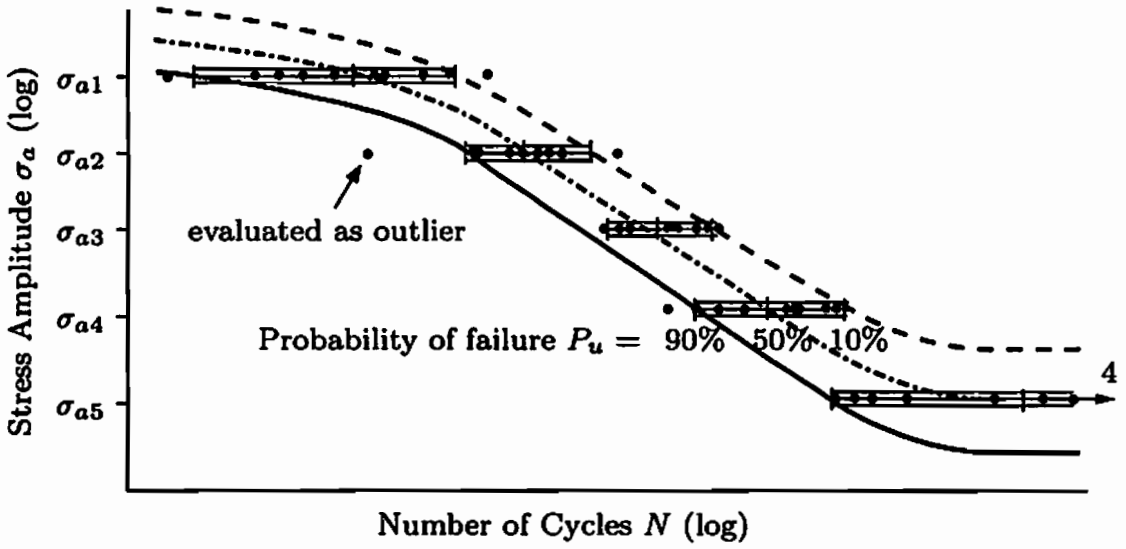

Figure 3.32: Scattering of results by Wöhler tests (Haibach)

equations for the description of the S-N curve (see Table 3.2). B, a, b, c, and σ_e in Table (3.2) are parameters which can be determined from experiments. The influence of the specimen geometry can be taken into account using stress concentration factors, which represent the proportion of stress raising for known geometry.

1870	Wöhler	$\lg N$	$= a - b \cdot \sigma$
1910	Basquin	$\lg N$	$= a - b \cdot \lg \sigma$
1914	Stromeyer	$\lg N$	$= a - b \cdot \lg(\sigma - \sigma_e)$
1924	Palmgren	$\lg(N + B)$	$= a - b \cdot \lg(\sigma - \sigma_e)$
1949	Weibull	$\lg(N + B)$	$= a - b \cdot \lg[(\sigma - \sigma_e)/(\sigma_u - \sigma_e)]$
1955	Stüssi	$\lg(N)$	$= a - b \cdot \lg[(\sigma - \sigma_e)/(\sigma_u - \sigma)]$
1963	Bastenaire	$\lg(N)$	$= a - \lg(\sigma - \sigma_e) - b \cdot (\sigma - \sigma_e)^c$

Table 3.2: Equations for the description of S-N curve according to Haibach (2002)

The characterisation of total fatigue life on the principle of stress-life approach is only relevant for constant amplitude fatigue loading. In reality, engineering components are subjected to different cyclic stress amplitudes, mean stresses and loading frequencies.

3.4.1.2 Block loading experiments

One of the most important load sequences in the study of variable amplitude fatigue fracture is based on involving blocks of different cyclic stress amplitudes

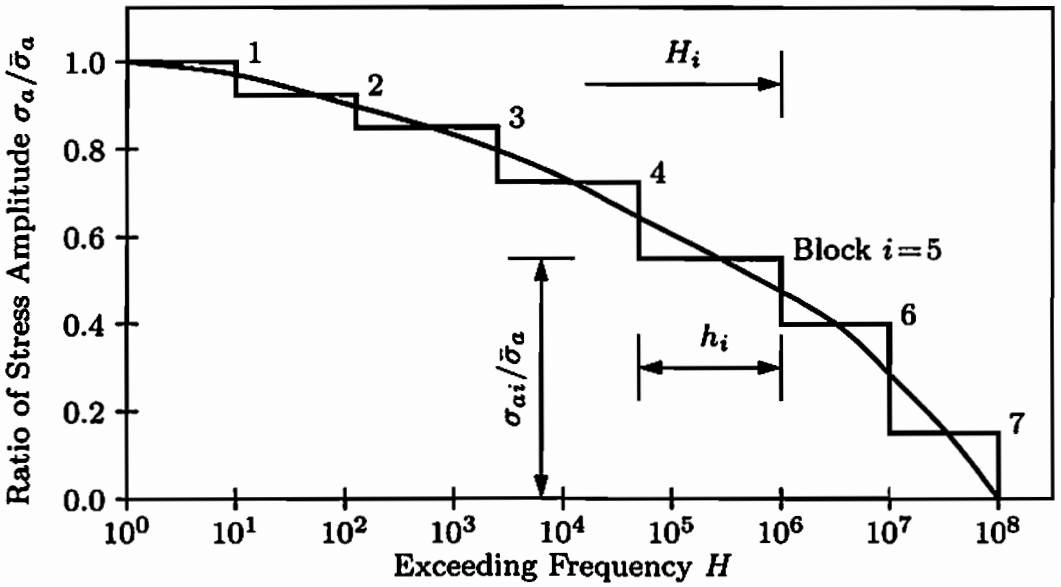

Figure 3.33: Distribution of load amplitude levels (Haibach)

and/or load ratios. Basis of such block tests is the classification of load spectra according to different load amplitude levels and their exceeding frequency (see Figure 3.33). The tests with the known duration of constant load amplitudes can be defined according to this statistical analysis. Typical block load distributions for different block tests are shown in Figure 3.34.
The width of the single block of load amplitude represents in the same time the frequency of the event. Further on, it is possible to vary the mean stress or the load frequency as additional changeable variables in order to get a better representation of the real load conditions through block test experiments. The blocks of load amplitude will be applied on the specimen up to its failure. This gives a statement over the fatigue life of specimen for specific load distribution and geometry form. Using only one block loading sequence in the block test leads to the Wöhler test with constant load amplitude.
If high-low or low-high block loading sequences are applied the following transient effects are commonly observed:

- Depending on the relative amplitudes and load ratios of the blocks, a stretch zone or a bifurcated crack tip profile can be caused by application of a low-high loading sequences.

- If the blunting of the crack tip by the high block reduces the pre-existing level of fatigue crack closure, the initial stages of a high amplitude block which follows a low amplitude block can induce a transient acceleration in crack growth.

- Pronounced retardation or even complete crack arrest can be caused by sudden reductions in maximum stress corresponding to a high-low sequence

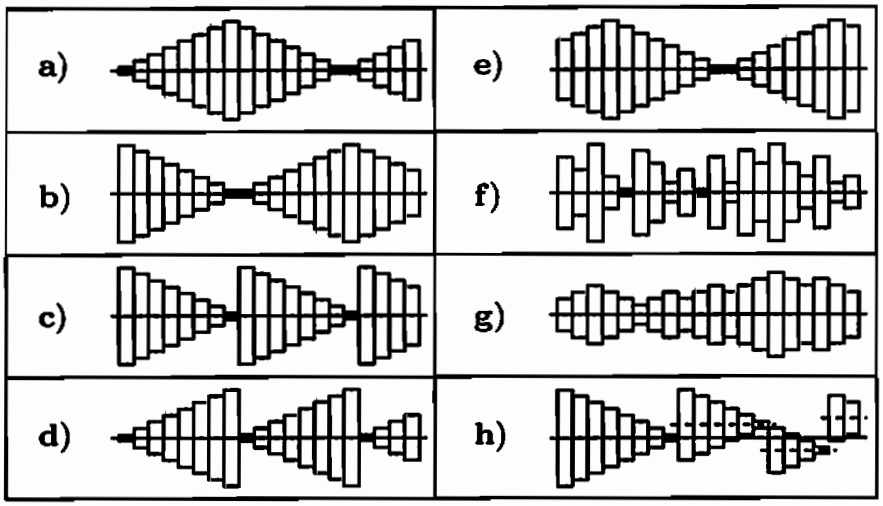

Figure 3.34: Variants of different block program tests: **a)** low-high-low sequences, **b)** high-low-high sequences, **c)** high-low sequences, **d)** low-high sequences, **e)** Gaßner's low-high-low sequences, **f)** random sequences with arbitrary transitions, **g)** random sequences with Markov's transitions, **h)** amplitudes with different mean stress (Haibach)

with a reduced stress ratio R or stress range $\Delta\sigma$.

- Changing from one block to another can lead to significant changes in the mechanism of crack growth.

Specific microstructural properties of the material dictate the attendant transient effects. The so-called *acceleration factor* γ represents load interaction effects associated with block loading sequences, and is defined as

$$\gamma = \frac{(\mathrm{d}a/\mathrm{d}N)_{s,exp}}{(\mathrm{d}a/\mathrm{d}N)_{s,p}}\,, \tag{3.132}$$

where $(\mathrm{d}a/\mathrm{d}N)_{s,exp}$ is the experimentally measured crack growth rate per block loading sequence, and $(\mathrm{d}a/\mathrm{d}N)_{s,p}$ is the growth rate per sequence predicted on the basis of linear summation of the constant amplitude crack growth response. For $\gamma = 1$ no interaction effects exist, $\gamma > 1$ represents an acceleration in the crack growth due to load interactions, and $\gamma < 1$ indicates retardation in the crack growth.

The order in which tensile and compressive overloads are applied has a strong influence on the rate of fatigue crack growth. Figure 3.35 represents typical effects on transient crack growth during constant amplitude fatigue (A), during the tensile-compressive overload sequences (B) and during variable amplitude loading involving single tensile overloads (C). The crack length locations, at which each variable amplitude sequence is applied, are represented by open circles.

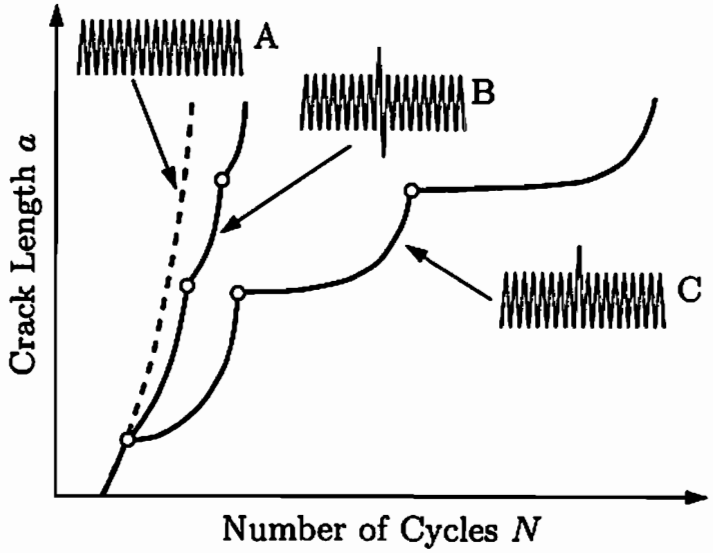

Figure 3.35: Schematic illustration of transient crack growth

3.4.1.3 Variable loading experiments

There are other possibilities to define the load spectra in a fatigue test. One such possibility is using random functions, which can be given as deterministic or stochastic load distribution. Deterministic load distribution can be described exactly as periodic or non-periodic function, and can be directly applied in the experiment as a command signal (target value) for load regulation. On the other hand, stochastic load distribution can be detected statistically with the description in the time or frequency domain. If a different statistical procedure is used, the calculated load distribution can be determined from the measured load data in order to achieve a realistic fatigue response during the service life. Such a procedure requires a considerable work in the acquisition and storage of measured data. In the light of the growing possibilities of the digitalisation, the representation of the load distribution using a stochastic procedure is in the focus of active research. By means of these procedures, complex load distributions can be created using digital regulations with considerably reduced work on the preparation of data.

Another possibility is to use a single load history, which can be recurrently applied to the appropriate structural component whose fatigue life needs to be determined. This load distribution is a periodic and deterministic load superposed to the stochastic part of the loading. Therefore, the single load history test is a special case of a random loading test, with a typical always recurring load distribution applied during the service life. In order to prove the fatigue life of a component, the component can be subjected to the corresponding load distribution in the laboratory, whereby the fatigue life is determined by the number of applied single load histories. The typical stress history to which the root of the wing of a transport aircraft is subjected during the flight is given in Figure

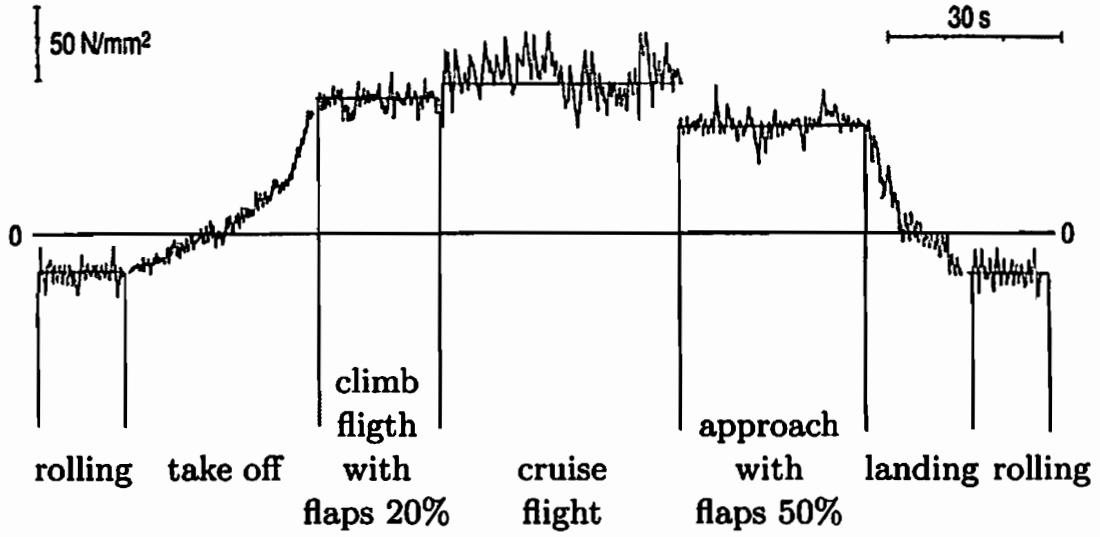

Figure 3.36: Typical stress-time plot for one structural component of transport aircraft (Haibach)

3.36. On the ground, the root of the wing is loaded in compression. The transition from a compressive stress on the ground to a tensile stress during flight is an important load cycle in itself, and is usually referred to as the ground-air-ground cycle. During flight, variable loads due to gust are superimposed to a mean tensile load corresponding to the undisturbed flight.
All introduced experimental procedures for the determination of fatigue life are not in a position to give real information in the case of variation in a geometry or load. Also, the effects resulting from the sequence loading cannot be considered appropriately. This leads to an enormous experimental work for the determination of fatigue life in the case of new or modified structures or unambiguous load histories.

3.4.2 Concept of cumulative damage in fatigue life calculation

A simple and frequently used criterion for the estimation of fatigue damage of structures is introduced by Palmgren (1924) and Miner (1945). It is called *linear cumulative damage rule* or *Palmgren-Miner rule.* Linear cumulative damage rule estimates the fatigue damage induced by a certain block of constant amplitude cyclic stresses in a loading sequence consisting of various blocks of different stress amplitudes. In Palmgren-Miner rule, it is assumed that:

- The number of stress cycles applied on a component, which are expressed as a percentage of the total number of stress cycles of same amplitude necessary for causing failure, represents the fraction of expended fatigue life.

- The fatigue life is not affected by the order in which the stress blocks of different amplitudes are imposed.

The Palmgren-Miner rule introduces a scalar damage measure D to the description of current damage state

$$D = \sum_{i=1}^{m} \frac{n_i}{N_i}, \tag{3.133}$$

where n_i is the number of cycles corresponding to the ith block of constant stress amplitude σ_{ai} in a sequence of m blocks, and N_i is the number of cycles to failure at σ_{ai}. The condition $D = 0$ characterises the undamaged material, and $D = 1$ the completely damaged material. At the same time, use of (3.133) requires a constant mean stress σ_m or a constant stress ratio R.
In the case of structural components with non-uniform cross section or with notches and holes, the stress amplitudes can be expressed using a *nominal stress* σ_{nom} or a *local stress* σ_{loc}. The ratio between local stress and nominal stress is called the theoretical *stress concentration factor* k_t. The local stress is given as

$$\sigma_{loc} = k_t \, \sigma_{nom} \, . \tag{3.134}$$

The nominal stress is not always defined in the same manner. It can be defined in the full cross section away from the notch, or as the average stress in the cross section through the notch. The local stress is the same in both cases. Use of different definitions of the nominal stress leads to different values of stress concentration factor. This is not problematic as long as the proper combinations are used to obtain the local stress.
Prerequisite for the use of the nominal stress concept is the definition of a nominal cross section that approximately represents the real complex geometry of a structural component. In addition, the following criterion is proposed by Haibach (2002): the nominal stress concept can be used for one- or two-dimensional structures, whose forms allow simple definitions of a nominal cross section or whose geometric inhomogeneities (notches, holes) can be adequately taken into account through the stress concentration factors. Then, it is possible to calculate the expected (remaining) fatigue life of a structural component by applying the nominal stress in the cumulative damage rule.
In the case of three-dimensional structures or for structural components with complex cross sections for which stress concentration factors cannot be determined, Haibach proposes the local stress concept. In this concept, local stresses can be calculated using an appropriate finite element or boundary element analysis with the assumption of elastic material behaviour. Calculated local stresses can be used in the cumulative damage rule for the calculation of the expected fatigue life of structural components.
In the original linear cumulative damage rule published by Miner (1945), only the load steps with the maximum stress above the endurance limit σ_e are considered.

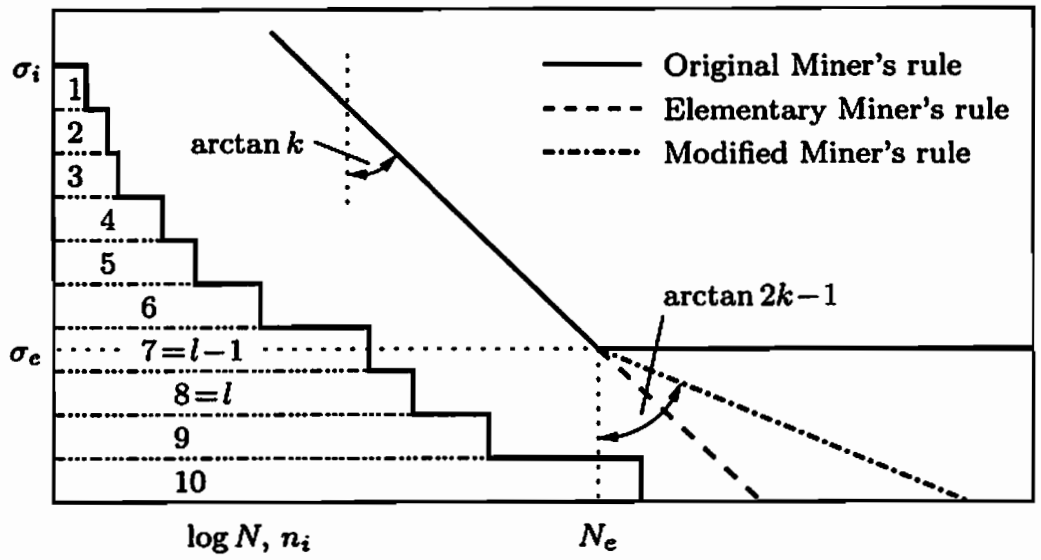

Figure 3.37: Different forms of Miner's rule

It is evident from Figure 3.37 that the only load steps to fulfil this condition are those with

$$\sigma_{l-1} \geq \sigma_e \,. \tag{3.135}$$

Here, the parameter l represents a load sequence with the stress immediately below the endurance limit. The calculated (durable) number of loading cycles N_{OM} based on the original Miner's damage rule for all $i<l$ is given as

$$N_{OM} = \frac{\sum_{i=1}^{j} n_i}{\sum_{i=1}^{l-1} \frac{n_i}{N_i}} \,. \tag{3.136}$$

If a linear representation of Wöhler curve in the high cycle fatigue range

$$N_i = N_e \left(\frac{\sigma_e}{\sigma_i}\right)^k \tag{3.137}$$

is used in (3.136), the original form of Miner's damage rule can be given as

$$N_{OM} = \frac{N_e \sigma_e^k \sum_{i=1}^{j} n_i}{\sum_{i=1}^{l-1} n_i \sigma_i^k} \,. \tag{3.138}$$

Neglecting all load blocks below the endurance limit leads to a systematic overestimation of the fatigue life. However, the endurance limit is defined for undamaged material, not for already damaged material after N load cycles. Hence,

decrease in the endurance limit due to the micromechanical changes following the stress concentration in the vicinity of the damaged material cannot be taken into account.
In an effort to take into account load blocks below the endurance limit, the elementary form of Miner's rule is introduced. In this hypothesis, the linear representation of Wöhler curve is extended through the additional fictive line with the slop $k' = k$ in the area below the endurance limit (see Figure 3.37). Therefore, all loads below endurance limit can influence damage from the first load cycle. According to the elementary form of Miner's rule the calculated (durable) number of loading cycles N_{EM} is given as

$$N_{\mathrm{EM}} = \frac{\sum_{i=1}^{j} n_i}{\sum_{i=1}^{j} \frac{n_i}{N_i}}, \tag{3.139}$$

or using stress representation

$$N_{\mathrm{EM}} = \frac{N_e \sigma_e^k \sum_{i=1}^{j} n_i}{\sum_{i=1}^{j} n_i \sigma_i^k}. \tag{3.140}$$

The calculation of fatigue life using this method shows a systematic underestimation of the fatigue life. Moreover, the existence of an endurance limit cannot be seized even for the load which is completely below the real endurance limit.
Based on numerous experiments during the investigation of fatigue life, Haibach (1970) proposes a modified Miner's damage rule for the estimation of the fatigue life. Similar to the elementary Miner's rule, the linear representation of Wöhler curve is extended through the additional fictive line with the slope $k' = 2k - 1$ below the knee point (see Figure 3.37). With this procedure, the influence of the damage effects below the endurance limit is taken into account. The calculated (durable) number of loading cycles N_{MM} defined by the modified Miner's rule is given as

$$N_{\mathrm{MM}} = \frac{N_e \sigma_e^k \sum_{i=1}^{z} n_i}{\sum_{i=1}^{j} n_i \sigma_i^k + \sigma_e^{(1-k)} \cdot \left(\sum_{i=j+1}^{z} n_i \sigma_i^{(2k-1)} \right)}, \tag{3.141}$$

where j is the number of load blocks above the endurance limit, and z is the total number of load blocks. Therefore, the modified Miner's rule represents a compromise between the original and the elementary Miner's rule.
The linear damage rule (3.133) is not the only possible representation of the fatigue damage. Other proposals for the calculation of the current damage state

can be found in the literature. Those are, for example, the nonlinear damage rule also known as the damage curve approach, or the bi-linear approximation of the damage curve approach known as the double linear damage curve (cf. Manson 1966, Manson & Halford 1981a, 1981b, 1986, Halford 1997).

3.4.3 Concept of strain-life approach in fatigue life calculation

Mainly an unconstrained deformation mode is related to the experimental information derived from stress-based continuum analysis. On the other hand, many structural components in practical applications undergo a certain degree of structural constraint, specially at locations where stress concentration occurs. In these situations, it is more appropriate to consider the constrained deformation loading situation in which the fatigue life of the component is calculated under a strain-controlled condition.
Working independently on thermal fatigue problems, Manson (1953) and Coffin (1954) proposed a characterisation of fatigue life based on the plastic strain amplitude. They detected a linear relationship between the logarithm of the plastic strain amplitude ε_{pa} and the logarithm of the number of load cycles to the failure $2N$ for metallic materials

$$\varepsilon_{pa} = \varepsilon'_f \cdot (2N)^c \,, \tag{3.142}$$

where ε'_f is the fatigue ductility coefficient, and c is the fatigue ductility exponent. In the case of constant strain amplitude test, the total strain amplitude can be written as a sum of elastic and plastic strain amplitude[2]

$$\varepsilon_a = \varepsilon_{ea} + \varepsilon_{pa} \,. \tag{3.143}$$

Coffin-Manson relation (3.142) gives a convenient engineering expression for characterising the total fatigue life. Using the relation between the stress amplitude σ_a in a constant amplitude test and the number of load cycles to the failure $2N$ (Basquin 1910)

$$\sigma_a = \sigma'_f \cdot (2N)^b \,, \tag{3.144}$$

where σ'_f is the fatigue strength coefficient, b is the fatigue strength exponent or Basquin exponent, and noting that

$$\varepsilon_{ea} = \frac{\sigma_a}{E} \,, \tag{3.145}$$

leads to

$$\varepsilon_{ea} = \frac{\sigma'_f}{E} \cdot (2N)^b \,. \tag{3.146}$$

[2] In classical theory for small deformations (see Xiao et al. 2006).

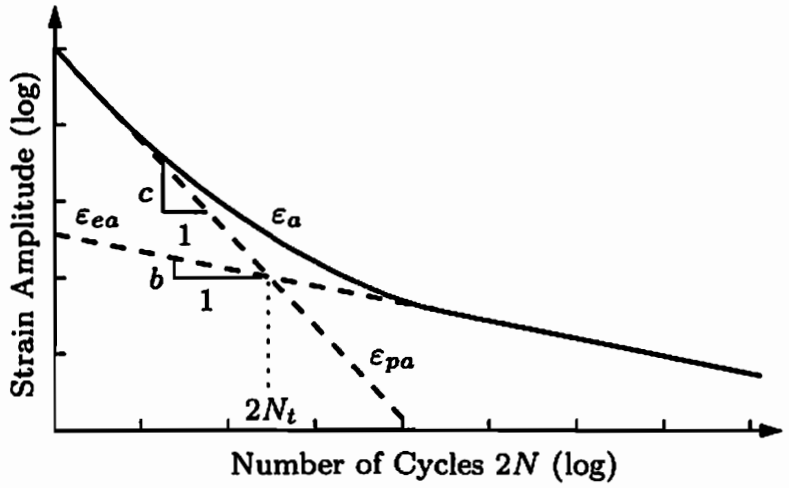

Figure 3.38: Representation of Wöhler curve with strain amplitude

Combining (3.142), (3.143) and (3.146), one obtains

$$\varepsilon_a = \frac{\sigma_f'}{E} \cdot (2N)^b + \varepsilon_f' \cdot (2N)^c \,. \tag{3.147}$$

This equation forms the basis for strain-life approach to fatigue design and has found widespread application in industrial practice. Variations of elastic, plastic and total strain amplitudes as functions of the number of load cycles to failure $2N$ from equations (3.145), (3.142) and (3.147) respectively are plotted in Figure 3.38. Number of cycles to failure at which the elastic and plastic strain amplitudes are equal characterises the transition life $(2N)_t$. It follows from (3.146) and (3.142) that

$$(2N)_t = \left(\frac{\varepsilon_f' E}{\sigma_f'}\right)^{1/(b-c)} \,. \tag{3.148}$$

For low cycle fatigue when $2N \ll (2N)_t$, the plastic strain amplitude is more significant than the elastic strain amplitude and the fatigue life of material is controlled by ductility. For high cycle fatigue when $2N \gg (2N)_t$, the elastic strain amplitude is more dominant than the plastic strain amplitude and the fatigue life of the material is controlled by fracture strength.
Ramberg-Osgood relationship follows from (3.142)÷(3.147) and has the form

$$\varepsilon_a = \left(\frac{\sigma_a}{E}\right) + \left(\frac{\sigma_a}{K'}\right)^{1/n'} \,, \tag{3.149}$$

with

$$n' = \frac{b}{c}, \quad K' = \sigma_f' \cdot \varepsilon_f'^{\,-n'} \,, \quad \text{and} \quad \varepsilon_{pa} = \left(\frac{\sigma_a}{K'}\right)^{1/n'} \,. \tag{3.150}$$

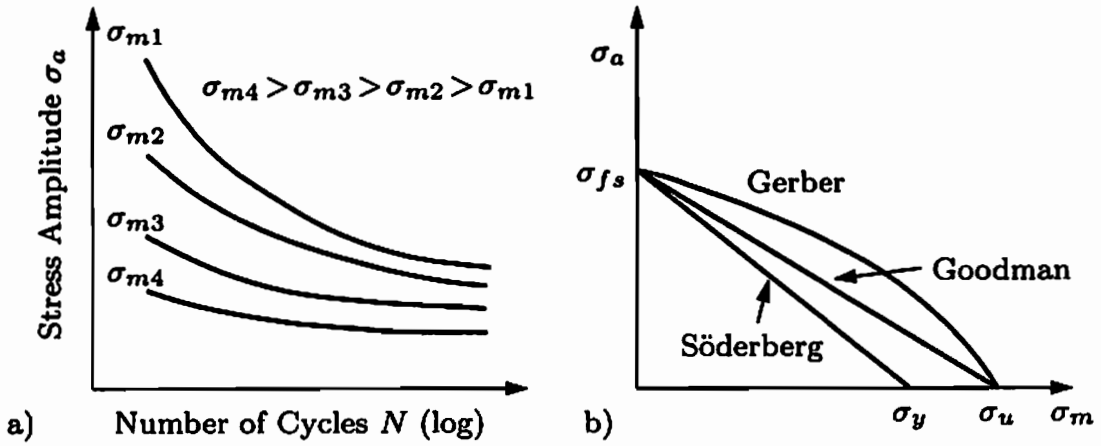

Figure 3.39: Wöhler curve for different mean stresses: a) stress amplitude versus fatigue life plots for different mean stress values, b) constant fatigue life diagrams for fatigue loading with a nonzero mean stress

3.4.4 Influence of mean stress and mean strain on fatigue life

It is well known that the mean stress level of the imposed fatigue cycle plays an important role in the fatigue behaviour of engineering materials. Typical Wöhler curves for metallic materials as a function of different mean stress levels are plotted in Figure 3.39a. The plot shows that an increase of the mean stress value leads to a decrease in fatigue life. Another possibility to represent mean stress effects in fatigue is to use constant-life diagrams in which different combinations of the stress amplitude and the mean stress are plotted to provide a constant fatigue life. Plots of models proposed by Gerber (1874), Goodman (1899) and Söderberg (1939) are given in Figure 3.39b. These three empirical models are described by the following expressions

$$\text{Gerber relation}: \quad \sigma_a = \sigma_{fs}\left[1 - \left(\frac{\sigma_m}{\sigma_u}\right)^2\right], \tag{3.151}$$

$$\text{Goodman relation}: \quad \sigma_a = \sigma_{fs}\left(1 - \frac{\sigma_m}{\sigma_u}\right), \tag{3.152}$$

$$\text{Söderberg relation}: \quad \sigma_a = \sigma_{fs}\left(1 - \frac{\sigma_m}{\sigma_y}\right), \tag{3.153}$$

where σ_a is a stress amplitude denoting fatigue strength for a nonzero mean stress, and σ_{fs} is the fatigue strength for a fixed life for fully reversed loading ($\sigma_m = 0$ and $R = -1$). According to Suresh (1991), (3.151) provides good results for ductile alloys, (3.152) matches quite closely experimental observations for brittle metals, but is very conservative for ductile alloys, and (3.153) provides a conservative estimation of fatigue life for most engineering alloys.

In the strain-based characterisation of fatigue life, the mean stress effects can be incorporated using the assumption that a tensile mean stress reduces the fatigue strength σ'_f, such that

$$\sigma_a = (\sigma'_f - \sigma_m)(2N)^b \,. \tag{3.154}$$

The strain-life relationship (3.147) can be rewritten as

$$\varepsilon_a = \frac{\sigma'_f - \sigma_m}{E} \cdot (2N)^b + \varepsilon'_f \cdot (2N)^c \,. \tag{3.155}$$

The cycle dependent relaxation of the mean stress is a counterpart of a cyclic creep mechanism under strain-controlled fatigue loading. If a ductile solid which is subjected to a fixed cyclic strain amplitude with mean strain in tension exhibits cyclic softening behaviour, a progressive reduction in the mean stress with increasing strain cycling can be observed. The rate of decrease in mean stress progressively diminishes as the mean stress level approaches zero.
The mean stress relaxation can also occur in cyclically hardening materials. Increasing of the stress range and reducing of the plastic strain range during cyclic hardening for a fixed total strain amplitude can be observed.
The influence of the mean strain during fatigue tests and appropriate relaxation of mean stress can be considered using a damage parameters (cf. Smith et al. 1970, Haibach & Lehrke 1976, Vormwald & Heuler 1993). It is possible to define so-called Wöhler damage parameters curve (Haibach 2002) from Wöhler strain curve given in Figure 3.38 and to calculate the fatigue life for given loading conditions if damage parameters are defined.

4 Nondestructive methods for detection of crack growth

As pointed out in Chapter 3, crack growth due to fatigue and stress corrosion is normally a slow degradation process up to a point beyond which failure may be sudden and catastrophic. This is a reason why early detection of crack growth during this initial period is essential for the prevention of failure, especially for engineering structures subjected to a fatigue loading. Experiments involving stable crack growth and measurement of the instantaneous crack length are essential in fracture mechanics. That is the reason why many experimental methods have been developed to monitor such crack growth.
Some of these methods belong to the group of methods of nondestructive testing. Nondestructive testing represents a testing without destroying the test object. Representative methods of nondestructive testing are: radiographic testing, ultrasonic testing, direct and alternating current potential drop measurement, acoustic emission testing, infrared and thermal testing, liquid penetrant inspection and others.
In this chapter, two nondestructive methods which are used in experimental investigation of crack growth in this work will be presented. These two methods are detection of acoustic emission and measurement of electrical resistance.

4.1 Basics of acoustic emission

It is not possible to define the moment in history when the acoustic emission was heard for the first time, but it is probable that fracture processes such as the cracking of rocks and the breaking of bones were among the earliest. Restricting the attention to the acoustic emission in metalworking, researchers state that the first observation of this phenomenon could be a tin cry, the audible emission produced by mechanical twinning of pure tin during plastic deformation, and it could have occurred only after man learned to smelt pure tin, i.e after 3700 BC. The first documented acoustic emission could be found in the Latin edition of the book *Summa Perfectionis Magisterii* by the eight century Arabian alchemist Jabir ibn Hayyan (also known as Gerber), published in Berne in 1545. In his book, he writes about different noises made by tin and iron during the treatment. The possible reason for this sounding of iron is the formation of martensite during cooling (Holmyard. & Litt (1928) in Drouillard (1987)).
During the study of twinning and martensitic phase transformation, sounds emitted by metals such as tin, zinc, cadmium and some alloys of iron were perceived.

A first report in the literature about the association of tin and zinc cry to twinning is given by Czochralski (1917). Later on, some other scientists also reported about the existence of noise in the experiments with aluminium and steel alloys during formation of shear bands and martensitic transformation (Portevin. & LeChatelier (1923), Anderson (1925), Classen-Nekludowa (1929), Scheil (1929)).
The basis of today's technology in acoustic emission is the work of Josef Kaiser (1950). In his Ph. D. Thesis, he presented first comprehensive investigation of the phenomena of acoustic emission. He investigated conventional engineering materials under tensile stress in order to determine what kind of noise is generated from within the specimen, the frequency level and the relation between the frequencies registered at various stress levels and the stress-strain curve. The work of Kaiser is further analysed by Schofield (1958), who has given one of the most detailed descriptions of acoustic emission in metallic crystals. Many other scientists contributed to the development of acoustic emission technology (Pollock (1968), Dunegan et al. (1968), Hsu & Breckenbridge (1979), Berkovits & Fang (1993)).

4.1.1 Acoustic emission phenomenon

Metals absorb and release strain energy under stress using mechanisms which can be different and complicated. The acoustic emission represents the elastic energy that is spontaneously released by materials when they undergo deformation and fracture. For this reason, the stress waves which result from this sudden release of elastic energy due to micro-fracture events are of great interest to the structural engineer. These events are typically 10μm to 100μm in linear dimension.
Crack growth, moving dislocations, slip, twinning, grain boundary sliding and fracture and decohesion of inclusion represent sources of acoustic emission identified in metals. These mechanisms symbolise the classical response of materials to applied load. Other mechanisms, detectable with acoustic emission equipment, such as friction, cavitation and leaks, solid-solid phase transformation, liquefaction and solidification should be distinguished from the classic acoustic emission sources due to mechanical deformation of stressed materials. They are sometimes called *secondary sources*.
In the past few decades, examination of acoustic emission as a nondestructive testing method proved capable in monitoring structural integrity, detecting leaks and incipient failures in mechanical equipment and characterising material behaviour.
Compared to other nondestructive methods, acoustic emission is evidently different in two significant respects:

- The detected energy is released from within the test object rather than being supplied by the nondestructive method, as in ultrasonics or radiography.

- The acoustic emission method is capable of detecting the dynamic processes associated with the degradation of structural integrity.

4.1.2 Sources of acoustic emission

Depending on the scale level from which sources of acoustic emission arise, it is possible to distinguish microscopic and macroscopic sources. According to Wadley & Simmons (1987), microscopic acoustic emission sources are dislocations, initiation and growth of microcracks and martensitic phase transformations. In contrast to acoustic emission related to microscopic sources, the macroscopic sources refer to cases where a relatively large part of the test material contributes to the acoustic emission. In this case, sources of acoustic emission according to Bassim (1987) are stresses around and above the yield stress and plastic deformation, fracture and macrocrack growth, fatigue cracking, corrosion and stress corrosion.

At the same time, although the stresses may be well below the elastic design limit, the region near the crack tip may undergo plastic deformation due to stress concentration and the propagating discontinuity can produce stress waves, whereby the possibility to detect stress waves depends on the load level (cf. Spanner et al. 1987).

4.1.3 Kaiser effect

The irreversible material response in most metals is an important feature affecting acoustic emission applications. *Kaiser effect* is the phenomenon that a material under reloading conditions emits acoustic waves only after the primary load level is exceeded. These materials behave elastically during reloading and little or no acoustic emission will be recorded before the previous maximum stress level is achieved. Also, the magnitude and the duration of the earlier loading and the time between the earlier loading and the test loading have no importance (Kaiser 1953). This is true only for materials in which no change in microstructure, such as dislocation movement or crack initiation, can be observed in the meantime.

The case when acoustic emission is recorded before the previous maximum load is reached is known as *felicity effect* and describes the breakdown of the Kaiser effect. If the ratio between the load level at which the acoustic emission appears and previous maximum load level is defined as felicity ratio, it can be used as the associated quantitative measure of the felicity effect. In the case of the Kaiser effect, the value of the felicity ratio is 1. Felicity effect occurs in situations where time dependent mechanisms control the deformation, in corrosion processes and hydrogen embrittlement.

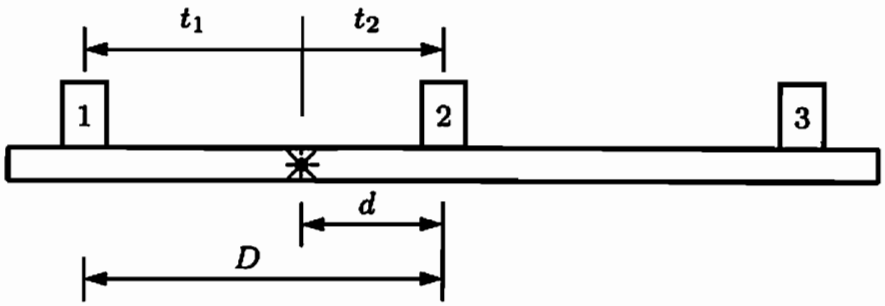

Figure 4.1: Linear location of the source

4.1.4 Location of acoustic emission sources

One of the most important functions of the multichannel instrumentation system used in field application is the ability to locate the sources of acoustic emission. One of the methods for detecting the source of acoustic emission is the measurement of the time differences in the reception of stress waves at a number of sensors (so-called hits) in an array under the assumption that acoustic wave has a constant velocity. One, two and three dimensional problems can be defined depending on the sensor location. One dimensional problems are also known as linear problems.

4.1.4.1 Linear location of acoustic emission sources

Consider the situation where sensors are mounted on a linear structure. Assume that an acoustic emission event occurs somewhere on the structure between sensors 1 and 2, and that the resulting stress waves propagate in both directions at the same velocity (see Figure 4.1). It is possible to locate the position of the acoustic emission source by using the measurement of the time differences between hits (see Figure 4.1 and Baron & Ying 1987). In general, the time difference between hits is equal to

$$\Delta t = t_1 - t_2 \,. \tag{4.1}$$

For the constant velocity of the acoustic emission waves V, it follows

$$V = \frac{D-d}{t_1} = \frac{d}{t_2} \,. \tag{4.2}$$

Consequently, the linear location of acoustic emission source is given by

$$d = \frac{1}{2}(D - V\,\Delta t) \,. \tag{4.3}$$

Here, t_1 and t_2 are the times of the hits at sensors 1 and 2 respectively, D is the distance between sensors, V is the constant wave velocity, Δt is the time difference and d is the distance between the location of the source and sensor

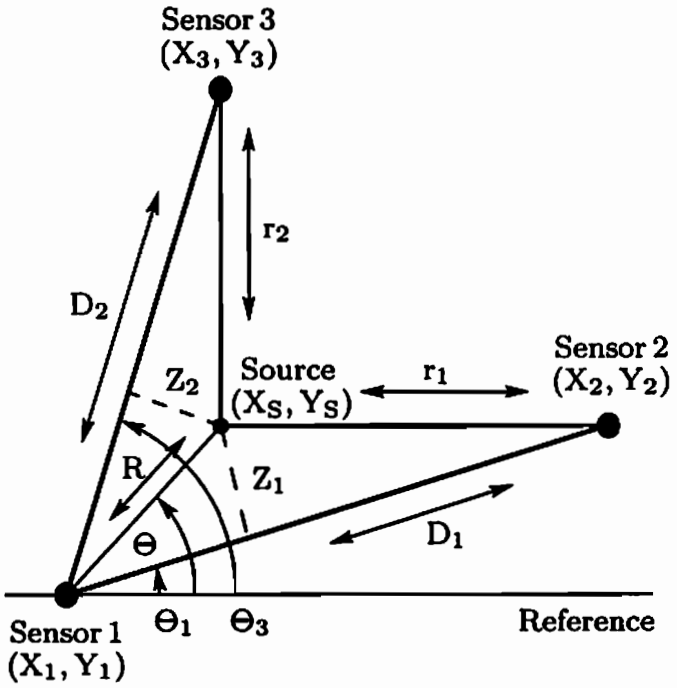

Figure 4.2: Location of the source in two dimensional case

2. If the time difference between the hits of both sensors is zero, it would indicate a source precisely midway between the sensors. In the case when the source is outside the sensor array (in Figure 4.1 the pair 1-2), the time difference measurement corresponds to the time of flight between the sensor pair 1-2 and remains constant. The position of the source is in that case assumed under or beyond the sensor (in the sensor pair 1-2) closest to the actual source position.

4.1.4.2 Location of acoustic emission sources in two dimensions

Based on a measurement of time differences in reception of stress waves with constant velocity for two sensors on an infinite plate, it can be easily shown that the emission sources lie on a hyperbola. Therefore, the location of sources in two dimensions requires a minimum of three sensors (Tobias 1976, Baron & Ying 1987). The input data now include a sequence of three hits and two time difference measurements, between the first and second hit sensors and the first and third hit sensors, as can be seen in Figure (4.2). Then:

$$\Delta t_1 V = r_1 - R, \quad \Delta t_2 V = r_2 - R, \tag{4.4}$$

which yields

$$R = \frac{1}{2} \frac{D_1^2 - \Delta t_1^2 V^2}{\Delta t_1^2 V + D_1 \cos(\Theta - \Theta_1)}, \tag{4.5}$$

and

$$R = \frac{1}{2} \frac{D_2^2 - \Delta t_2^2 V^2}{\Delta t_2^2 V + D_2 \cos(\Theta_3 - \Theta)} . \tag{4.6}$$

Hyperbolic equations (4.5) and (4.6) can be solved simultaneously to provide the location of a source in two dimension. However, for any given array of three sensors, there exist areas where this solution is not unique because it corresponds to two points of intersection of the corresponding hyperbolae. Both intersections satisfy the input data well and it is not possible to separate the true source from the false source without additional information. Therefore, a fourth sensor is added to the array. The fourth sensor generates extra time difference measurement and produces a third hyperbola which should have a single common point of intersection defining the true source.

4.1.5 Characteristics of acoustic emission

The acoustic emission expected in fatigue studies is primarily of the burst type. Burst type emission signals originate from sources such as intermittent dislocation motion and crack growth in metals. Occurrences of individual signals are well separated in time. The signal usually rises rapidly to the maximum amplitude and decays nearly exponentially to the level of background noise. The burst signal, given in Figure (4.3), has the following characteristic parameters: acoustic emission event, count, event energy, signal amplitude, signal duration and rise time. Cumulative representation of these parameters can be defined as a function of time or test parameter including total events, amplitude distribution and accumulated energy.
The terminology of characteristic parameters of burst signal is taken from *Nondestructive Testing Handbook, Vol.5, Acoustic Emission Testing* (Spanner et al. 1987) and is in accordance with ASTM[1]:

- amplitude: Maximum signal amplitude within duration of the burst.
- burst: A signal whose oscillations have a rapid increase in amplitude from an initial reference level, followed by a decrease to a value close to the initial value.
- counts: The number of times the signal amplitude exceeds the preset threshold.
- decay time: The time interval between the maximum amplitude of the burst and the last threshold crossing.
- duration: The interval between the first and the last time the threshold was exceeded by the burst.

[1] American Society for Testing and Materials

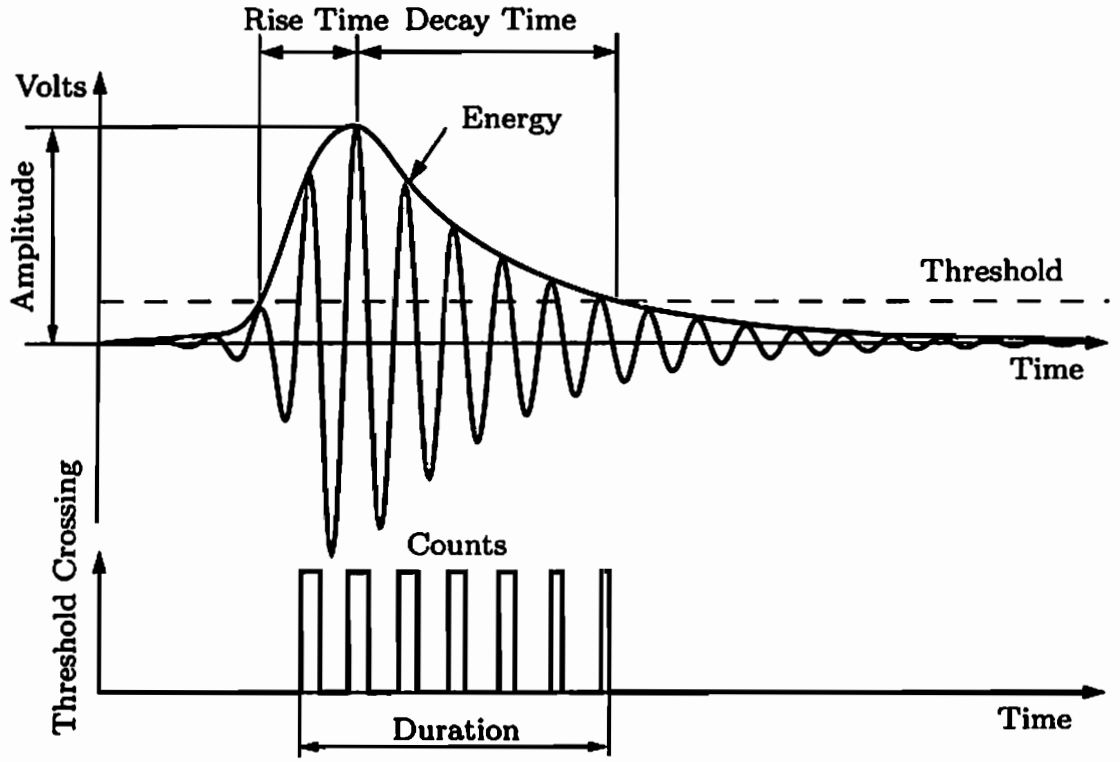

Figure 4.3: Definition of a simple waveform parameters for a burst-signal

- event: A microstructural displacement that produces elastic waves in a material under load or stress, which are detected by several acoustic emission transducers. The origin of acoustic emission signal can be detected using the time analysis.
- event counts: Counts which belong to a distinct event. In the case of multiple events, the sum of event counts for all events is equal to the total number of counts.
- hit: Total signal from the first to the last threshold crossing.
- rise time: The time interval between the first threshold crossing and the maximum amplitude of the burst.
- threshold: A preset voltage level that has to be exceeded before an acoustic emission signal is detected and processed. The threshold is chosen upon the level of the background noise.

The parameters which are important for the measurement of acoustic emission signals are represented in Figure 4.4:

- Peak Definition Time (PDT): The interval of the time after the last threshold crossing, available for the search of the global maximum of the signal. PDT is restarted after every threshold crossing.

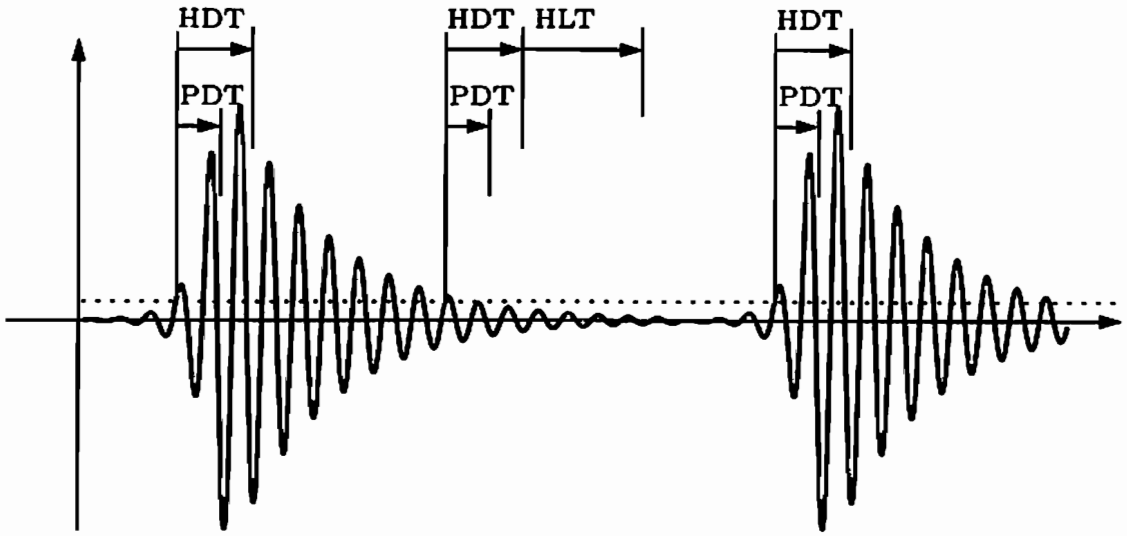

Figure 4.4: Definition of system timing parameters (PDT, HDT, HLT)

- Hit Definition Time (HDT): The interval of the time after the last threshold crossing, available for the search of the new threshold crossing. HDT is restarted after every threshold crossing.
- Hit Lockout Time (HLT): Dead time at the end of the HDT if no threshold crossing appeared. HLT is started only at the end of such HDT. During this time the input is closed and acoustic emission signals cannot be received.

A proper setting of the PDT ensures correct identifications of the signal peak for rise time measurements. Proper setting of the HDT ensures that each acoustic emission signal is reported as one and only one hit. With a proper setting of the HLT, spurious measurements during the signal decay are avoided and data acquisition speed can be increased. Since, acoustic emission signals are represented by recorded data about parameters such as sum of counts, energy, amplitude or frequency, the correct definition of PDT, HDT and HLT has great importance. Inadequate definition of these three parameters can lead to the split of a single signal into several parts or to the merge of different signals into one signal. In both cases, the recorded data leads to a false representation of acoustic emission signals.

4.1.6 Application of acoustic emission

Acoustic emission has found a huge application not only in laboratory testing but also in production and structural testing (cf. Pollock 1989).
Acoustic emission inspection in a production testing can be considered whenever the process, which stresses the material and produces permanent deformation, produces a typical response signal of acoustic emissions, whose change may indicate an erroneous (defective) process. Acoustic emission inspection is used for

checking and controlling welds, brazed joints, thermocompression bonding and forming operations such as shaft straightening.
One of the earliest use of acoustic emission in production testing is the monitoring of welding processes (cf. Vahaviolos et al. 1987). In the case of a resistance welding, various phases of the weld process are treated separately and the acoustic emission monitoring is carefully synchronised to the weld cycle. Acoustic emission during solidification and cooling is correlated with nugget size and weld strength, while high-amplitude signals from expulsions can be used to switch off the weld current at the optimum time. As the nugget cools during the hold period, acoustic emission can result from the solid-solid phase transformation and the post-weld cracking. A deviation of the standard acoustic emission response signal during welding, for example through a crack initiation in the weld seam or a complete separation of the weld point, can be recognised during the monitoring. This can indicate further investigation of the critical zone using other nondestructive testing methods.
In the case of production testing, acoustic emission inspection is used in monitoring pressure vessels, storage tanks, pipelines and piping, aircraft and space vehicles, bridges and dams, railroad tank cars, and a range of other equipment items (cf. Green et al. 1987, Hopwood & McGogney 1987). Acoustic emission structural testing is used to find defects and to evaluate and ensure structural integrity. The stress concentrations that cause defects and other areas of weakness, which emit acoustic waves while the rest of the structure is silent, are the key to structural testing with acoustic emission inspection. The acoustic emission testing has a major advantage over other nondestructive testing methods in that it does not require access to the whole examination area. For this reason, the acoustic emission inspection is usually complemented to the other nondestructive testing methods that are used to assist in determining the type, severity and acceptability of the acoustic emission sources. As is pointed in Section 4.1.3, previously applied stresses have a very strong influence on the emission that will be observed, and therefore, a special attention must be paid to the type, magnitude and rate of the applied loading during acoustic emission structural testing.

4.2 Measurement of electrical resistance

In the past decades, many experimental methods for monitoring processes such as crack initiation and rate of crack propagation are developed. The electrical resistance method (or potential drop method) is one of the most accurate and most sensitive nondestructive methods for monitoring crack initiation and measuring crack growth (see Ritchie et al. 1971). In the electrical resistance method a constant direct current is usually passed through the specimen and the electrical resistance between two measurement points located on opposite sides of the crack is monitored. As the crack propagates, the uncracked cross-sectional area of the test specimen decreases, and electrical resistance between two points on either side of the crack increases.

The electrical potential method is applied for the first time by Trost (1944) for the detection of surface cracks in large scale structures. After that, this method is used in monitoring the propagation of fatigue, stress corrosion and creep cracks, hydrogen embrittlement, determining initiation of ductile crack growth in crack-opening displacement tests and assessing the proportion of crack closure in fatigue crack growth studies (cf. Ritchie & Knott 1973, Barnett & Troiono 1957, Haigh et al. 1976, Lowes & Featnehough 1971, Unangst et al. 1977, Saxena 1980, Gangloff 1981).
The advantage of the electrical resistance method is in the simplicity of its system compared with other nondestructive techniques such as acoustic emission, vortex current, ultrasonic testing, etc. The advantage of the electrical resistance method over the optical measurement of the crack propagation is the fact that tests may be conducted in any sealed environment because electrical resistance method does not require visual accessibility. Continuous output of measured electrical resistance permits automated data collection and processing together with all day usage of testing machine capacity. The technique is capable of detecting small increments of crack growth, which cannot be resolved optically. This method is particularly useful in the study of fatigue thresholds and very slow crack propagation rates, which occur in high cycle fatigue tests, as an addition to the majority of fatigue testing methods, which concentrate on intermediate and high stress intensities.
The electrical resistance method is based on the fact that the electrical resistance (R_a) increases if the test specimen is under cyclic fatigue loading. The crack length (a) or the crack length-to-specimen width ratio (a/w) may be determined by comparing (R_a) to a reference electrical resistance (R_0) measured on the test specimen before the beginning of the test, if suitable calibration curves are used. In practice, the accuracy of an electrical resistance measurement of the crack length may be limited by a number of factors:

- The electrical stability and resolution of the electrical resistance measurement system.
- Electrical contact between crack surfaces where the fracture morphology is rough or where significant crack closures are present.
- Changes in electrical resistance with plastic deformation.
- Changes in electrical resistance with temperature change.

This accuracy limitations are present in particular in the process of determination of calibration curves relating changes in electrical resistance across crack length (R_a) to the crack length (a). In most cases, experimental calibration curves have been obtained by measuring the electrical resistance across:

- Machined slots of increasing length in a single test specimen.

- A growing fatigue crack, where the length of the crack at each point of measurement is marked on the fracture surface by a single overload cycle or by a change in the mean stress.

- A growing fatigue crack in thin specimens where the length of the crack is measured by surface observation.

One of the most used procedures of potential drop calibration is the one derived by Johnson (1965). Johnson gives mathematical formulas relating the crack length to the electrical potential drop across the crack in several fracture specimen geometries, including the centre-cracked panel. However, Johnson's expressions are applicable to symmetric crack growth and for voltage probe location on the centreline of the specimen.
In the case of an asymmetrical crack propagation, an approximate solution to Laplace's equation for the potential in a current-carrying centre-cracked panel is proposed (cf. Read & Pfuff 1991, McKeighan et al. 1995). Also, it is possible to find analytical solutions for evaluating the potential drop for half-circular and half-elliptic surface cracks in the literature. Nevertheless, these solutions are applicable to the case where the size of the crack is much smaller then the dimensions of the specimen (see Ikeda et al. 1991, Tada 1992).
Another noteworthy calibration procedure is the correlation of elastic and electrical properties (Sevostianov et al. 2002a, 2002b).
In the experiments with complicated specimen or crack geometry or in experiments with highly asymmetrical crack growth, all of this calibration procedures are inappropriate and computer simulations based on finite element or boundary element techniques can be used to generate new potential drop calibration procedure (cf. Ritchie & Bathe 1979, Hicks & Pickard 1982).

5 Experimental setup

For the experimental investigation of the damage process during high cycle fatigue and the parameter identification of a respective material model, it is necessary to realise an experimental setup, which can lead to a meaningful damage detection under appropriate load and boundary conditions.
At the same time, special attention is paid to the best possible application of two chosen nondestructive methods in the investigation of a crack growth, namely the measurement of acoustic emission and electrical resistance.
For example, the reduction of background noise is an important task in order to enable detection of low energy signals during the damage evolution in the case of the measurement of acoustic emission. This is achieved through the reduction of the threshold amplitude of acoustic emission. The measurement of electrical resistance demands an electrical decoupling between the specimen, where the electrical resistance is measured, and the rest of the experimental setup.
One of the most important features in the process of realisation of the suitable experimental setup is the construction of an adequate specimen. All experiments presented in this work are conducted on two specimen forms, developed in accordance with a number of specific demands regarding the quality of the damage detection and the form of the damage.
This chapter is subdivided into five sections. The specimen material and the specimen geometries are presented in Section 5.1. This is followed by the detailed review of the procedure of clamping of specimen to the machine in Section 5.2. The details about the mechanical loading during the high cycle fatigue experiments are given Section 5.3. The methods for nondestructive detection of crack growth are described in Section 5.4, as well as temperature measurement, data acquisition and macroscopic documentation. This chapter is concluded with the schematic representation of the complete testing system.

5.1 Specimen material and geometry

All specimens used in experiments presented in this work are made from the heat treatable steel 42CrMo4 (Mat. No. 1.7225). The chemical composition and mechanical properties of the applied steel are given in Tables 5.1 and 5.2, respectively (see Wegst (1992) and DIN EN 10083-3).
All experimental tests are completed on specimens with two geometries given in Figures 5.1 and 5.2. The choice of the geometry is based in both cases on a number of design constraints.

Chemical composition in weight %						
C	Si	Mn	P	S	Cr	Mo
0.38-0.45	$\leq$0.40	0.60-0.90	$\leq$0.035	$\leq$0.035	0.90-1.20	0.15-0.30

Table 5.1: Chemical composition of 42CrMo4

Yield stress σ_y N/mm^2	Tensile strength σ_u N/mm^2	Young's modulus E N/mm^2	Elongation A %
900	1100-1300	$\approx 2.1 \cdot 10^5$	10

Table 5.2: Mechanical properties of 42CrMo4

One of those constraints is the minimisation of the vibration of the specimen during cyclic loading experiment in order to reduce the threshold value for the recording of acoustic emission. This threshold value should be kept low, if the low elastic energy acoustic waves characteristic for the slow advancement of damage are to be detected.
The installation of acoustic emission transducers is another important constraint in the design process. The minimum characteristic length of the specimen is calculated based on the minimum dimension of installation area. The installation area of an acoustic emission transducer must be a planar surface.
Additionally, the characteristic equation describing the change of thickness of the specimen in Figure 5.2 is defined based on the desired position of the damage.
Furthermore, the specimen needs to be designed in such a way to maximise the performance of the equipment used for the measurement of electrical resistance.
A specimen with a geometry given in Figure 5.1 is called a *plain specimen* and is designed by Heiderich (2004). All specimens of this type are cut in the same direction from the 5 mm thick plate using a water jet cutter process. In this process, the cutting edges are not perpendicular to the surface, and an additional treatment of the cutting edges is necessary. The desired form of cutting edges and final dimensions of the specimen are secured through a finishing procedure using a milling cutter. The localisation of the damage initiation is achieved by a variation of the cross section in the middle of the strait part of the specimen (see the dashed line circle in Figure 5.1), which generates a stress concentration. The cross section variation has a form of a hole with the diameter of 1 mm or both side notches with 0.2 mm depth (see Figure 5.3).
In order to perform experiments with cyclic load in different directions, a completely new specimen form is developed. The geometry of this specimen is given in Figure 5.2. The specimen with this geometry is called a *circular specimen.*

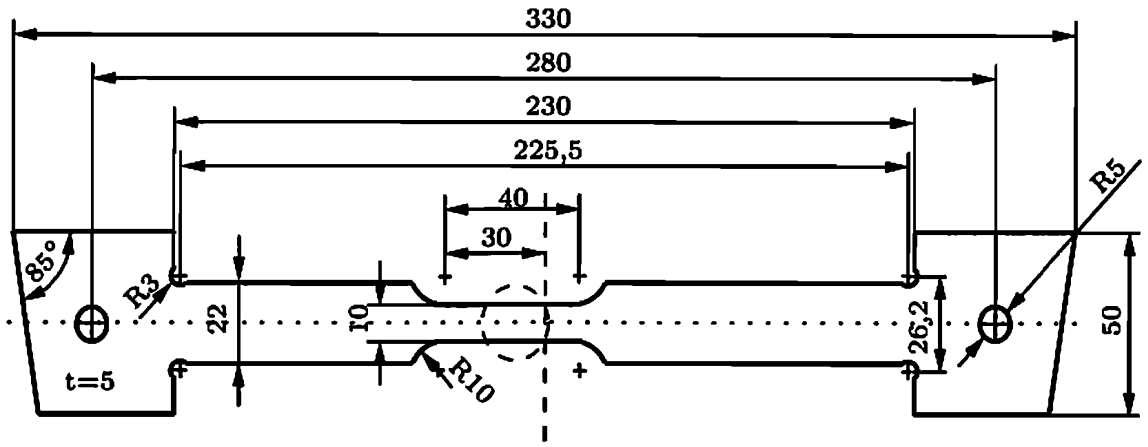

Figure 5.1: Geometry of the plain specimen (dimensions in mm)(Heiderich)

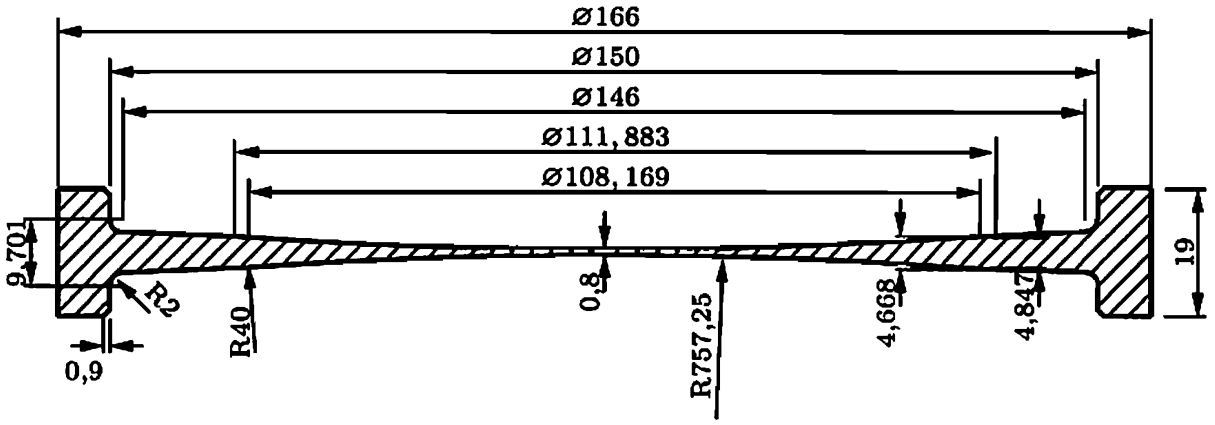

Figure 5.2: Geometry of the circular specimen (dimensions in mm)

The circular form of the specimen is chosen based on the fact that it allows arbitrary loading direction.

All circular specimens are cut from the round bar with a diameter of 180 mm. Specimens are at first rough machined using a bench lathe. The final dimensions of the specimen are achieved using a CNC lathe[1]. Since the final surface of the specimen after the treatment with the CNC lathe does not guaranty the desired position of the damage initiation, the finishing procedure includes a surface polishing of the central area of the specimen. The ring of the specimen has an outer diameter of 166 mm, an inner diameter of 150 mm, and a thickness of 19 mm. Specimen surface has a spherical form with a minimum thickness of 0.8 mm in the centre of the specimen. Non-constant thickness of the specimen leads to the maximum of the stress in the central part of the specimen, and to the initiation of the damage in the centre of the specimen.

[1]Co. Pinacho GmbH, Smart Turn 180

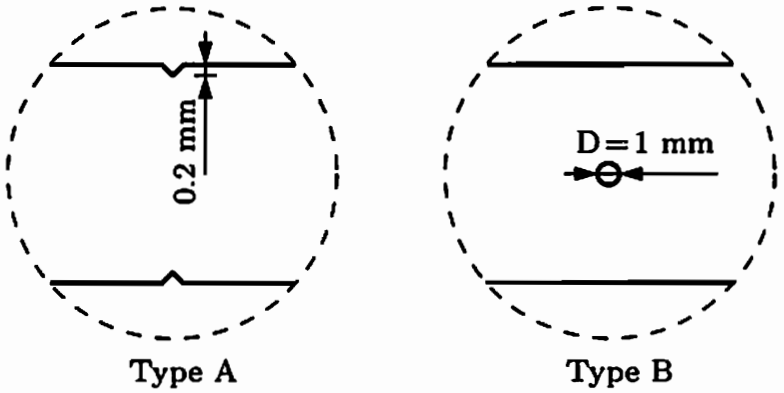

Figure 5.3: Types of cross section reduction by plain specimen

5.2 Clamping of the specimen

In order to achieve better results in the measurement of acoustic emission, it is necessary to decouple the specimen from the extraneous noise. Main part of the extraneous noise comes from the hydraulic parts of machine and the natural vibration of the machine frame. The decoupling is achieved by inserting two universal joints in the clamping device, above and below the specimen (see Figure 5.4). In this manner, the amplitude of the background noise is reduced by 40 dB or by factor 100, and the threshold value of the amplitude of acoustic emission can be chosen at approximately 35 dB.
The measurement of electrical resistance requires an electrical decoupling between the specimen and the rest of the experimental setup. The electrical decoupling of the specimen includes:

- Inserting a plastic[2] disk between universal joint and clamping jaw (Figure 5.5a).
- The isolation of screws through isolation washes made from glass-fibre reinforced plastic[3] (Figure 5.5b).
- Sheathing of screw body with rubber tube (Figure 5.5b).

Isolation washes made from a conventional plastic material have a relatively small compressive strength and exhibit a plastic deformation if the range of the applied load is significant (as in the case of circular specimens in this experimental setup). The glass-fibre reinforced plastic has a compressive strength significantly higher than the compressive strength of a conventional plastic, and therefore, this material is used for the production of isolation washes.
Two previously introduced specimen forms are clamped to the machine with the universal joints using two different clamping jaw devices.

[2]PVC grey
[3]Co. AGK GmbH, DuroBest 180

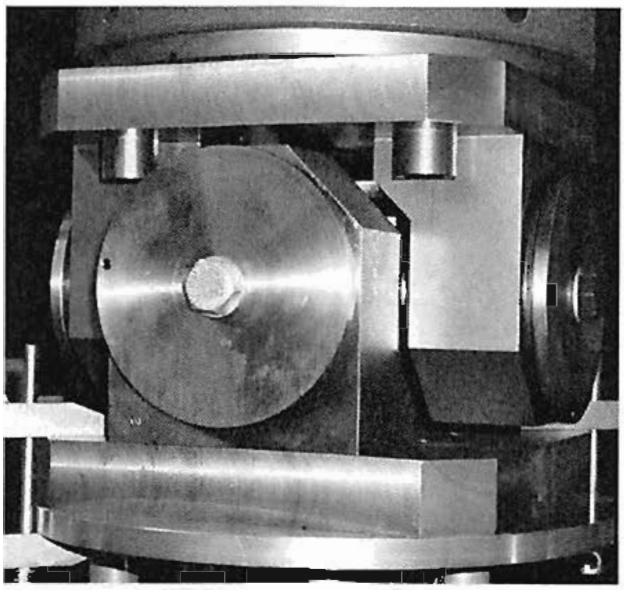

Figure 5.4: Upper universal joint

a) b)

Figure 5.5: Electrical isolation of the specimen: a) plastic isolation disc, b) electrical isolation of the screw

In the case of the plain specimen, the clamping jaw designed by Heiderich (2004) has a form given in Figure 5.6a. This form of the clamping jaw leads to the form closure between the specimen and the clamping jaw in the case of a tension load. In addition, the specimen is prestressed during the mounting procedure in order to produce a corresponding form closure. Under the prestressing, the specimen is fixed using a metal block screwed to the clamping jaw. This clamping procedure prevents a shrinkage behaviour during the experiment, as well as a discontinuous change of the measured reaction force and the specimen elongation.

The circular specimen is clamped using a two-jaw clamping device. Only one half of the symmetric clamping jaw is shown in Figure 5.6b. The two parts are

a) 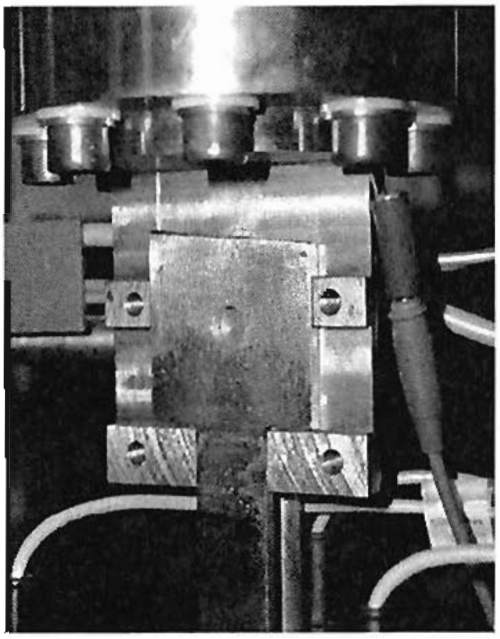 b) 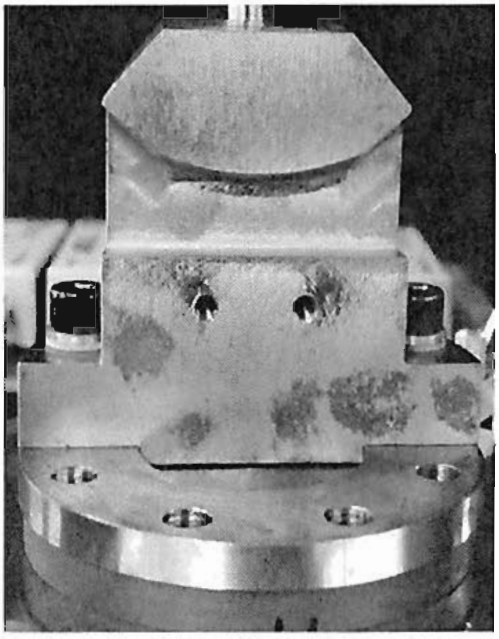

Figure 5.6: Clamping jaw: a) plain specimen, b) circular specimen

fixed to each other using two screws. The arc form in the clamping jaw gives a possibility to load the specimen in different directions by applying the rotation of the specimen about the axis perpendicular to the circular specimen surface. Both types of clamping jaws are fixed to the universal joints using isolated screws introduced above.

5.3 Mechanical loading

The core of the experimental setup is a hydro-dynamic tension/torsion testing machine. It consists of a loading frame[4], hydraulic aggregate[5], loading cell, and a digital machine control tower[6]. A testing actuator is integrated in the machine base, and allows a maximum movement of the bottom clamping jaw of ±50 mm and a maximum rotation of ±50°.

The hydraulic aggregate generates a maximum pressure of 300 bar and it produces a maximum loading in axial and torsional direction of 160 kN and 1000 Nm, respectively. The hydraulic aggregate with a maximum flow rate of 40 $^{l}/_{min}$ and servo valves on axial and torsional hydraulic cylinder with a flow rate of 19 $^{l}/_{min}$ allows a maximum velocity of 100 $^{mm}/_{sec}$ in axial direction or 1000 $^{\circ}/_{sec}$ in torsional direction. Applied velocities are also dependent from the operating conditions. Minimum velocities are influenced by resolution of the transducers, the quality of the closed loop control and the quality of servo valves.

[4]Co. Schenck Trebel GmbH, Frame: PC400M
[5]Co. Schenck Trebel GmbH, Aggregate: PP 40 B
[6]Co. Instron GmbH, Fast Track 8800

Some specific features of the loading frame should also be highlighted. The crosshead can be hydraulically moved and secured. Strain gauge load cells[7] for the measurement of the axial force and the torque are located between the crosshead and the upper clamping jaw. Inductive displacement[8] and torsion[9] transducers are located close to the respective hydraulic cylinder. The measurement range of the applied transducers is in the range of the above given characteristics of the machine.

The hydro-dynamic machine can operate in manual and digitally programmable regime. During the preparation of the experiment, the manual control of the machine is used. After that, the machine is controlled completely using a digital control system. The digital control system is connected to a PC using parallel IEEE-488 digital communications bus[10]. By means of an appropriate software package[11], the complete control of the machine through a digital control system is achieved.

In addition to four internal regulation measures (axial force, torque, axial displacement and rotation), it is possible to apply one more signal to each of the two axes. In the axial direction, an analogue signal containing the mean value of three external displacements measured by three external inductive displacement transducers is applied. Additional analogue signal in the torsional direction is evaluated based on the electrical resistance measurement. Both procedures will be later explained in detail. Both analogue signals have the range ± 10 V. Moreover, all measurement data concerning six above defined regulation measures can be further used as an analogue output signal in the range of ± 10 V.

The force controlled experiments are carried out using an axial force generated in the machine internal load cell. The load cell is situated direct in the force axis, and the position of the specimen has no influence on the result of the force measurement. The measured signal is amplified in the machine control tower, and used for the closed loop control. The closed loop control is integrated in the software package, and uses the PID-algorithm[12]. The values for proportional, integral, differential and lag gain are determined using the loop tuning tool, which is a part of the software package. Hence, a good quality of the control process during force controlled experiments is achieved.

In contrast to the force controlled experiments, the displacement controlled experiments are not carried out using a displacement coming from the internal machine inductive displacement transducer. Namely, the internal displacement and torsion transducers measure the movement and the rotation of the hydraulic cylinders and not the elongation and the rotation of the specimen. In this manner, the measured displacement includes the deformation of the universal joints,

[7] Co. Schenck Trebel GmbH, Lebow 6488/102

[8] Co. Schenck Trebel GmbH, LVDT ± 50 mm

[9] Co. Schenck Trebel GmbH, TR 10

[10] IEEE-488, also known as HP-IB (Hewlett-Packard Instrument Bus) or GPIB (General Purpose Interface Bus) is a 8-bit parallel bus which allows to connect up to 15 devices.

[11] Co. Instron GmbH, RS LabSite

[12] Proportional-Integral-Derivative algorithm

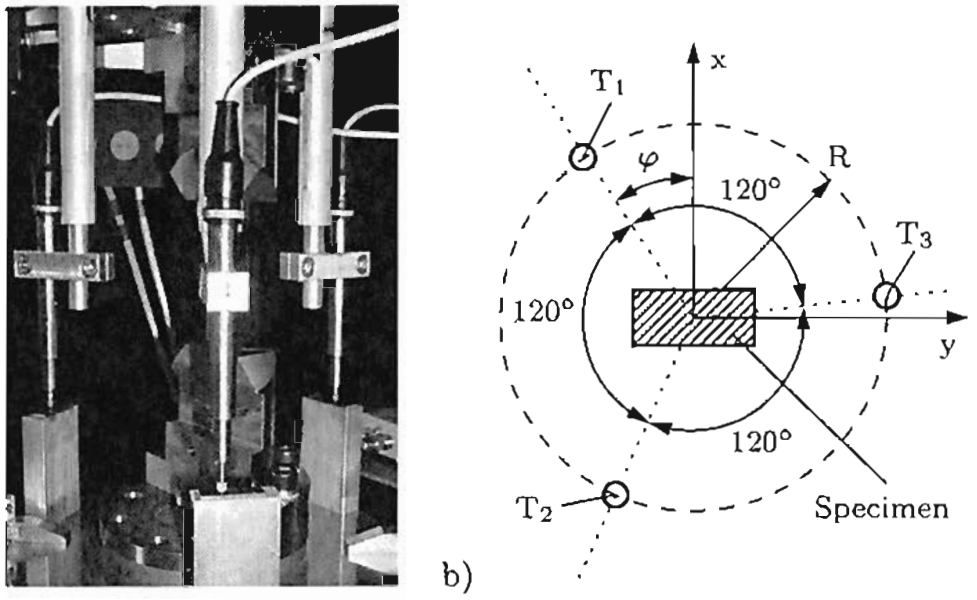

Figure 5.7: The arrangement of the external displacement transducers: a) three-dimensional view of the circular specimen arrangement, b) two-dimensional projection for both types of the specimen

the clamping jaws, the specimen, the load cell, the crosshead and the columns. Consequently, external displacement transducers must be used in order to obtain the necessary measurement data.

It is not possible to use only one external displacement transducer parallel to the specimen, because applying universal joints enables additional rotational degrees of freedom. Therefore, even small changes in the symmetry conditions render an invalid measured displacement. To overcome these difficulties during the displacement controlled experiments, a special controlling procedure is designed. The system of three external inductive displacement transducers[13] is applied. They are arranged concentric around the vertical axis of the specimen. The angle between transducers is 120°. In the case of the plain specimen, they are mounted between the bottom and the upper clamping jaw. In the case of the circular specimen, they are mounted between the bottom and the upper universal joint (see Figure 5.7).

Taking into account the rotations ϕ_x and ϕ_y about the hinges of the universal joint in x and y direction and the rotation φ about the vertical axis, the displacement of the displacement transducers can be given by

$$u_{z_1} = u_z - \phi_x R \sin(\varphi) - \phi_y R \cos(\varphi)\,, \tag{5.1}$$

$$u_{z_2} = u_z - \phi_x R \sin(120^\circ + \varphi) - \phi_y R \cos(120^\circ + \varphi)\,, \tag{5.2}$$

$$u_{z_3} = u_z - \phi_x R \sin(240^\circ + \varphi) - \phi_y R \cos(240^\circ + \varphi)\,, \tag{5.3}$$

[13] Co. Hottinger Baldwin Messtechnik GmbH, W5TK, accuracy class 0.4, nominal range ±5 mm

where u_z is the elongation of the vertical axis between the points in which the construction for measurement of external displacement is mounted. In (5.1)÷(5.3), the rotations ϕ_x and ϕ_y are taken into account as small quantities. The elongation u_z can be calculated as the arithmetic mean of three measured displacements u_{z_1}, u_{z_2} and u_{z_3}

$$u_z = \frac{1}{3}\sum_{i=1}^{3} u_{z_i} \tag{5.4}$$

by using the following identities

$$\sin(\varphi) + \sin(120^\circ + \varphi) + \sin(240^\circ + \varphi) = 0\,, \tag{5.5}$$

$$\cos(\varphi) + \cos(120^\circ + \varphi) + \cos(240^\circ + \varphi) = 0\,. \tag{5.6}$$

In order to use the mean value of the measured displacement as a signal for the regulation of displacement controlled experiments the following procedure is applied. After the amplification of all three measurement signals using modular measuring amplifier[14], three analogue signals in the range ±10 V are sent to the analogue electronic circuit, where the mean value of these three signals is produced. After that, the mean value as an output analogue signal in the range ±10 V is sent from the analogue electronic circuit to the analogue input on the machine control tower. This analogue signal is used for the closed loop control. As in the case of the force controlled experiments, the loop tuning tool is used for the determination of appropriate proportional, integral, differential and lag gains, which are needed for the PID-algorithm.
The geometry of the specimen and the measurement of acoustic emission influence the range in which the fatigue load is applied. In both the force and the displacement controlled experiments, the fatigue load is applied only in the tension range in the form of haversine (see Figure 5.8). The experiments are performed either with constant amplitude for the entire duration of the test, or as a block-test with the amplitude which is constant inside the block and differs between the blocks. The stress ratio R is 0.05 or 0.25. The load frequency is 9 Hz for experiments with a plain specimen and 6 Hz for experiments with a circular specimen.
As pointed out above, the measurement of electrical resistance is used as an additional signal in the machine control system. The measured values of electrical resistance are used to stop the experiment if the appropriate threshold value is exceeded. In this manner, the failure of specimens is defined by a certain value of the electrical resistance. In addition to this criterion, other criteria are defined as a signal for the failure of the specimen and the interruption of the experiment. In the case of the plain specimen, two alternative criteria are used depending on the load control form. In the case of the force controlled experiments the additional criterion is the time when the specimen is broken in two pieces. The

[14] Co. Hottinger Baldwin Messtechnik GmbH, MGC, accuracy class 0.03

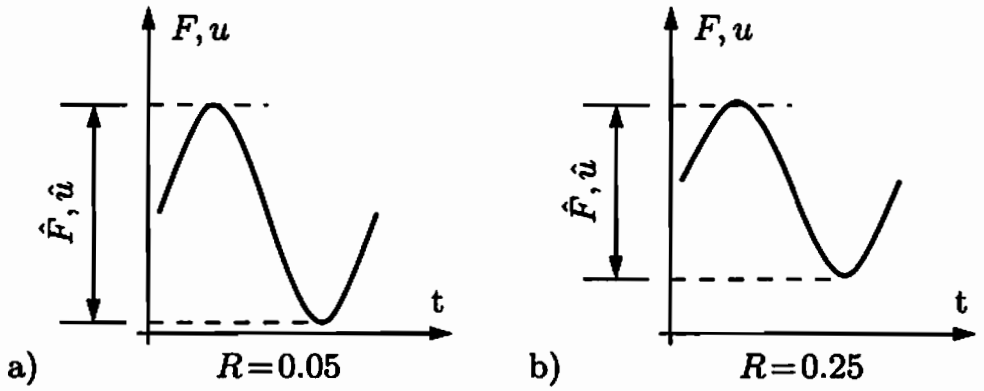

Figure 5.8: Load function in the haversine form with amplitude $\hat{F}$ or $\hat{u}$: a) stress ratio 0.05, b) stress ratio 0.25

experiment is stopped in the moment when the threshold value of the position sensor in the tension direction is exceeded. For the displacement controlled experiments, the additional criterion is the compression force. Shortly before the final failure, the plastic strain which shifts the force response to the compression range plays a decisive role in the definition of failure. Since the geometry of the specimen and the type of clamping allow limited compression load, the threshold value for the maximum allowed compression force is set to 4 kN. If the threshold is exceeded, the experiment is interrupted and the specimen is treated as destroyed.

In the case of the circular specimen, the additional criterion for the definition of the failure of the specimen is also based on the measurement of the electrical resistance. The applied construction of external displacement measuring devices allows a visual contact with the crack growth up to a crack length of approximately 90 mm. For this reason, the crack length of approximately 90 mm is used as an additional criterion for the definition of the failure of the specimen. This length criterion cannot be applied directly to the machine control system, but it can be taken into account through the definition of a corresponding electrical resistance measurement signal.

As soon as one of the failure criteria is satisfied, the experiment is interrupted and the analogue stop signal is generated. This signal is used to stop other measurement systems. In order to protect the applied measurement system in the case of potentially unstable response of the machine, two additional limits are used. Minimum limits are set on the internal and the external position sensor, and the motion of the hydraulic cylinder in the compression direction beyond applied limits is prevented.

Special attention must be given to the contact points between the deformation measuring device and the head of the probe pin of the inductive displacement transducers. Namely, the head of the probe pin is a carbide ball and it is sig-

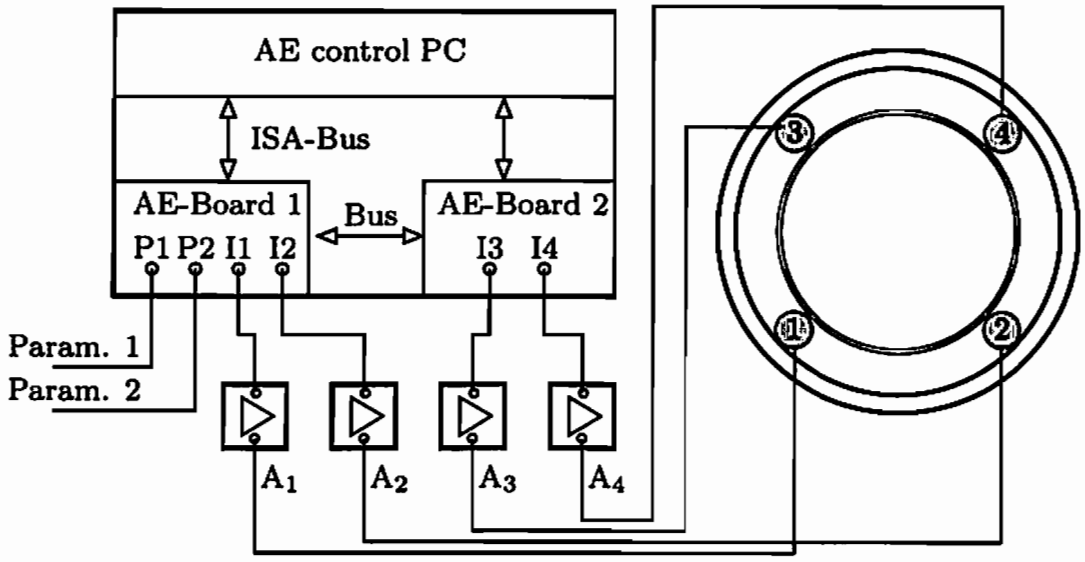

Figure 5.9: Measurement of acoustic emission - schema

nificantly harder than the aluminium parts of the measuring device. In the case of high cycle fatigue experiments, the head of probe pin produces scratches and holes on the aluminium surface, which leads to the jumps in the displacement and load measurements. To reduce this effect, the gauge blocks, with hardness higher than that of the aluminium, are glued to the contact surface between the head of the probe pin and the measuring device.

5.4 Measurement methods

The aim of this work is to prove the applicability of two different nondestructive measurement methods in the examination of crack growth during fatigue load. The examined methods are the method of measurement of acoustic emissions and the method of measurement of electrical resistance. Results derived from these two methods are compared to the global evolution of the stiffness of the damaged specimen. The global stiffness of the specimen is calculated using the measurement of the force and the elongation of the specimen.

5.4.1 Measurement of acoustic emission

The acoustic emission is measured on both types of the specimen using a completely independent measurement system given in Figure 5.9. All procedures during measurement of acoustic emission are controlled using an appropriate software package[15]. Two types of acoustic emission transducers with appropriate preamplifiers are used for the detection of acoustic emission. First set

[15]Co. Euro Physical Acoustic GmbH, AEWin

consists of four wideband piezoelectric transducers[16] and four voltage preamplifiers 2/4/6[17]. Second set includes four piezoelectric transducers R15[18] and four single In-Line 40 dB preamplifiers[19].
In order to investigate the frequency range of acoustic emission response during crack growth, the first set of acoustic emission transducers and amplifiers is used. After the determination of the predominant frequency band of acoustic emission sources, the second set with four resonant acoustic emission transducers is applied.
The acoustic emission signals are amplified with 40 dB and received on a two Two-Chanel-AE-Boards[20] in all experiments. The interconnection between these two AE-Boards synchronises measured signals. The signals are stored directly on the board in a flash storage memory and processed thereafter by the on-board 32-bit DSP parallel processor. The storage of processed signals on the control PC for later processing includes only a group of selected signal parameters. The characteristic parameters of an acoustic emission signal are explained in Section 4.1.5. The waveform of the signal is in general not recorded, due to its large accumulating amounts of data. Sample rate for all measurements is 10 MHz.
In addition to acoustic signals, two analogue ± 10 V signals can be received over two independent parameter inputs. Therefore, the force and the mean external displacement are sent from the machine control system to the acoustic emission measurement system as analogue ± 10 V signals. In the moment when the experiment is stopped, the machine control system sends the constant analogue signal of 10 V instead of the real value of the mean external displacement. This signal initiates the production of an unrealistic value of the displacement by the acoustic emission measurement system and it indicates that the experiment is stopped. This procedure is necessary due to the fact that the acoustic emission measurement system cannot be synchronised with the other measurement systems and the start and the stop of the acoustic measurement must be manually activated. Hence, it is possible to connect measured values from all measurement systems through the reverse synchronisation in the post-processing. Both input parameters are stored only at times when the active acoustic emission is recorded.
All acoustic emission transducers are clamped to the specimen with a spring clamp. The coupling between the specimen and the transducers is made with a silicon gel. The bonding between transducers and the specimen requires special attention. If the contact between the specimen surface and the surface of a transducer is direct without couplant, or if the couplant is not thick enough, it can lead to a continuous emission of acoustic signals on the basis of generated

[16] Co. Euro Physical Acoustic GmbH, WD, operating frequency range $100 \div 1000$ kHz
[17] Co. Euro Physical Acoustic GmbH, 2/4/6, AST, amplification 20/40/60 dB, bandpass filter $100 \div 1200$ kHz
[18] Co. Euro Physical Acoustic GmbH, R15, resonant frequency 150 kHz
[19] Co. Euro Physical Acoustic GmbH, In-Line, AST, amplification 40 dB, bandpass filter $100 \div 300$ kHz
[20] Co. Euro Physical Acoustic GmbH, AEDSP-32/16, 2 Channel

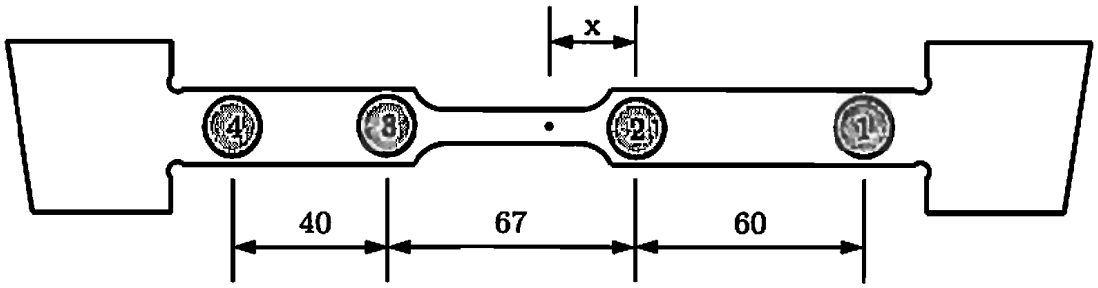

Figure 5.10: The position of acoustic emission transducers on the plain specimen (dimensions in mm)

friction between contact surfaces. These signals have the same characteristics as the acoustic emission signals from a crack initiation and propagation and cannot be recognised as noise. In this case, the measurement of acoustic emission becomes useless.
The setting of the amplitude threshold value depends on the experimental conditions. As pointed out earlier, the universal joints are used in order to reduce the background noise. For this reason, the threshold value of acoustic emission is set to 35 dB, as a compromise between effectively avoiding background noise and cutting off low level signals during damage evolution. The absolute threshold value a^* can be calculated by

$$a^*[\mathrm{dB}] = 20 \log \left(\frac{u}{100\mu\mathrm{V}} \right) , \tag{5.7}$$

which for $a^* = 35$ dB leads to the threshold value of the electrical signal u of 5.6 mV.
The time parameters for the measurement of acoustic emission signals introduced in Section 4.1.5 are dependent on the material, the position of acoustic emission transducers and the specimen geometry. They are empirically determined, and have the following values for plain and circular specimen respectively

$$\begin{aligned} &\mathrm{PDT} = 10\mu\mathrm{sec}\,, \quad \mathrm{HDT} = 80\mu\mathrm{sec}\,, \quad \mathrm{HLT} = 500\mu\mathrm{sec}\,, \\ &\mathrm{PDT} = 16\mu\mathrm{sec}\,, \quad \mathrm{HDT} = 50\mu\mathrm{sec}\,, \quad \mathrm{HLT} = 500\mu\mathrm{sec}\,. \end{aligned} \tag{5.8}$$

With these four parameters (a^*, PDT, HDT, HLT), a reasonably sensible measurement of the acoustic emission is possible for given experimental conditions. The measurement of time differences introduced in Section 4.1.4 represents a successful method of post-processing of the acoustic emission measurements. If this method is used to prove a valid origin of the acoustic emission, the reduction of the observed acoustic events can be achieved through the elimination of all signals which originate outside the specimen test area.
The position of acoustic emission transducers on the plain and circular specimen is shown in Figures 5.10 and 5.11, respectively. The position of transducers on

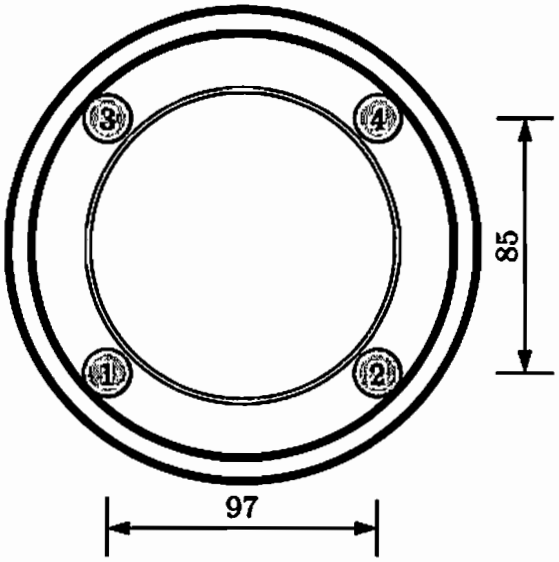

Figure 5.11: The position of acoustic emission transducers on the circular specimen (dimensions in mm)

the plain specimen is given in such a way that transducers 1 and 4 are so-called guard transducers with the function to eliminate signals originating outside the specimen test section from the recorded data. Thus, extraneous signals such as those emanating from load-chain noise or from servo valves and hydraulic pump are avoided without loss of data. The acoustic emission signals which are first detected by guard transducers are disregarded. Transducers 2 and 3 are used as measuring sensors. In the case of the circular specimen, due to the two-dimensional constellation of transducers it is not possible to define guard sensors, and all four transducers serve as measuring sensors.

5.4.2 Measurement of electrical resistance

The measurement of the electrical resistance is performed using an industry device[21] with a maximum resolution of 10 nΩ, a testing range up to 200 $\mu\Omega$ and a constant direct current of 10 A through the specimen. The geometry of the specimen and the distance between two points in which the electrical potential is measured are adjusted to reach this high resolution. The measurement of the electrical resistance is performed on both the plain and the circular type of specimen, introduced in Figures 5.1 and 5.2, respectively. The measurement of the electrical resistance R_x in the observed area of the specimen is achieved using Kelvin-procedure.
In this procedure, a regulated constant direct electrical current of 10 A is driven through the specimen and an internal reference resistance (R_k) is measured. The

[21] Co. Buster GmbH, Resistomat 2304

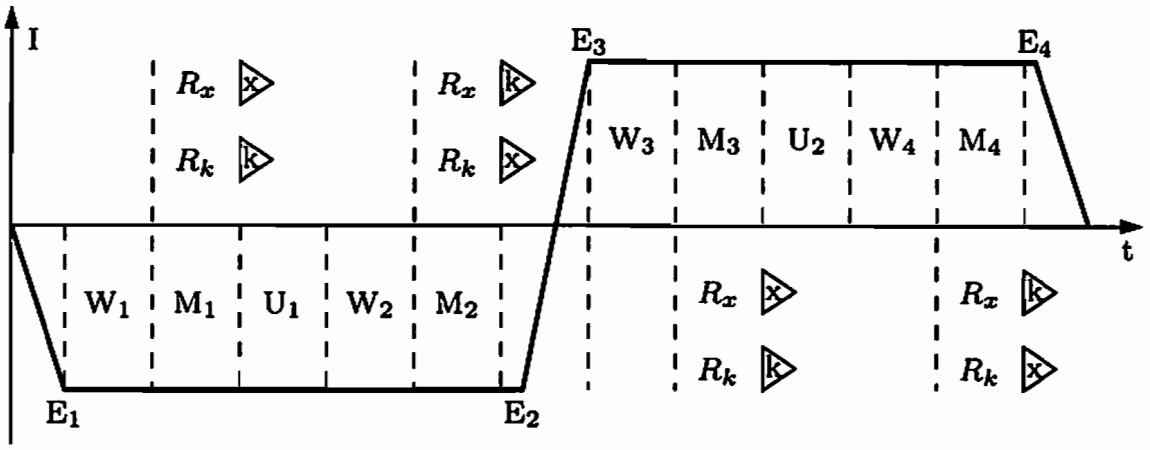

Figure 5.12: One cycle of measurement of electrical resistance

difference in the electrical potential at any two points of the specimen can be measured, and the electrical resistance can be calculated. The potential drop over the testing range of the specimen can be related to the potential drop over the high-precision internal reference resistance and can be calculated using the known value of this reference resistance. The advantage of this procedure is the independence of the measured values of the parasitic resistance in the measuring system, such as contact resistance and transition resistance in the measurement connection. The measured values depend only on the quality of the internal reference resistance. To eliminate possible electrostatic effects or differences of the two amplifiers, the direction of the driven current and the polarity of the potential measurement are changed within one period of the resistance measurement. For this reason, the measured value is the mean value from 4 different measurements. The sequence of four measurements is represented in the schema given in Figure 5.12.

The first phase of the measurement is the settling time E_1 of the direct current I to a negative value followed by an adjustable holding time W_1. At this point of time, a measurement of R_x through the amplifier A_x and R_k through the amplifier A_k is carried out over an adjustable time M_1. After that, the amplifiers A_x and A_k are shifted during the time U_1, according to Figure 5.13, followed by the holding time W_2. The second measurement of R_x and R_k with a duration M_2 and with the same current direction through the inverted amplifiers is performed. In the case of a bipolar measurement, which is used in all experiments featured in this work, the next step in the measurement progression is the change of the direct current from a negative to a positive direction in the time between E_2 and E_3. Afterwards, two new measurements take place according to the above described principle, with the measurement phases M_3 and M_4, holding times W_3 and W_4 and the shifting of the amplifiers U_2.

One output value can be calculated as a mean value of 1 to 255 measurement cycles. For all experiments, the setting of the device is selected with very long

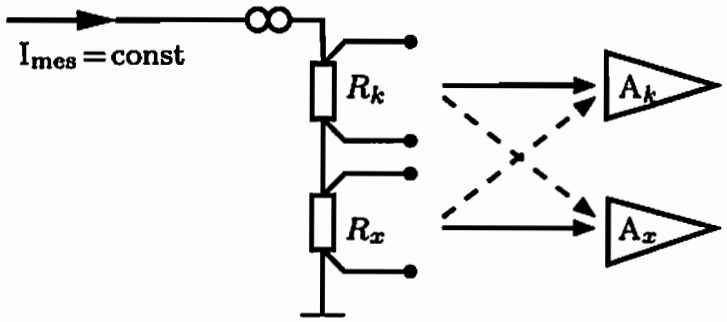

Figure 5.13: Inversion of amplifiers during the measurement of electrical resistance

measurement times and short holding times, as well as with determination of a new output value after each measurement cycle. In this manner, the values of electrical resistance are obtained with a frequency of approximately 1 Hz and one value of the electrical resistance represents an average value of the electrical resistance over 9 loading cycles for the plain specimen and over 6 cycles for the circular specimen. Hence, the effects of elastic elongation of the specimen during the measuring time for one value of the electrical resistance are eliminated.

The measurement of the difference in electrical potential is designed using two short-circuited type K thermocouples, which are welded onto the specimen. The distance between the welded thermocouples is 20 mm for the plain specimen and 40 mm for the circular specimen. The advantages of the welding of thermocouples over other methods of connecting the thermocouples to the specimen as well as the chosen type of thermocouples are introduced in Section 5.4.3.

Resistomat is connected with a separate control PC over the parallel IEEE-488 digital communications bus. The control PC initialises the Resistomat before the experiment begins and starts the measurement. The measured values are read from the same control PC over the IEEE-488 bus and sent to the external digital-analogue converter. The converter yields a corresponding ± 10 V analogue signal, which is usable in the machine control system.

The electrical resistance is measured in three directions in the experiments with a circular specimen. The angles between chosen directions are 30° (see Figures 5.14 and 5.15b). Since the Resistomat measures electrical resistance only in one direction, an additional control process engaging an automatic gauge head selector switch[22] is developed. It selects a direction to be used for the measurement of the electrical resistance. Its control is achieved using the control PC which controls the Resistomat, over two parallel ports[23] and a custom-made electronic control device[24]. In all experiments with circular specimen, the direction of the

[22] Co. Burster GmbH, Nanomat 1634

[23] Parallel port, also known as printer port or Centronics port

[24] Lehrstuhl für Technishe Mechanik, Ruhr Universität Bochum

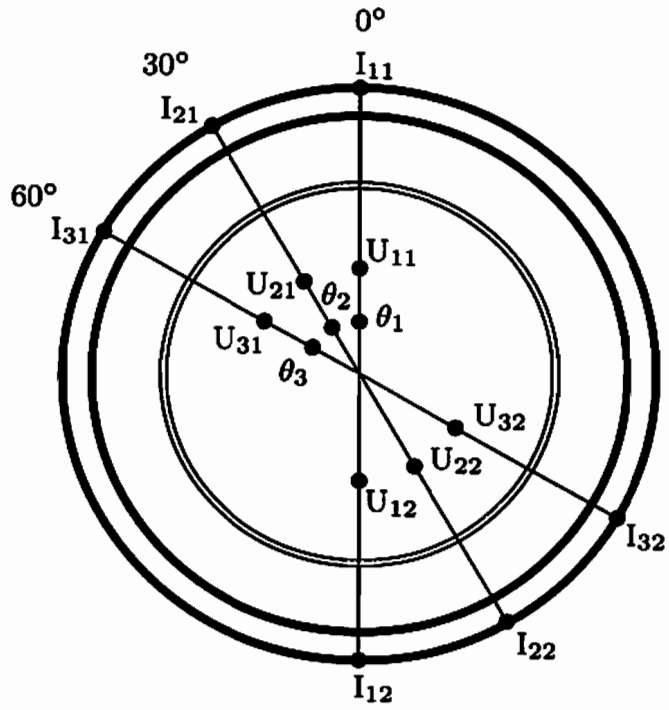

Figure 5.14: Arrangement of the thermocouples on the circular specimen: θ_1, θ_2, θ_3 - temperature thermocouples in directions 1(0°), 2(30°) and 3(60°); I_{ij} - electrical current wires (i-direction, j-position); U_{ij} - electrical potential thermocouples (i-direction, j-position)

measurement of electrical resistance is changed after approximately 30 sec, i.e. after 30 measured values.
The method of measurement of electrical resistance is similar to another method used in the detection of crack growth and known as the method of potential drop.

5.4.3 Temperature measurement

It is well known fact that the electrical resistance depends on the temperature of the specimen. For this reason, the temperature measurement is an important part of the measurement procedure. Temperature measurements are performed using thermocouples. The principle by which a thermocouple works is known as *Seebeck* or *thermoelectric* effect. The temperature difference between two junctions of two conductors of different material or alloy, which are part of the same electronic circuit, generates an *electromotive force* also known as *Seeback voltage* (cf. DIN EN 60584-2 1994).
The thermoelectric effect is the production of small electric voltage across the length of an electrical conductor due to a difference in temperature along the conductor. The material of the conductor has a strong influence on the value of

the voltage. If the second conductor is used, the electronic circuit is closed and the voltage can be measured. In addition, if both conductors are of the same material and they are subjected to the same temperature gradient, they exhibit identical electrical potentials and the measured voltage is 0 V. Therefore, the pair of wires is chosen to maximise the measurable voltage. If the type of the pair of wires and the voltage are known, the temperature gradient can be calculated. However, the absolute value of the temperature is to be measured and not the temperature gradient. For this reason, one junction of the thermocouple (known as *cold junction*) has to be maintained at a constant (reference) temperature, while the other end is attached to a specimen. In temperature measuring amplifiers, the cold junction is often simulated by temperature sensitive electrical components. This type of electronic circuit is known as *cold junction compensation.*

Type K[25] thermocouples are used for temperature measurements in all experiments featured in this work. Type K thermocouple is composed of two wires, a Chromel[26] and Alumel[27] wire. This type of thermocouples is widely used because of its moderate cost and large temperature range[28], and despite its comparatively low accuracy[29]. The choice of the type of thermocouples used in this experimental set up is made on some additional criteria.

The temperature of specimen is to be measured in the neighbourhood of the crack growth and the position of the electrical resistance measurement. Some of the possible choices of the measurement procedure are the thermooptical procedure, *PT100-* and *resistance*-thermometers, and type K thermocouples. A thermocamera can be used only if a clear view of the specimen can be found. Since this condition cannot be guaranteed because the specimen itself is shadowed by large parts of the other measuring devices, the thermooptical procedure is not an option. More accurate PT100- and resistance-thermometers are rejected due to the limited available space and the thermocouples of the type K are chosen.

There are many different techniques to connect the thermocouple to the surface of the specimen. The correct choice of the connecting technique leads to the correct measurements. The quality of the measured data is also influenced by the shape and the type of the junction of the two thermo wires in the thermocouple. The technique of connecting type K thermocouples to the surface of the specimen adopted in this experimental setup is introduced by Vogelsang (2001).

Körtvélyessy (1998) shows that the connection between the specimen surface and the thermocouple whose junction is produced by twisting of the two thermo wires leads to a virtual measuring point. This virtual measuring point does not lie on the specimen surface, and it produces incorrect measuring of the temperature. Furthermore, Vogelsang (2001) shows that the step voltage might

[25] Co. Conatex, TM12K02GG2, wire diameter 0.2 mm, class 1 (DIN 43722 1994)
[26] Ni-Cr alloy
[27] Ni-Al alloy
[28] −200°C to +1200°C (DIN EN 60584-2 1994)
[29] ±1.5°C between −40°C and +375°C (DIN EN 60584-2 1994)

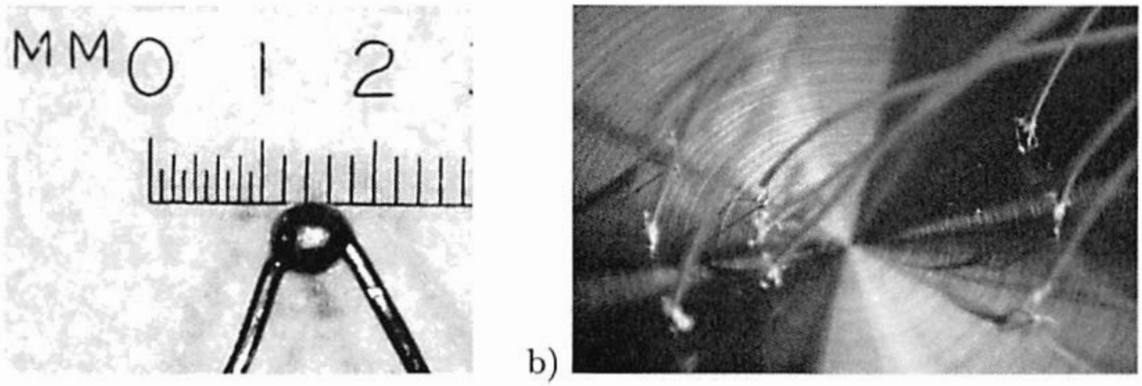

a) b)

Figure 5.15: Thermocouple: a) thermocouple bead (Grabe), b) general view of the thermocouples on the circular specimen

occur at the thermocouple when a direct current for the measurement of the electrical resistance is driven through the specimen, if the contact points with the specimen are not precisely defined. This phenomenon leads also to incorrect temperature measurements.

To overcome all these difficulties, Vogelsang (2001) introduced a new way to create significantly improved thermocouple junction. The two wires in the thermocouple are twisted in such manner that the twisted part contains a strictly defined constant amount of the material. This junction of two wires is arc welded in the neutral environment of argon atmosphere. The produced junction is a sphere with almost constant diameter of 0.6 mm (see Figure 5.15a).

The contact between the thermocouple and the surface of the specimen is usually created by clamping or gluing the sensor onto the specimen. Clamping the thermocouple has two disadvantages. A required additional clamping device consumes additional unavailable space and the friction between the clamping device and the specimen can produce acoustic emission during the fatigue loading test. As pointed out earlier, the acoustic emission originating from friction has similar characteristics as the acoustic emission originating from crack propagation, and it can lead to useless results. Gluing the thermocouple leads to comparatively poor thermal contact resulting in slow temperature measurements. Also, in the case of high cycle fatigue load testing, the contact may be broken due to the vibration of the wires. Furthermore, in the case of the measurement of electrical resistance, the glued thermocouple has a comparatively poor electrical contact resulting in inaccurate electrical resistance measurements.

In order to overcome all these problems, the thermocouples are welded onto the specimen using a single-pulse welding procedure proposed by Vogelsang (2001). The advantage of this procedure is that the microstructure of the specimen is not altered due to the welding process being completed on a very small welding zone (see Figure 5.16). Later improvements and modifications of this welding setup lead to the increased accuracy and repeatability of the procedure.

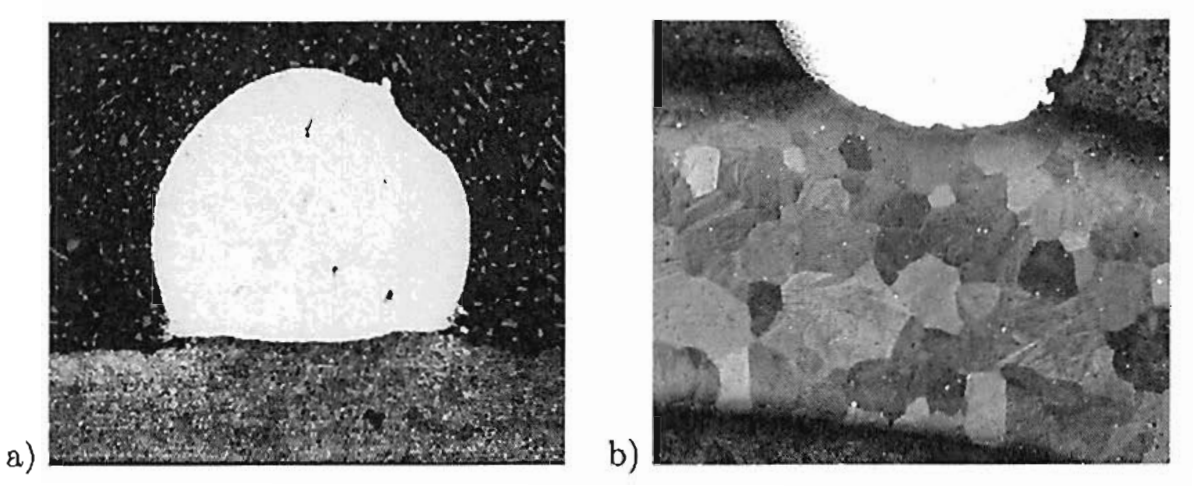

Figure 5.16: Join patch between thermocouple and specimen - polished micrograph section: a) thermocouple bead (Vogelsang), b) magnification of 100x (Grabe)

In the experiments with the plain specimen, one thermocouple is used for the temperature measurement and two for the measurement of the electrical resistance. In the case of circular specimen, where the electrical resistance is measured in three directions, three thermocouples are used for the temperature measurement and six for the measurement of the electrical resistance (see Figures 5.14 and 5.15b).

5.4.4 Data acquisition

The data acquisition is carried out with a central data acquisition system[30]. The system is a multi-channel electronic PC measurement unit for parallel, dynamic measurement data acquisition using a PC. The measurement unit includes a *sample-and-hold* circuit for all channels. The mechanical measurement values are sent from the machine control system or from external amplifiers to a data acquisition system as an analogue ± 10 V signal. The thermocouples for the temperature measurement are directly connected to internal DC measuring modules. The sample rate is chosen such to guarantee the qualitative acquisition of wave form signals (according to the cyclic load frequency of 9 Hz or 6 Hz) and the applicable post-processing of recorded data from high cycle fatigue experiments with $\leq 10^7$ load cycles. The amount of recorded data plays an important role in high cycle fatigue experiments, due to the number of different quantities which are recorded during the testing. After a thorough comparative investigation with different sample rates has been performed, the optimal combination of these two conditions is observed for a sample rate of 150 Hz in both types of experiment.

[30] Co. Hottinger Baldwin Messtechnik GmbH, Spider8, accuracy class 0.1, max. sample rate 9.6 kHz, 16 bit A/D converter for each measuring channel

Therefore, the sample rate of 150 Hz is adopted in all experiments. The results of these investigations are given in Appendix A for the experiments with a plain specimen loaded with 9 Hz load frequency and for experiments with a circular specimen loaded with 6 Hz load frequency.
The Spider system is connected to the control PC using a parallel port. The controlling and the programming of the Spider are achieved using an appropriate measurement software package[31]. The data storage takes place on the same control PC.

5.4.5 Documentation of macrocrack

In order to compare measured data to the macroscopic crack propagation, the photographs of the growing crack are made during the fatigue experiments. Hence, a CCD camera[32] is integrated into the system according to the procedure proposed by Heiderich (2004). The CCD camera is driven by a frame grabber card, which is triggered by an external TTL signal. An analogue comparator receives two inputs. The first one is the measured signal of the mean external displacement, which represents a control variable, and second one is the constant comparison signal. The comparison signal is sent from the machine control system over an analogue output.
The magnitude of the comparison signal can be selected freely in the programming of the test procedure. In all experiments, the magnitude of the comparison signal is set to 90% of the maximum control variable. The analogue comparator compares these two signals, and produces TTL signal which drives the tact of the photographing. This selected magnitude of the comparison signal guarantees that the photograph is made near the time of the maximum load and consequently the maximum opening of the crack. Due to the problems with the temperature of the frame grabber card for a TTL tact of 9 Hz, the output signal is scaled down to 1/10 of the tact.
Due to the high resolution of the photographs, the length of the crack which could be photographed is limited. Therefore, the second CCD camera[33] with smaller resolution and bigger broadness is used to take the general view of the crack growth in the circular specimen.

5.5 The complete system

The introduced experimental setup is suitable for the application of a cyclic fatigue load in the tension region. By using two universal joints in the clamping device and the electrical isolation of the specimen from the rest of the experimental setup, the appropriate conditions are adapted to the related measurement technology. Controlling of all processes is executed using five control PCs. These

[31] Co. Hottinger Baldwin Messtechnik GmbH, Catman Professional ver.5.0 R5
[32] Co. JAI GmbH, CV-M1, monochrome progressive scan, resolution 1300 x 1030 x 8 bit
[33] Co. Sony GmbH, AVC-D5CE, monochrome, resolution 768 x 576 x 8 bit

five PCs control the machine control system, the measurement of the electrical resistance and the acoustic emission, the acquisition data system and the realisation of photographs of the crack propagation. All processes are synchronised, and by using a stop signal generated through the machine control system, the measurements of different experimental values on separate measurement systems are synchronised for the post-processing. The view of the testing machine with a circular specimen and the schematic representation of the complete experimental system are presented in Figures 5.17 and 5.18.

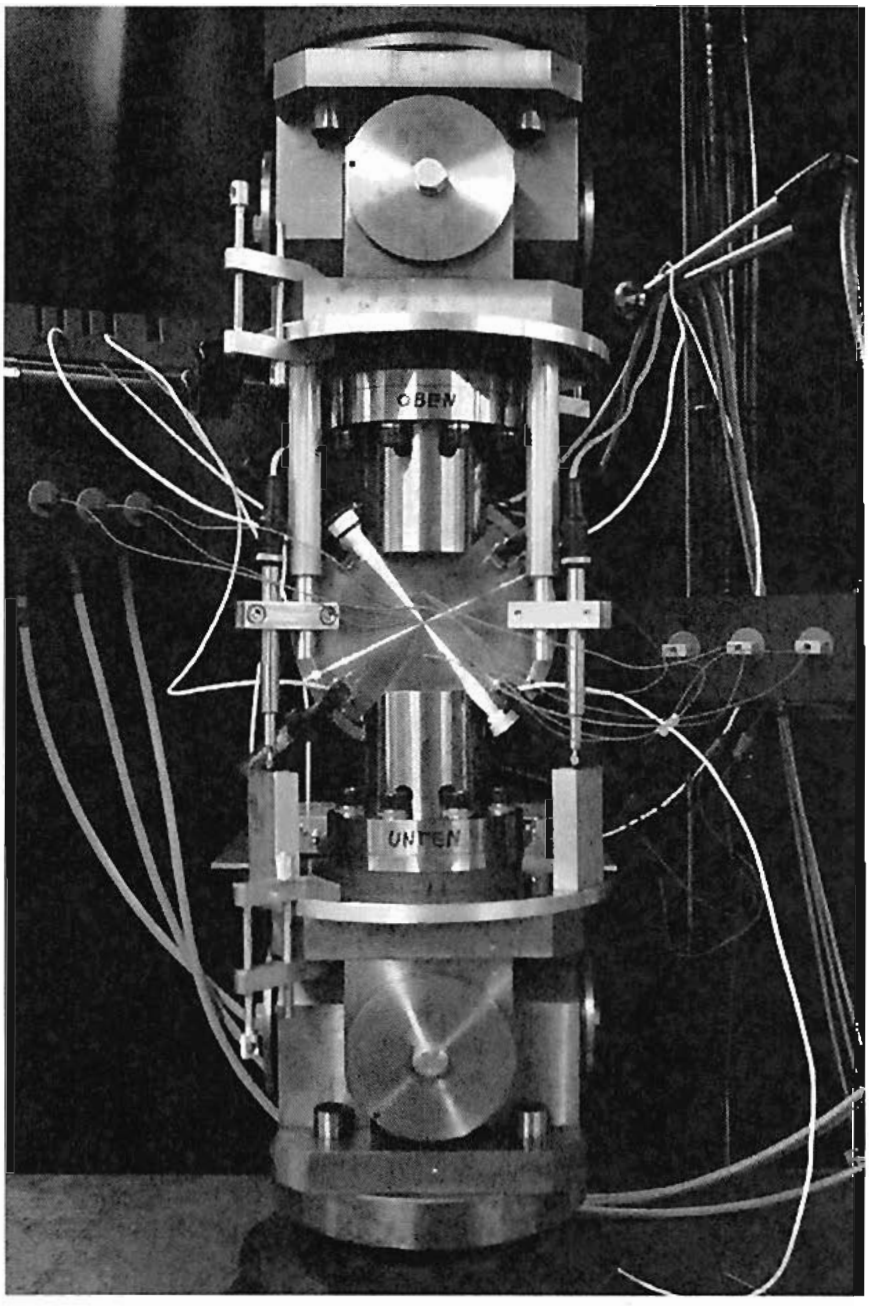

Figure 5.17: Frontal view of the testing machine with a circular specimen

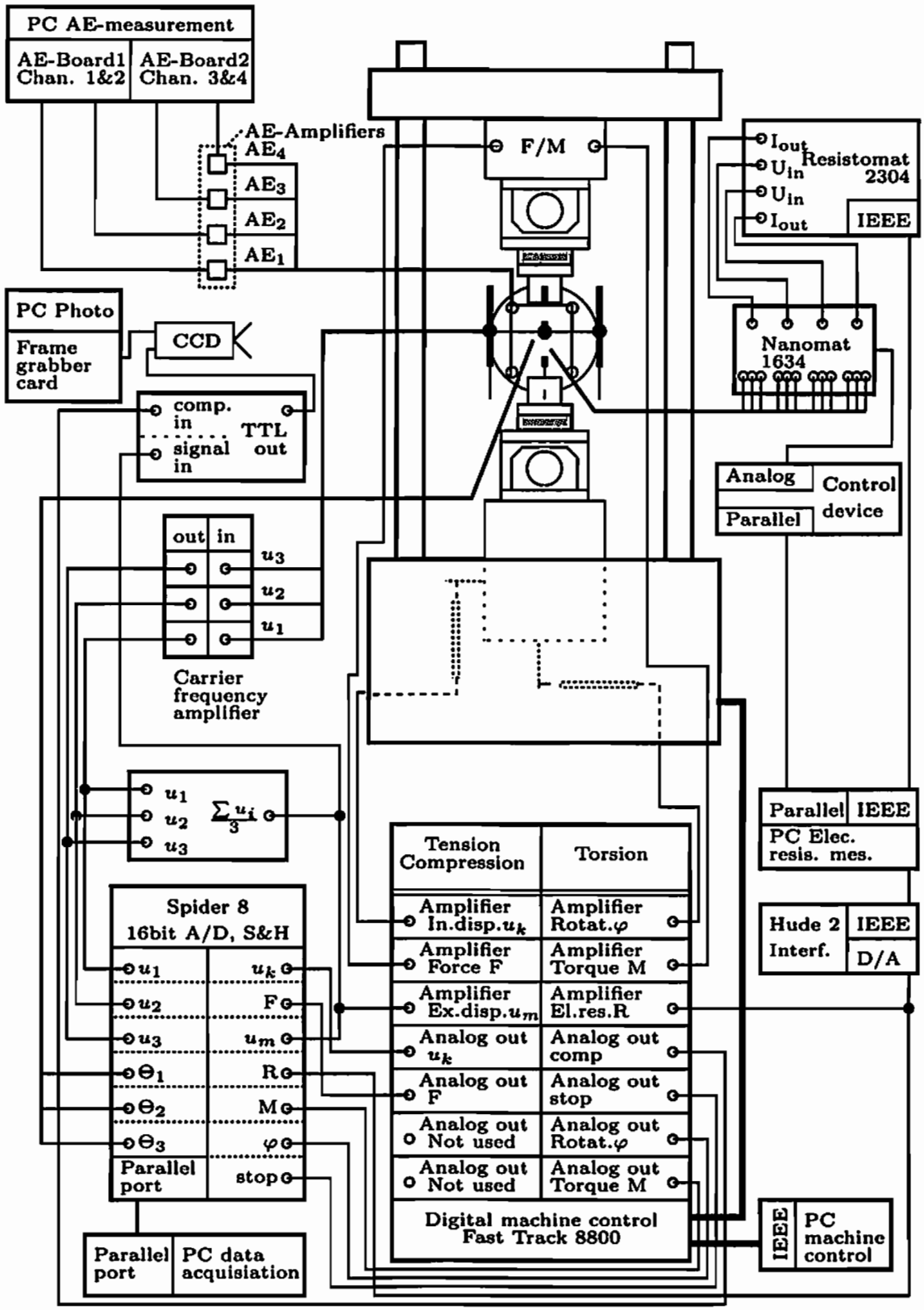

Figure 5.18: Schematic representation of the complete experimental system

6 Experimental results

Experimental data which can be used for the determination of significant material parameters in the case of damage processes in fatigue are obtained by performing appropriate experiments. The experimental setup used in these experiments is introduced in Chapter 5. The applied cyclic load is in the range which leads to the high cycle fatigue and brittle damage in the material.
Methods used for the detection of damage evolution are the measurement of the specimen elongation and the applied force, the detection of acoustic emission and the measurement of the electrical resistance. At the same time, the capability of the chosen nondestructive methods to detect the damage evolution on the microscopic level is tested. The experimental data obtained during the service life is used for the parameter identification based on the material model introduced in Section 3.3.
After the introduction of methods for the calibration of the experimental setup, the procedures for the evaluation of the measured data are given, followed by experimental results of cyclic fatigue loading of two specimen geometries.

6.1 Calibration of the experimental equipment

To ensure the appropriateness of the measured data, the experimental equipment needs to be calibrated. The calibration of the experimental equipment applied in this work (see Chapter 5) includes the calibration of the external displacement transducers, the acoustic emission equipment and the electrical resistance device.

6.1.1 Calibration of the external displacement transducers

In order to calibrate an external displacement transducer, it is set in the rigid laboratory frame and connected to the modular measuring amplifier introduced in Section 5.3. Since this modular measuring amplifier consists of three measurement amplifiers[1], it is important to note that the displacement transducer stays connected to the same measurement amplifier during all experiments. The calibration of displacement transducers is performed using gauge blocks[2]. After the clamping of the displacement transducer to the rigid frame, the probe pin is set in the middle position, and the zero-point adjustment in the measurement amplifier is operated using an appropriate procedure. The defined displacement of

[1] Co. Hottinger Baldwin Messtechnik GmbH, MGC, connection plate AP01, amplifier MC55

[2] Co. Cary GmbH, tolerance norm 2

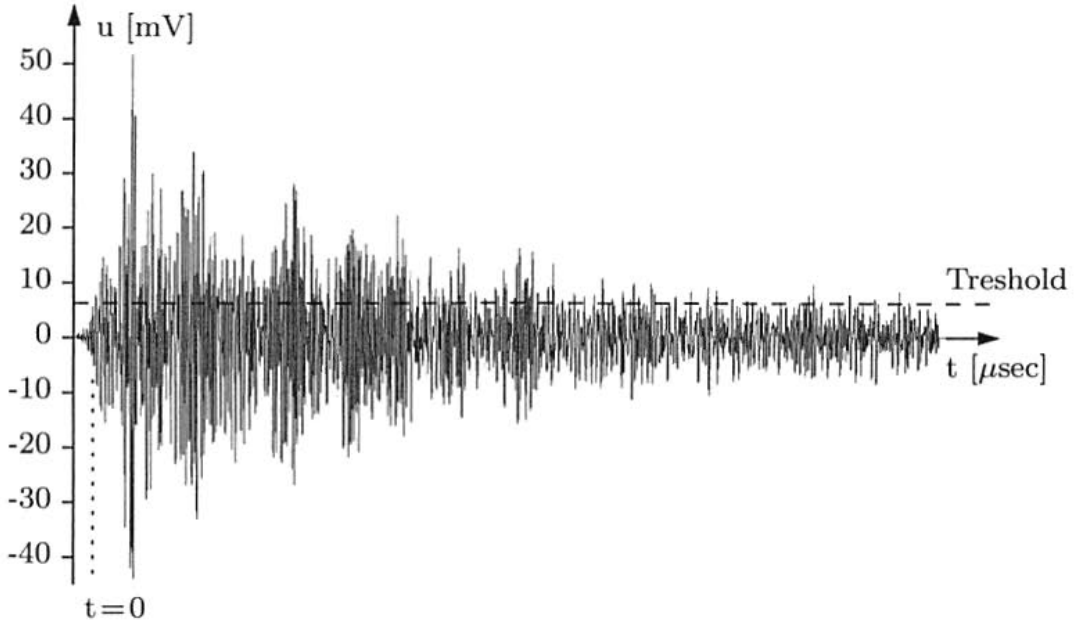

Figure 6.1: Burst signal from the pencil lead break

the probe pin is performed by laying the gauge block under the pin and adjusting the corresponding value in the amplifier. By using gauge blocks with different thickness, the same procedure is repeated in order to get the mean value of the amplification factor. In this manner, the nonlinearity deviation of the transducer in the measuring range of interest can be reduced. The same procedure is used for all three pairs of displacement transducers and measurement amplifiers.
To secure the elimination of possible errors during the production of the mean displacement value of three displacement measurements in the analogue circuit, the same calibration procedure is used on the complete system of three transducers connected to the deformation measuring device.
Before the beginning of each test, the specimen is loaded with the tension force of 0.5 kN in the case of a plain specimen and 2.0 kN in the case of a circular specimen. The signals of all external displacement transducers are calibrated to the zero value. Hence, all mobile parts of universal joints in the clamping device can be positioned in the defined zero position.

6.1.2 Calibration of the acoustic emission

After the determination of time parameters for the measurement of acoustic emission signals (PDT, HDT and HLT given in Section 5.4.1), the calibration of acoustic emission transducers clamped to the specimen is performed. The qualitative calibration of acoustic emission transducers has a significant influence on the received acoustic emission signals.
The calibration of the acoustic emission measurement is achieved on the basis of two different methods. The first method is the pencil lead break. Namely,

the breaking of the pencil lead on the surface of the specimen would act as a simulated source of acoustic emission signals. Furthermore, this signal has similar characteristics as a burst signal from the crack growth. The calibration procedure consists of the recording of wave signal through all acoustic emission transducers and their comparison. Also, by using the time difference measurement method, a position of the pencil lead break is calculated and compared with its actual position. In the case of coincidence between the real and the calculated position of the acoustic emission source and the coincidence of received wave forms from all transducers, it is possible to conclude that the quality of the bonding between the transducers and the specimen surface is satisfying. It can additionally be confirmed that the transducer positions are correctly chosen. The typical burst signal from a pencil lead break is depicted in Figure 6.1. The signal has approximate length of 2100 μsec, and its reception occurs with an adjusted pre-trigger of 50 μsec.

The possibility to use the acoustic emission transducer to work as a pulser is used as the second method for the calibration of acoustic emission transducers. This method is known as the automatic sensor testing (AST). One transducer (pulser) transmits an impulse signal on the surface of the specimen and it simulates an acoustic emission source. Other transducers receive and record this signal. The time difference measurement method is again performed in order to detect the source of the acoustic emission known to be at the position of the pulser. During one calibration cycle, all four transducers alternate as transmitters. It is possible to evaluate the performance of the acoustic emission transducers by comparing the calculated positions of acoustic sources.

The threshold value of the acoustic emission is determined on the specimen which is clamped in the clamping device. The specimen is subjected to the force of 0 kN and the testing machine is idle. At this point, the threshold is set to unable all transducers from detecting acoustic emission signals and therewith the background noise is eliminated from the measurement.

During the experiment, acoustic emission signals from the perturbations occurring under the applied load cannot be separated from the acoustic emission resulting from the damage evolution. This must be additionally considered in the post-processing of the recorded data.

6.1.3 Calibration of the electrical resistance

The calibration of the industry device Resistomat is performed using a highly precise industry calibration resistor[3] of 100 $\mu\Omega$ connected to the measuring device. The same calibration resistor is used for the inspection of the influence of the applied cables and gauge head selector switch on the change of electrical resistance. The investigation must prove that the equipment has no influence on the electrical resistance measurement.

[3]Co. Burster GmbH, calibration resistor 1240, measuring resistance 100 $\mu\Omega$

6.2 Procedures for the evaluation of measured data

The goal of processing measured data is to establish a physically reasonable procedure, which has the ability to produce meaningful experimental results from the raw data. Force and displacement measurement data are used to evaluate the development of the global stiffness of the specimen over the duration of fatigue experiments. Furthermore, the acoustic emission measurements are utilised to monitor the development of the acoustic emission during fatigue and the distribution of acoustic emission based on frequency and amplitude. Electrical resistance measurements are used for the assessment of damage during the service life of specimen.

6.2.1 Determination of the specimen stiffness

The determination of the specimen stiffness is performed on the basis of the recorded data for the force and for the averaged elongation of the specimen. The specimen stiffness is then calculated using a linear least squares fitting.

Vertical linear least squares fitting proceeds by finding the sum of the squares of the vertical deviations R^2 of a set of n data points (x_i, y_i)

$$R^2 = \sum [y_i - f(x_i, a, b)]^2 , \tag{6.1}$$

from a function $f(a, b) = a + b\,x_i$. To find the best fit line, the square deviations from each point are summarised, and the resulting residual needs to be minimised. Taking the partial derivatives of (6.1) with respect to the coefficients a and b

$$\frac{\partial(R^2)}{\partial a} = -2 \sum_{i=1}^{n} [y_i - (a + b\,x_i)] = 0 , \tag{6.2}$$

$$\frac{\partial(R^2)}{\partial b} = -2 \sum_{i=1}^{n} [y_i - (a + b\,x_i)] x_i = 0 , \tag{6.3}$$

leads to the system of equations

$$n\,a + b \sum_{i=1}^{n} x_i = \sum_{i=1}^{n} y_i , \tag{6.4}$$

$$a \sum_{i=1}^{n} x_i + b \sum_{i=1}^{n} x_i^2 = \sum_{i=1}^{n} x_i y_i . \tag{6.5}$$

Solving the system of equations (6.4) and (6.5) provides the least squares coef-

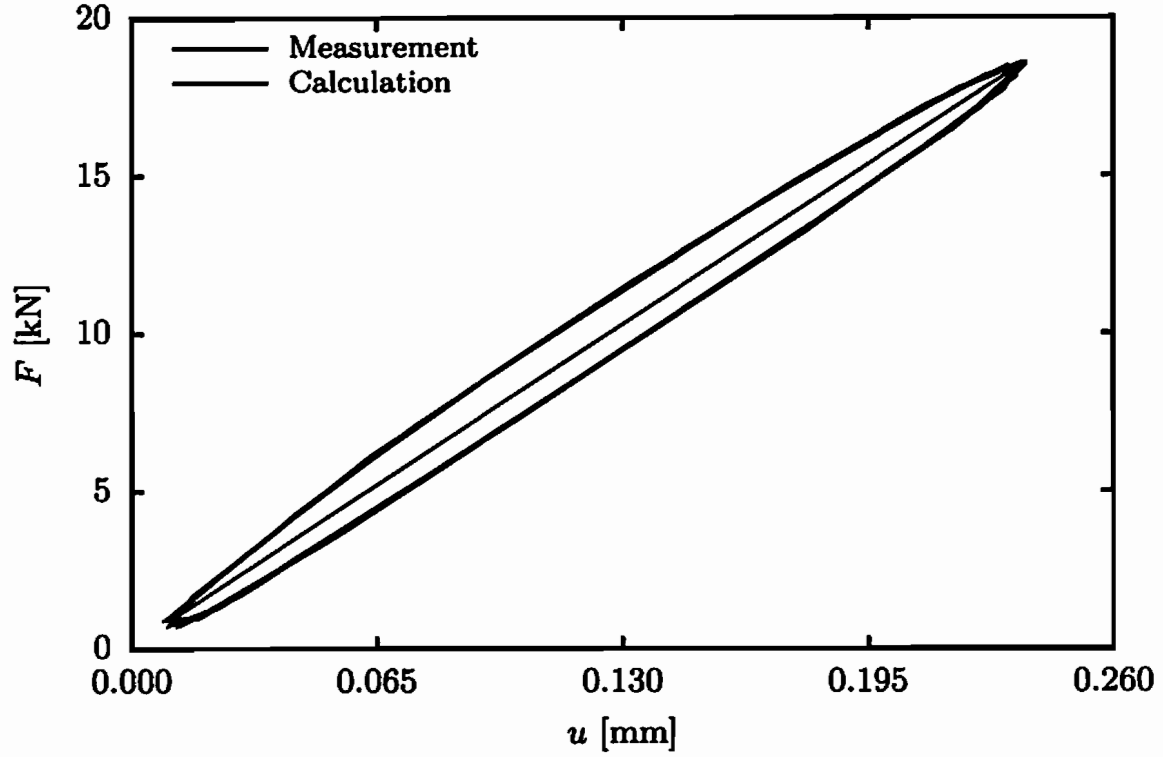

Figure 6.2: Force-elongation plot and regression line for the determination of the specimen stiffness

ficients

$$a = \frac{\sum_{i=1}^{n} y_i \sum_{i=1}^{n} x_i^2 - \sum_{i=1}^{n} x_i \sum_{i=1}^{n} x_i y_i}{n \sum_{i=1}^{n} x_i^2 - \sum_{i=1}^{n} x_i \sum_{i=1}^{n} x_i}, \tag{6.6}$$

$$b = \frac{n \sum_{i=1}^{n} x_i y_i - \sum_{i=1}^{n} x_i \sum_{i=1}^{n} y_i}{n \sum_{i=1}^{n} x_i^2 - \sum_{i=1}^{n} x_i \sum_{i=1}^{n} x_i}. \tag{6.7}$$

The coefficient b, which is the slope of regression line, represents the calculated stiffness of the specimen.

As pointed out in Section 5.4.4, the sample rate of the data acquisition is set to 150 Hz, such that the specimen stiffness is calculated from 150 pairs of force-elongation measurements. In this manner, the stiffness represents an averaged value of stiffness over 9 load cycles for a plain specimen, and over 6 load cycles for a circular specimen. This procedure minimises the influence of possible single measurement errors on the calculated stiffness.

A typical plot of the measured data (force and elongation) and an appropriate regression line from the linear least squares fitting is given in Figure 6.2.
The evolution of the global specimen stiffness is represented through the normalised values of specimen stiffness. Before the specimen stiffness is normalised, it is smoothed using an exponentially weighted average. After that, it is normalised using two different procedures, which depends on the choice of the ordinate scale. For the representation using a logarithmic scale, specimen stiffness is normalised using the equation

$$S_{\mathrm{nor}} = \frac{S_{\mathrm{max}}}{S_{\mathrm{i}}} - 1.0\,, \tag{6.8}$$

where S_{nor} is the normalised specimen stiffness, S_{max} is the maximum value of the specimen stiffness during the whole experiment and S_{i} is the instantaneous specimen stiffness. In the case of the linear ordinate scale, the specimen stiffness is normalised using an average stiffness S_{avg} by

$$S_{\mathrm{nor}} = \frac{S_{\mathrm{i}}}{S_{\mathrm{avg}}}\,, \tag{6.9}$$

where S_{avg} is the arithmetic mean stiffness over the stabilised strength behaviour between 20% and 50% of the fatigue life. Both representations correspond to the goal of the experiment to document the evolution of damage during the damage process.

6.2.2 Post-processing of the measured acoustic emission data

During the detection of the acoustic emission, acoustic emission transducers may detect signals (interference signals) that do not belong to the acoustic emission waves from the damage evolution, but to other sources, such as friction between transducers and specimen surface, movement of the clamping jaw parts, or signals from the machine itself. Even in the case of a plain specimen, where transducers 1 and 4 serve as guard sensors, it is possible to detect records which are obviously not from the damage evolution. In the case of a circular specimen, where all transducers are used as measuring transducers this appearance is even more dominant.
One part of the recoded data from the measurements of acoustic emission on the circular specimen during cyclic load is given in Table 6.1. The gray records belong to the two events from the damage evolution, and the other records are from interference signals. The difference between these two groups of signals is evident. Signals from the damage evolution are recorded by all four transducers in short time intervals. Furthermore, these signals are longer than the interference signals (DUR), they have more counts (COUN) and they carry a significantly bigger amount of energy (ENER). The differences in the characteristics of the detected damage evolution signals result from modifications of the signal during its travel from the point of origin to the acoustic emission transducers.

TIME	PARA1	PARA2	CH	COUN	ENER	DUR	AMP
1617.9963155	14.6196	0.0804	3	2	2	61	38
1617.9964492	14.2680	0.0798	2	1	0	15	35
1617.9986282	12.5248	0.0705	3	1	0	13	35
1618.0004003	11.0208	0.0638	2	1	0	36	35
1618.0056440	7.6125	0.0433	3	1	0	3	36
1618.1065375	52.3746	0.2401	3	33	18	344	48
1618.1065385	52.3746	0.2401	1	33	20	426	46
1618.1065397	52.3746	0.2401	2	50	26	416	48
1618.1065402	52.3746	0.2401	4	42	25	421	51
1618.1209905	49.9673	0.2342	4	39	27	481	48
1618.1209945	49.9673	0.2342	2	37	24	466	45
1618.1209950	49.9673	0.2342	3	32	19	383	47
1618.1209990	49.9673	0.2342	1	16	11	193	45
1618.1378895	37.8918	0.1859	2	3	1	23	40
1618.1379215	37.8918	0.1859	3	4	2	56	40
1618.1484660	28.0966	0.1434	3	1	0	14	39

Table 6.1: Summary of recorded data from the acoustic emission measurement

In order to analyse a valid evaluation of the acoustic emission damage evolution signals, it is necessary to eliminate all interference signals from the recorded data. The elimination of these records is achieved using a time difference measurement method. In the case of the experiments with a plain specimen, where transducers 1 and 4 serve as guard sensors, the records which belong to these two transducers are also eliminated. In that manner, the recorded data contain records from transducers 2 and 3 in the case of the experiments with a plain specimen and from all four transducers for the experiments with a circular specimen.
As pointed out earlier in Sections 4.1.4.1 and 4.1.4.2, the time difference measurement method is based on the assumption of a constant velocity of the acoustic emission waves. For this reason, the determination of the true constant velocity has a great influence on the calculation of the origin of the acoustic emission. In the case of an infinite medium, the velocity of the dilatational or longitudinal wave c_L and the distortional or transverse wave c_V are given by

$$c_L = \sqrt{\frac{2\mu(1-\nu)}{\rho(1-2\nu)}} \quad \text{and} \quad c_T = \sqrt{\frac{\mu}{\rho}}\,. \tag{6.10}$$

Here, ρ is the density, ν is the Poisson's ratio and μ is the shear modulus or Lamé constant given by

$$\mu = \frac{E}{2(1+\nu)}\,. \tag{6.11}$$

On the other hand, if the medium is represented as an infinite plate, even if the source is the centre of compression and radiates only longitudinal waves, as each longitudinal wave reaches the free surface, it is reflected as both a longitudinal and a transverse wave. Each of these two components in turn intersects the opposite surface and generates two more waves. Therefore, after a short time a very large number of reflected waves echoing back and forth between the two surfaces is generated. The apparent wave velocity of the disturbance in the plate then falls between the velocity of the longitudinal and the velocity of the transverse waves. It is found that the velocity c_p' of the mode carrying the largest portion of energy corresponds to the first longitudinal plate mode which is about nine percent lower than the plate velocity c_p given by (cf. Egle (1987))

$$c_p = c_T \sqrt{\frac{2}{1-\nu}}\,. \tag{6.12}$$

In the case of 42CrMo4, the introduced material parameters and velocities are

$$\begin{aligned} &\nu \approx 0.3\,, \quad E \approx 2.1 \cdot 10^5 \text{ N/mm}^2\,, \quad \rho \approx 7900 \text{ kg/m}^3\,, \\ &c_L \approx 5982 \text{ m/sec}\,, \quad c_T \approx 3197 \text{ m/sec}\,, \\ &c_p \approx 5405 \text{ m/sec}\,, \quad c_p' \approx 4958 \text{ m/sec}\,. \end{aligned} \tag{6.13}$$

Based on the two calibration procedures introduced in Section 6.1.2, it is found that the characteristic constant velocity is approximately equal to the longitudinal velocity c_L for the plain specimen, and to the velocity c_p' for the circular specimen.
After the time difference measurement method has been used for the elimination of interference signals, the remaining recorded data is used for the evaluation of the single event count distribution and for the cumulative event count evolution during the service life of the specimen, as well as to represent the relationship between frequency or amplitude of acoustic emission signals and event counts.
The evolution of cumulative event counts is employed by many researchers for the estimation of acoustic emission activity in the specimen during the damage evolution. Murakami et al. (1998) uses it in the case of damage evolution under a monotonic tension loading, Berkovits & Fang (1993, 1995), Fang & Berkovits (1994, 1995), Huang et al. (1998), Nam (1999), Murav'ev et al. (2002), Murav'ev et al. (2003) and Heiderich (2004) in the case of recording the crack evolution under cyclic fatigue loading, and (Prosser (1996, 1998), Prosser et al. (1995), Soboyejo & Ramasundaram (1996)) in the case of experiments with glass-fibre reinforced materials.

6.2.3 Calculation of the electrical resistance

All experiments in this work are performed at room temperature. However, the room temperature changes between 20°C and 30°C which may influence the measurement of the electrical resistance. For this reason, the measured values

of the electrical resistance need to be corrected in the post-processing in order to include the temperature influence.
The correction proceeds as follows: consider a beam with a constant cross section area along the gauge length in which the electrical resistance is measured. A variation of the electrical resistance can be calculated as a function of the possible temperature change of the specimen, using the conditional temperature change of the specific electrical resistance $\rho(\Theta)$

$$\rho(\Theta) = \rho_{20}(1 + \alpha_p \Delta\Theta_{20}), \tag{6.14}$$

the temperature dependence of the length of the specimen

$$l(\Theta) = l_{20}(1 + \alpha_\epsilon \Delta\Theta_{20}), \tag{6.15}$$

the temperature dependence of the cross sectional area of the specimen

$$A(\Theta) = A_{20}(1 + \alpha_\epsilon \Delta\Theta_{20})^2 \tag{6.16}$$

and relation

$$R(\Theta) = \rho(\Theta)\frac{l(\Theta)}{A(\Theta)} = R_{20}\frac{1 + \alpha_p \Delta\Theta_{20}}{1 + \alpha_\epsilon \Delta\Theta_{20}}. \tag{6.17}$$

Here, R_{20} is the electrical resistance at 20°C, α_p is the temperature coefficient of specific electrical resistance, α_ϵ is the linear thermal expansion coefficient and $\Delta\Theta_{20}$ is the temperature difference between the current temperature and the reference temperature of 20°C.
However, in the case of structural components with a non-constant cross section area and non-constant magnitude of the electrical field, (6.17) is not valid and its integral form must be used. In order to determine the relationship between the temperature and the electrical resistance, the experiments are performed on the plain and circular specimen. The results are given in Figure 6.3. The linear relationship between electrical resistance and temperature can be observed. In the case of the circular specimen experiments, the results are given for the undamaged specimen as well as for partially damaged specimen with the crack length of 18.6 mm.
As in the case of the calculation of the specimen stiffness, the linear least squares fitting is used to evaluate the linear relationship between the electrical resistance and the temperature. Resulting equations for the plain specimen as well as for the undamaged and damaged circular specimen are

$$\begin{aligned} R(\Theta) &= 0.2340 \cdot \Theta + 87.1654, \\ R(\Theta) &= 0.0600 \cdot \Theta + 23.7244, \\ R(\Theta) &= 0.0625 \cdot \Theta + 24.7885, \end{aligned} \tag{6.18}$$

respectively. It follows from (6.18) that a temperature change of 1°C leads to the change of electrical resistance of 0.2340 $\mu\Omega$ for the plain specimen, 0.0600 $\mu\Omega$

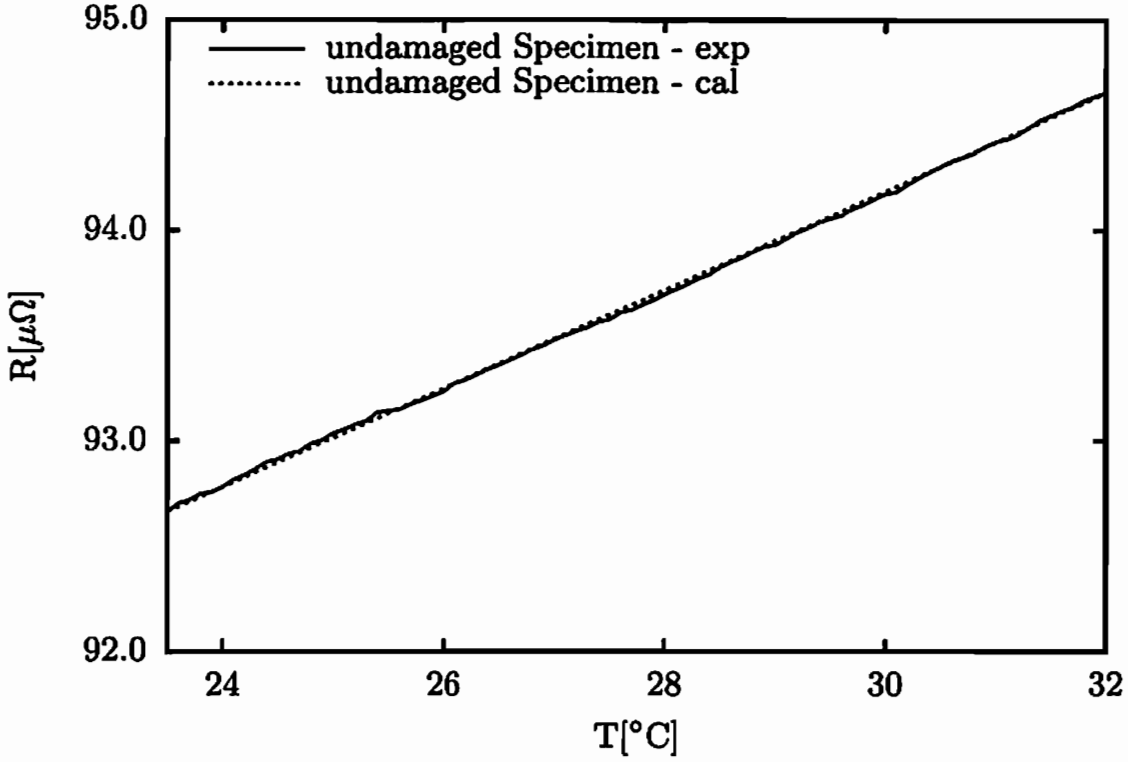

(a) Plain specimen

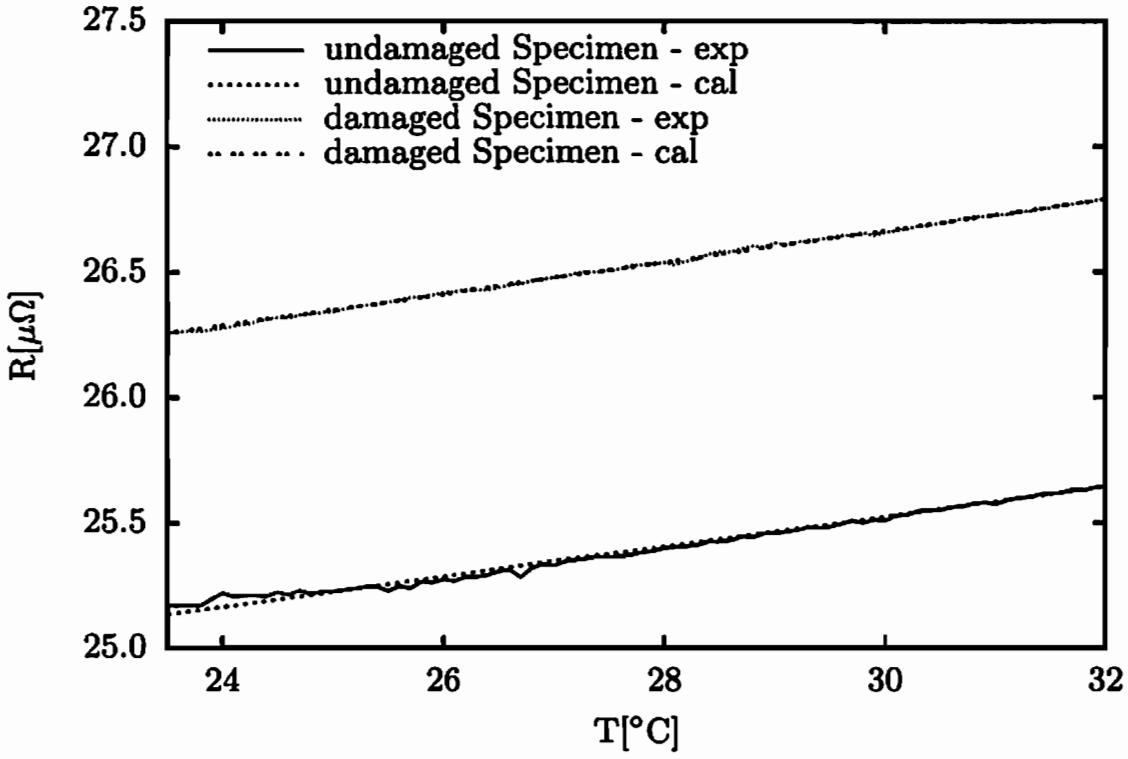

(b) Circular specimen

Figure 6.3: Electrical resistance as a function of temperature

$l_n \backslash l_g$	P1	P2	P3	P4	P5	P6	P7	P8	P9
P1	—	6.17	10.77	16.29	21.12	26.18	31.22	36.16	40.94
P2	5.48	—	5.31	10.84	15.65	20.72	25.75	30.68	35.49
P3	10.09	4.61	—	6.22	11.05	16.10	21.15	26.08	30.80
P4	15.59	10.12	5.51	—	5.55	10.61	15.64	20.58	25.37
P5	20.45	14.96	10.37	4.85	—	5.72	10.80	15.70	20.48
P6	25.49	20.01	15.40	9.89	5.03	—	5.75	10.68	15.46
P7	30.52	25.04	20.45	14.92	10.11	5.04	—	5.66	10.44
P8	35.46	29.96	25.37	19.85	15.00	9.96	4.94	—	5.52
P9	40.26	34.79	30.11	24.66	19.80	14.76	9.74	4.81	—

Table 6.2: Summary of measured gross and net lengths between electrical resistance thermocouples (lengths in mm)

$\rho \backslash R$	P1	P2	P3	P4	P5	P6	P7	P8	P9
P1	—	24.58	45.43	70.73	92.47	115.61	138.57	160.80	182.53
P2	222.90	—	20.75	46.05	67.78	90.93	113.85	136.11	157.84
P3	223.67	223.44	—	25.24	46.95	70.12	93.05	115.29	137.04
P4	225.33	225.90	227.43	—	21.62	44.82	67.77	90.01	111.74
P5	224.56	224.96	224.80	221.32	—	23.16	46.11	68.35	90.09
P6	225.23	225.61	226.06	225.00	228.64	—	22.88	45.13	66.88
P7	225.41	225.78	225.96	225.59	226.57	225.61	—	22.20	43.92
P8	225.17	225.56	225.62	225.13	226.24	224.96	223.35	—	21.71
P9	225.12	225.25	225.97	224.97	225.91	224.97	223.99	224.13	—

Table 6.3: Summary of the electrical resistance and the specific electrical resistance (R[$\mu\Omega$], ρ[nΩm])

for the undamaged circular specimen and 0.0625 $\mu\Omega$ for the damaged circular specimen. These values are used for the temperature correction of the measured electrical resistance values during the post-processing.

The specific electrical resistance ρ is an additional material parameter to be determined from (6.17). The plain specimen without any cross section reductions in the middle of the strait part is used for its determination. The cross section of the strait part is 4.95x10.03 mm. For this purpose, nine thermocouples are welded on the strait part of the specimen. The distances between the thermocouples are given in Table 6.2 as gross and net lengths. The gross lengths in the upper diagonal part of Table 6.2 represent the length between the outer edges of the thermocouple beads. The net lengths in the lower diagonal part of Table 6.2

represent the distance between the middle points of the thermocouple beads. During the measurement of the electrical resistance, the temperature changes between 22.1°C and 22.5°C. For this reason, all values of electrical resistance are scaled down to the temperature of 22°C. These values are given in the upper diagonal part of Table 6.3. The corresponding values of specific electrical resistance are given in the lower diagonal part of Table 6.3. The final value of the specific electrical resistance is calculated as the arithmetic mean value of the single values. The calculated value of the specific electrical resistance is 0.225 $\mu\Omega m$. It is used in the finite element calculation of the electrical resistance evolution.

After the determination of the specific electrical resistance and the relationship between the temperature and the electrical resistance (6.18), the temperature coefficient of the specific electrical resistance α_p is determined using (6.17) and the electrical resistance-temperature relationship for plain specimen $(6.18)_1$. The calculated value of α_p is 0.00261 $^1/^\circ\text{K}$.

The evolution of the electrical resistance during the service life is represented using the normalised values of the electrical resistance, similar as in the case of the specimen stiffness evolution. Before normalisation, the electrical resistance is smoothed using an exponentially weighted average. The normalisation procedure depends on the chosen ordinate scale. For the logarithmic ordinate scale, the electrical resistance is normalised using

$$R_{\text{nor}} = \frac{R_{\text{i}}}{R_{\text{min}}} - 1.0, \tag{6.19}$$

where R_{nor} is the normalised electrical resistance, R_{min} is the minimum value of electrical resistance during the whole experiment and R_{i} is the instantaneous electrical resistance. In the case of the linear ordinate scale, the electrical resistance is normalised using the average resistance R_{avg}

$$R_{\text{nor}} = \frac{R_{\text{i}}}{R_{\text{avg}}}, \tag{6.20}$$

where R_{avg} is the mean value of the electrical resistance between 20% and 50% of the fatigue life.

6.3 Experiments with cyclic loading

The main task of this work is the detection of the initiation and the evolution of damage under fatigue loading. To realise this goal, a number of experiments are performed on two specimen geometries with displacement and force controlled loading. The load is applied as constant amplitude loading during the entire duration of the experiment, or as a block experiment with amplitude which is constant inside the block and which differs between blocks. Additionally, in the case of the circular specimen, one group of experiments is performed with a load applied in two different directions.

Two introduced nondestructive methods, i.e. the measurement of electrical resistance and the measurement of acoustic emission, are compared with the evolution of the specimen stiffness during the service life of the specimen. Furthermore, the investigation of the frequency and the amplitude range of the acoustic emission output, as well as the detection of the position of acoustic emission sources is performed.
The results of the measurement of electrical resistance and the evolution of specimen stiffness are used for the parameter identification using the material law described in Section 3.3, as well as for the calibration procedure for the connection between the electrical resistance and the crack length.
The summary of experimental results for the plain and the circular specimen is given in the next sections.

6.3.1 Plain specimen with a hole

The experiments on the plain specimen with the reduction of cross section area in the form of a hole with the diameter of 1 mm are performed with the constant amplitude haversine loading during the whole service life and with the stress ratio $R=0.05$ or $R=0.25$. For the stress ratio 0.05, the applied loading is controlled using the displacement control, and for $R=0.25$ using the force control. The outlook of the conducted experiments is presented in Table 6.4. In the given table, $\sigma_{a,nom}$ is the nominal stress amplitude calculated from the measured or applied force amplitude for the net cross section area in the vicinity of the cross section reduction.
Based on the results of the experiments with the constant displacement amplitude and Palmgren-Miner damage rule introduced in Section 3.4.2, the experiments with block load amplitudes are designed. The experiments are constructed according to the schemas introduced in Figure 6.4. Load amplitudes and the duration of the single blocks are listed in Table 6.5. It is assumed that the block with the displacement amplitude 0.155 mm has no influence on the fatigue life of the specimen since the applied loading is below the endurance limit. Other blocks are supposed to contribute with 5% damage during each block. In this manner, if Palmgren-Miner rule is applied, four block sequences are needed for the final failure. The stress ratio is set to 0.05 in all block program experiments. Block program experiments are conducted applying block sequences given in Figure 6.4 up to the final failure of the specimen. The experiments are summarised in Table 6.6. The fatigue life represents the sum of all load cycles from different block sequences, which are made during the service life of the specimen. The block program schema for the specimen PHB6 is the same as for the specimen PHB1, with a two times smaller duration of single blocks.
Based on the achieved fatigue life of the specimen under block program loading represented in Table 6.6, it is evident from (3.133) that for different block program sequences Palmgren-Miner rule is not always conservative ($D<1$). Namely, by using (3.133) and the fatigue life of specimens given in Tables 6.4 and 6.6, the

Spec.	Load control	Stress ratio	Amplitude [mm]/[kN]	$\sigma_{a,nom}$ MPa	Fatigue life Load cycles
PH01	Displ.	0.05	0.155	264	>3600000
PH02	Displ.	0.05	0.160	257	777555
PH03	Displ.	0.05	0.160	275	546516
PH04	Displ.	0.05	0.165	281	723978
PH05	Displ.	0.05	0.165	290	>2000000
PH06	Displ.	0.05	0.170	292	314163
PH07	Displ.	0.05	0.170	303	399384
PH08	Displ.	0.05	0.175	290	409347
PH09	Displ.	0.05	0.180	304	284112
PH10	Displ.	0.05	0.185	321	196956
PH11	Displ.	0.05	0.185	325	129537
PH12	Displ.	0.05	0.190	317	241182
PH13	Displ.	0.05	0.200	339	128988
PH14	Force	0.25	11.250	271	>3000000
PH15	Force	0.25	11.850	278	>2250000
PH16	Force	0.25	12.000	286	431064
PH17	Force	0.25	12.150	293	310608
PH18	Force	0.25	12.750	301	262377
PH19	Force	0.25	12.750	312	145233

Table 6.4: Experiments on the plain specimen with a hole

damage measure D is calculated to be between 0.67 and 2.50 in the case of block program experiments. If alternatively the elementary Miner's rule is used and all block sequences influence the fatigue life of the specimen[4], the resulting damage measure D lies between 0.789 and 2.736. This range also shows nonconservative results for some block program sequences.

6.3.1.1 Evolution of the global specimen stiffness

The evolution of the global specimen stiffness is calculated using the procedure described in Section 6.2.1. The evolution of specimen stiffness under the fatigue loading for the stress ratio 0.05 and the displacement controlled loading and for the stress ratio 0.25 and the force controlled loading are plotted in Figure 6.5

[4]The fatigue life of the specimen for the load amplitude of 0.155 mm is assumed to be four million load cycles.

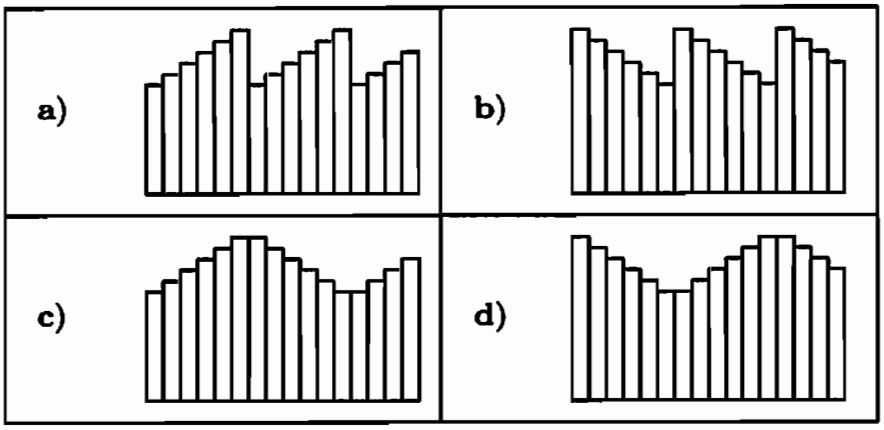

Figure 6.4: Block program experiments: a) low-high sequences (LH), b) high-low sequences (HL), c) low-high-low sequences (LHL), d) high-low-high sequences (HLH)

Block	Displ. [mm]	Load cycles
1	0.155	100000
2	0.160	37500
3	0.170	16750
4	0.180	13500
5	0.190	11250
6	0.200	5750

Table 6.5: Load amplitude and number of cycles for single blocks

for different specimens. In order to get better overview of specimen stiffness evolution, the ordinate in diagrams presented in Figure 6.5 is represented in logarithmic scale. As can be seen in Figure 6.5, after the stabilisation of the normalised specimen stiffness during the beginning period, its value stays nearly constant over a long time of the service life. Difference between minimum and maximum value of the specimen stiffness in this period is less than 1%. Depending on the applied load amplitude level, it is possible to observe a decrease in the specimen stiffness after 80% to 90% of the service life. In the last phase of the service life, the decrease of the specimen stiffness has an exponential behaviour and leads to the final failure of the specimen. In the case of plain specimen with a hole, this exponential decrease of the specimen stiffness occurs in the short time period compared to the whole service life of the specimen. The obtained evolution of the specimen stiffness is in accordance with the observations in the works of Haibach (2002) and Heiderich (2004).

Spec.	Load control	Stress ratio	Block program	Fatigue life Load cycles
PHB1	Displ.	0.05	LH	825347
PHB2	Displ.	0.05	HL	670011
PHB3	Displ.	0.05	LHL	543699
PHB4	Displ.	0.05	HLH	687411
PHB5	Displ.	0.05	LHL	1789830
PHB6	Displ.	0.05	LH	1273535

Table 6.6: Block program experiments on the plain specimen with a hole

The evolution of the normalised specimen stiffness for two specimens under low-high and low-high-low block program sequences is shown in Figure 6.6. As can be seen, the normalised specimen stiffness shows small deviations between the loading blocks. As in the case of the experiments with a constant amplitude loading during the whole service life, the specimen stiffness has a stabilised behaviour over a 90% of the service life. The decrease of the specimen stiffness follows that period with the exponential behaviour at the end of the service life. This leads to the final failure of the specimen.
For the sake of a better representation of the normalised specimen stiffness evolution, the normalised specimen stiffness for the specimen PH16 (Figure 6.5b) is visualised separately in Figure 6.7 for the range between 0.985 and 1.015.
The results presented in Figures 6.5, 6.6 and 6.7 indicate a brittle behaviour of the material, which is characteristic for the applied high cycle fatigue loading. However, the decrease of the normalised specimen stiffness is in connection with the macroscopic crack initiation and propagation. The changes on the microscale level, such as microcrack initiation and propagation, cannot be detected based on the change of the normalised global specimen stiffness.

6.3.1.2 Evolution of the acoustic emission

As presented in Section 5.4.1, two sets of acoustic emission transducers with appropriate preamplifiers are used to identify frequencies at which the acoustic emission from the damage evolution occurs. In the case of the plain specimen with a hole, the wideband transducers are used in the displacement controlled experiments with a constant load amplitude during the whole service life and the stress ratio 0.05 (specimens PH01 to PH13). A typical frequency response for this type of acoustic emission transducers is presented in Figure 6.8 for the specimen PH06. It shows that most of the event counts have the frequency between 80 and 250 kHz. For this reason, the resonance acoustic emission transducers with the resonant frequency of 150 kHz are used in all other experiments with the plain

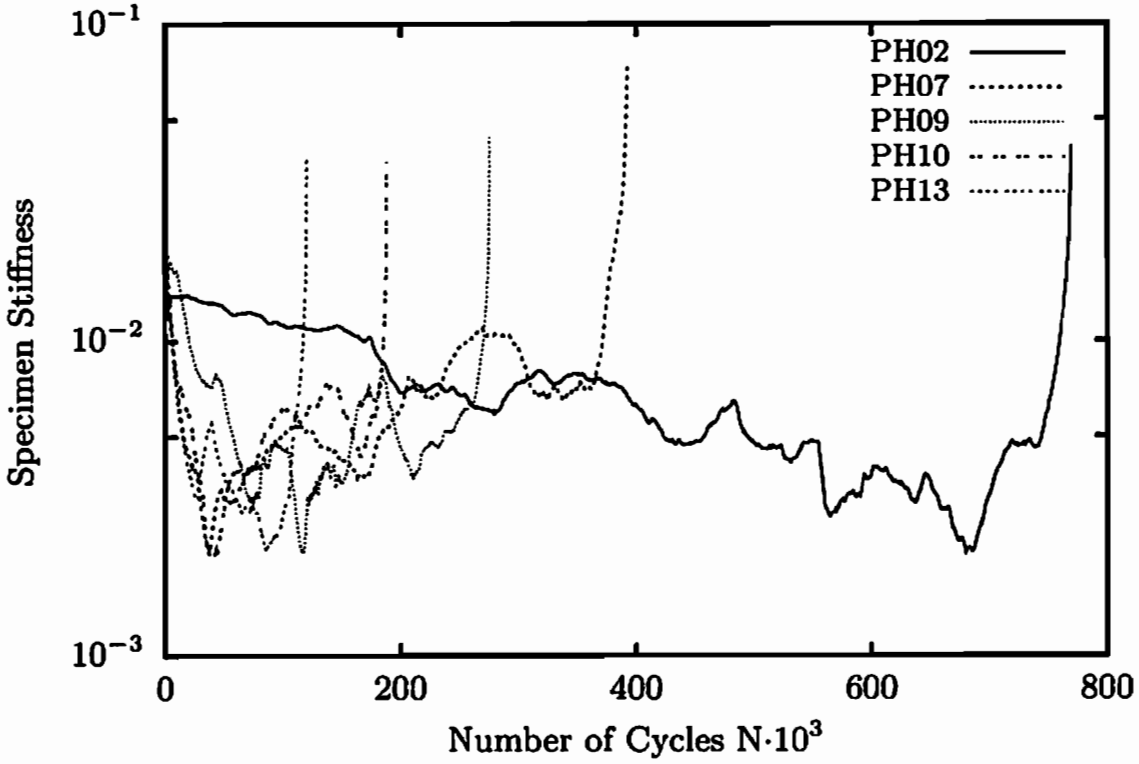

(a) Stress ratio $R=0.05$

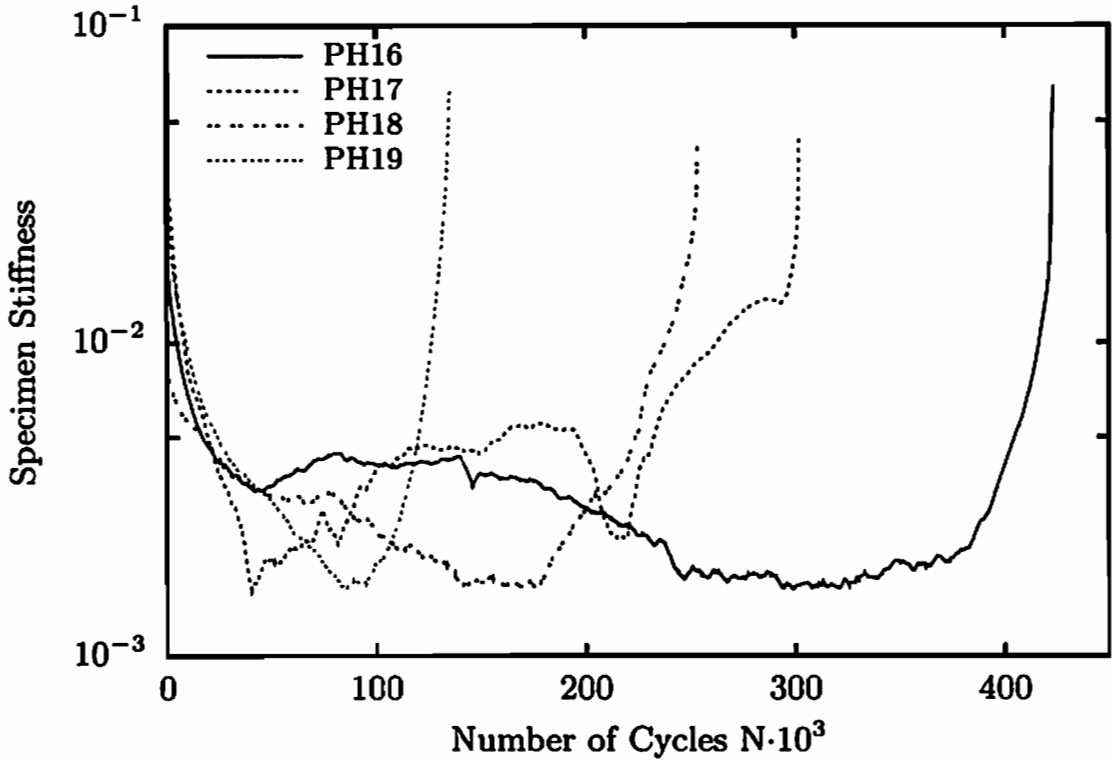

(b) Stress ratio $R=0.25$

Figure 6.5: Evolution of the normalised specimen stiffness

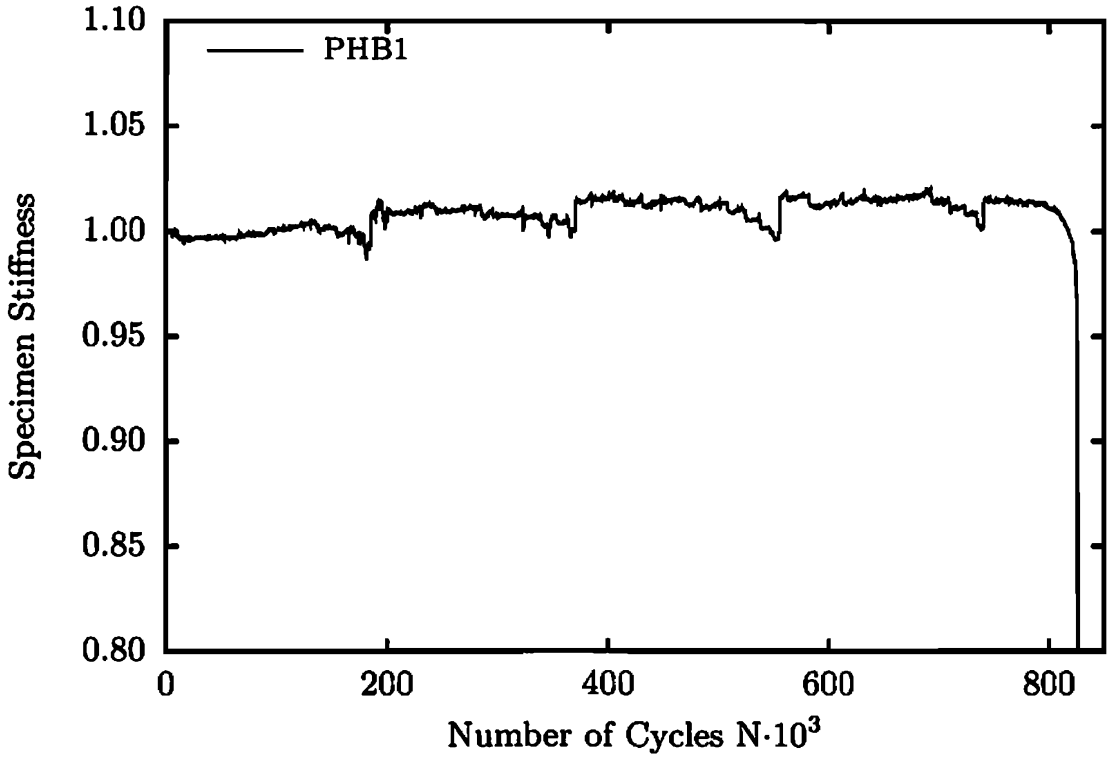

(a) LH block experiment

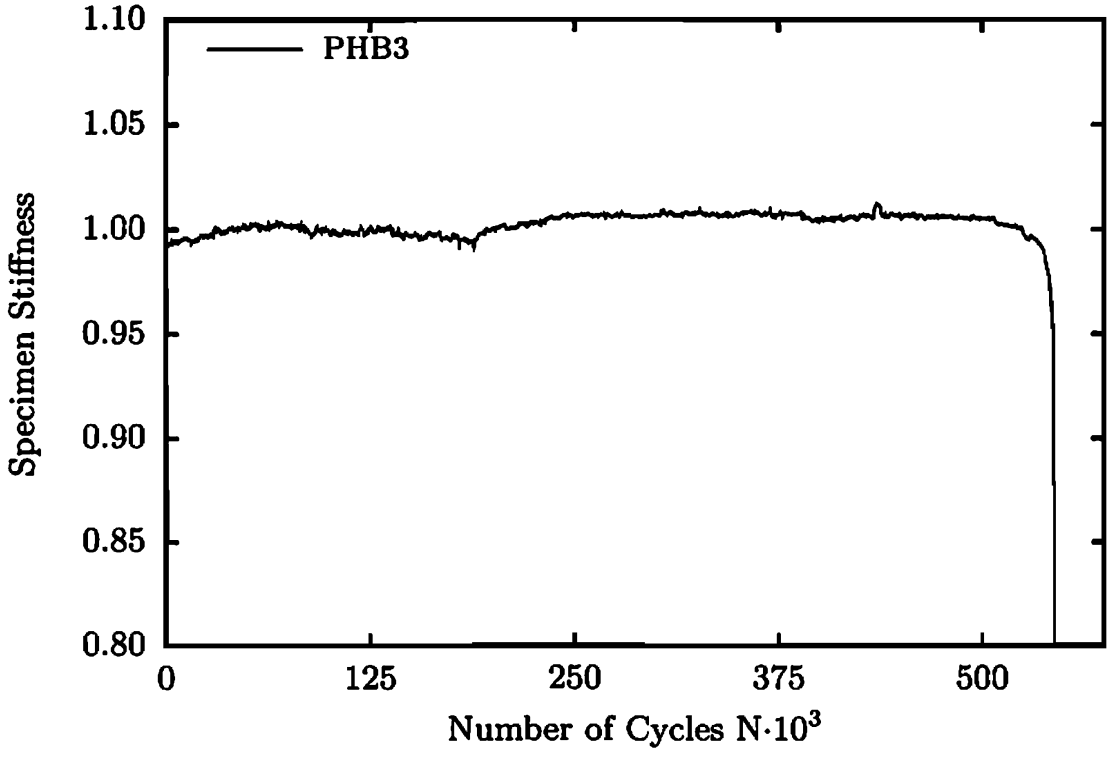

(b) LHL block experiment

Figure 6.6: Evolution of the normalised specimen stiffness

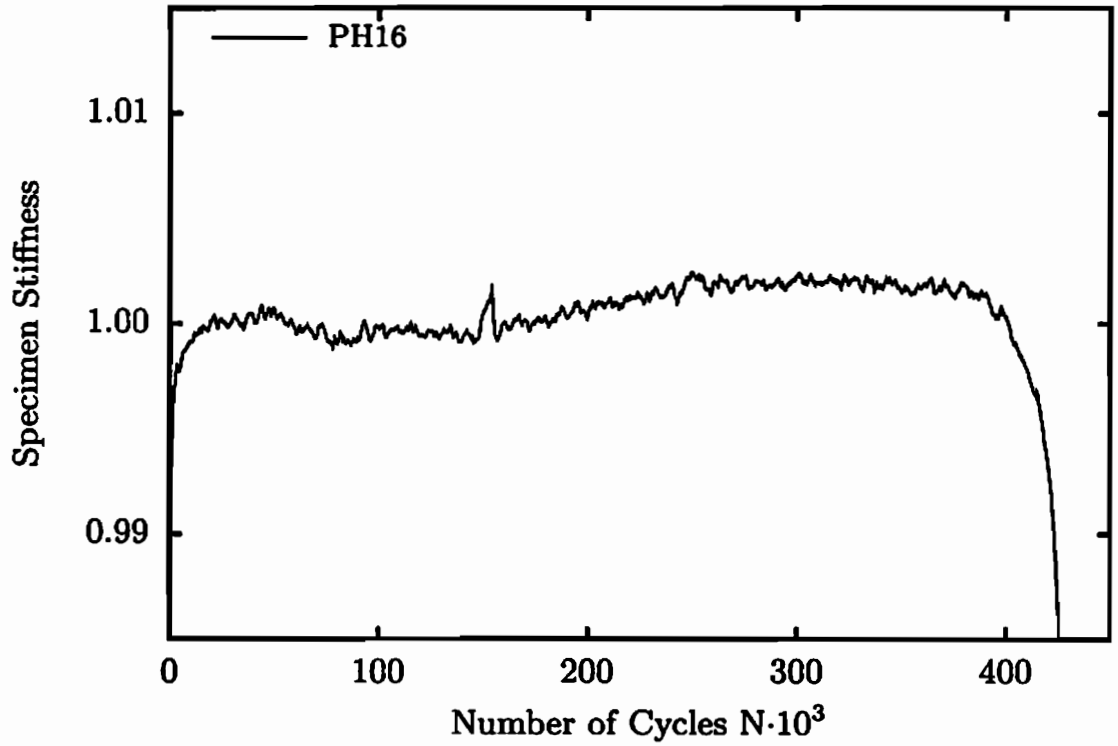

Figure 6.7: Evolution of the normalised specimen stiffness - enlarged representation

specimen with a hole. A typical result of the frequency response for resonance acoustic emission transducers is plotted in Figure 6.8 for specimen PHB1. Based on the results for both sets of acoustic emission transducers, it is evident that the acoustic emission from damage evolution occurs with the frequency between 50 and 250 kHz.

For the better understanding of characteristics of acoustic emission signals, the amplitude of acoustic emission signals is investigated. The characteristic amplitude response for both sets of acoustic emission transducers is depicted in Figure 6.9. As can be seen, most of the acoustic emission event counts have an amplitude between 35 and 70 dB in both cases. This behaviour is used as an additional condition in the elimination of the extraneous noise.

One more condition is used for the elimination of signals which do not belong to the damage evolution. Namely, the analogue parameter input which indicates the force value at the detection moment of the acoustic emission signal is used for the elimination of these acoustic emission signals. In this manner, it is possible to eliminate all signals which occur bellow a certain value of the force and which can originate from the crack closure and the friction between crack surfaces. This type of signal has the same characteristics and originates from the same position as signals from the damage evolution. An additional possibility for its

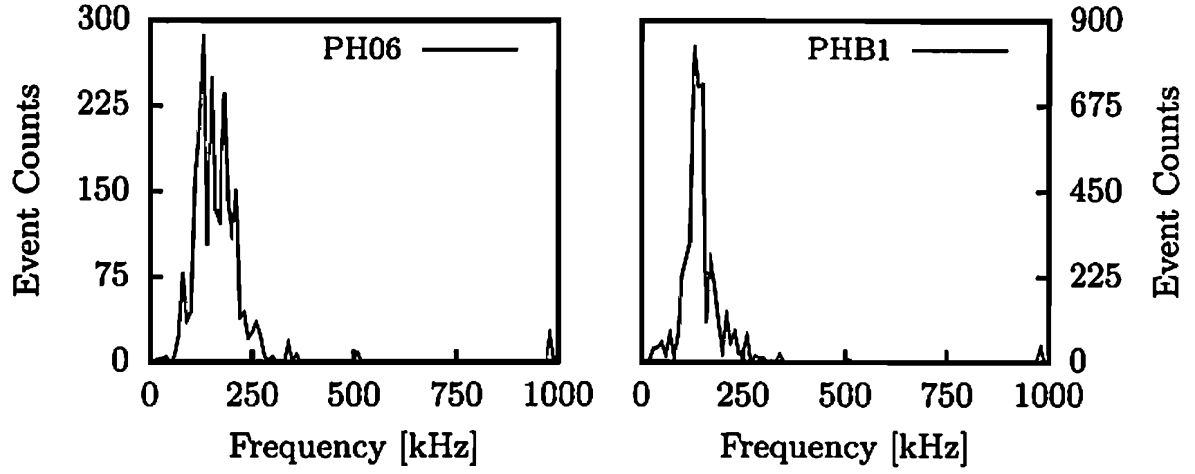

Figure 6.8: Acoustic emission event counts versus frequency

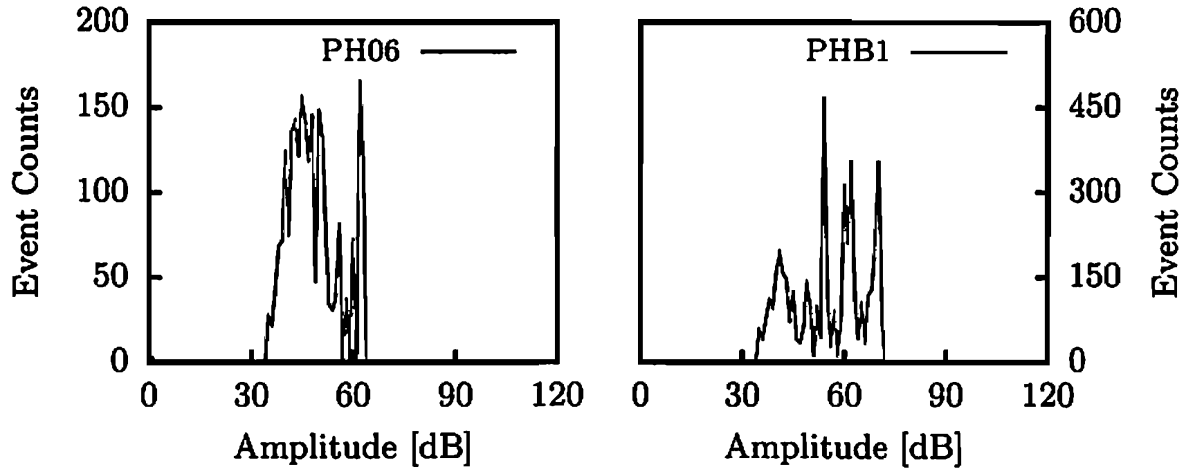

Figure 6.9: Acoustic emission event counts versus amplitude

elimination is gained by setting the force threshold value to 5 kN.
However, the main procedure for the distinction of the acoustic emission signals which originate from the damage evolution is the time difference measurement method for the detection of the acoustic emission origin introduced in Section 4.1.4.1. The distance obtained using the time difference measurement method represents the distance between the origin of the acoustic emission and the acoustic emission transducers. The location of the acoustic emission origin for the plain specimen with a hole is plotted in Figures 6.10 and 6.11. In the case of the specimens given in Figure 6.10, acoustic emission is recorded using wideband transducers, in contrast to specimens presented in Figure 6.11 where acoustic emission is detected using resonance transducers. Both figures show that the computed location of the origin for both types of transducers is in good agree-

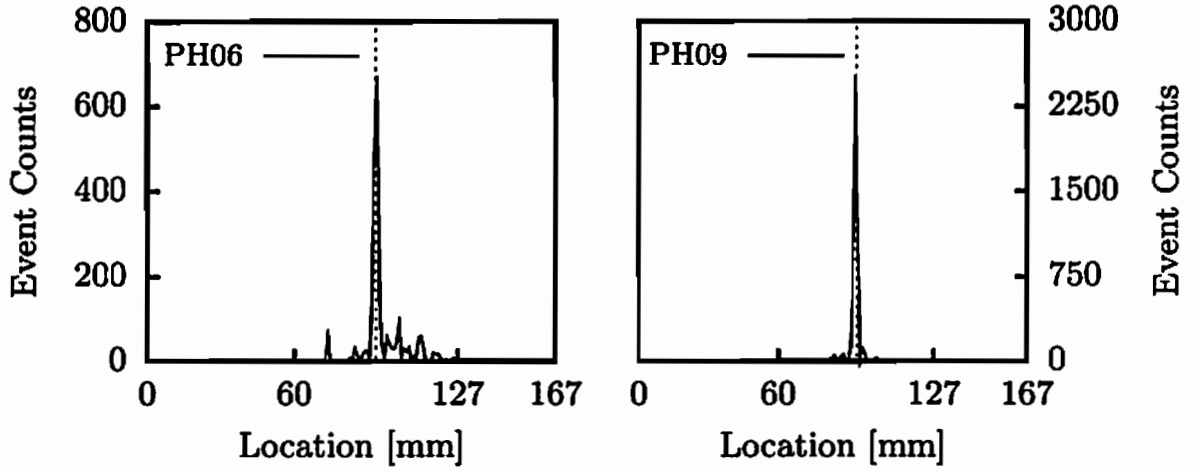

Figure 6.10: Location of the acoustic emission origin

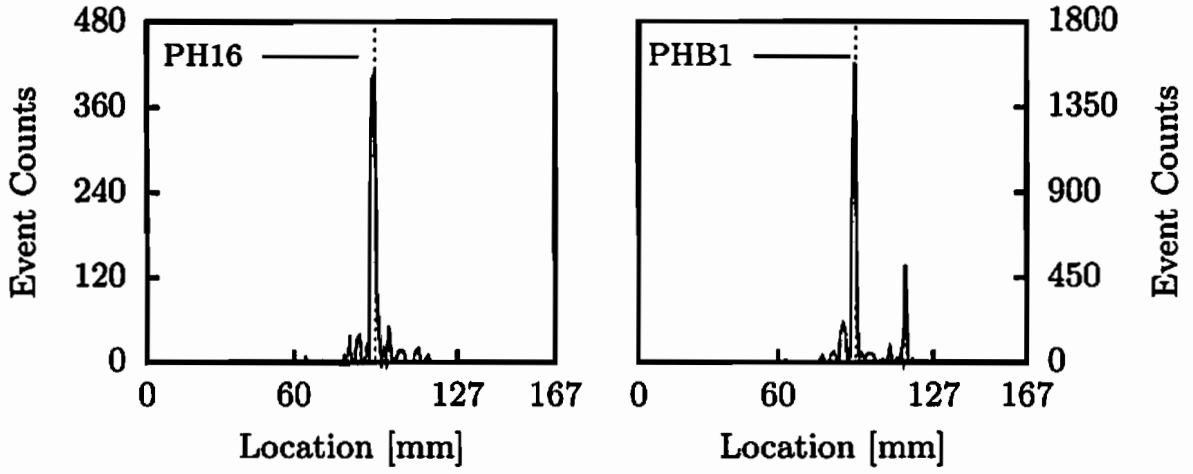

Figure 6.11: Location of the acoustic emission origin

ment with the real position of the fatigue damage. Most events are located at the position where the crack is present, confirming that the acoustic emission is from the crack. As a consequence of the specimen size, there are inherent problems with the determination of the location due to the size of the acoustic emission transducers compared to their spacing. Namely, the spacing between transducers 2 and 3 in the case of the plain specimen is 67 mm and the diameter of transducers is 17 mm, which excludes the point representation of acoustic emission transducers. For this reason, signals which are located within 5 mm of the real crack position are regarded as well located.

After the elimination of all signals which do not originate from the damage evolution using the conditions introduced above, acoustic emission is represented based on acoustic emission event counts per cycle and cumulative acoustic emis-

sion event counts during the service life. In contrast to other methods for the detection of the damage evolution, acoustic emission is based directly on the damage process, and therefore a steady development of the acoustic emission is to be expected during the whole damage process. As stated before, the load is in the range which leads to the high cycle fatigue with the brittle damage for all experiments. This type of load and the brittle damage behaviour lead to the significant increase in the acoustic emission output, as the crack advances towards the final failure.

The rate of the acoustic emission in the form of acoustic emission event counts per cycle over the service life is plotted in Figure 6.12. The figure shows the existence of acoustic emission during the whole damage process. The development of the acoustic emission can be divided in three phases (see Fang & Berkovits 1994, Heiderich 2004). When the load is in the elastic range, the low acoustic emission output is evident during initial cycles, due mostly to microscopic dislocation dynamics. This stage is followed by a period with almost no acoustic emission. In this stage of fatigue, damage accumulation results in the long crack-initiation lifetime. Low energy dislocation motion, which generates acoustic emission waves, is frequently under background noise and is relatively hard to detect. Only discrete acoustic emission event counts represent the existence of acoustic emission and consequential evolution of fatigue damage on the microscale level through the microcrack incubation and initiation. The macrocrack initiation and propagation, which is in connection with the high rate of the acoustic emission, occurs in the third stage. The release of the elastic energy due to the macrocrack propagation has a significant level and the detection of the acoustic emission is not influenced by the background noise as in the second stage of fatigue.

The evolution of cumulative acoustic emission event counts during fatigue damage is presented in Figure 6.13 for constant amplitude experiments and in Figure 6.14 for block experiments and represents the cumulative fatigue damage process. This process can be divided into the same three stages as indicated for the rate of the acoustic emission: (i) microscopic dislocation dynamics; (ii) microcrack incubation and initiation; (iii) macrocrack initiation and propagation. For the sake of better representation of the cumulative acoustic emission evolution, specially for the microscopic dislocation dynamics and microcrack incubation and initiation stages, the ordinate in the corresponding figures is given in the logarithmic scale.

In both types of representations (Figures 6.12÷6.14), the step-growth evolution of cumulative acoustic emission event counts during fatigue damage, which indicates a discontinuous damage evolution, is evident. This kind of progression of the acoustic emission finds confirmation in a number of publications about the acoustic emission activity during cyclic loading (Fang & Berkovits 1995, Huang et al. 1998, Heiderich 2004).

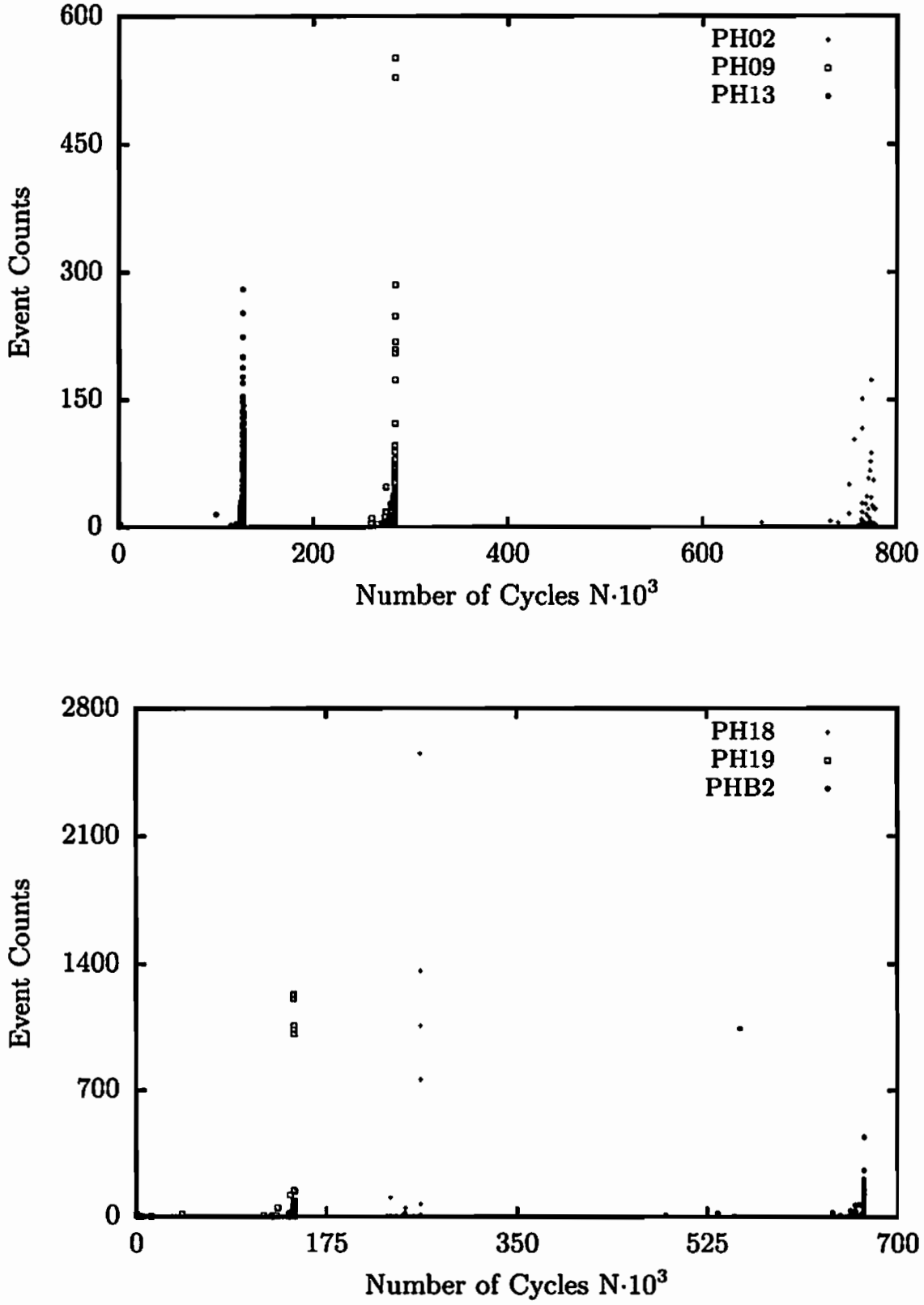

Figure 6.12: Rate of the acoustic emission event counts

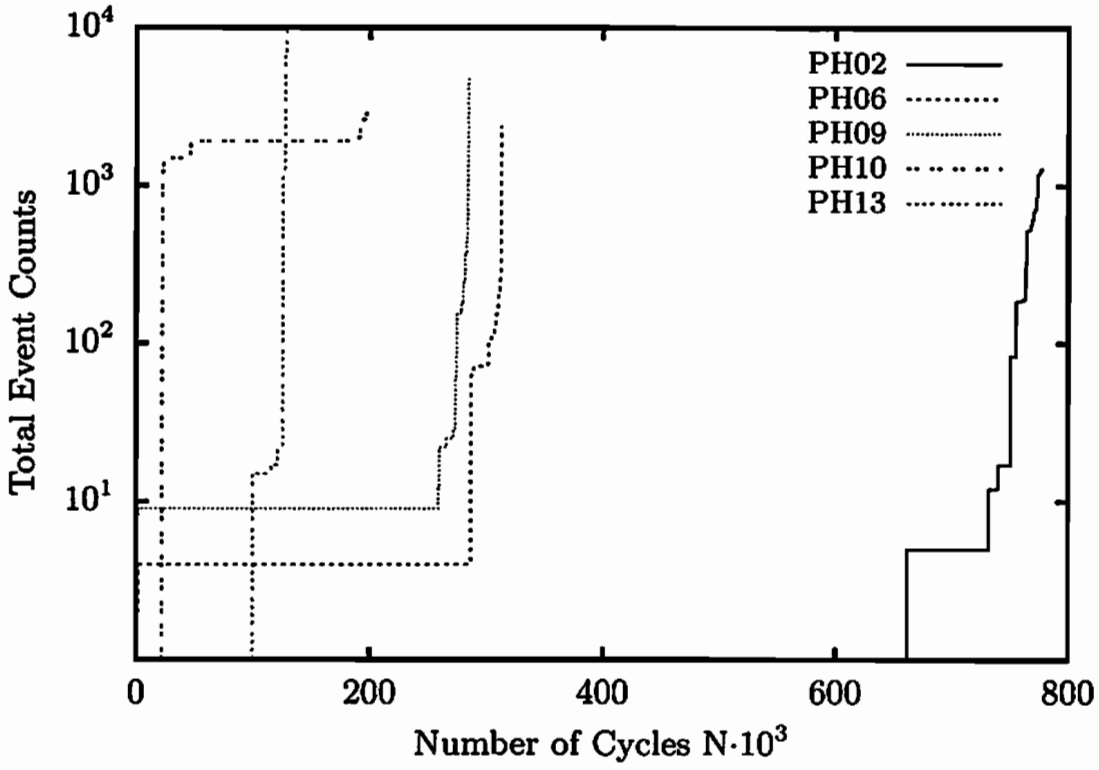

(a) Stress ratio $R=0.05$

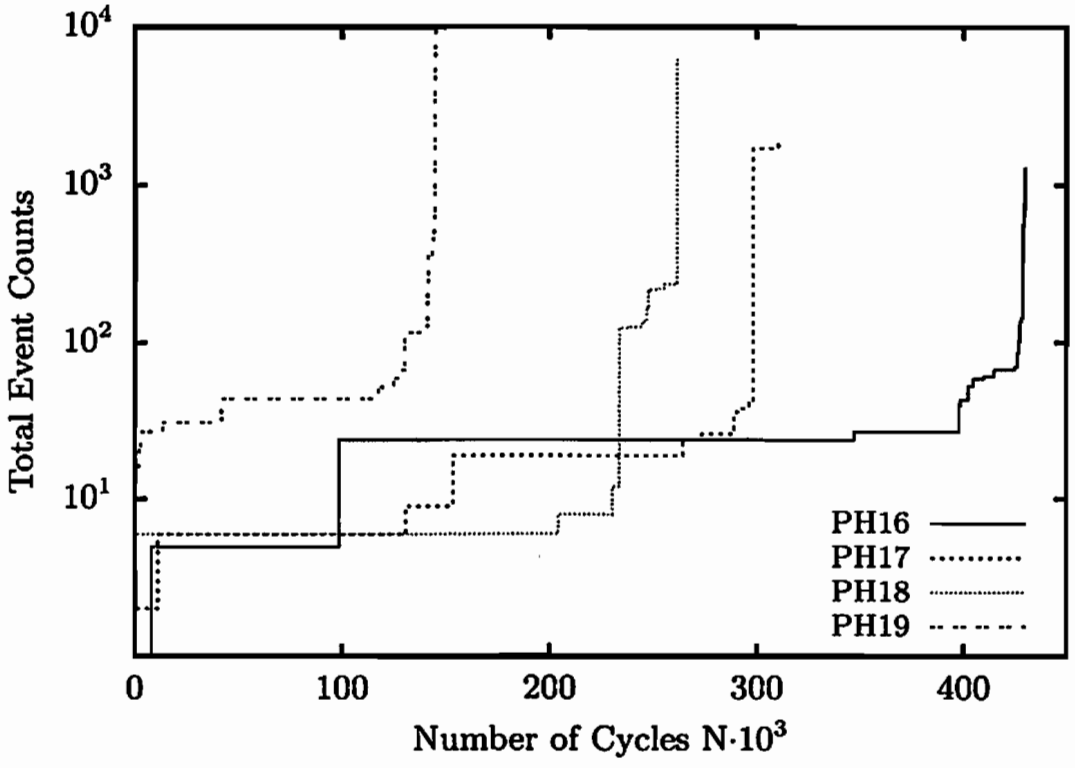

(b) Stress ratio $R=0.25$

Figure 6.13: Evolution of the acoustic emission event counts

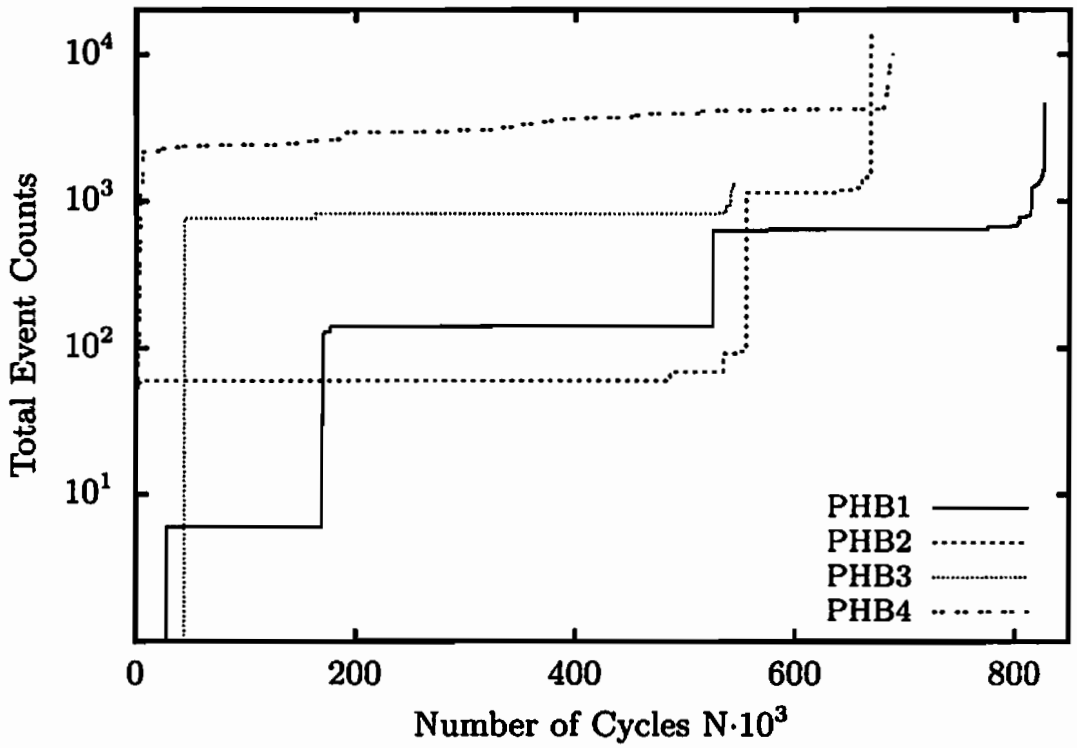

Figure 6.14: Evolution of the acoustic emission event counts

6.3.1.3 Evolution of the electrical resistance

The evolution of the normalised electrical resistance in the damaged area of the plain specimen with a hole is visualised in Figures 6.15 and 6.16. In both figures, the ordinate of all diagrams is given in logarithmic scale. The results for the displacement and force controlled single block constant amplitude load are represented in Figure 6.15, and for the displacement controlled block program experiments in Figure 6.16.

As can be seen in Figure 6.15, the evolution of the electrical resistance has a similar behaviour as the evolution of the specimen stiffness. After a stabilisation during the first couple of load cycles, the electrical resistance is constant over a long time of the service life. To the end of the service life, an exponential growth of the electrical resistance is to be observed. Depending on the level of the cyclic load amplitude, an exponential evolution of the electrical resistance occurs between 60% and 80% of the service life.

Figure 6.16, in which results of the block experiments are represented, shows that the normalised electrical resistance is not constant between the blocks. Although one value of the electrical resistance represents an average value of electrical resistance over 9 loading cycles in the case of the plain specimen, the influence of the different load amplitude levels between the blocks on the electrical resistance can be seen clearly.

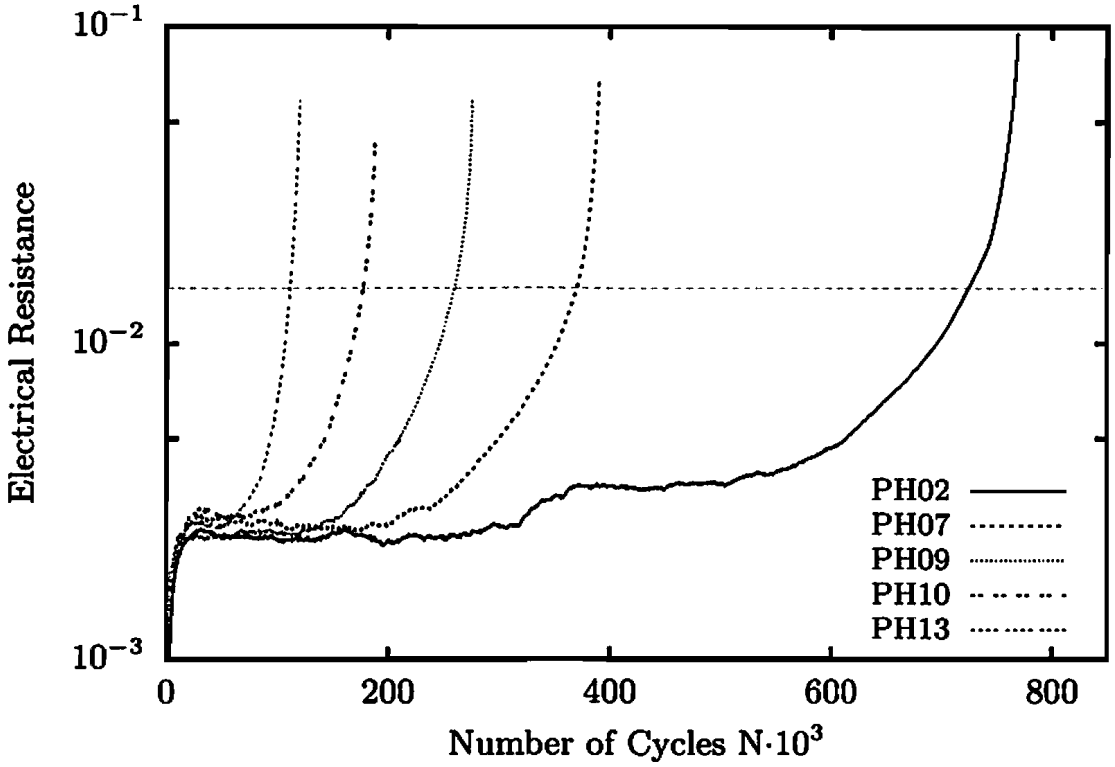

(a) Stress ratio $R=0.05$

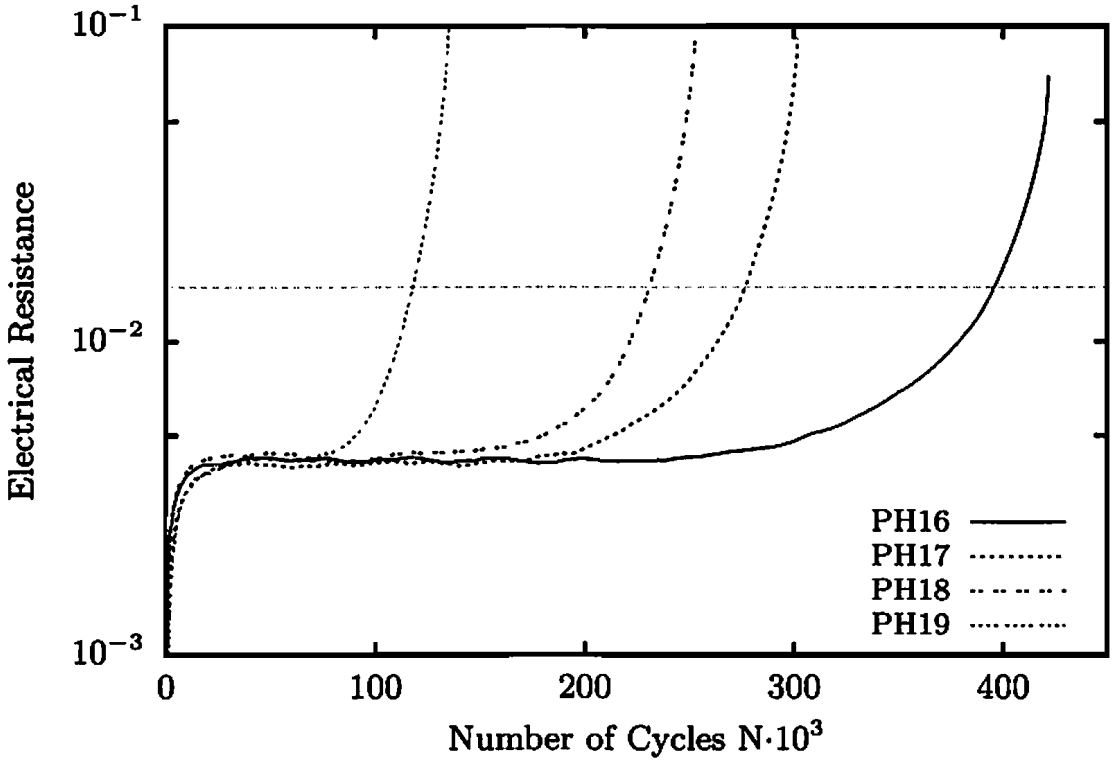

(b) Stress ratio $R=0.25$

Figure 6.15: Evolution of the normalised electrical resistance

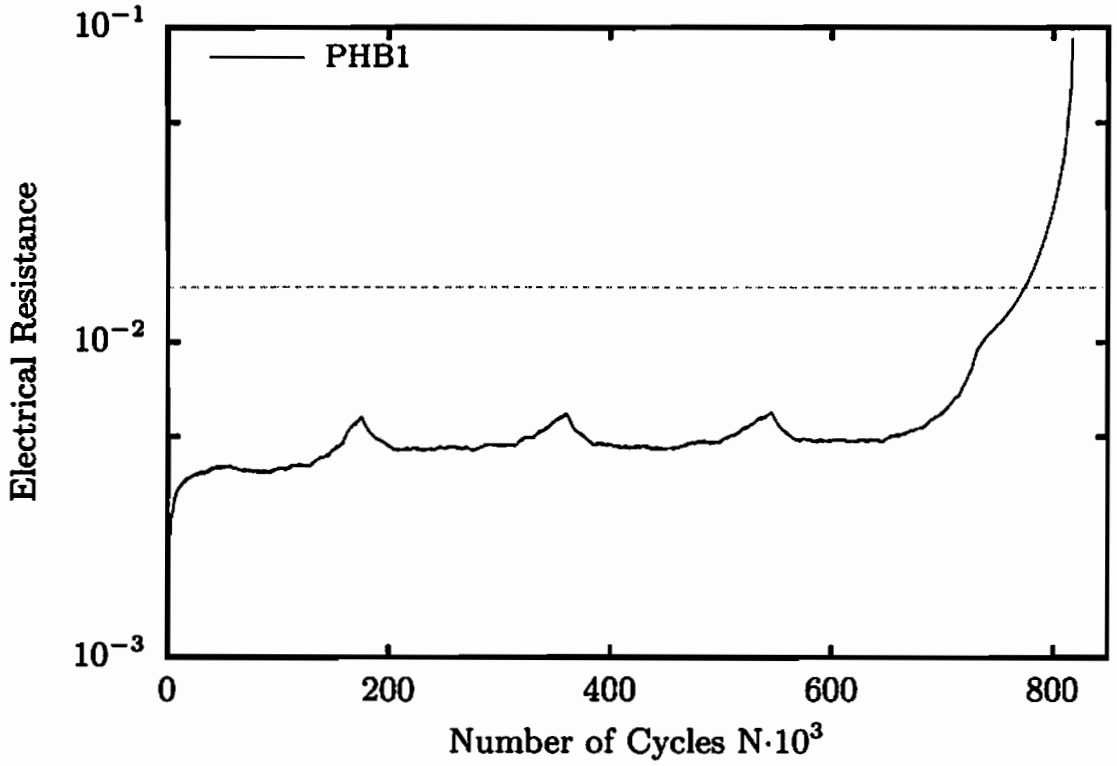

(a) LH block experiment

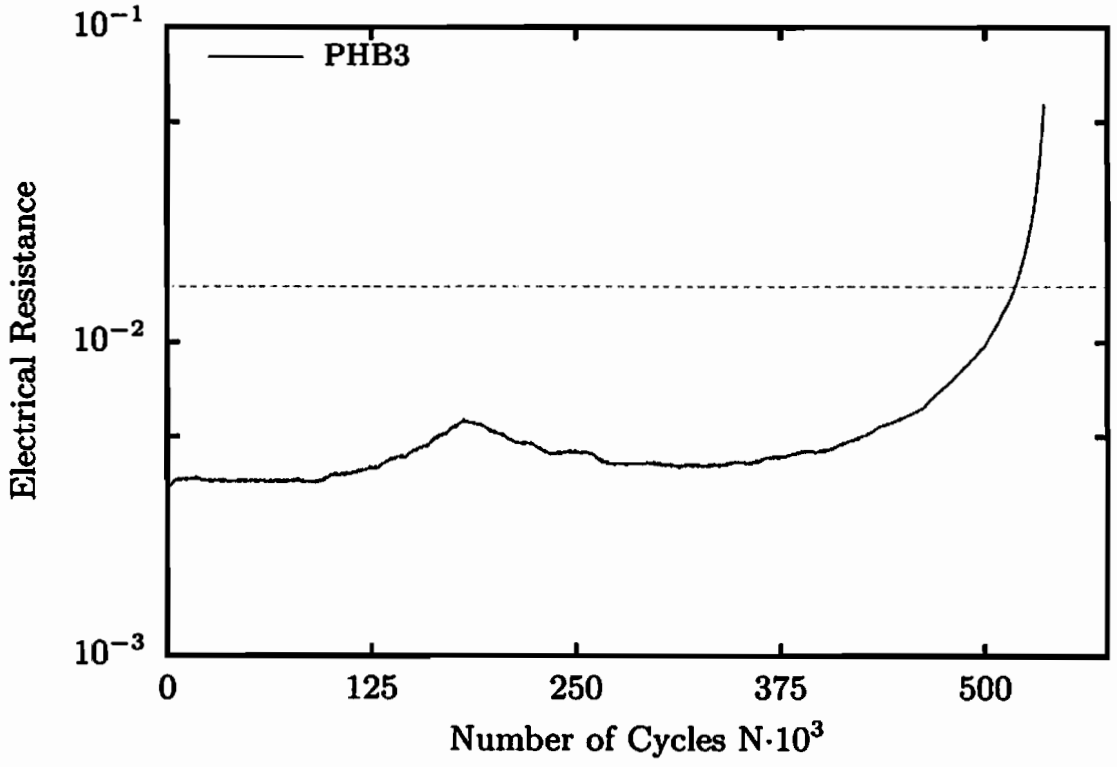

(b) LHL block experiment

Figure 6.16: Evolution of the normalised electrical resistance

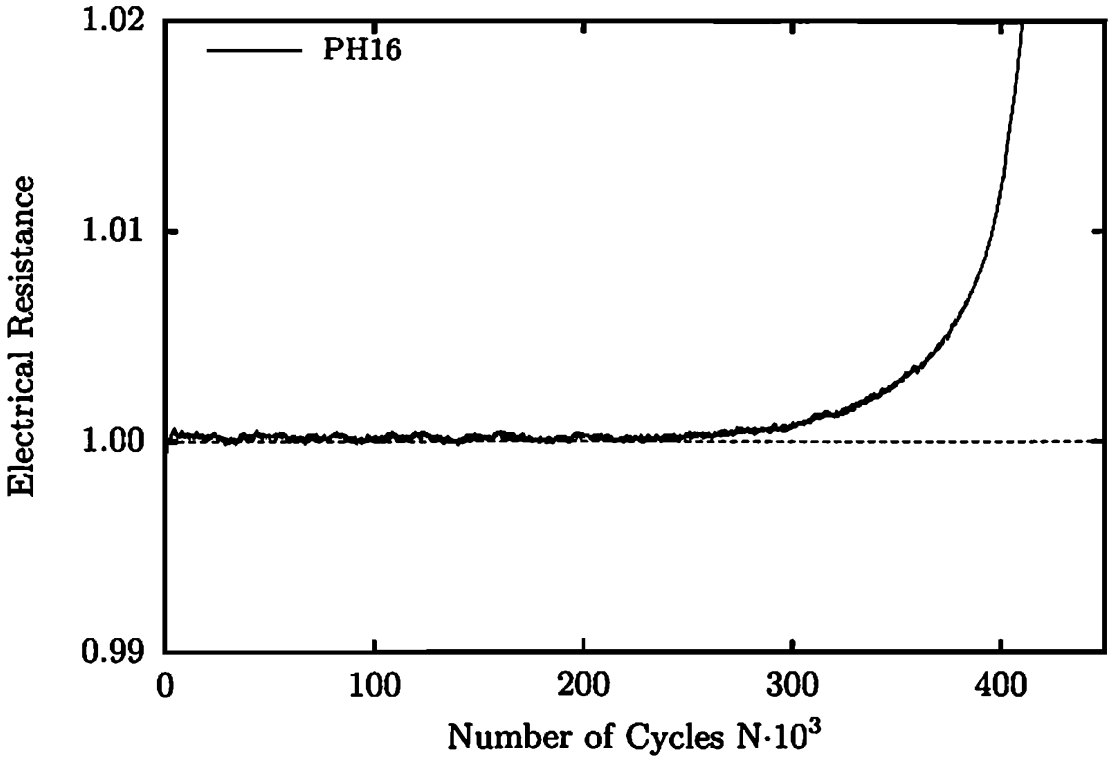

(a) Specimen - PH16

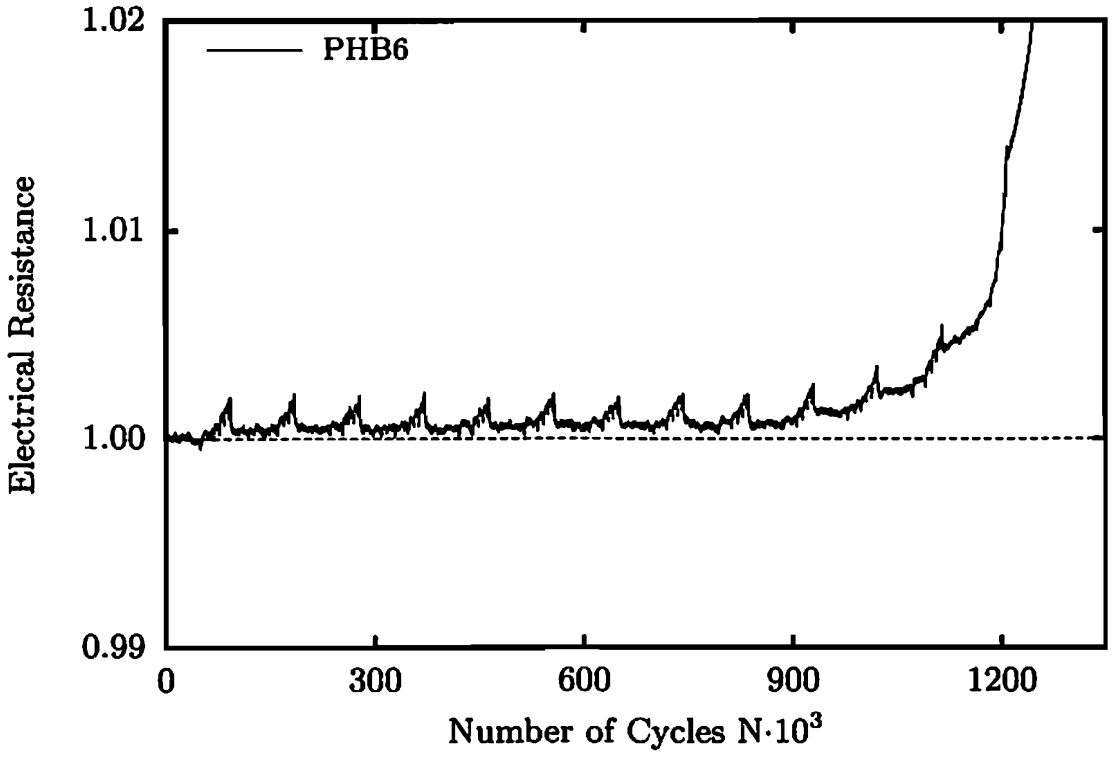

(b) Specimen - PHB6

Figure 6.17: Evolution of the normalised electrical resistance - enlarged representation

The horizontal line, which is placed at 0.015 on the ordinate, represents the change of the electrical resistance at the moment when it is possible to observe the macrocrack initiation at the specimen surface.
In order to get a better overlook of the electrical resistance evolution, it is given in the enlarged representation in Figure 6.17.
In case of the specimen PH16 in Figure 6.17a, it is possible to see that the electrical resistance begins to grow after 50% of the service life. The increase in the electrical resistance has an almost linear behaviour in the first phase. As the damage grows, it accelerates and close to the final failure it develops the characteristic exponential behaviour. If this evolution of the electrical resistance is compared with the evolution of the specimen stiffness plotted in Figure 6.7, it is evident that the electrical resistance indicates changes in the microstructure of the specimen significantly earlier. It can be concluded that the method of the electrical resistance measurement is in the position to detect the damage evolution in the early phase of the service life and it enables the formulation of the damage evolution on the basis of the microcrack growth.
The enlarged representation of the electrical resistance evolution for the block experiment is depicted in Figure 6.17b. Although the electrical resistance differs between the blocks, the begin of the increase of the electrical resistance can be observed at about 70% of the service life, in the moment when the macrocrack cannot be identified on the specimen surface. The waiting periods between blocks when the load is set to the given starting value are indicated in the diagram by repeating sequences of vertical drops in electrical resistance. They represent the influence of the load on the electrical resistance, which needs to be taken into account in the correction of the electrical resistance for unloaded and loaded specimen.

6.3.2 Plain specimen with both side notches

As in the case of the plain specimen with a hole, the experiments on the plain specimen with the reduced cross section area with both side notches of 0.2 mm depth are performed with both single block and multiple blocks loading. The experiments with the constant amplitude haversine loading during the whole service life are displacement controlled for the stress ratio $R = 0.05$ and force controlled for the stress ratio $R = 0.25$. The outlook of conducted experiments is given in Table 6.7.
The experiments with block load amplitudes are constructed based on the schemas presented in Figure 6.4, as in the case of plain specimen with a hole. However, one block sequence consists in this case of four instead of six load blocks. Load amplitudes and the duration of single blocks are given in Table 6.8. It is assumed that each block contributes with 5% damage. Hence, by using Palmgren-Miner damage rule five block sequences are necessary for the final failure. The loading is displacement controlled and stress ratio is set to 0.05 in all block experiments.

Spec.	Load control	Stress ratio	Amplitude [mm]/[kN]	$\sigma_{a,nom}$ MPa	Fatigue life Load cycles
PN01	Displ.	0.05	0.210	326	1693440
PN02	Displ.	0.05	0.210	334	1635300
PN03	Displ.	0.05	0.215	352	467396
PN04	Displ.	0.05	0.215	351	248526
PN05	Displ.	0.05	0.220	356	1104849
PN06	Displ.	0.05	0.220	348	745119
PN07	Displ.	0.05	0.225	361	191637
PN08	Displ.	0.05	0.230	360	208242
PN09	Displ.	0.05	0.230	354	169740
PN10	Displ.	0.05	0.240	389	81090
PN11	Displ.	0.05	0.240	394	73836
PN12	Displ.	0.05	0.250	378	158940
PN13	Force	0.25	13.125	288	>3000000
PN14	Force	0.25	13.500	301	302616
PN15	Force	0.25	14.250	309	254493
PN16	Force	0.25	15.000	335	97182
PN17	Force	0.25	15.750	346	73701

Table 6.7: Experiments on the plain specimen with both side notches

The block program experiments are summarised in Table 6.9. As in the case of the plain specimen with a hole, it is evident from the results of different block experiments that Palmgren-Miner damage rule is not always conservative. In the case of the plain specimen with both side notches, the damage measure D for the block experiments is calculated between 0.388 and 2.397.

6.3.2.1 Evolution of the global specimen stiffness

As in the case of the plain specimen with a hole, the global specimen stiffness evolution for the plain specimen with both side notches is calculated using the procedure described in Section 6.2.1. Evolutions of specimen stiffness for the displacement controlled loading with the stress ratio 0.05 and for the force controlled loading with the stress ratio 0.25 are plotted in Figure 6.18. After the stabilisation of the normalised specimen stiffness during the beginning period of the service life, the specimen stiffness shows an almost constant behaviour over a long time of the service life. The difference between minimum and maximum value of the specimen stiffness in this period is less than 1%. Depending on

Block	Displ. [mm]	Load cycles
1	0.200	80000
2	0.208	45000
3	0.216	12000
4	0.224	7500

Table 6.8: Load amplitude and number of cycles for single blocks

Spec.	Load control	Stress ratio	Block program	Fatigue life Load cycles
PNB1	Displ.	0.05	LH	359247
PNB2	Displ.	0.05	HL	280512
PNB3	Displ.	0.05	LHL	514368
PNB4	Displ.	0.05	HLH	1731686
PNB5	Displ.	0.05	LH	1673235
PNB6	Displ.	0.05	HL	968389

Table 6.9: Block program experiments on the plain specimen with both side notches

the loading amplitude level, it is possible to observe a decrease in the specimen stiffness after 80 to 90% of the fatigue life. In the last phase of the service life, its decrease has an exponential behaviour and leads to the final failure of the specimen. This exponential decrease of the specimen stiffness for the plain specimen with both side notches occurs in the short time period compared to the whole service life of specimen. The complete evolution of the specimen stiffness is in accordance with the evolution of the specimen stiffness observed for the plain specimen with a hole.

The evolution of the normalised specimen stiffness for two specimens under high-low and low-high-low block program sequences is shown in Figure 6.19. In contrast to the results for the plain specimen with a hole, the deviations of the normalised specimen stiffness between the loading blocks are not distinct. The reason for this is a relatively small difference between the load amplitudes compared to the difference between the load amplitudes for the plain specimen with a hole. The evolution of the specimen stiffness shows a stabilised behaviour over a 90% of the service life, followed by an exponential decrease of the specimen stiffness, which leads to the final failure of the specimen.

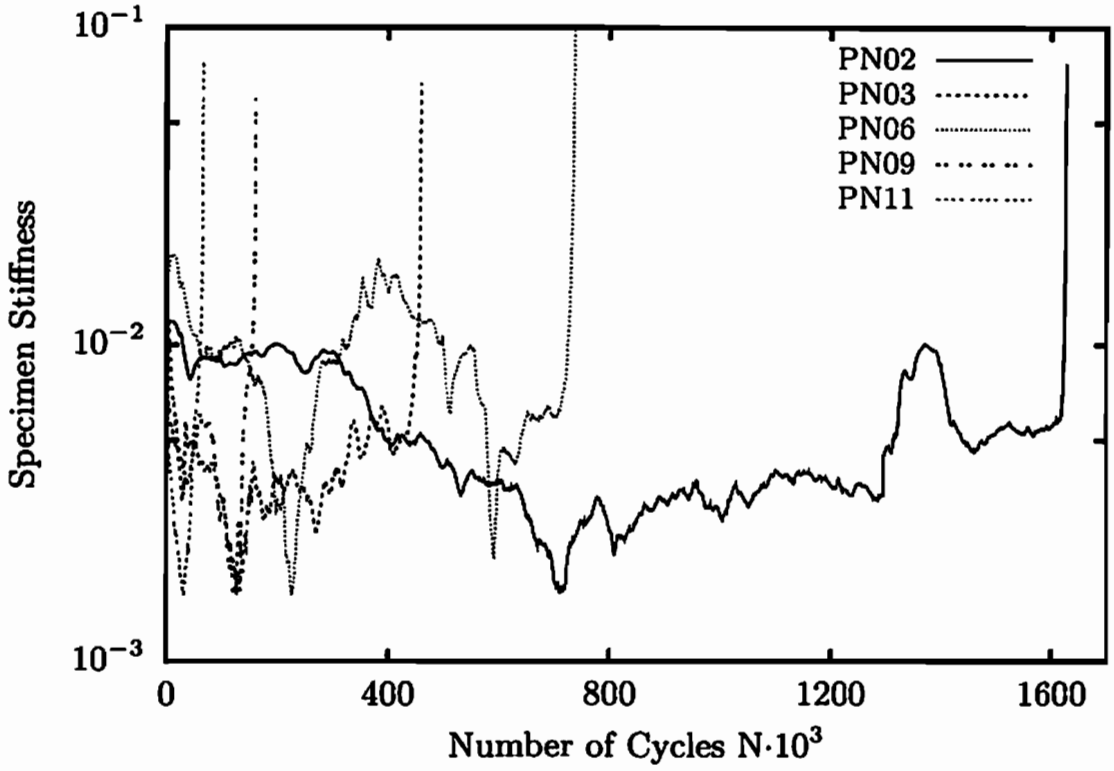

(a) Stress ratio $R=0.05$

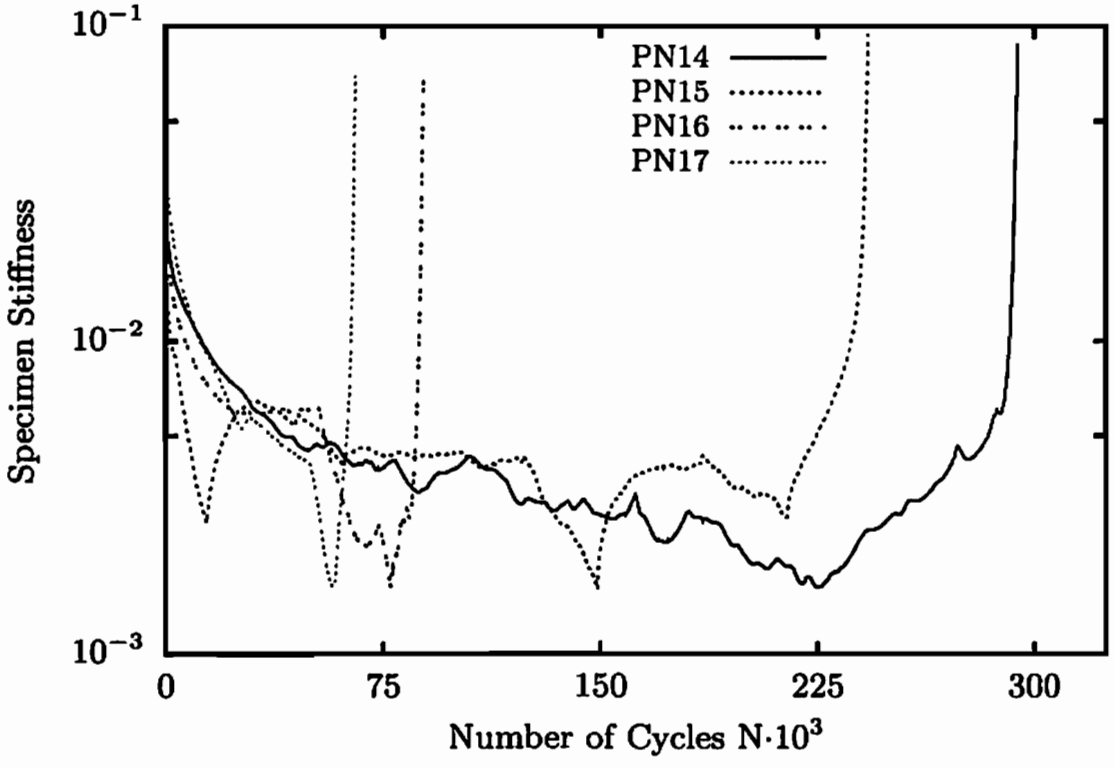

(b) Stress ratio $R=0.25$

Figure 6.18: Evolution of the normalised specimen stiffness

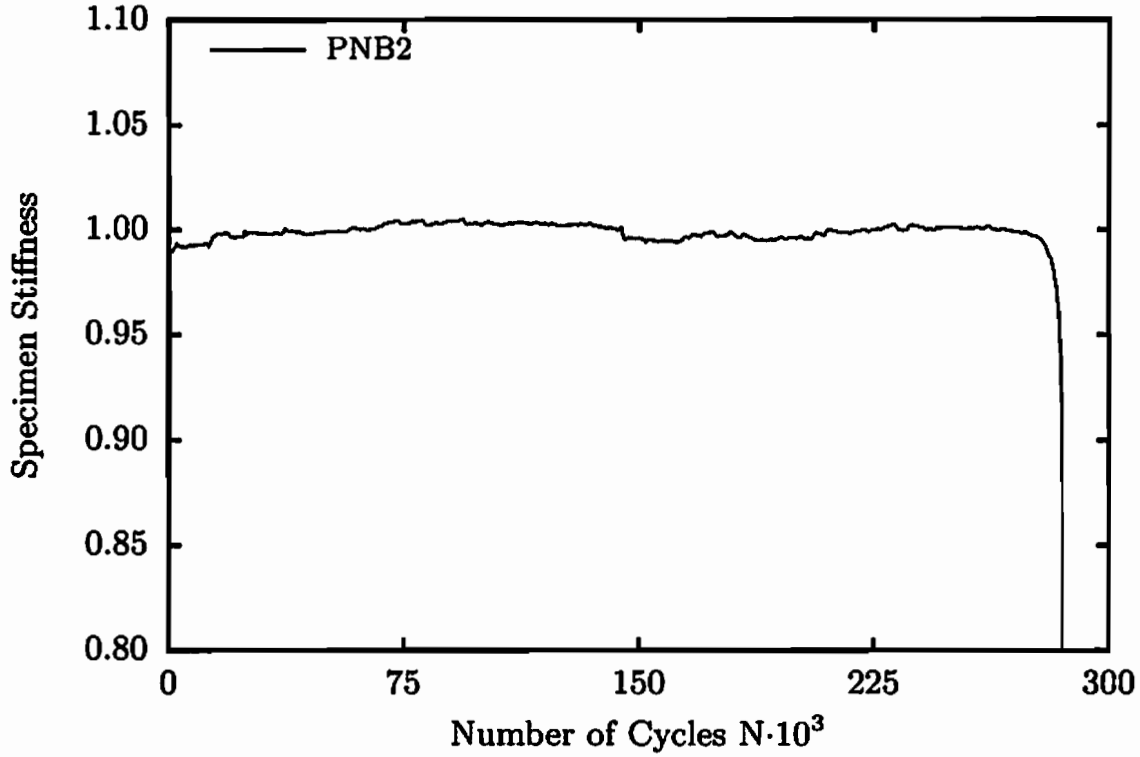

(a) HL block experiment

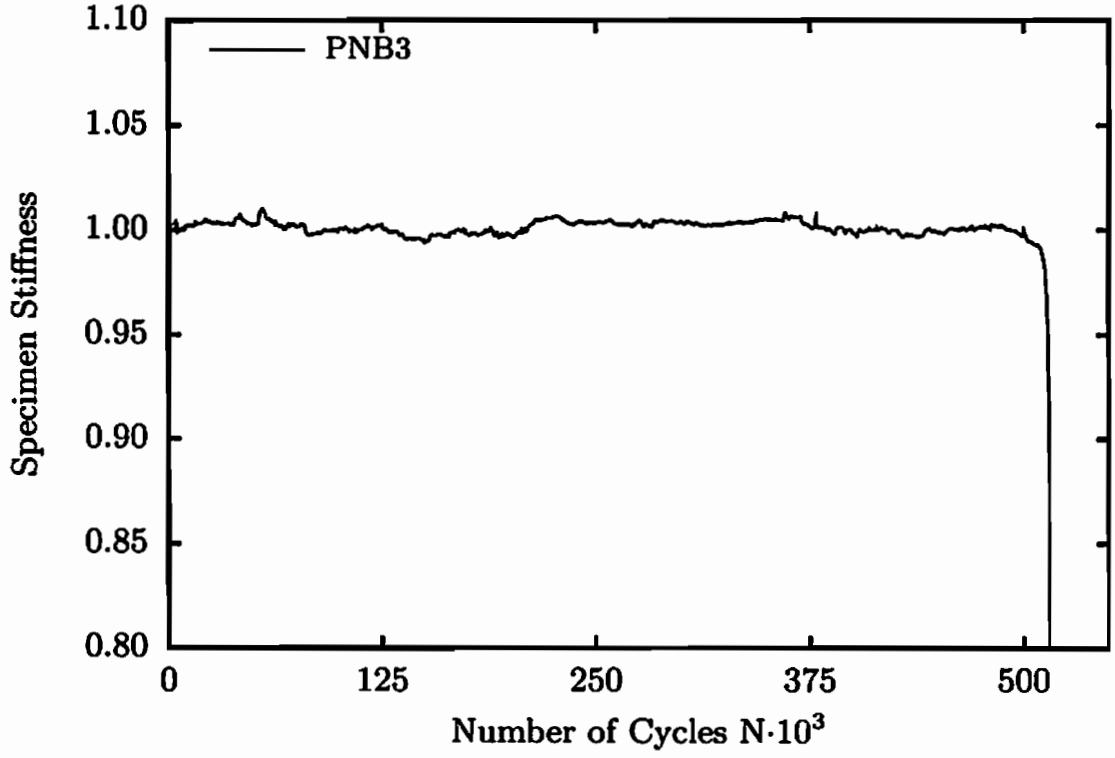

(b) LHL block experiment

Figure 6.19: Evolution of the normalised specimen stiffness

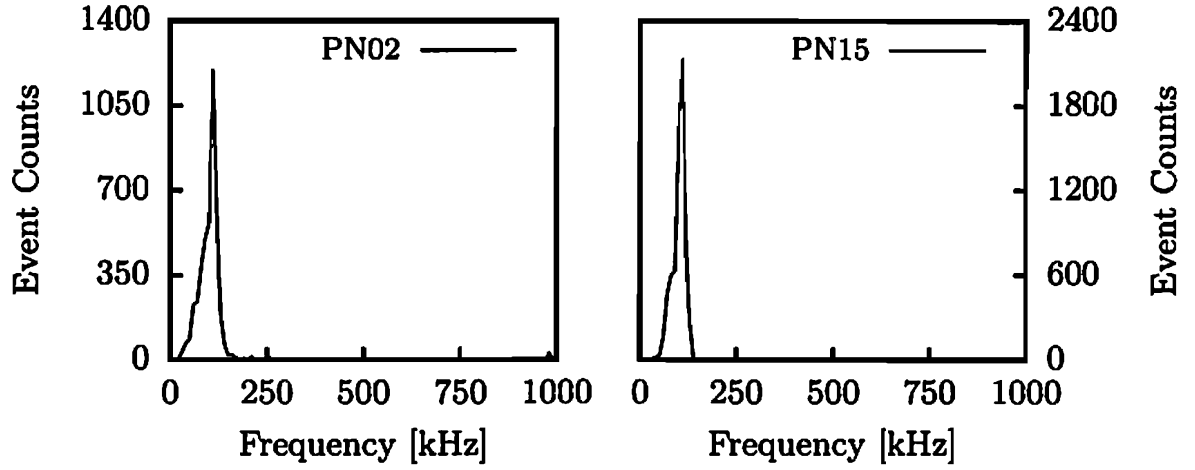

Figure 6.20: Acoustic emission event counts versus frequency

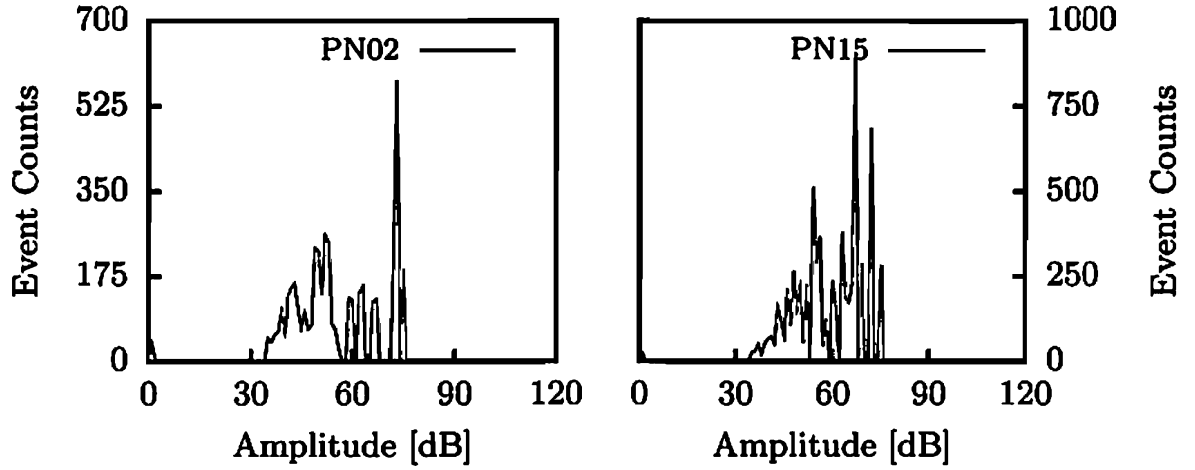

Figure 6.21: Acoustic emission event counts versus amplitude

6.3.2.2 Evolution of the acoustic emission

Two sets of acoustic emission transducers are used in the experiments on plain specimens with both side notches, as in the case of the experiments on the plain specimen with a hole. The wideband transducers are utilised in the displacement controlled experiments with the stress ratio 0.05 and a constant load amplitude during the service life (specimens PN01 to PN11). A typical frequency response for this type of acoustic emission transducers is visualised in Figure 6.20 for specimen PN02. It is evident that most of the event counts exhibit a frequency between 80 and 200 kHz. Based on this finding, the wideband transducers are replaced by the resonance acoustic emission transducers with a resonant frequency of 150 kHz in additional experiments on the plain specimen with both side notches. A typical result for the frequency response of the second set of

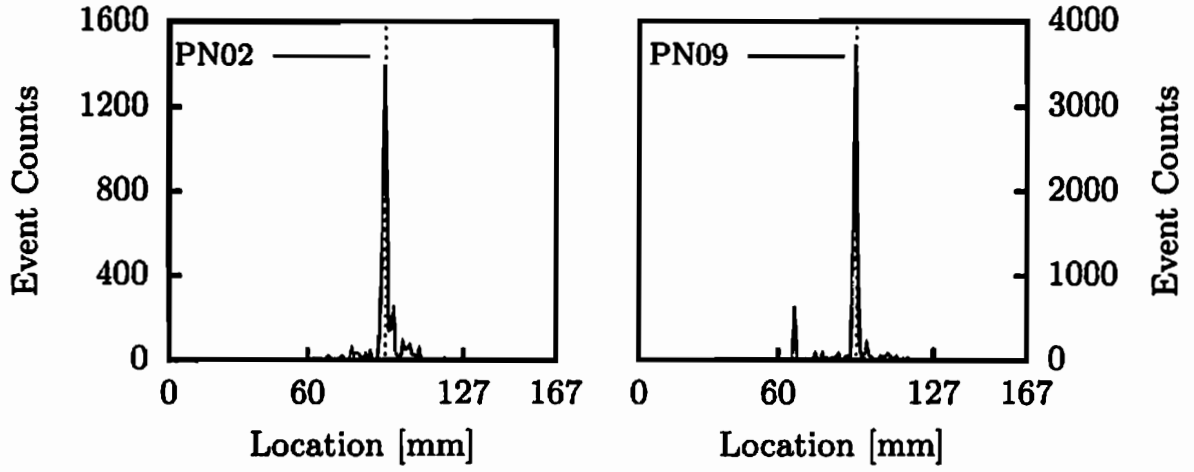

Figure 6.22: Location of the acoustic emission origin

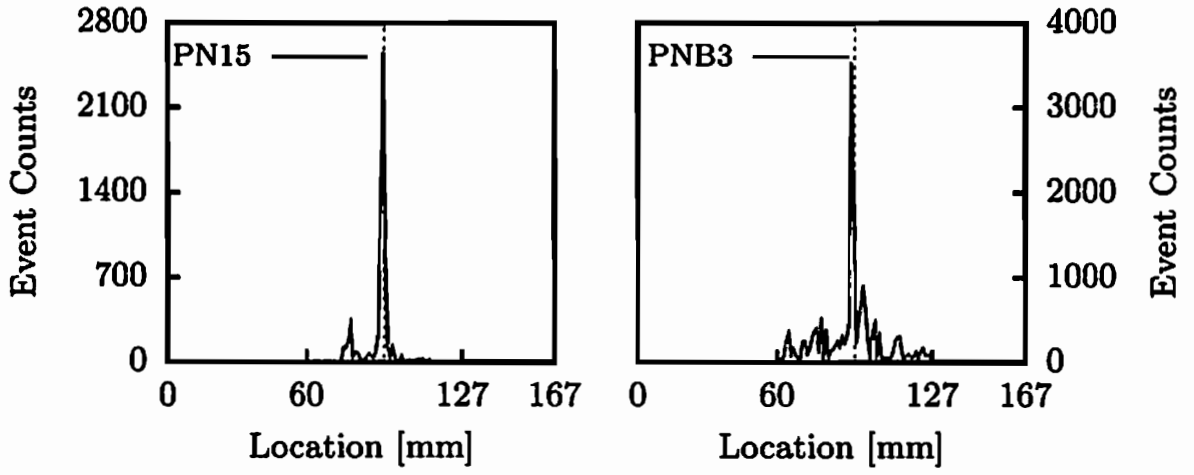

Figure 6.23: Location of the acoustic emission origin

transducers is plotted for the specimen PN15 in Figure 6.20. It is clear from both plots that the acoustic emission from the damage evolution occurs within the frequency range between 50 and 200 kHz.

The dependence between acoustic emission event counts and the amplitude for both sets of acoustic emission transducers is shown in Figure 6.21. As in the case of plain specimen with a hole, it may be inferred that most of the acoustic emission event counts have an amplitude between 35 and 70 dB. This information as well as the force threshold value set to 5 kN are used as additional conditions in the elimination of the extraneous noise.

The location of the acoustic emission origin is computed using time difference measurement method introduced in Section 4.1.4.1. The results of the computation are presented in Figures 6.22 and 6.23 for different specimens. In the case

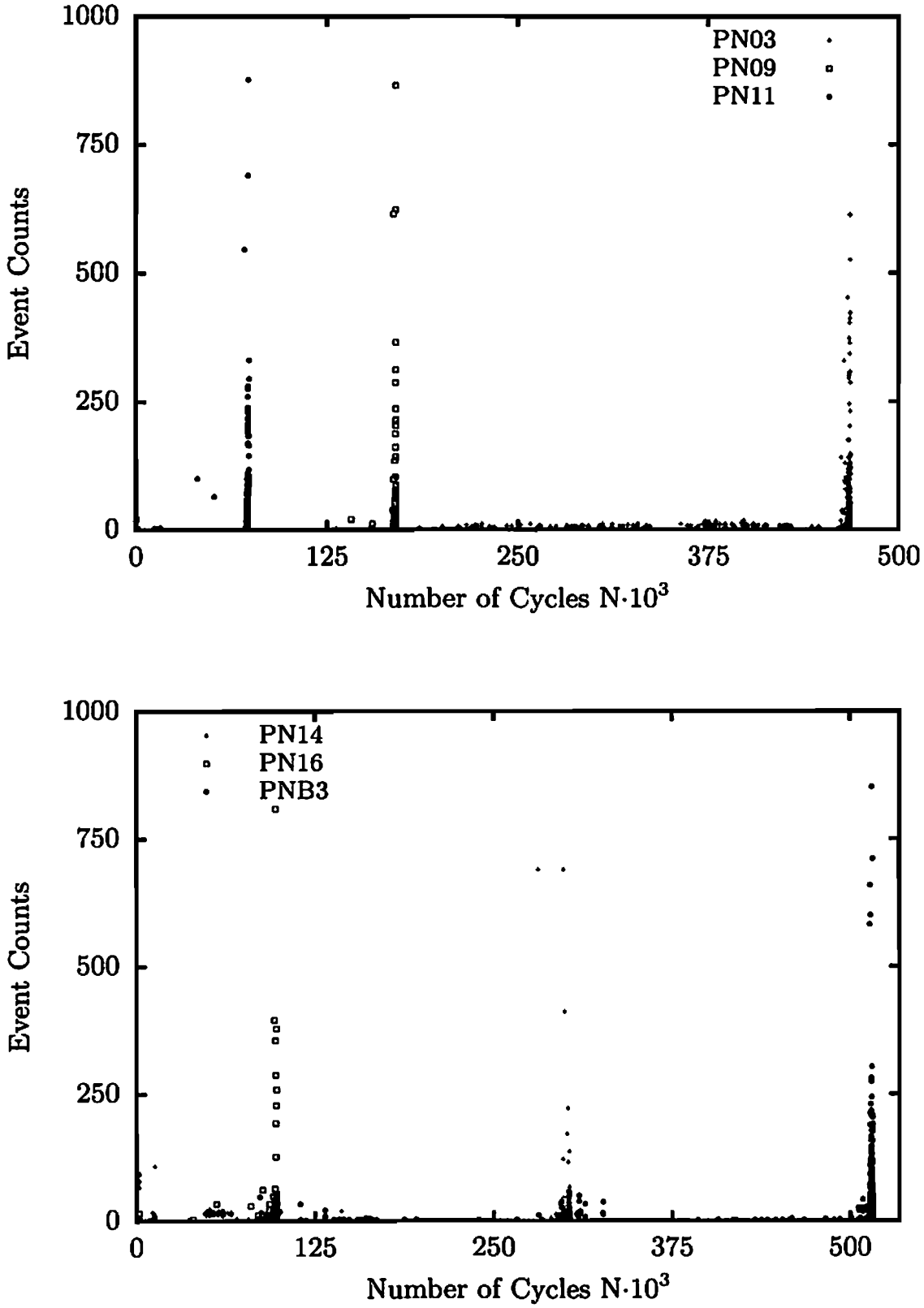

Figure 6.24: Rate of the acoustic emission event counts

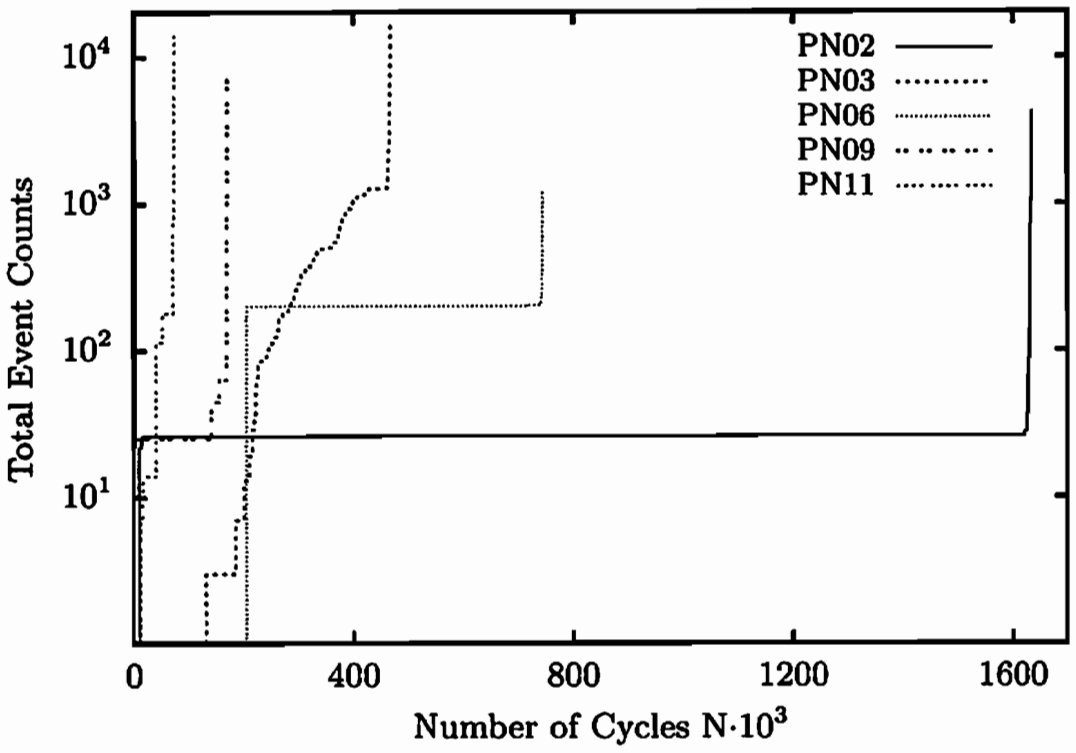

(a) Stress ratio $R=0.05$

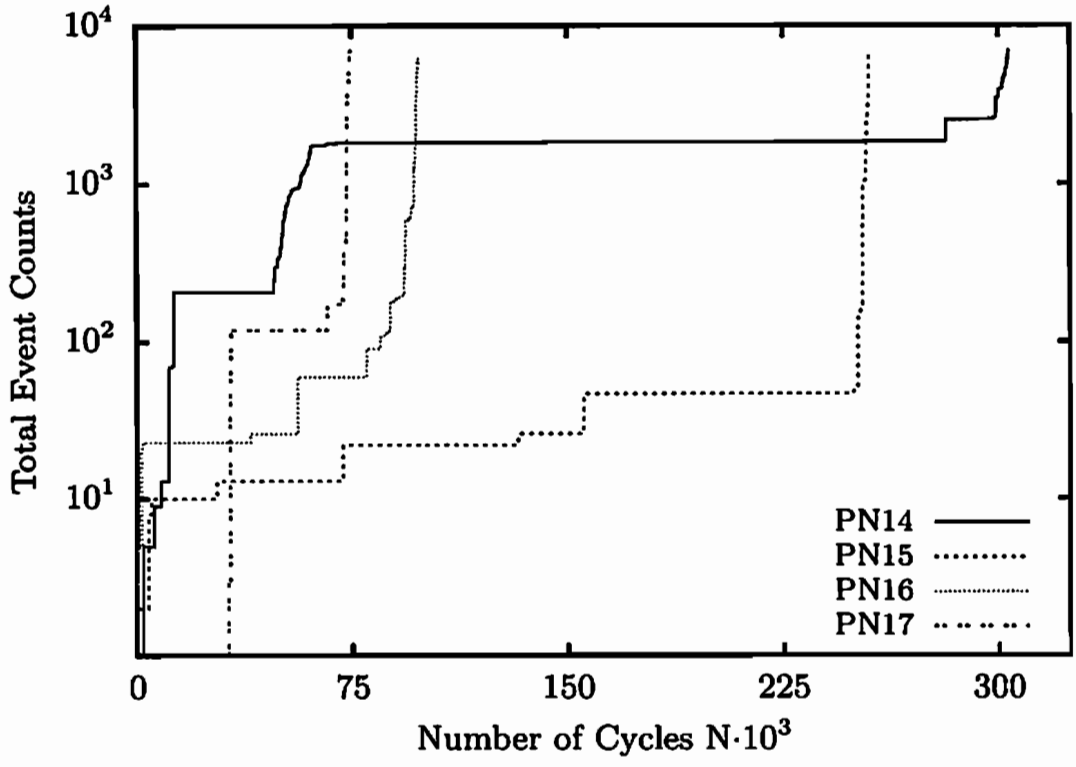

(b) Stress ratio $R=0.25$

Figure 6.25: Evolution of the acoustic emission event counts

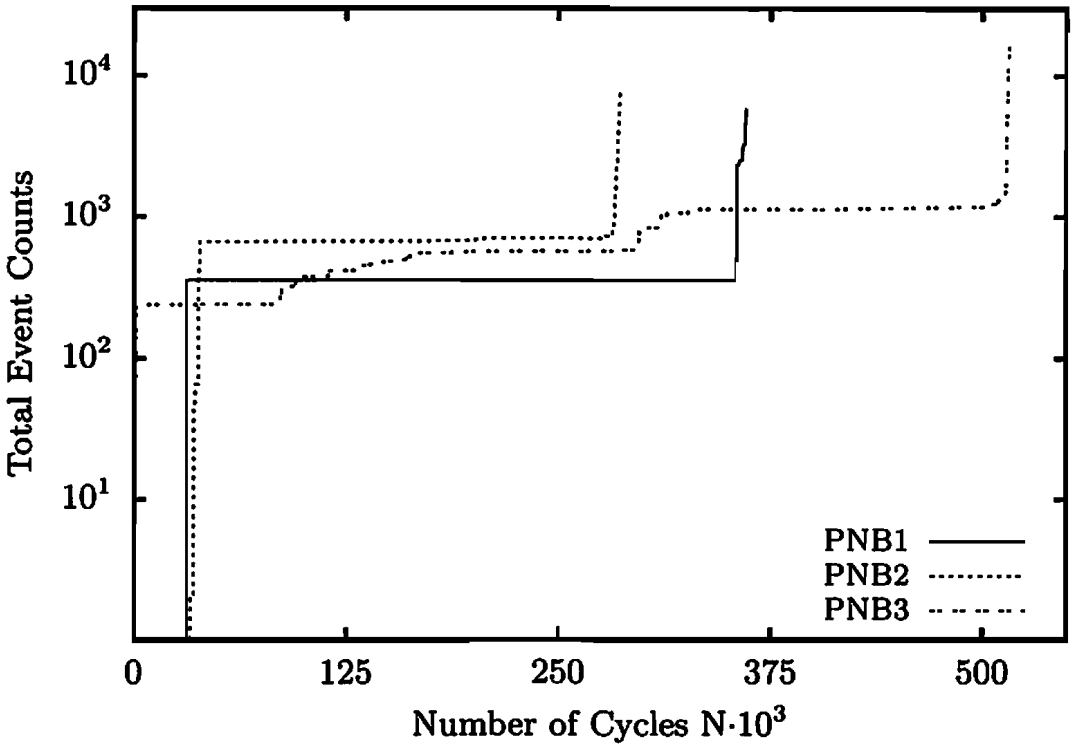

Figure 6.26: Evolution of the acoustic emission event counts

of specimens given in Figure 6.22, acoustic emission is recorded using wideband transducers, in contrast to the specimens shown in Figure 6.23, where acoustic emission is detected using resonance transducers. The computed location of the origin for both types of transducers is in good agreement with the real position of the fatigue damage. Most event counts originate from the position where the crack is present. In that manner, the determination of the origin of the acoustic emission is used as a main criterion in the elimination of the acoustic emission signals which do not originate from the damage evolution. Since all plain specimens have a unique geometry, problems in the determination of the damage location connected with the specimen size, distance between the acoustic emission transducers and their size, already discussed in Section 6.3.1.2, are present.

The evolution of the acoustic emission signals originating from the damage growth is represented using the rate of the acoustic emission and the evolution of cumulative event counts during the service life. The rate of the acoustic emission in the form of the acoustic emission events counts per cycle over the service life is plotted in Figure 6.24. The evolution of the cumulative acoustic emission event counts during fatigue damage represents the cumulative fatigue damage process. It is given in Figures 6.25 and 6.26.

The expected steady detection of the acoustic emission during the whole service life can be confirmed from the Figure 6.24. Namely, it is evident that the single

acoustic emission events exist not only at the end of the service life when the crack advances towards the final failure but also during the whole service life. They are rare in the second phase of the evolution and they are relatively hard to detect due to the low level of the released elastic energy which is frequently under background noise. As in the case of a plain specimen with a hole, the applied load and the brittle damage behaviour lead to the exponential increase in the acoustic emission output at the end of the service life.

6.3.2.3 Evolution of the electrical resistance

The electrical resistance in the damaged area of the specimen is normalised and its evolution is given in Figures 6.27 and 6.28. The results for the displacement controlled experiments with stress ratio 0.05 and for the force controlled experiments with stress ratio 0.25 are plotted in Figure 6.27. The evolution of the normalised electrical resistance for the block program experiments is depicted in Figure 6.28. The enlarged representation of the evolution of the normalised electrical resistance for two experiments is visualised in Figure 6.29.
The similarity between the evolution of the electrical resistance and the evolution of the specimen stiffness, addressed in Section 6.3.1.3, is evident in Figures 6.27, 6.28 and 6.29. After the stabilisation phase and the constant value evolution phase, the exponential growth occurs between 60% and 90% of the service life, depending on the load amplitude. Due to the small difference between the single load amplitude levels, the change of the normalised electrical resistance between blocks is visible (see the enlarged representation of the electrical resistance evolution for the block experiment in Figure 6.29b) but not significant (see Figure 6.28).
In order to show the experimental results in the case when the experiment is stopped and later continued, the result for the experiment on the specimen PN02 with a break after 1.3 million cycles is given in Figure 6.29a. After the experiment is continued, the measured data are recorded in new files. The diagram based on the gathered data shows that a break in the experiment does not influence the evolution of the electrical resistance.

6.3.3 Circular specimen

Depending on the load direction, the experiments on the circular specimen can be divided in two groups. The experiments with the constant loading direction during the service life belong to the first group. The second group includes the experiments with the loading applied in different directions, achieved by applying the rotation of the specimen around the axis perpendicular to the specimen surface. In all experiments the initial direction of the applied loading is the 0° direction of the electrical resistance (see Figure 5.14).
Experiments with constant amplitude loading and constant loading direction during the service life are summarised in Table 6.10. These experiments are per-

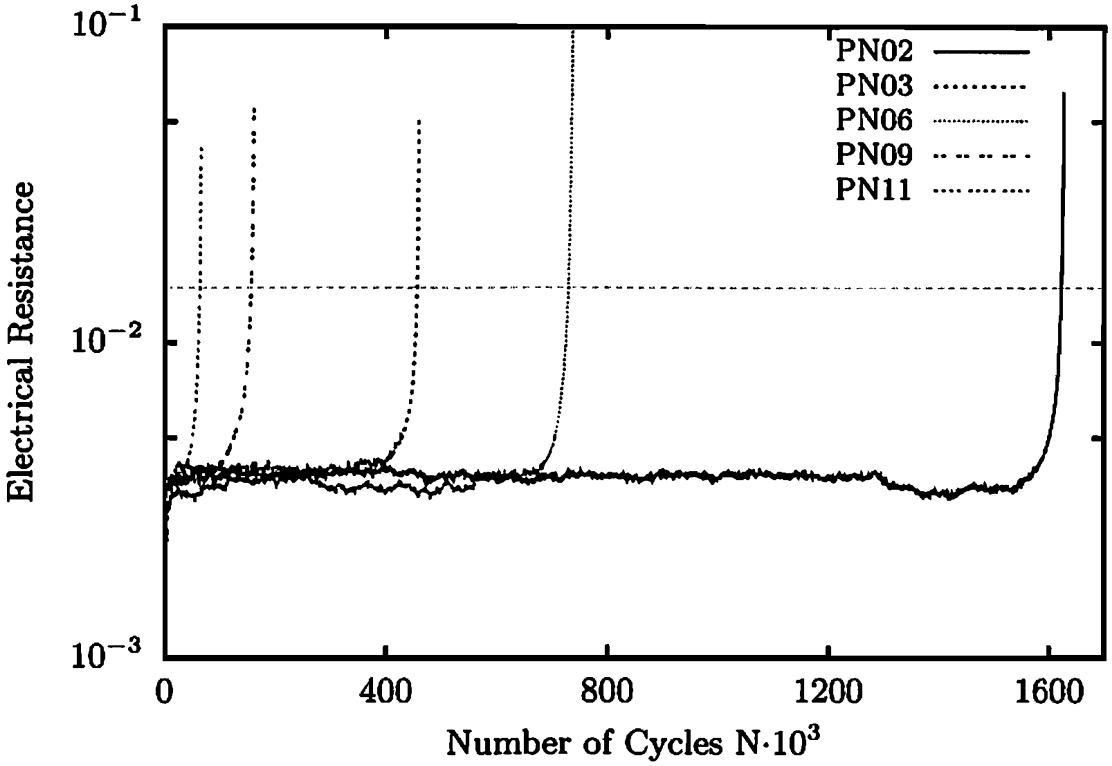

(a) Stress ratio R=0.05

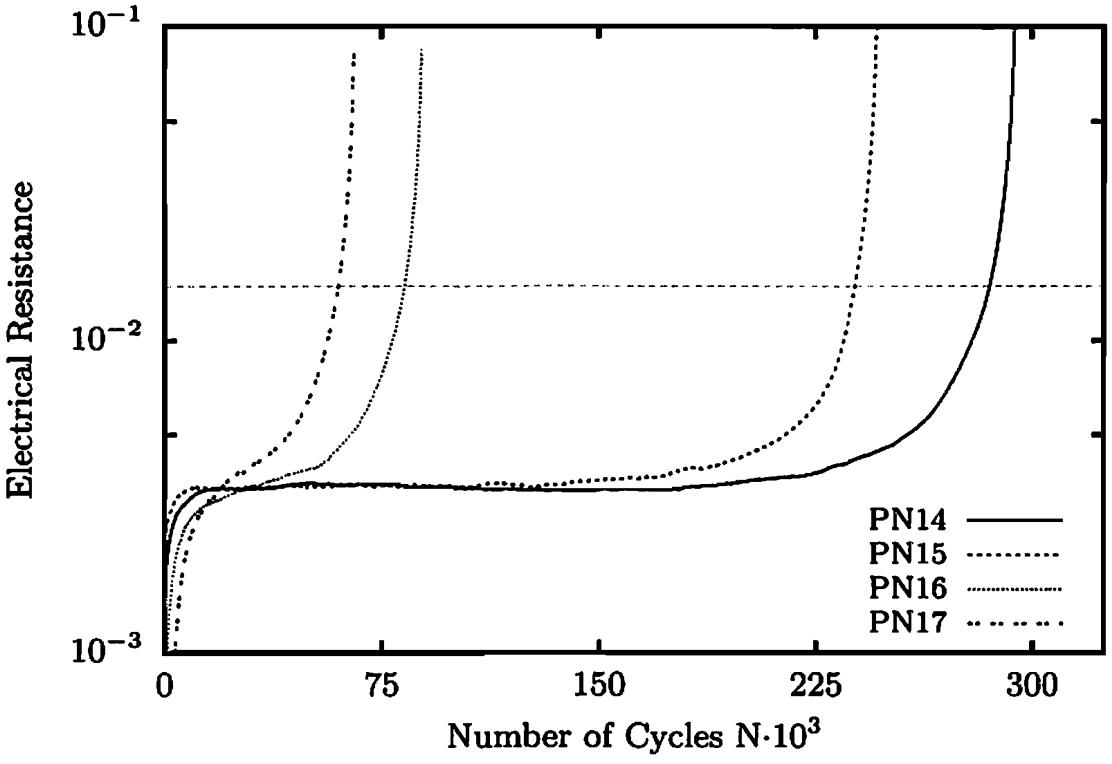

(b) Stress ratio R=0.25

Figure 6.27: Evolution of the normalised electrical resistance

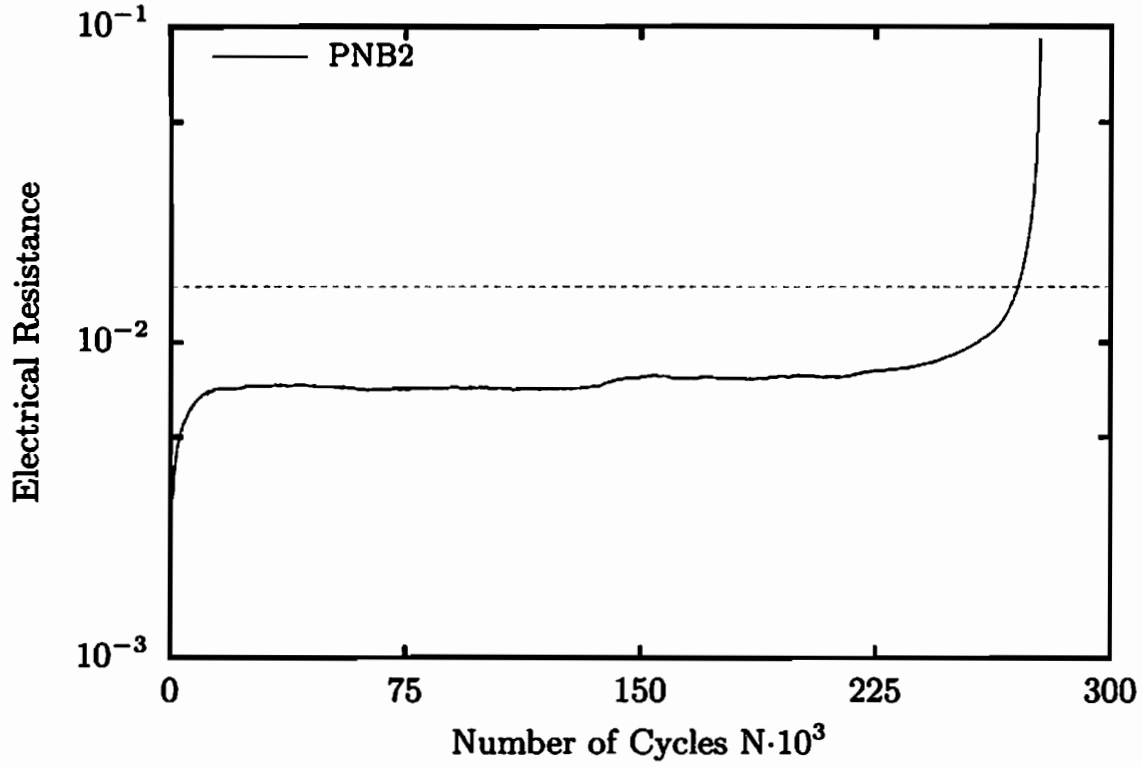

(a) HL block experiment

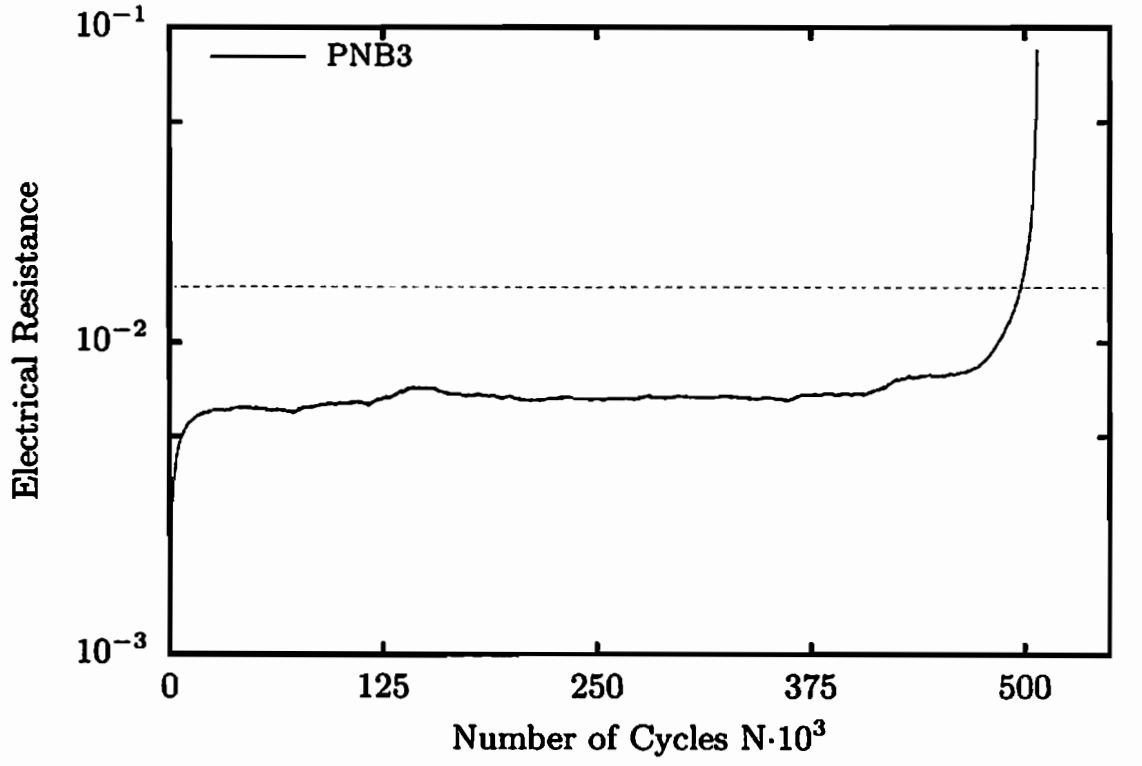

(b) LHL block experiment

Figure 6.28: Evolution of the normalised electrical resistance

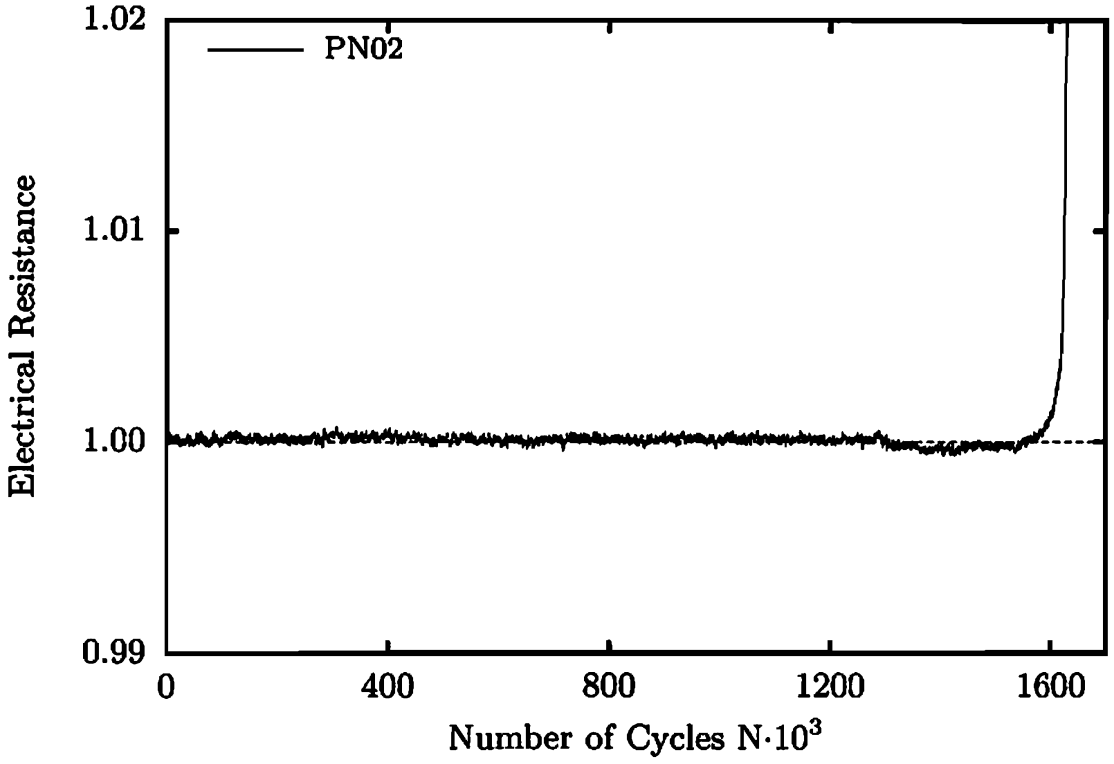

(a) Specimen - PN02

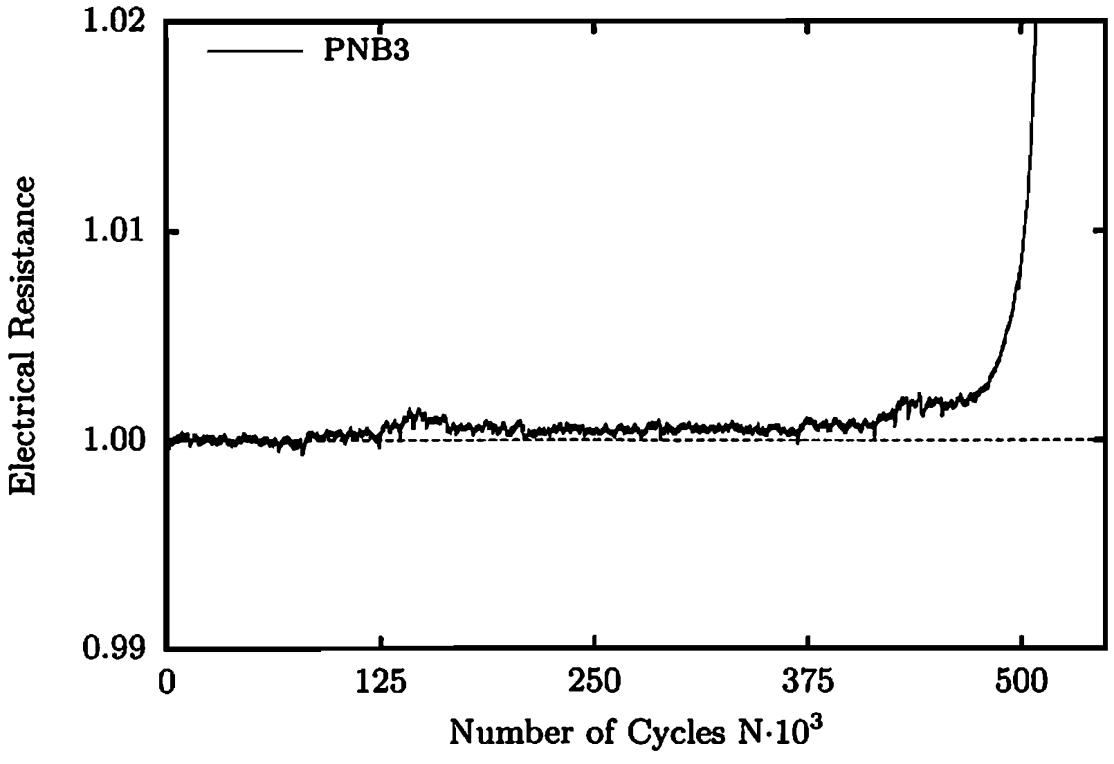

(b) Specimen - PNB3

Figure 6.29: Evolution of the normalised electrical resistance - enlarged representation

Spec.	Ampli. [mm]	$\sigma_{a,loc}$ MPa	Load cycles 1	Load cycles 2	Fatigue life Load cycles	$2a$ [mm]
1	2	3	4	5	6	7
C01	0.23	309	>2000000			
C02	0.25	345	269070	207522	476592	88.88
C03	0.27	341	230526	171594	402120	85.21
C04	0.29	417	91098	130746	221844	87.82
C05	0.31	447	91004	116640	207644	88.89
C06	0.33	462	78888	87078	165966	85.50
C07	0.35	482	129324	78900	208224	85.56
C08	0.40	499	51720	51588	103308	87.89

Table 6.10: Experiments on the circular specimen

Block	Displ. [mm]	Load cycles
1	0.23	100000
2	0.25	15000
3	0.27	10000
4	0.29	5000
5	0.31	4500
6	0.33	3500

Table 6.11: Load amplitude and number of cycles for single blocks

formed with the stress ratio 0.05 and a displacement controlled loading. In Table 6.10, $\sigma_{a,loc}$ is the local stress amplitude in the centre of the circular specimen, calculated from the measured force amplitude. The column 4 represents the number of load cycles in the moment when the increase in electrical resistance is about 0.5 $\mu\Omega$ from its start value. At this point, the experiment is stopped and the crack is evaluated. The length of the macrocrack in this moment is between 9 and 10 mm. The number of applied load cycles during the crack propagation from this break point given in column 4 to the final crack length (column 7) is listed in the column 5. The sum of these two columns is shown in column 6. It represents the fatigue life of the specimen.

Block program experiments are constructed based on the results of the experiments with a single constant amplitude loading presented in Table 6.10 and on Palmgren-Miner damage rule. Applied load amplitudes and the duration of single blocks are given in Table 6.11. The load is displacement controlled and stress

Spec.	Block program	Load cycles 1	Load cycles 2	Fatigue life Load cycles	$2a$ [mm]
1	2	3	4	5	6
CB1	LH	134106	272214	406320	89.00
CB2	HL	246668	188265	434933	84.00

Table 6.12: Block program experiments on the circular specimen

Spec.	Preload cycles	Load cycles 1	Load cycles 2	Fatigue life Load cycles	$2a$ [mm]
1	2	3	4	5	6
CRB1	100000	452850	242284	795134	85.93
CRB2	125000	183330	180780	489110	88.16

Table 6.13: Experiments on the circular specimen with the load in different directions - preload experiments

ratio is 0.05 in all blocks. As in the case of the plain specimen with a hole, it is assumed that the displacement amplitude of 0.23 mm has no influence on the fatigue life since the applied load is below the endurance limit. The displacement amplitude in other blocks is chosen in such a way that the single block contributes with 5% fatigue damage. Block program experiments are performed on low-high and high-low block sequences depicted in Figure 6.4. The results of fatigue life for this type of experiments are listed in Table 6.12. Values of applied load cycles given in columns 3 to 5 have the same meaning as the values presented in columns 4 to 6 in Table 6.10. The break point life represented in column 3 shows short service life of the specimens. The calculated damage measure D has the values 0.22 and 0.50.

Experiments with the load in different directions can be divided in two groups, which are summarised in Tables 6.13 and 6.14. In all experiments, the stress ratio is 0.05 and the loading is displacement controlled with a displacement amplitude 0.25 mm.

In the first group of experiments, the loading is applied with 100000 and 125000 cycles as a preload. At the end of this sequence, the specimens are without recognisable micro and macro damage. After the preloading, the specimen is rotated 30° about the axis perpendicular to the specimen surface and the loading is applied again. In this manner, the new stress state is rotated by 30° to the initial stress state. The specimen is loaded in this second direction until the final failure. Hence, the first applied load direction does not significantly influence

Spec.	$2a_1$ [mm]	Load cycles 1	Load cycles 2	Fatigue life Load cycles	$2a$ [mm]
1	2	3	4	5	6
CR1	9.98	114258	212676	326934	91.01
CR2	19.27	223392	139980	363372	81.39
CR3	29.91	200364	147468	347850	90.72
CR4	10.91	819870	244698	1064568	86.17
CR5	18.27	212148	174588	386736	91.98
CR6	29.73	146538	178086	324624	92.60

Table 6.14: Experiments on the circular specimen with the load in different directions

the damage evolution, and the second load direction produces macroscopic crack initiation and propagation in the direction perpendicular to its direction. Results of these experiments are summarised in Table 6.13. Values given in columns 3 and 4 have the same meaning as those in columns 4 and 5 in Table 6.10. The sum of values in columns 2 to 4 is shown in column 5.
The second group of experiments with the loading in different directions is summarised in Table 6.14. In these experiments, the load is applied in one direction up to a certain crack length ($2a_1$). After that, the specimen is rotated and further loaded. The rotation angle to the initial load direction is 30° for specimens CR1 to CR3 and 45° for specimens CR4 to CR6. The crack length in the moment of the change of loading direction is listed in column 2. Column 3 represents the number of applied load cycles up to the crack length given in column 2. The number of load cycles after the rotation of the specimen up to final crack length is shown in column 4. Column 5 represents the sum of all applied load cycles. The final crack length along the crack path is listed in column 6. In contrast to the experiments introduced in Table 6.13, the first load sequence in this group of experiments produces a macrocrack with the direction of crack propagation perpendicular to the direction of the applied load (Mode I loading). After the specimen is rotated the stress state also rotates and it influences the direction of crack propagation. In this moment, specimen is subjected to the mixed-mode I/II loading. It is possible to observe that, after some stabilisation period, the new direction of macrocrack propagation is almost perpendicular to the new load direction which again coincides with Mode I loading (see Figure 6.45).

6.3.3.1 Evolution of the global specimen stiffness

The evolution of the global specimen stiffness is calculated as in the case of the plain specimen by using the procedure introduced in Section 6.2.1. The evolution

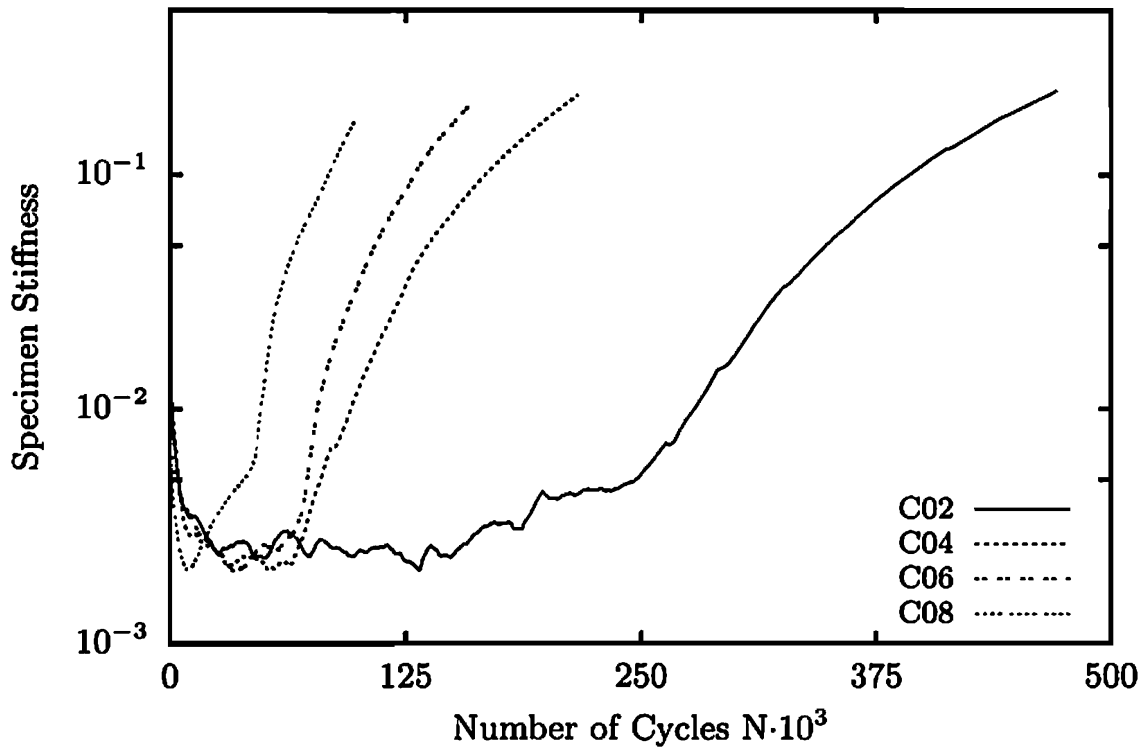

(a) Stress ratio R=0.05

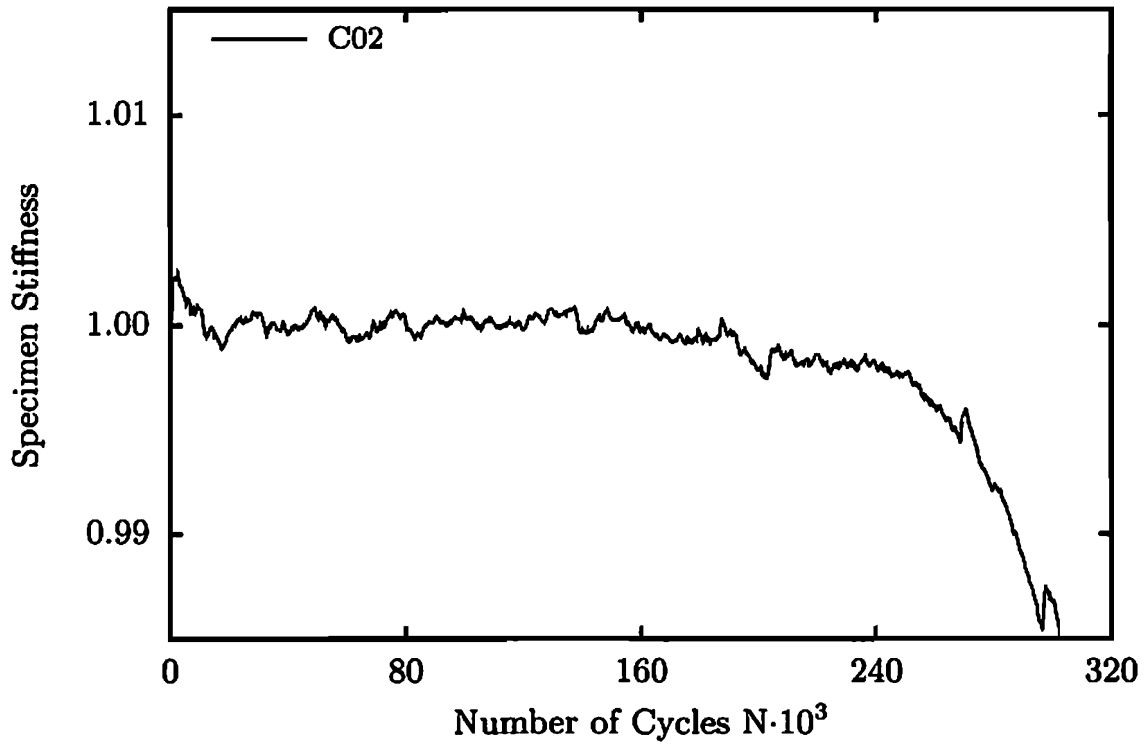

(b) Enlarged representation - specimen C02

Figure 6.30: Evolution of the normalised specimen stiffness

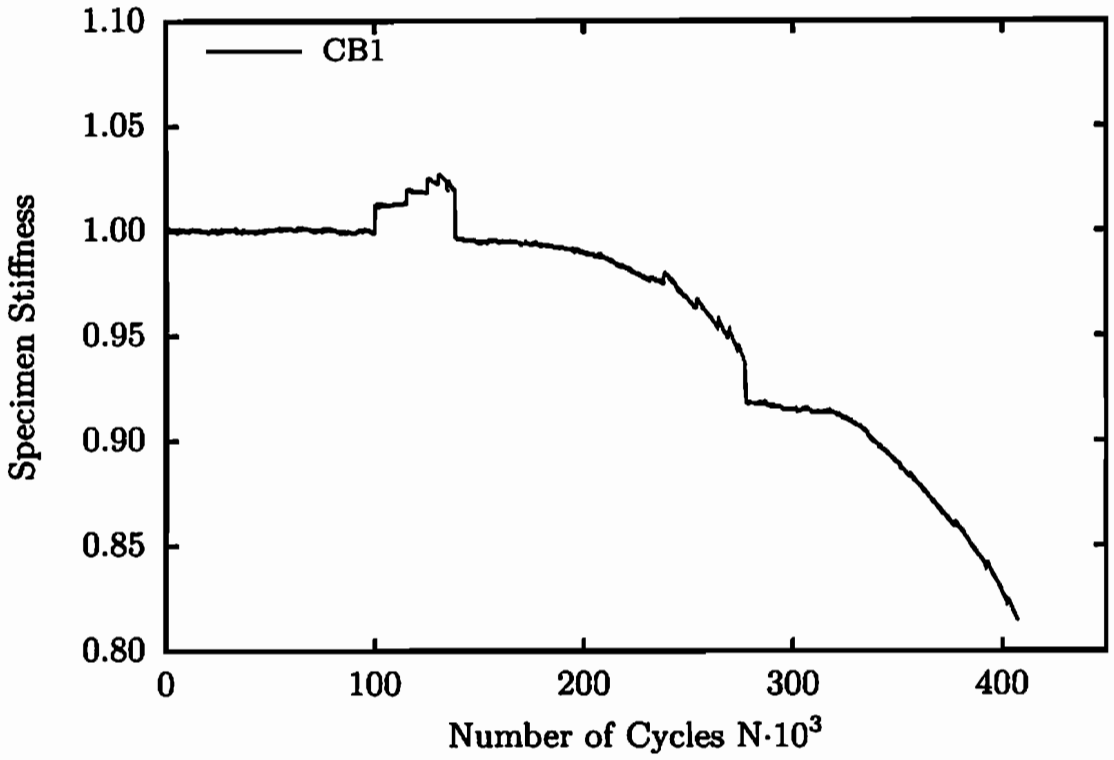

(a) LH block experiment

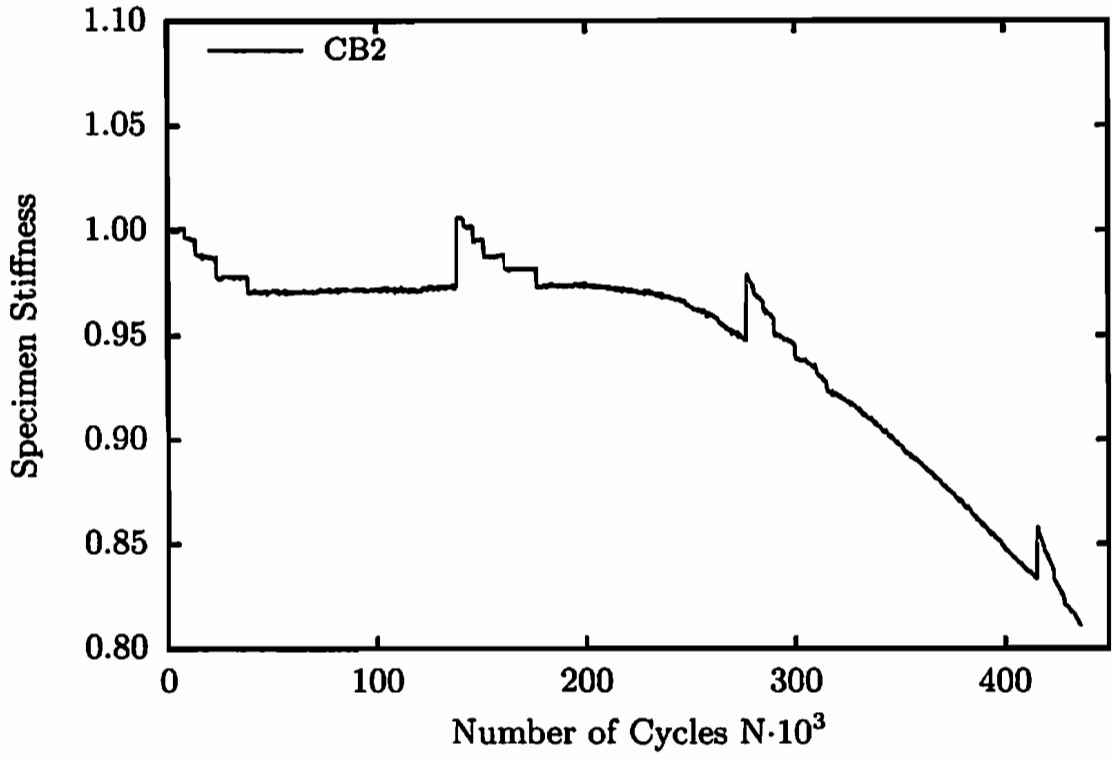

(b) HL block experiment

Figure 6.31: Evolution of the normalised specimen stiffness

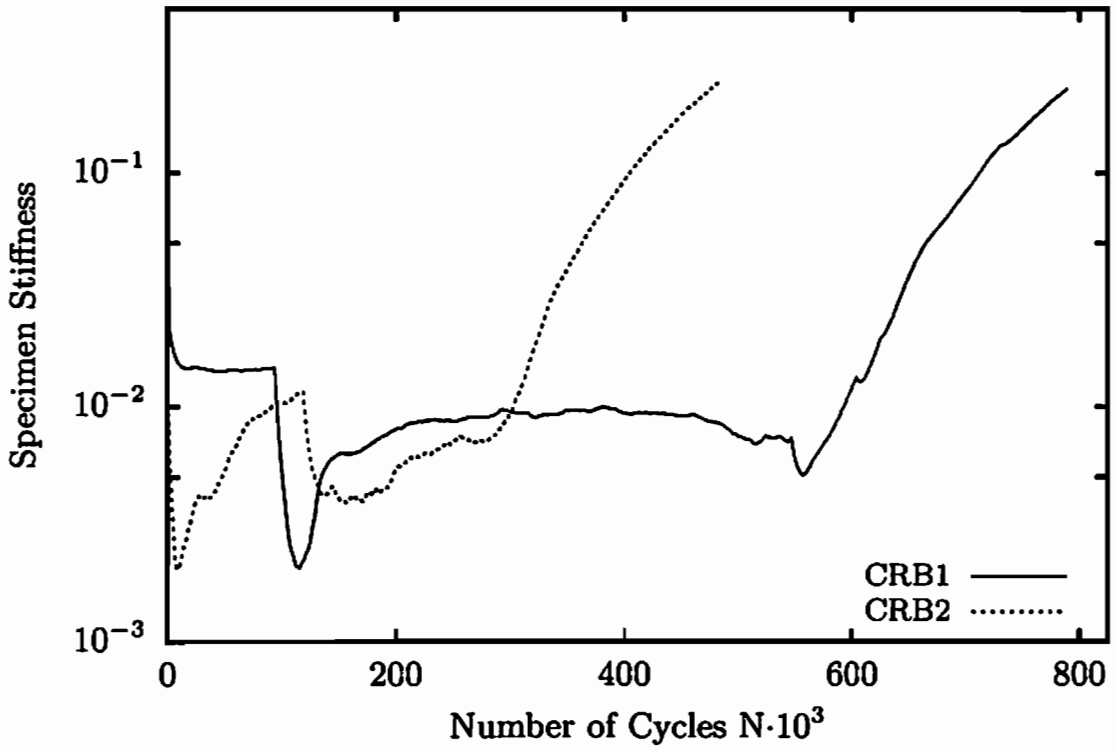

(a) Preload experiments

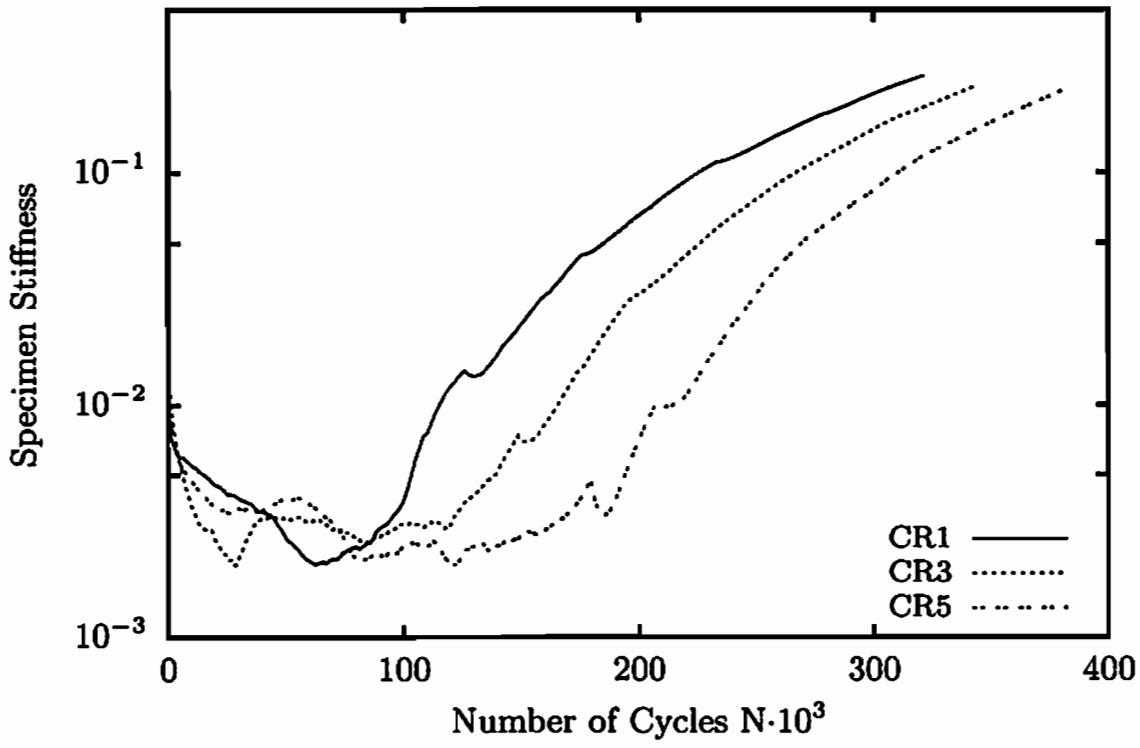

(b) Load in different directions - kinked crack

Figure 6.32: Evolution of the normalised specimen stiffness

of the normalised specimen stiffness for experiments with constant amplitude loading applied in one direction, with a typical stabilisation, constant value and final decrease phase, is plotted in Figure 6.30a. The decrease of specimen stiffness starts after 60% to 80% of the number of cycles given in column 4 in Table 6.10. Due to dimensions of the specimen and relatively long crack propagation, the final failure is not as rapid as in the case of a plane specimen. However, a steady acceleration in the decrease of the specimen stiffness may be observed.
The enlarged representation of the evolution of the normalised specimen stiffness for specimen C02 is shown in Figure 6.30b. After a decrease of specimen stiffness during the first 10% of the service life, it is stabilised until 160000 load cycles. After this point, the specimen stiffness decreases indicating a damage evolution. The decrease is almost linear in the first phase, but with the increase of the applied load cycles, the decrease of specimen stiffness accelerates.
The evolution of the normalised specimen stiffness for block program experiments is plotted in Figure 6.31. In the case of the low-high block experiment introduced in Figure 6.31a, it is possible to see the phenomenon of retardation of crack growth represented as a deceleration in the decrease of the specimen stiffness. Namely, when the block sequence with the maximum amplitude of 0.33 mm is followed by the load sequence with the minimum amplitude of 0.23 mm, the plastic zone at the crack tip abruptly diminishes and leads to the significant decrease in the velocity of the crack propagation (see Wheeler 1972, Lemaitre & Chaboche 1990, Suresh 1991). This effect disappears after a certain number of load cycles and the crack growth and the decrease of the specimen stiffness accelerate again. In the case of a high-low block program (see Figure 6.31b), the difference in the amplitude between the blocks is too small to produce the retardation of the crack growth. After 80% of the applied number of load cycles (column 3 in Table 6.12), a steady decrease of the specimen stiffness is observed.
The results of the experiments with a load applied in different directions are represented in Figure 6.32. The evolution of the normalised specimen stiffness for the experiments summarised in Table 6.13 is given in Figure 6.32a. The jump in the specimen stiffness corresponds to the change of the loading directions and can be attributed to the minimal and unavoidable processing related to incompatibilities in the boundary conditions during the rotation of the specimen. However, the global behaviour of the specimen stiffness evolution remains unaltered. The evolution of normalised specimen stiffness for the experiments represented in Table 6.14 is given in Figure 6.32b.

6.3.3.2 Evolution of the acoustic emission

Similar to the experiments on the plain specimen, experiments on circular specimens are performed with two sets of acoustic emission transducers with appropriate preamplifiers. The wideband transducers are used in the displacement controlled experiments with constant load amplitude applied in one direction (specimens C01 to C08). For this type of acoustic emission transducers a typical

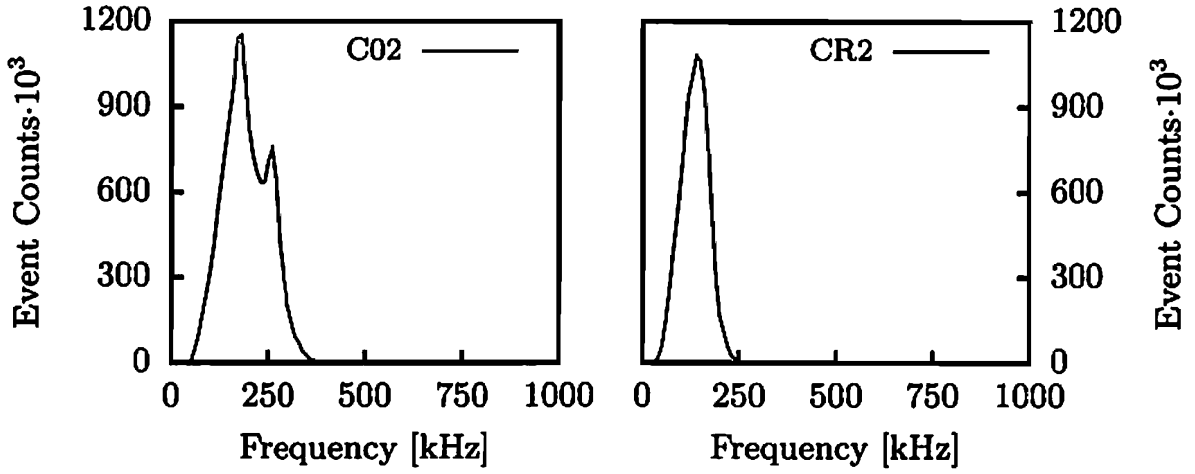

Figure 6.33: Acoustic emission event counts versus frequency

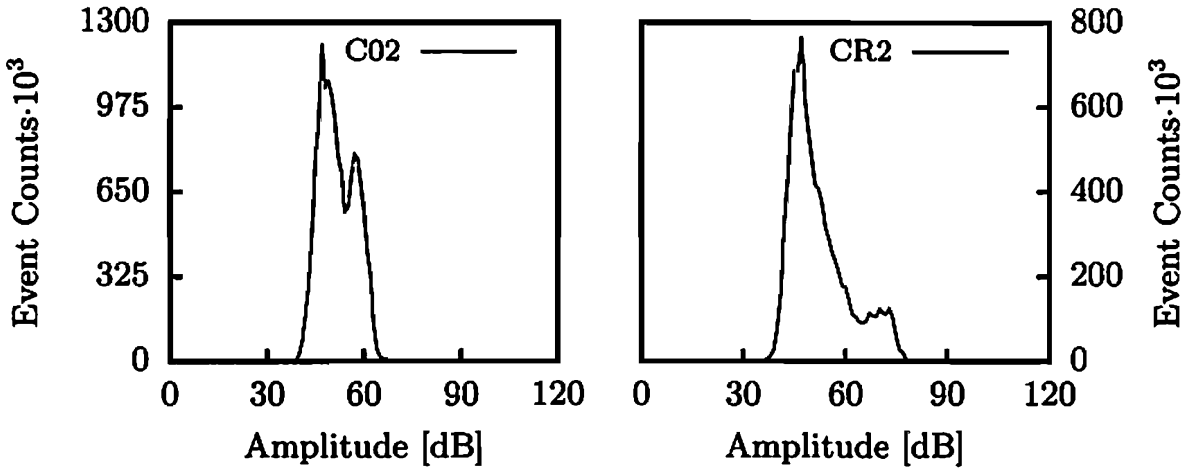

Figure 6.34: Acoustic emission event counts versus amplitude

frequency response is visualised in Figure 6.33 for the specimen C02. It shows that most of the acoustic emission event counts have a frequency between 80 and 300 kHz with a peak value of about 175 kHz. Therefore, resonance acoustic emission transducers with resonant frequency of 150 kHz are used in all other experiments on the circular specimen. The typical result of the frequency response for the set of resonance acoustic emission transducers is given for the specimen CR2 in Figure 6.33. Both results are in accordance with the investigation of the frequency response for plain specimen.

As in the case of a plain specimen, the amplitude of the acoustic emission event counts is investigated. The amplitude response for both sets of acoustic emission transducers is plotted in Figure 6.34. For both experiments, most of acoustic emission event counts have an amplitude between 35 and 70 dB. Same as for

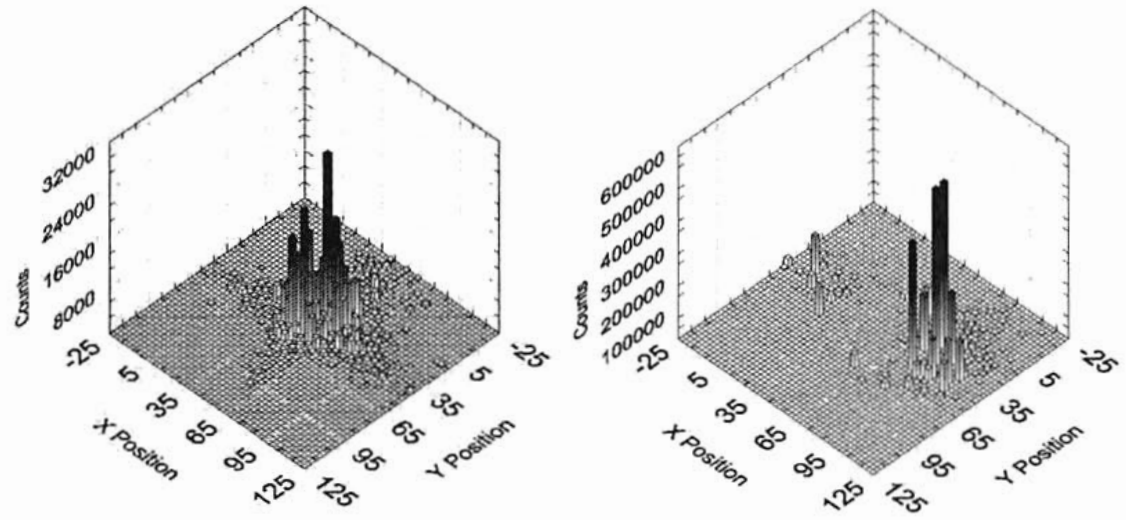

Figure 6.35: Location of the acoustic emission origin - specimen C02

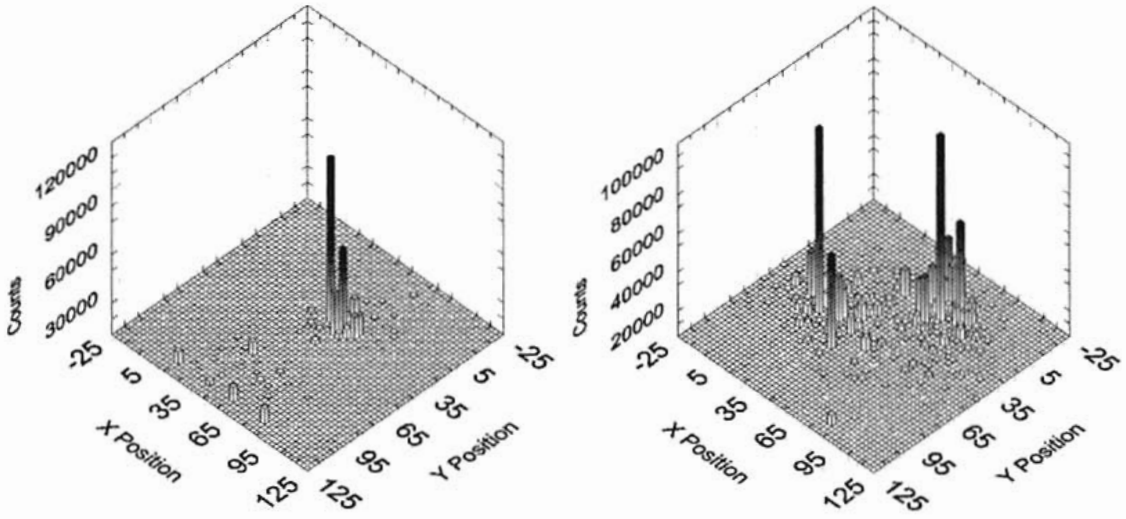

Figure 6.36: Location of the acoustic emission origin - specimen CR5

the plain specimen, this behaviour is used as an additional condition in the elimination of extraneous noise.
In order to eliminate signals which originate from the crack closure and the friction between crack surfaces, the force threshold value is set to 35 kN due to a significantly greater force in arising experiments with circular specimen.
Due to the fact that the two-dimensional constellation of acoustic emission transducers does not permit the definition of guard sensors, a huge amount of acoustic emission signals which do not originate from damage evolution is recorded. These acoustic emission signals are eliminated using the time difference measurement method presented in Section 4.1.4.2. The location of the acoustic emission origin for different stages of the crack growth for the circular specimen C02 is shown

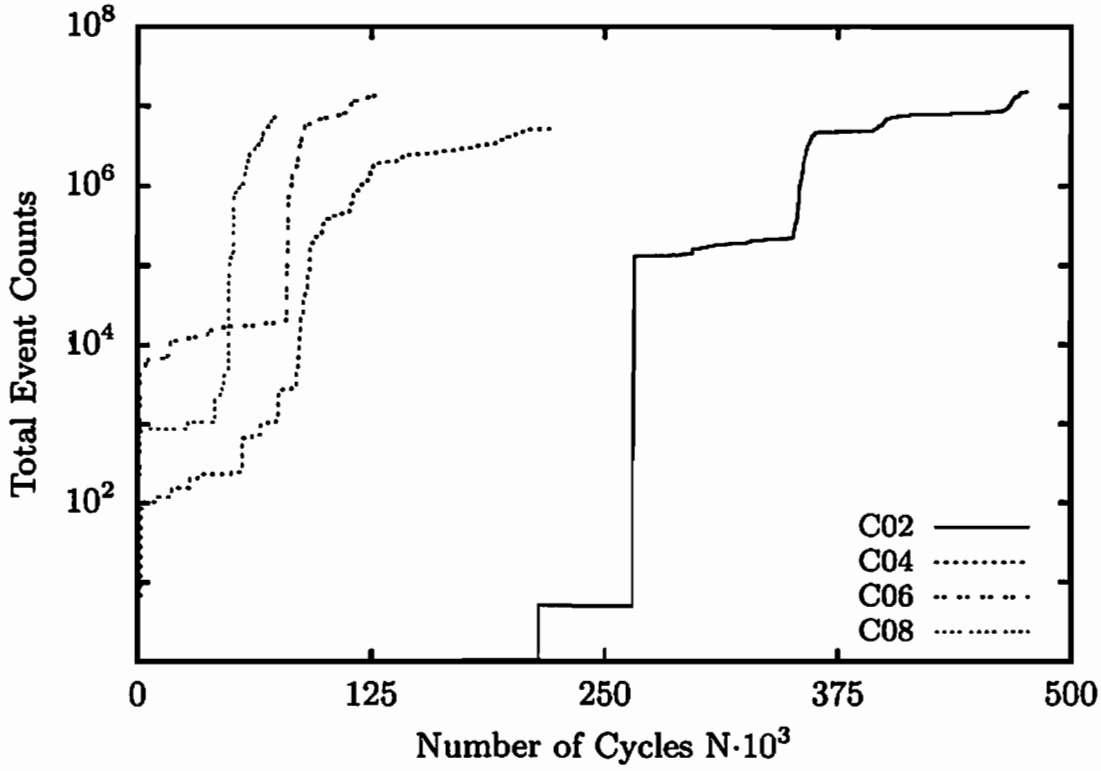

(a) Stress ratio $R=0.05$

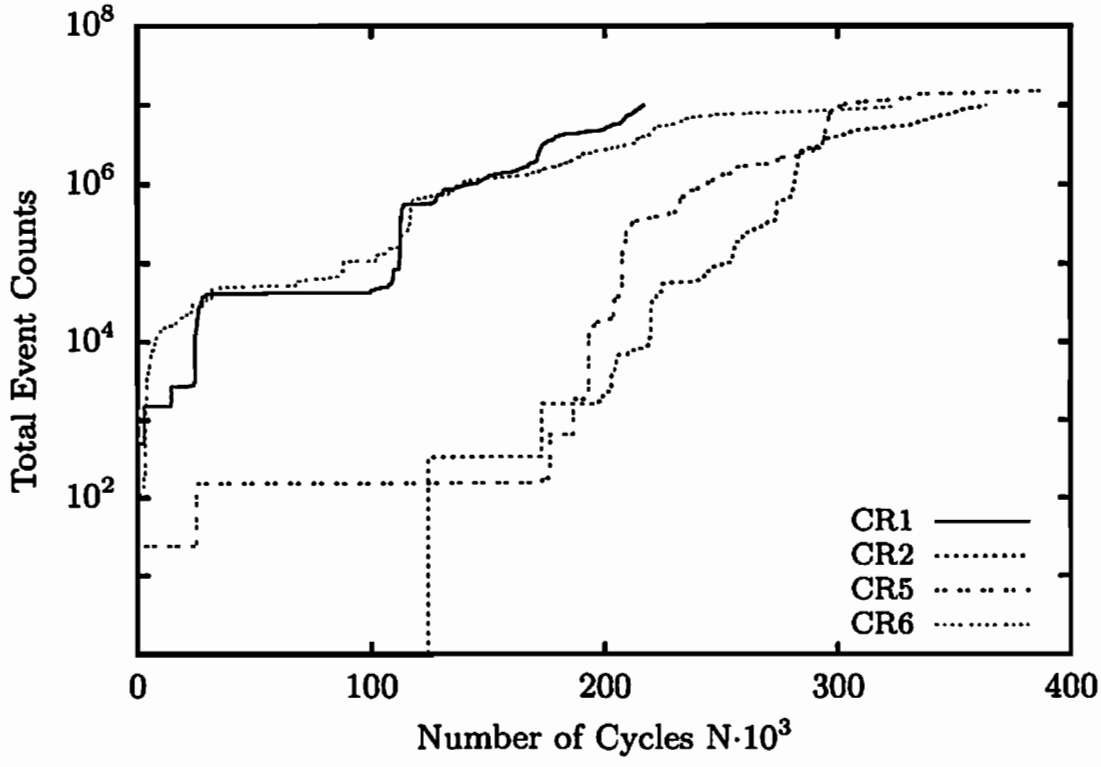

(b) Load in different directions - kinked crack

Figure 6.37: Evolution of the acoustic emission event counts

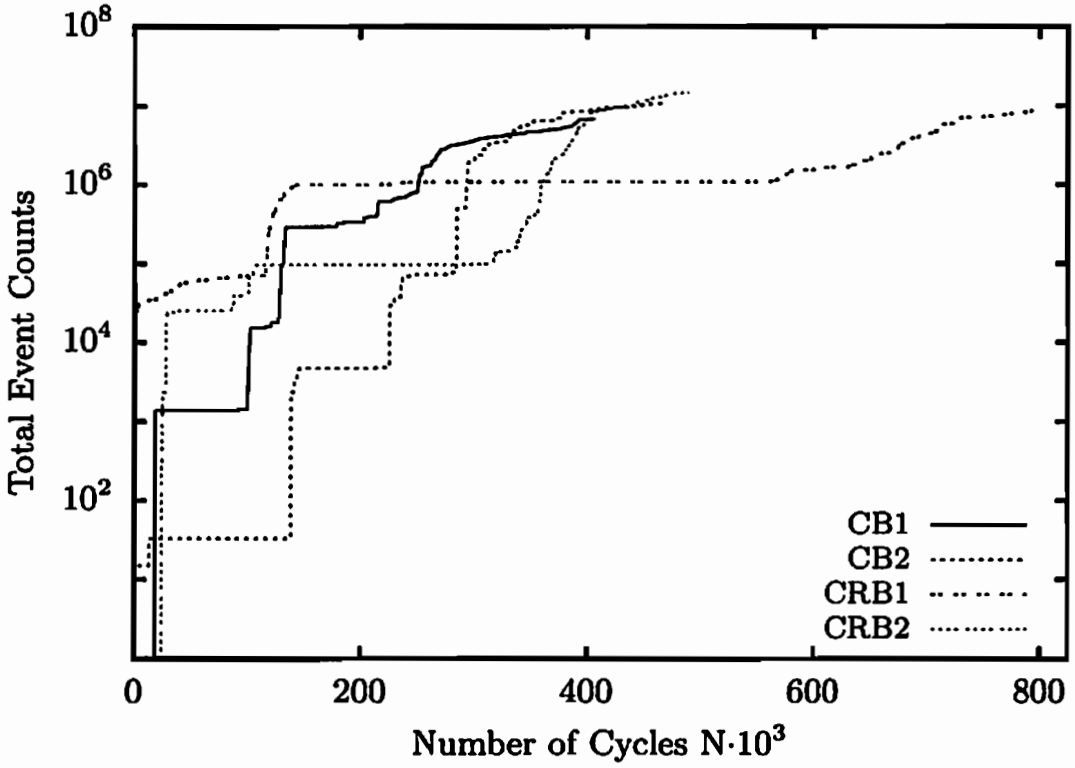

Figure 6.38: Evolution of the acoustic emission event counts

in Figure 6.35 and for the specimen CR5 in Figure 6.36. In the case of the specimen C02, the figure on the left represents the result in the moment when the crack length is 9.90 mm and the figure on the right represents the result for the crack growth between 77.50 mm and 89.05 mm. The concentration of acoustic emission event counts is in good agreement with the real position of the crack growth in both cases. For the specimen CR5, the left figure shows the result for the moment when the crack has a length of 9.65 mm. The right figure represents the result for the crack growth between 64.65 mm and 76.15 mm. Due to the rotation of the specimen about 45°, the crack is kinked and it is represented by the concentration of event counts at two positions in the y-direction. The dispersion of event counts may be assigned to the relatively small ratio between the diameter of the transducers and the specimen size and the distance between the transducers. Namely, the spacing between the transducers is 97 mm in the horizontal direction and 85 mm in the vertical direction and the diameter of the transducers is 17 mm, which excludes the point representation of acoustic emission transducers. For this reason, the signals which are located within 5 mm of the real crack position are regarded as well located.

By using all conditions introduced above for the elimination of acoustic emission signals which do not originate from damage evolution, the recorded data is cleared and acoustic emission is represented using the evolution of cumulative acoustic emission event counts during the service life. This representation

is visualised in Figures 6.37 and 6.38. The figures show that the evolution of cumulative event counts is similar to the corresponding evolution in the case of a plain specimen. After a small acoustic emission output in the first two phases (during the microscopic dislocation dynamics and microcrack incubation and initiation), a significant acoustic emission output in the phase of macrocrack initiation and propagation follows. In contrast to the plain specimen, the third phase has a significant duration due to the difference in the length of the possible crack growth.
Based on the presented results, it can be concluded that the method of acoustic emission gives reasonably good results in the qualitative identification of the fatigue damage which includes the recognition of the crack initiation and its propagation.

6.3.3.3 Evolution of the electrical resistance

The evolution of the normalised electrical resistance in the damaged area of the circular specimen is plotted in Figures 6.39 to 6.43 after the correction of the measured electrical resistance due to the change in temperature during the experiment. The directions for the measurement of the electrical resistance are represented in Figure 5.14. All evolutions of the electrical resistance shown in Figures 6.39 and 6.40a are for the direction perpendicular to the direction of the crack propagation.
For the experiments with constant amplitude loading applied in one direction, the evolution of the normalised electrical resistance is given in Figure 6.39a. The evolution of the electrical resistance has a similar behaviour as the evolution of the specimen stiffness. After a stabilisation period, the electrical resistance has a constant value over a long period of the service life. Depending on the applied load, the increase starts after 40% to 60% of the number of cycles listed in column 4 of Table 6.10. After the acceleration during the initial macrocrack propagation, the increase in the electrical resistance has almost linear behaviour during the long time of crack propagation. The reason for this behaviour is the non-constant specimen thickness, which influences the velocity of the crack propagation and consequently, the rate of the increase in the electrical resistance. The enlarged representation of the electrical resistance evolution for the specimen C02 is visualised in Figure 6.39b. If this evolution is compared to the evolution of the specimen stiffness for the same specimen given in Figure 6.30b, it is evident that the electrical resistance indicates changes in the material structure significantly earlier than the global specimen stiffness.
The evolution of the normalised electrical resistance for the block program and the preload experiments is plotted in Figure 6.40a. In the case of preload experiments (CRB1 and CRB2), the evolution of electrical resistance has the same behaviour as in experiments represented in Figure 6.39a. The result for the block experiment CB1 shows the retardation of the crack growth due to the significant difference between the maximum and minimum load amplitude already reported

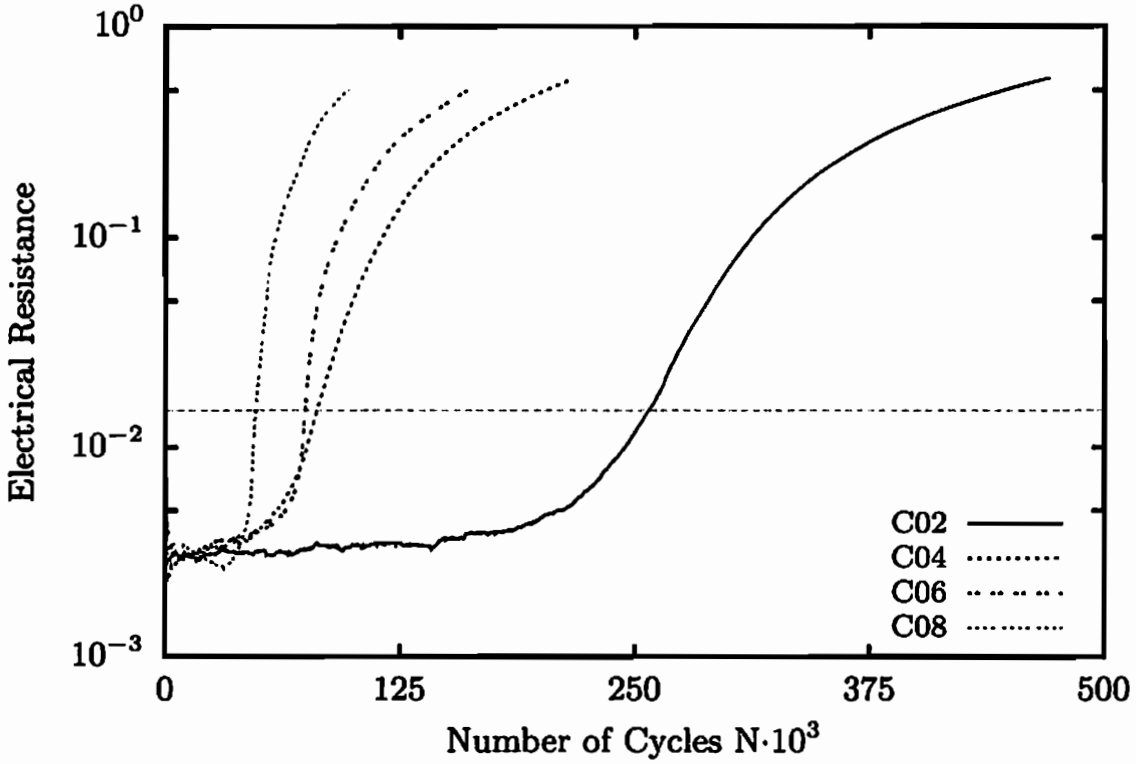

(a) Constant amplitude loading in one direction

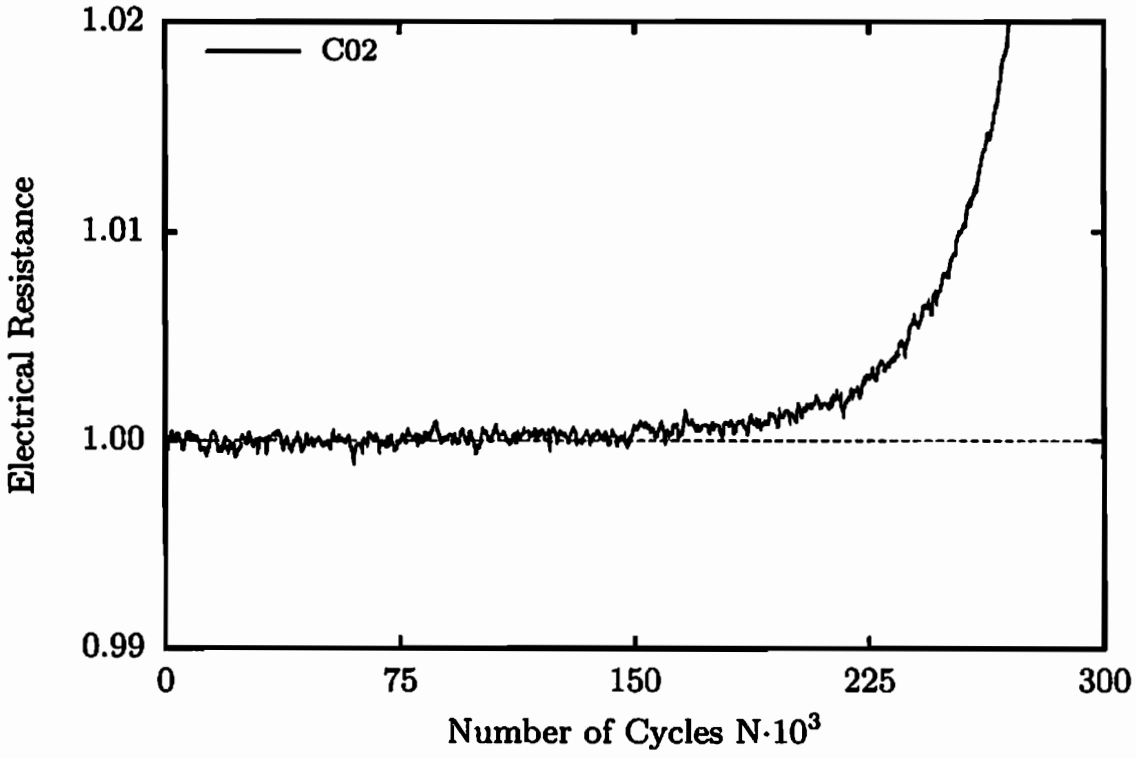

(b) Enlarged representation - specimen C02

Figure 6.39: Evolution of the normalised electrical resistance

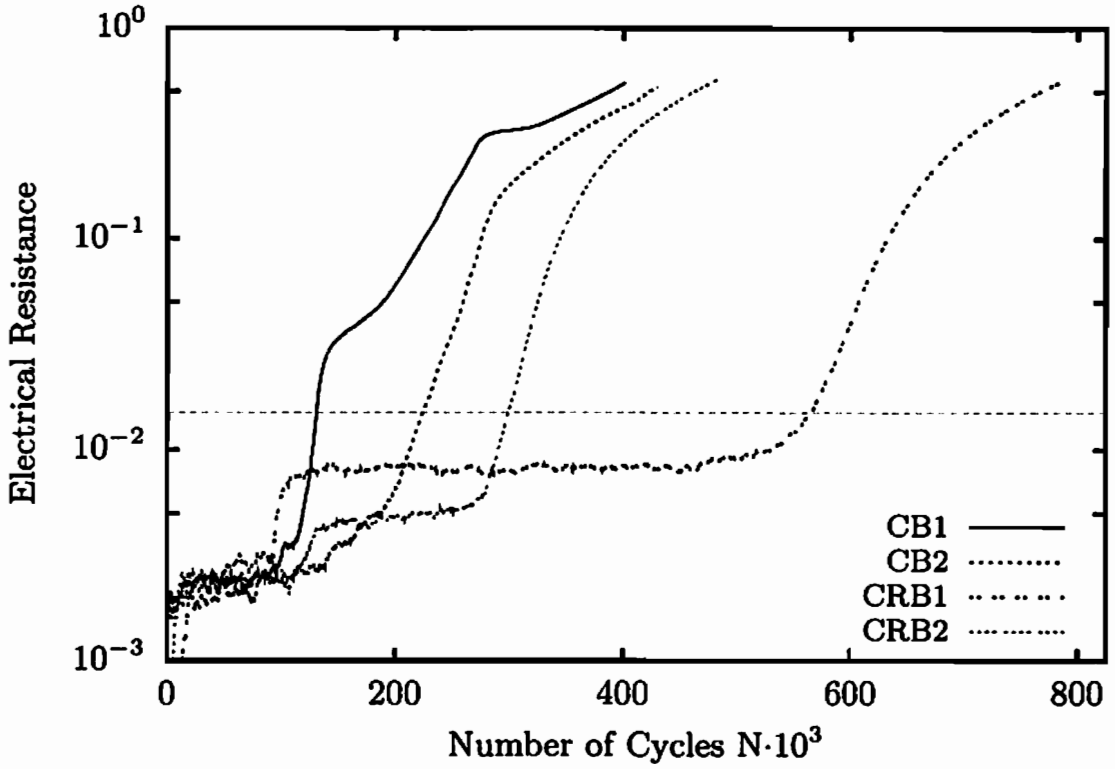

(a) Block and preload experiments

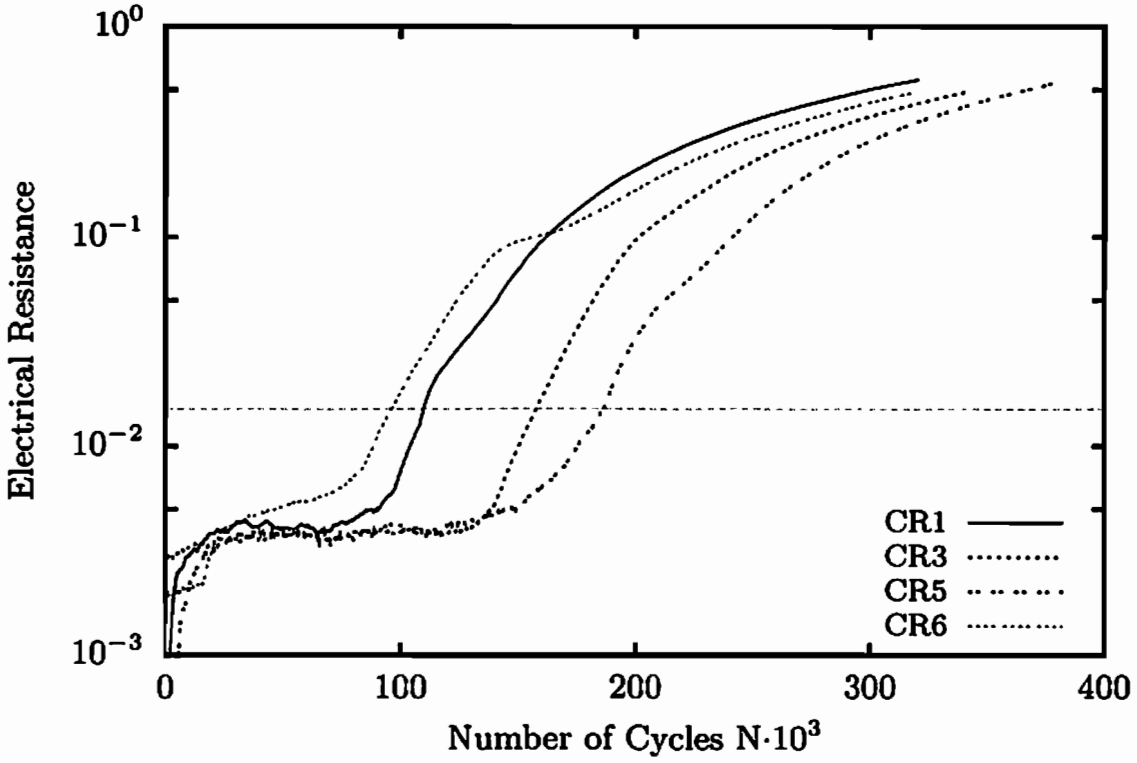

(b) Load in different directions - kinked crack

Figure 6.40: Evolution of the normalised electrical resistance

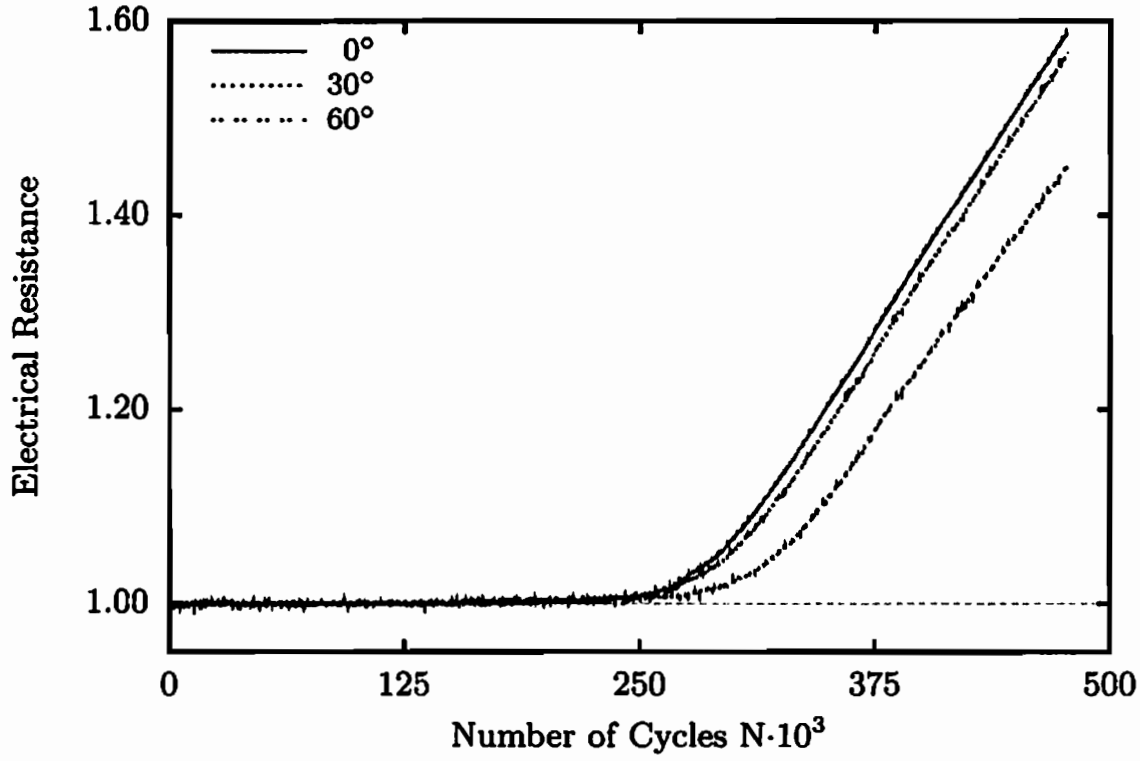

(a) C02

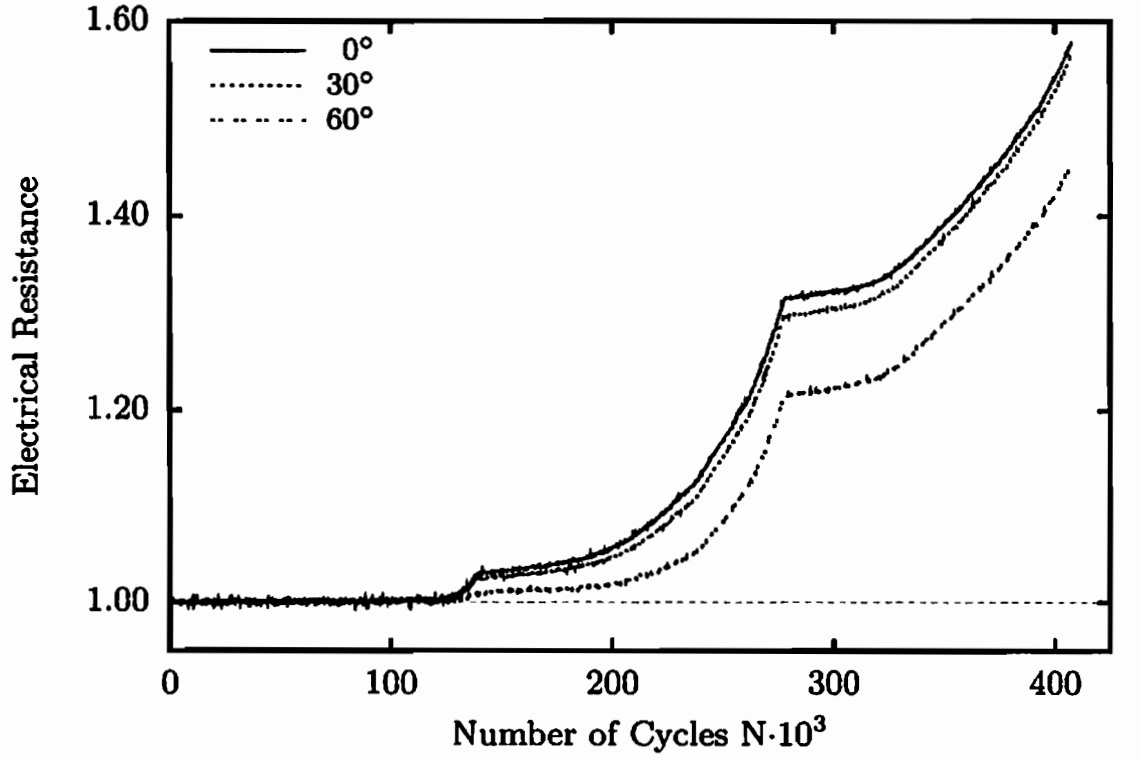

(b) CB1

Figure 6.41: Evolution of the normalised electrical resistance

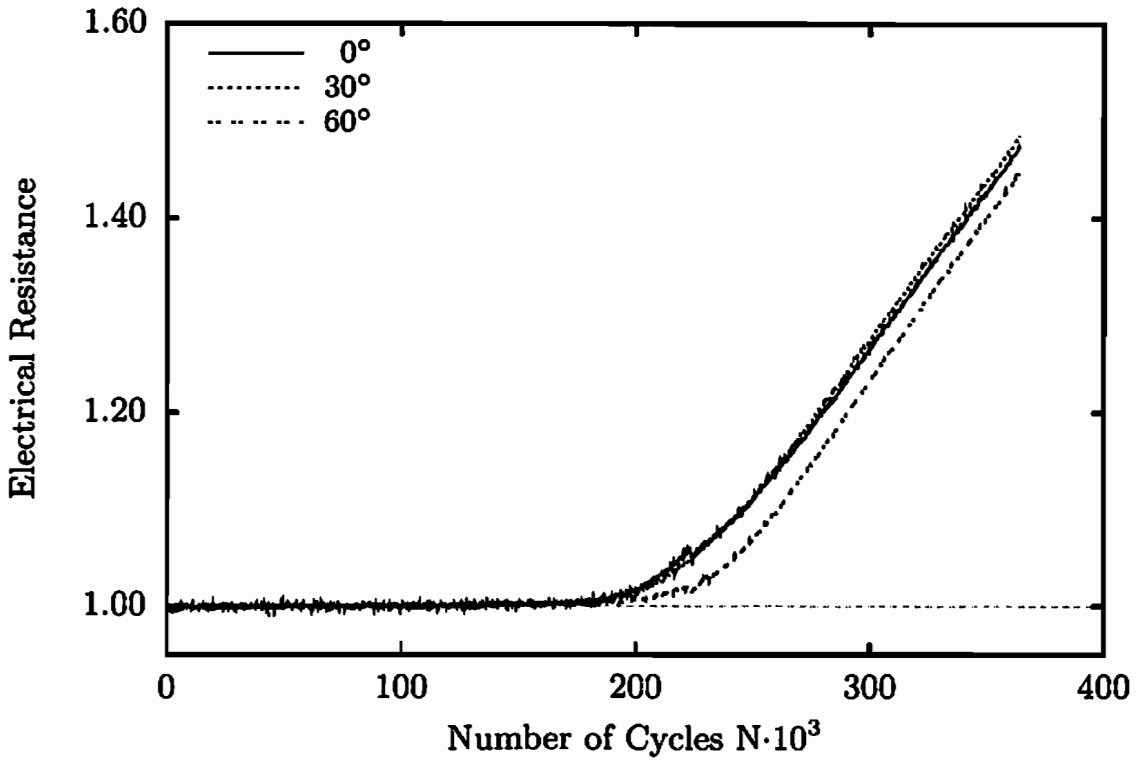

(a) CR2

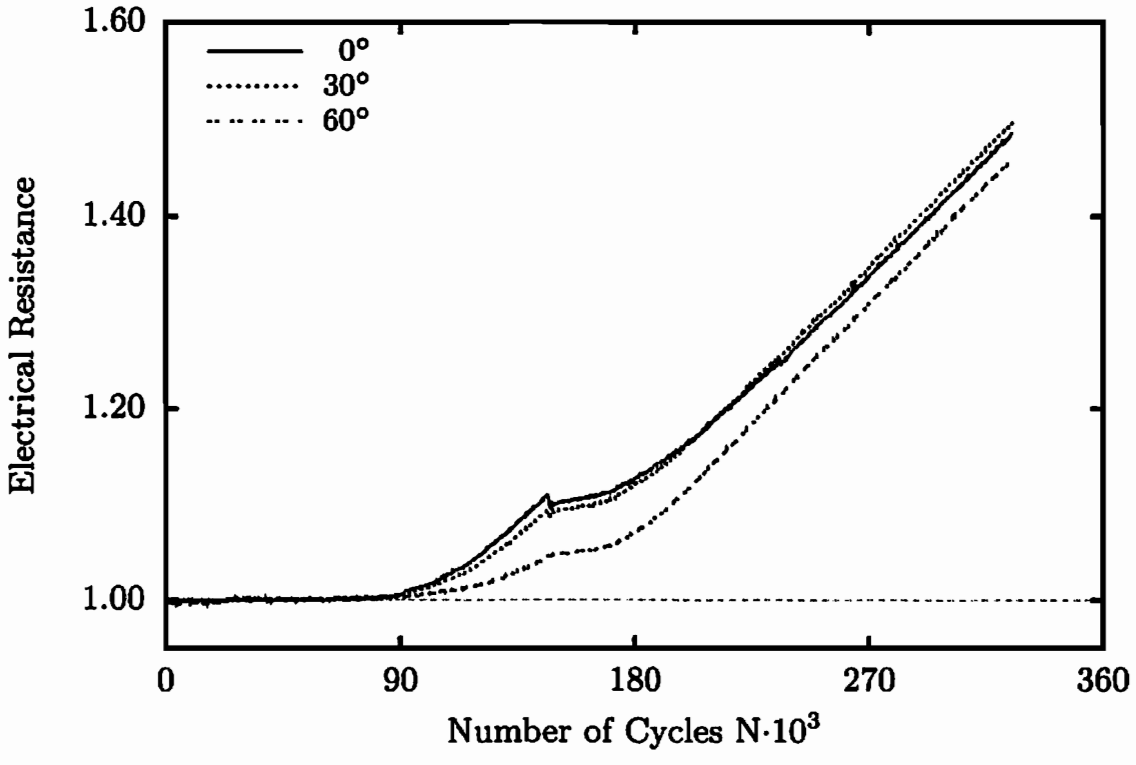

(b) CR6

Figure 6.42: Evolution of the normalised electrical resistance

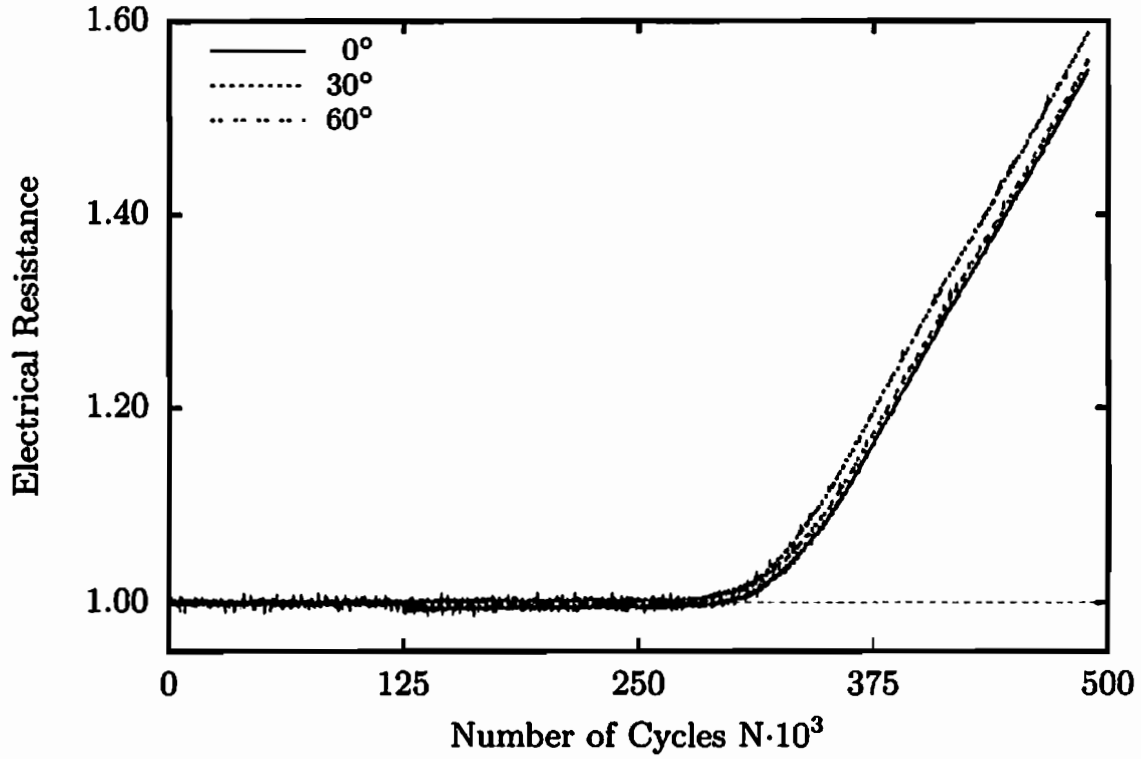

Figure 6.43: Evolution of the normalised electrical resistance - specimen CRB2

in Section 6.3.3.1. This is visible as a significant deceleration in the evolution of the electrical resistance. In the case of the specimen CB2, the retardation of the crack growth does not occur, but different load amplitudes influence the evolution of the electrical resistance.

The results for the experiments introduced in Table 6.14 are shown in Figure 6.40b for the 30° measuring direction of the electrical resistance (see Figure 5.14). This direction coincides with the loading direction after the rotation for experiments CR1 and CR3. In the case of specimens CR5 and CR6, the load changes direction by 45°. It is possible to recognise a decrease in the rate of change of the electrical resistance immediately after the rotation of the specimen in all experiments. However, the evolution accelerates and after a certain period becomes linear with a further crack propagation.

The evolution of the normalised electrical resistance in all three measuring directions is presented in Figures 6.41 to 6.43 for single experiments. It is evident that the rate of change of the electrical resistance is not equal in all directions. The reason for this is the nonuniform distribution of the electrical potential field across the specimen, especially in the vicinity of the crack tip. Results show that the direction of the fastest increase of the electrical resistance is the direction perpendicular to the crack propagation. With the inclination from this direction, the rate of change of the electrical resistance decreases. This fact renders the direction perpendicular to the crack propagation as the preferable measuring

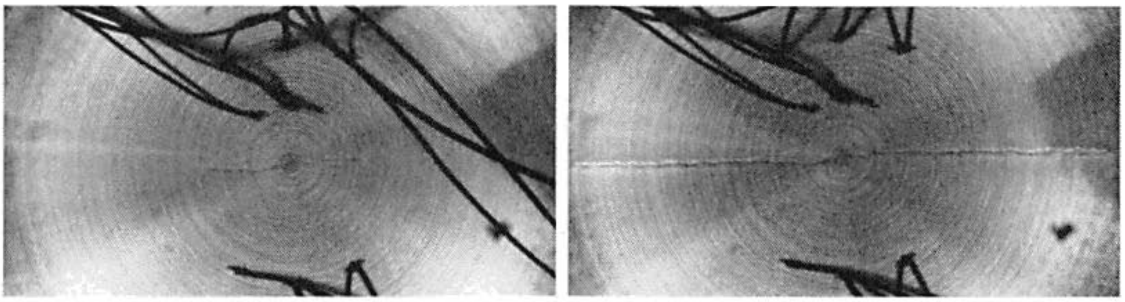

(a) 347792 load cycles (b) 489110 load cycles

Figure 6.44: Macrocrack growth - specimen CRB2

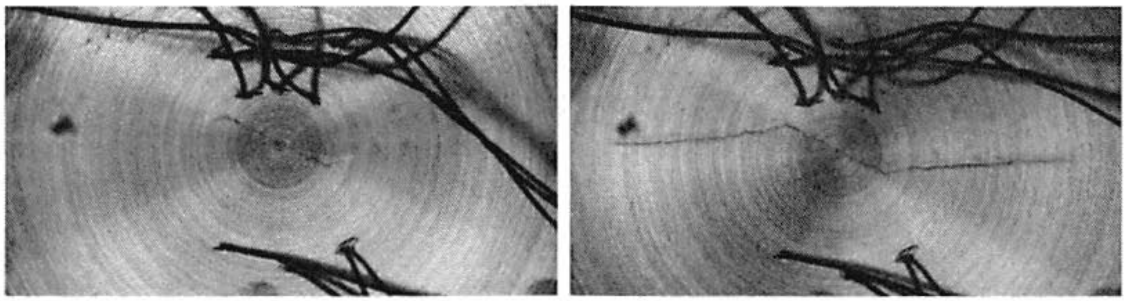

(a) 244200 load cycles (b) 363372 load cycles

Figure 6.45: Macrocrack growth - specimen CR2

direction. However, measuring in other directions does not lead to any loss of valuable information about the crack propagation.

6.4 Macrocrack documentation

The documentation of the macroscopic crack growth is created using the devices and the procedure presented in Section 5.4.5. The photograph of the damaged area of the specimen is used for the visual determination of the macrocrack propagation. Photographs from the high resolution CCD camera enable the measurement of the crack length with a maximal resolution of 12.5 μm. Several stages of the macrocrack growth for the experiments with the circular specimen are given in Figures 6.44 and 6.45.

Two stages of the macroscopic crack within the specimen CRB2 are given in Figure 6.44. Specimen CRB2 is preloaded with 125000 load cycles, rotated by 30° and further cyclic loaded. Figure 6.44a shows the damage after 347792 load cycles. In this moment, the macrocrack has the length of 25.95 mm. The final crack length of 88.16 mm is obtained after 489110 load cycles. This final damage stage is given in Figure 6.44b. The macrocrack propagates perpendicular to the

load direction which corresponds to the Mode I loading.
The specimen CR2 is cyclic loaded in the resistance measurement direction 0° (see Figure 5.14) up to the macrocrack length of 19.27 mm. Up to this point 223392 load cycles are applied. After that, the specimen is rotated by 30° and further cyclic loaded. Due to the change of the load direction, the stress state is changed and the direction of the crack propagation changes. Directly after the change of the loading direction, the specimen is subjected to a combined Mode I/II loading condition. After 244200 applied load cycles, the crack has the geometry given in Figure 6.45a. In this moment, the crack part left from the kinking point has a length of 4.80 mm and the right part has a length of 4.66 mm. The direction of the crack propagation in this phase of crack growth is not perpendicular to the load direction and changes with the crack propagation. Figure 6.45b shows the crack in the final stage of the experiment after 363372 applied load cycles. The crack part left from the kinking point has a length of 31.50 mm and the right part has a length of 30.62 mm. The initial change of the crack growth direction asymptotically moves to the direction which is perpendicular to the load direction and represents again a Mode I loading.

7 Numerical analysis

The aim of this part of the work is to determine the material parameters for the brittle damage material law proposed by Schütte (2001) based on the results of the conducted experiments. The first part of this chapter deals with the determination of the connection between the evolution of the electrical resistance during fatigue loading and the crack propagation. This is followed by the calibration of the material parameters and subsequently by their validation.

7.1 Calibration of the electrical resistance measurements

It is possible to connect the electrical resistance evolution and the crack growth during the service life of the specimen by using data from the electrical resistance measurements and the photographs of the crack propagation. In order to validate the relationship between the electrical resistance and the crack length, the numerical calculation of the electrical potential distribution across the damaged specimen with different crack lengths is performed. This calculation is performed by using the finite element software ANSYS.

The distribution of the electrical potential across the plain specimen with a hole and across the circular specimen is presented in Figure 7.1 for different crack lengths. Figures 7.1a and 7.1b show the distribution of the electrical potential across the plain specimen with a hole with crack lengths of 2.0 mm and 8.0 mm. The distribution of the electrical potential across the circular specimen with the straight crack of lengths 20.0 mm and 75.0 mm is plotted in Figures 7.1c and 7.1d. In these two figures, the distribution of the electrical potential is given for the case in which the constant direct electrical current is driven through the specimen into the direction perpendicular to the crack growth direction. This direction coincides with the 0° direction of electrical resistance measurement represented in Figure 5.14. Figures 7.1e and 7.1f show the circular specimen with the kinked crack. The central straight part of kinked crack has a length of 19.25 mm and inclination of 30° to the horizontal axis. Lengths of the horizontal cracks left and right from the kinking point are 10.00 mm in Figure 7.1e and 30.00 mm in Figure 7.1f. The distribution of the electrical resistance is calculated for the constant direct electrical current which is driven through the specimen into a 30° direction of the electrical resistance measurement. This direction is perpendicular to the direction of the crack growth after kinking.

It is possible to calculate the electrical resistance R between every two points

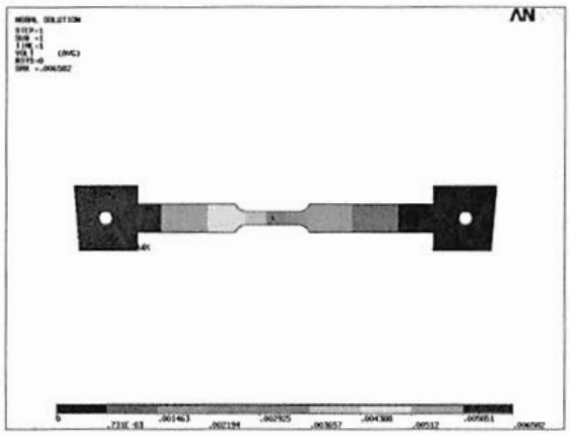

(a) $2a = 2.0$ mm

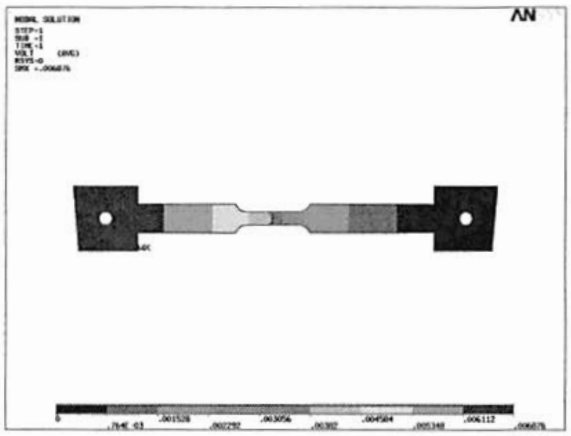

(b) $2a = 8.0$ mm

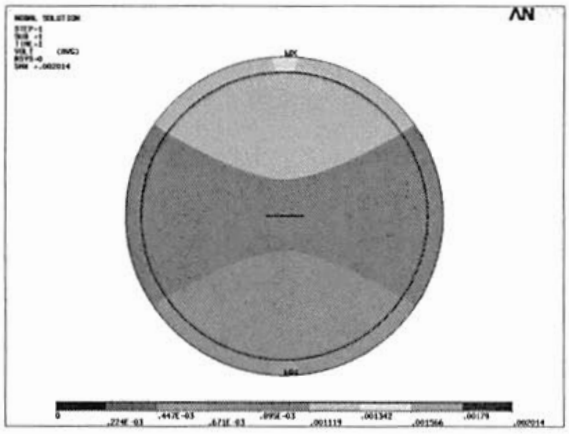

(c) $2a = 20.0$ mm

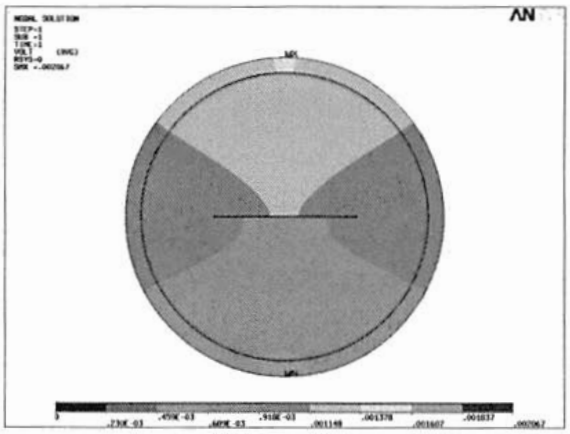

(d) $2a = 75.0$ mm

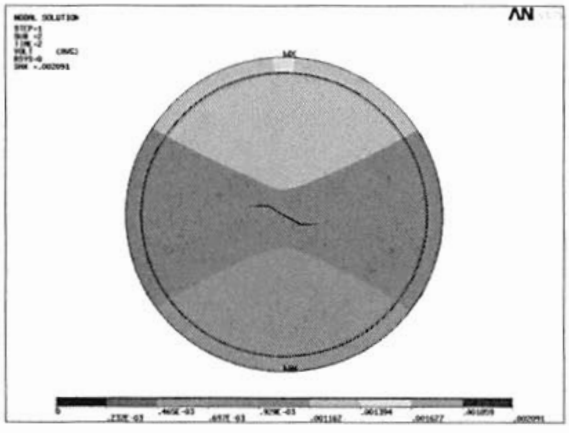

(e) $2a = 10.00 + 19.25 + 10.00$ mm

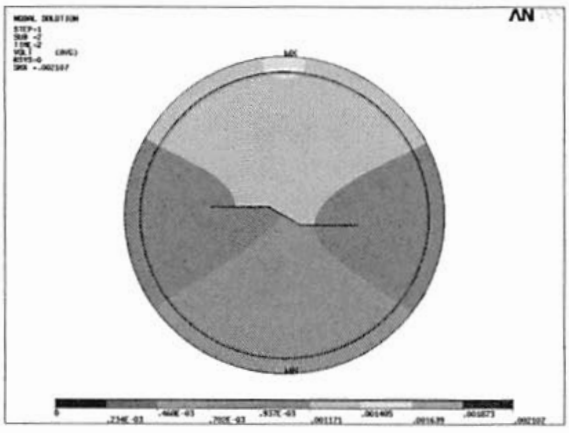

(f) $2a = 30.00 + 19.25 + 30.00$ mm

Figure 7.1: Distribution of the electrical potential

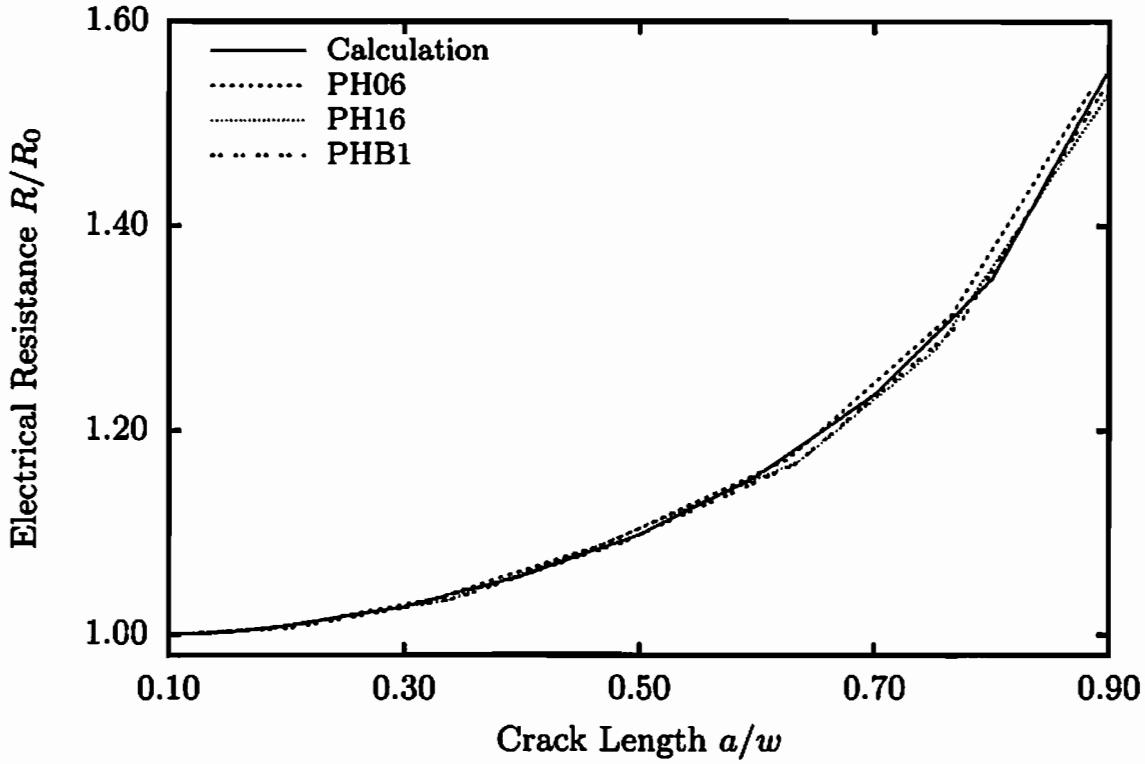

(a) Plain specimen with a hole

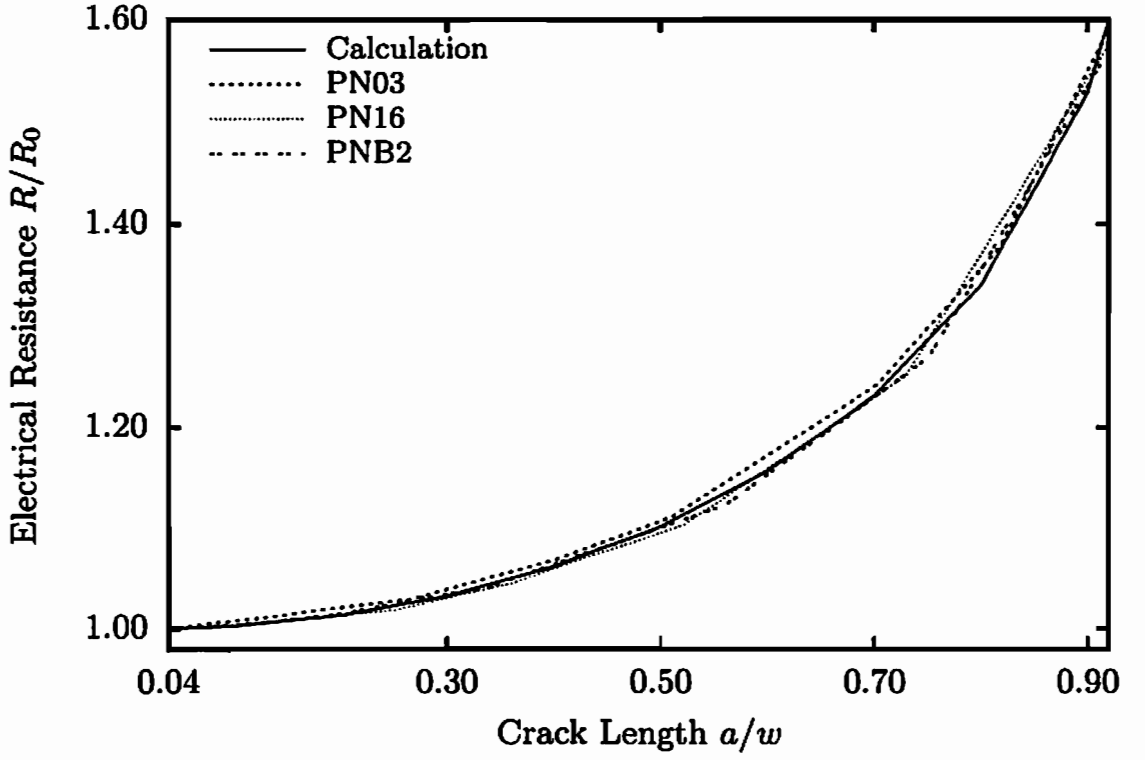

(b) Plain specimen with both side notches

Figure 7.2: Normalised electrical resistance versus crack growth

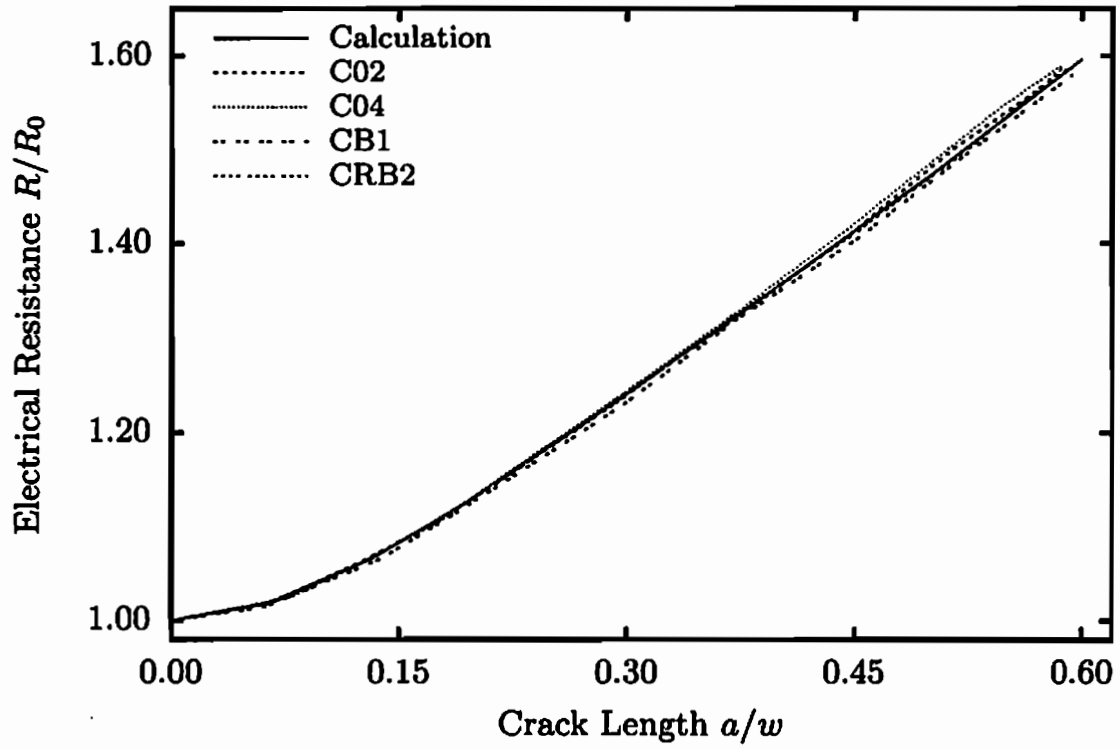

(a) Circular specimen

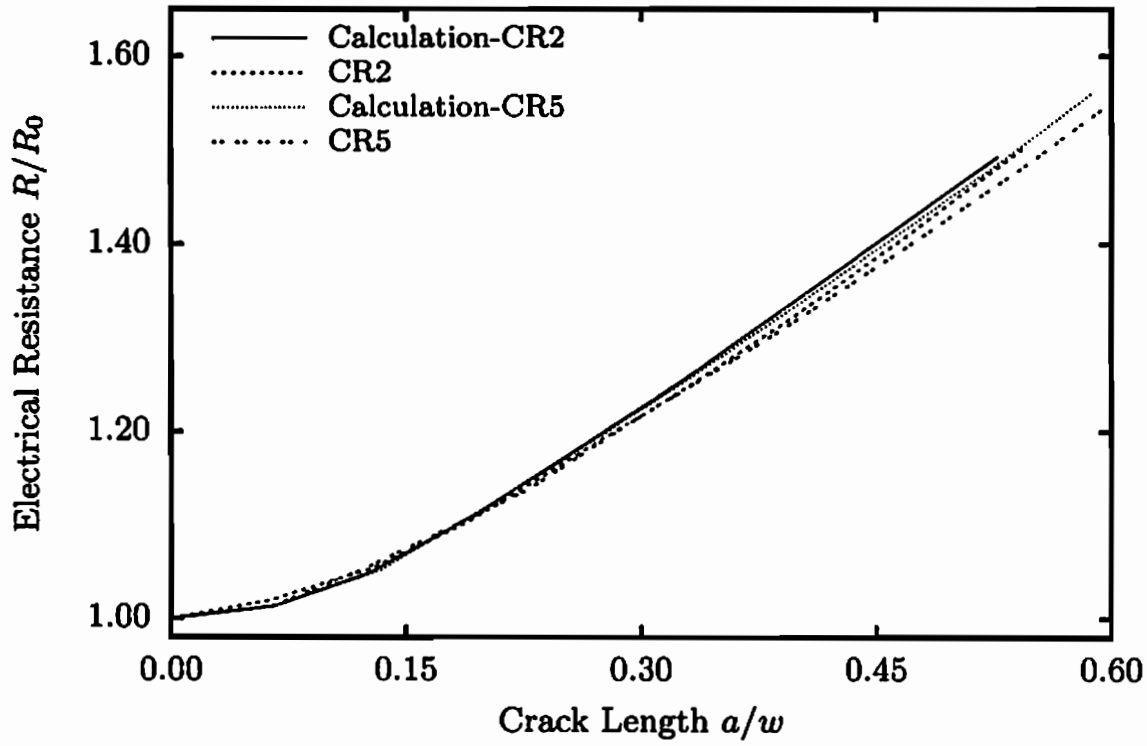

(b) Circular specimen - kinked crack

Figure 7.3: Normalised electrical resistance versus crack growth

from the distribution of the electrical potential by using the equation

$$R = \frac{\Delta U}{I}, \tag{7.1}$$

where ΔU is the difference in the electrical potential between these two points and I is the constant direct electrical current of 10 A.
The influence of the temperature on the measured electrical resistance is taken into account. Since the attachment of the potential thermocouples by welding is subjected to positioning errors, an additional corrective procedure is necessary. The difference between the real and the assumed position of the thermocouples is several tenths of a millimetre. These errors can be divided into errors parallel and perpendicular to the crack (see Bauschke & Schwalbe 1985). The influence of the positioning errors parallel to the crack on the measured electrical resistance can be neglected. On the other hand, the influence of the positioning errors perpendicular to the crack needs to be taken into account. The influence of this type of errors is corrected by virtue of a linear interpolation method.
The results of both the finite element analysis and the experiments for all three types of specimen are represented in Figures 7.2 and 7.3 as a dimensionless plot of the electrical resistance ratio R/R_0 against a/w. R_0 is the electrical resistance at the initial crack length $2a_0$, R is the electrical resistance at the crack length $2a$ and w is the half width of the specimen at the crack height. In the case of the plain specimen with a hole, the initial crack length is equal to the hole diameter of 1 mm. For the plain specimen with both side notches $2a_0$ is equal to two notch depths of 0.2 mm each. The initial crack length is equal to zero for the experiments with a circular specimen. The half width w is 5 mm for the plain specimen and 75 mm for the circular specimen.
Figures 7.2a and 7.2b show the results for the plain specimen with a hole and for the plain specimen with both side notches, respectively. The results for the circular specimen with the straight crack and for the circular specimen with the kinked crack are presented in Figures 7.3a and 7.3b. All figures show a good agreement between the experimental results and the numerical solution.
The results of the numerical solution for the electrical resistance evolution during the crack propagation and the appropriate experimental measurement data provide the possibility to use the relationship between the evolution of the electrical resistance and the corresponding crack length during the identification of the material parameters based on the material model introduced in Section 3.3. This relationship is determined using the best fit method.

7.2 Results of the parameter identification

The required material parameters for the brittle damage material model described in Section 3.3 are summarised in Table 7.1. In all numerical calculations first three material parameters are chosen as constant values

$$E = 210 \text{ GPa}, \quad \nu = 0.3, \quad \sigma_e = 300 \text{ MPa}.$$

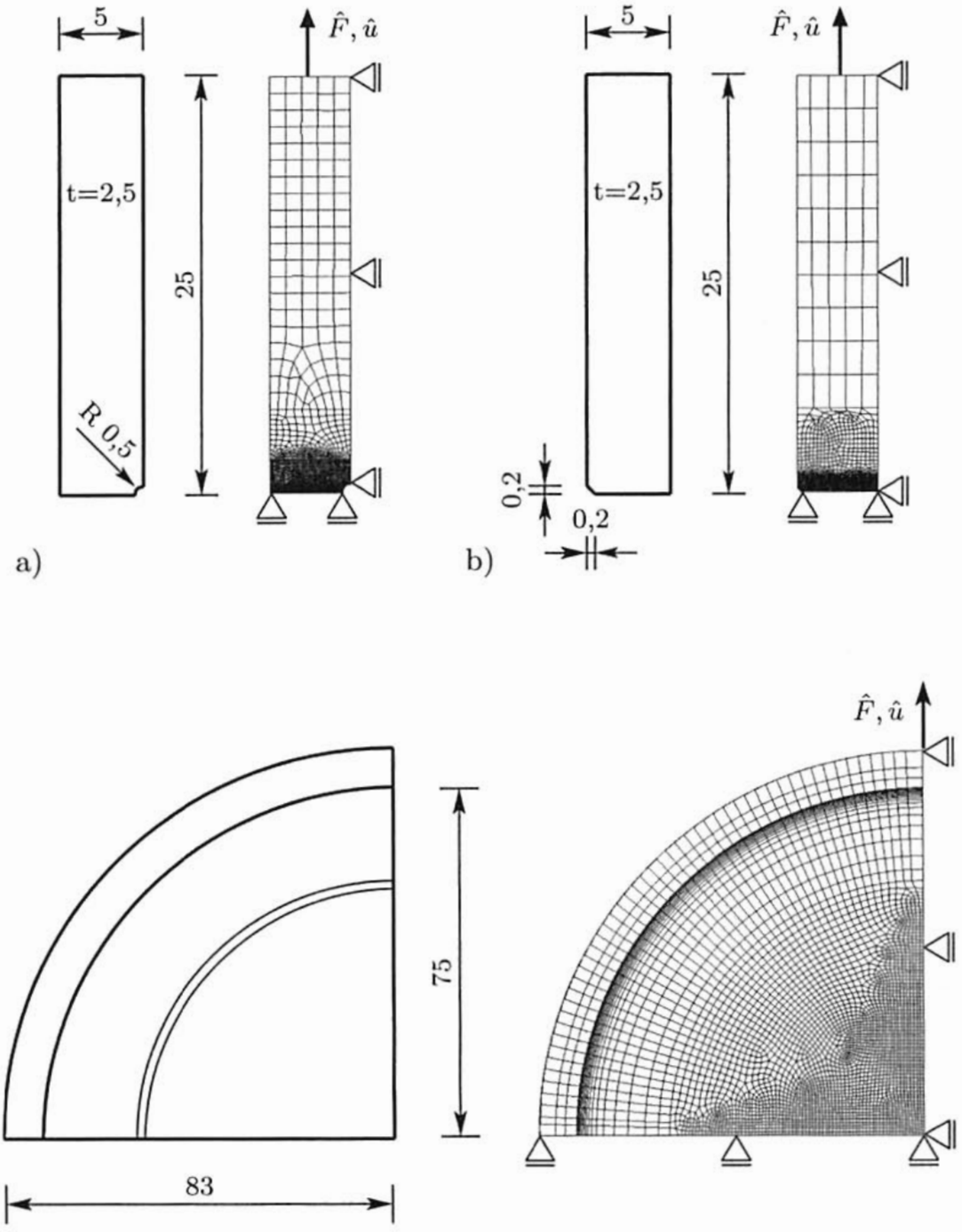

Figure 7.4: Geometry and mesh discretisation of: a) plain specimen with a hole, b) plain specimen with both side notches and c) circular specimen (dimensions in mm)

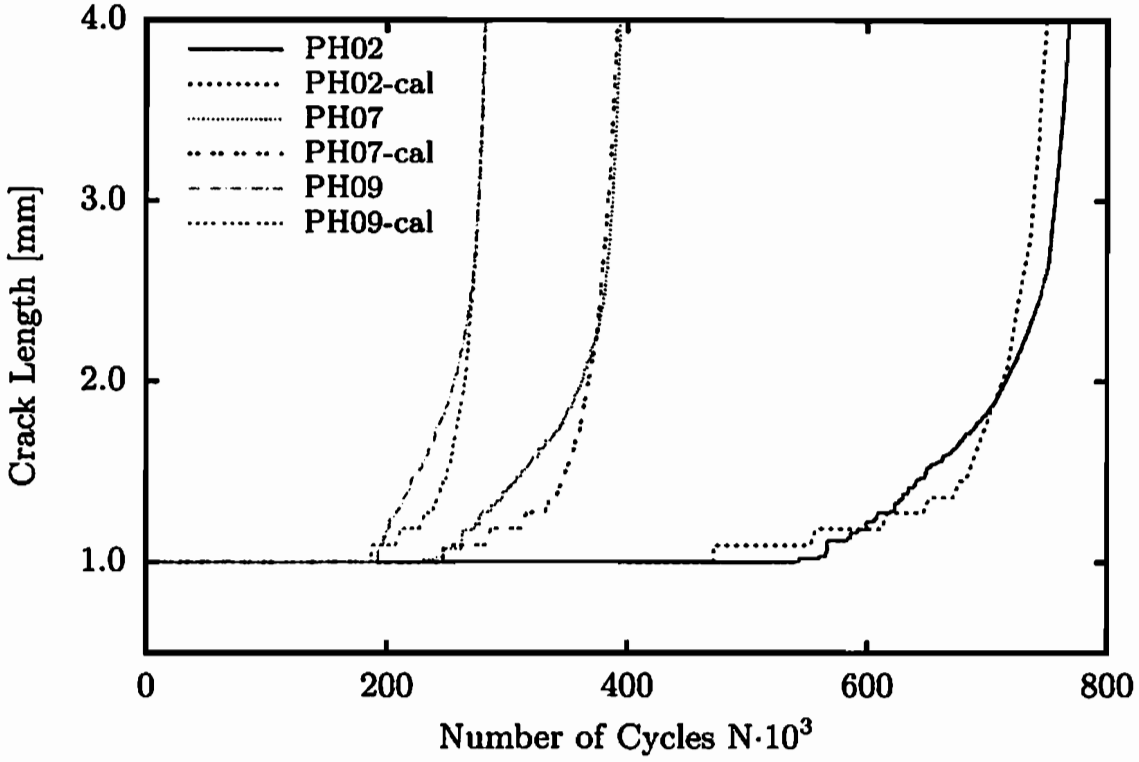

(a) Crack propagation

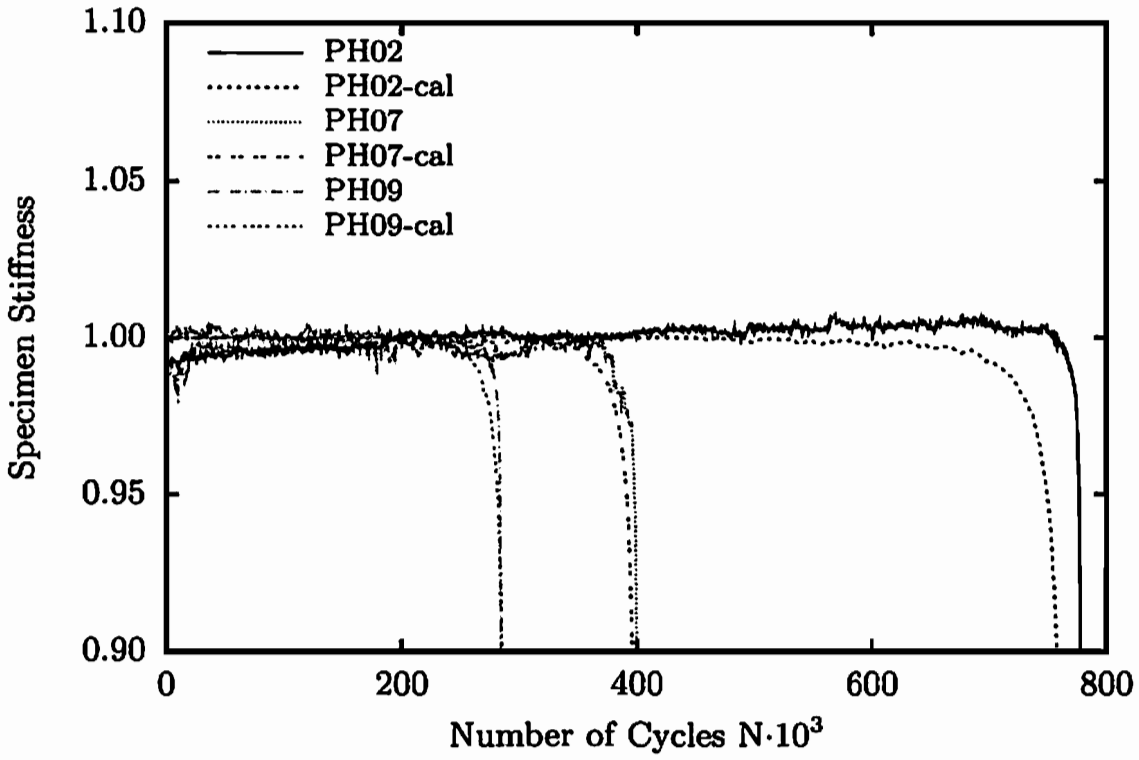

(b) Normalised specimen stiffness

Figure 7.5: Plain specimen with a hole

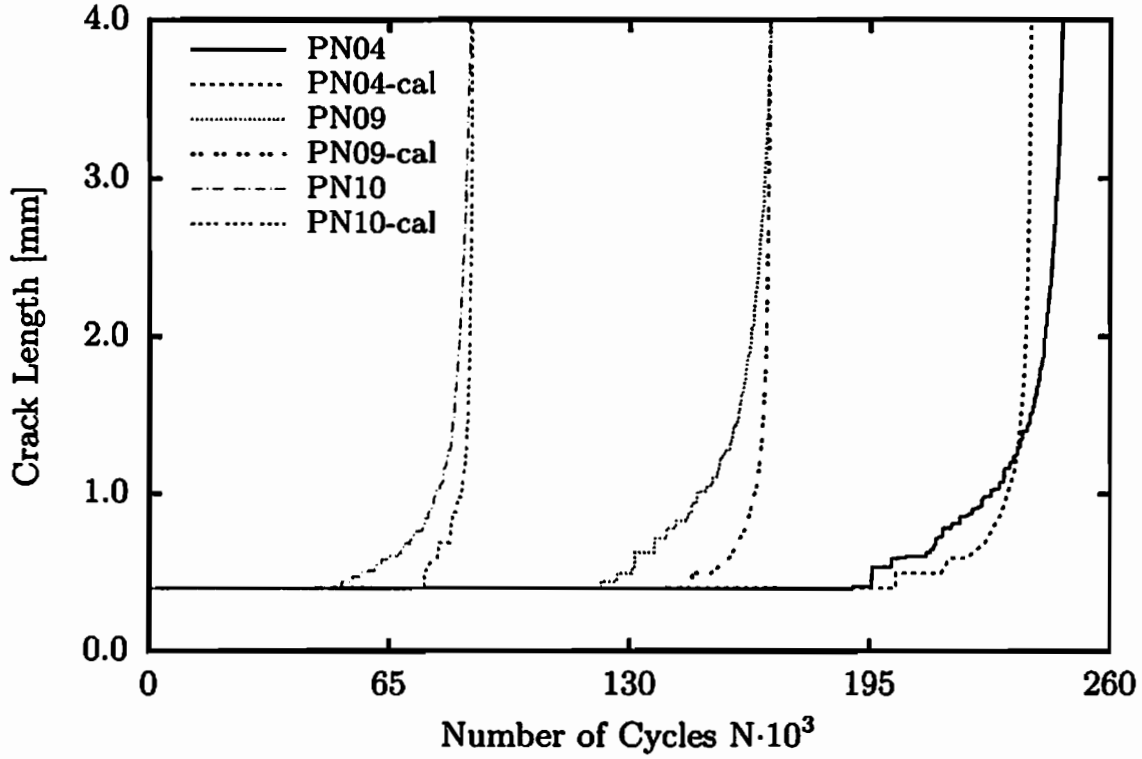

(a) Crack propagation

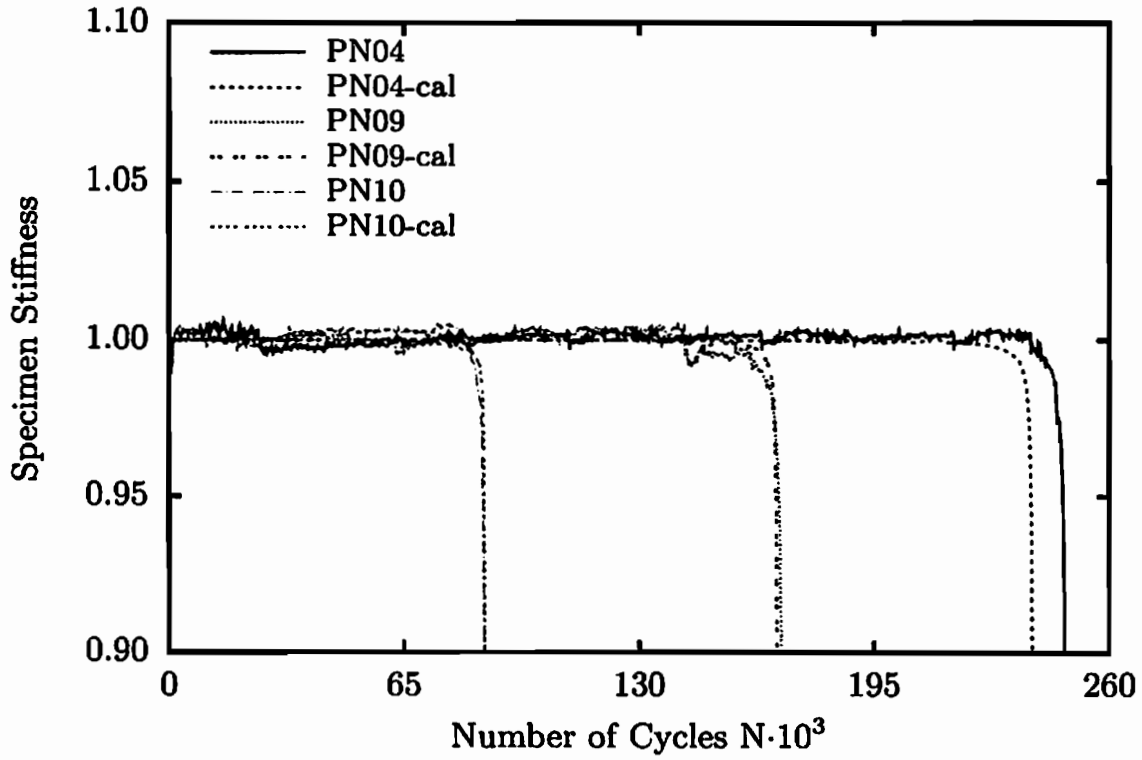

(b) Normalised specimen stiffness

Figure 7.6: Plain specimen with both side notches

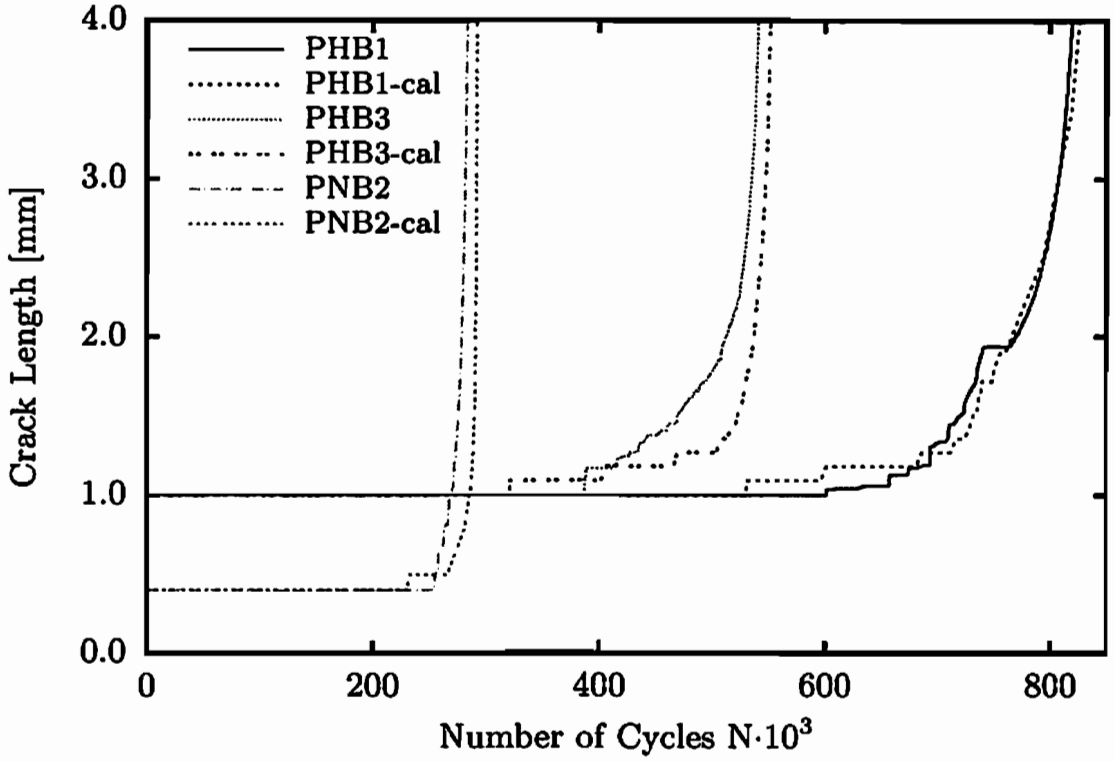

(a) Crack propagation

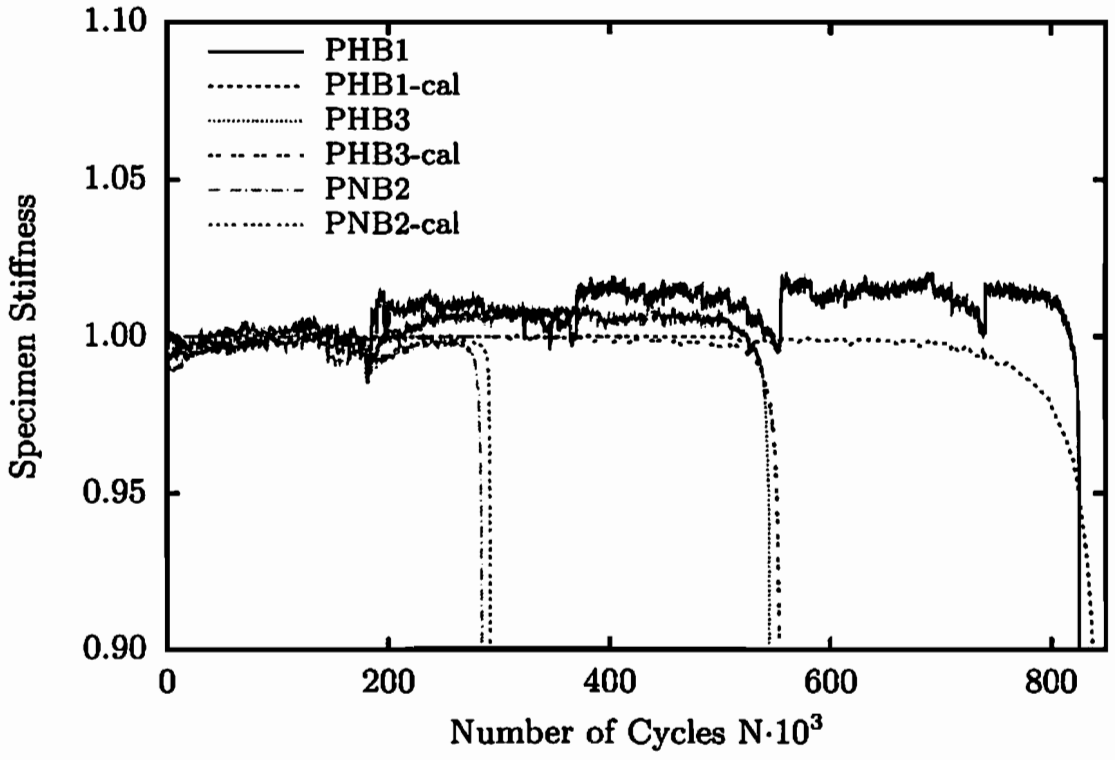

(b) Normalised specimen stiffness

Figure 7.7: Plain specimen - block program experiments

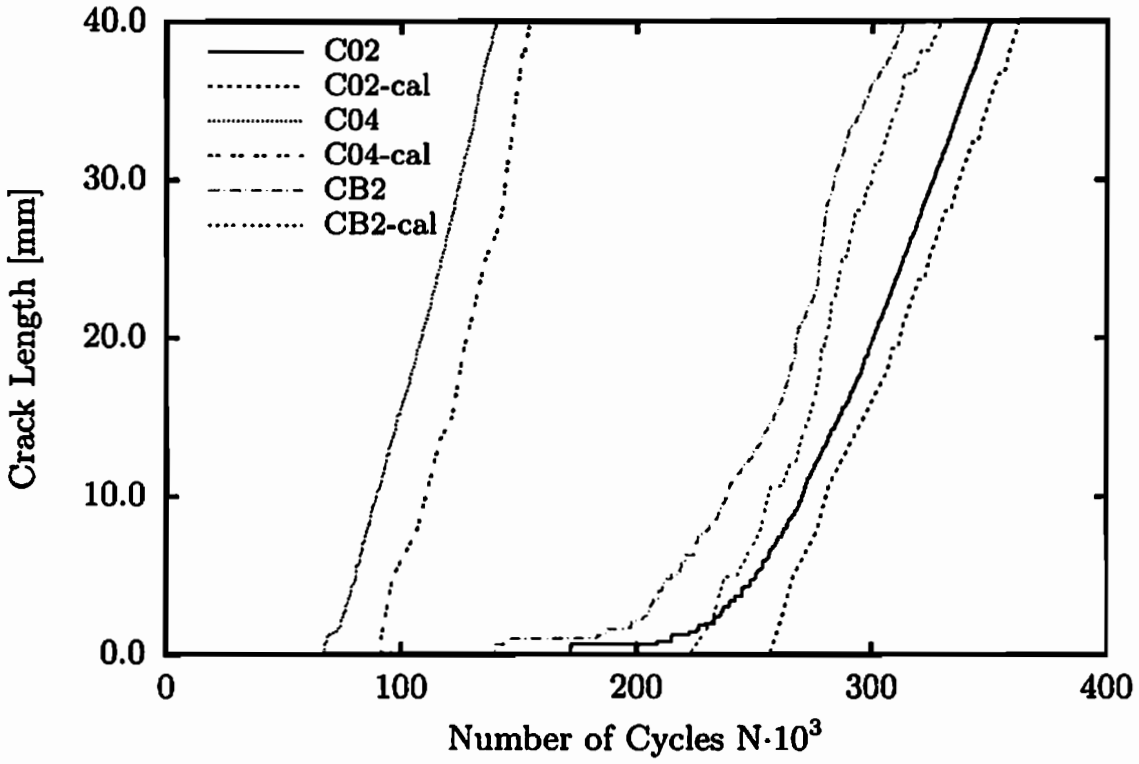

(a) Crack propagation

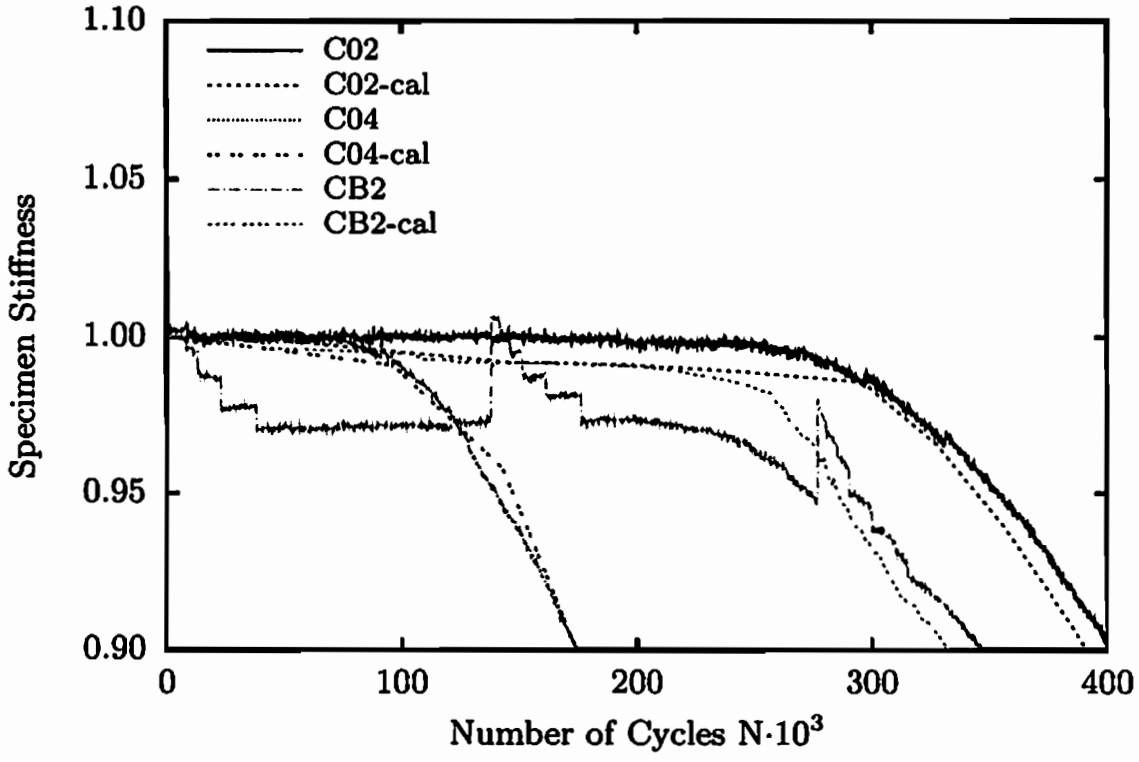

(b) Normalised specimen stiffness

Figure 7.8: Circular specimen

Symbol	Material parameter	Measuring unit
E	Young's modulus	GPa
ν	Poisson's ratio	-
σ_e	Endurance limit	MPa
C'	Paris' law material parameter	$\mathrm{Nmm}^{-(1+2\eta)}$
η	Paris' law material parameter	-

Table 7.1: Summary of material parameters

Specimen type	C'	η
Plain specimen - hole	4.000	0.001625
Plain specimen - notch	5.625	0.235000
Circular specimen	2.150	0.000152

Table 7.2: Paris' law material parameters

The other two material parameters, C' and η, are estimated on account of error minimisation between the calculated and the measured material response. For this purpose, two groups of measured data are used. The first group represents the evolution of the global specimen stiffness during the service life of specimen discussed in Chapter 6. The second group expresses the evolution of the crack propagation during the service life. It is calculated by virtue of the electrical resistance evolution given in Chapter 6 and the relationship between the evolution of the electrical resistance and the crack growth introduced in Section 7.1.
Unknown material parameters are separately determined for the plain specimen and the circular specimen. For their estimation, displacement controlled experiments with constant load amplitude are used. The resulting sets of material parameters for all specimen geometries are listed in Table 7.2. In order to validate these parameter sets, the block program experiments are recalculated, and experimental and numerical results are compared.
The numerical analyses are performed using the finite element software ANSYS, in which the material model according to Schütte (2001) is implemented. Geometry of the numerical model in the case of the plain specimen is chosen using only the strait part of the specimen and symmetry about all three planes. The geometry is given in Figure 7.4a and b for plain specimen with a hole and both side notches, respectively. In the case of circular specimen, symmetry about two planes is used and geometry of the numerical model is given in Figure 7.4c. Non-constant thickness of the circular numerical model coresponds to the geometry given in Figure 5.2. All models are meshed using 3D 8-node hexahedral elements. Number of generated hexahedral elements was 9320 for the plain specimen with

a hole, 6476 for the plain specimen with both side notches and 9562 in the case of the circular specimen. All three numerical models are given in Figure 7.4. The results of the numerical analyses and of the experiments are summarised in Figures 7.5 to 7.8. In all figures diagram (a) shows the evolution of the crack propagation and diagram (b) represents the evolution of the global specimen stiffness. The results for displacement controlled experiments for the plain specimen with a hole and with both side notches are plotted in Figure 7.5 and 7.6, respectively. Figure 7.7 shows the results for the block program experiments in the case of a plain specimen. Results for single constant amplitude experiments and a block program experiment for circular specimen are given in Figure 7.8. All figures show a good agreement between experimental and numerical results. Hence, it can be concluded that the applied brittle damage material model developed by Schütte (2001) is in a position to accurately predict the damage evolution in the case of the constant amplitude loading during the service life, as well as for the block program experiments for different specimen geometries.

8 Conclusions and outlook

In this thesis, two nondestructive testing methods are used for the investigation of crack propagation during cyclic fatigue loading. These two methods are the measurement of acoustic emission and the measurement of electrical resistance. The experiments are performed to obtain a database of different measurements which can be used for the identification of material parameters in brittle damage material model (Schütte 2001). The experimental setup is designed such that a meaningful damage detection is feasible under appropriate load and boundary conditions.

Special attention is given to the best possible application of two chosen nondestructive methods in the investigation of crack growth. The reduction of background noise during the detection of acoustic emission is achieved by inserting two universal joints in the clamping device and by using the procedure, proposed by Vogelsang (2001), for the production of thermocouple junctions and welding thermocouples on the specimen surface. To enable measurement of electrical resistance the specimen and the rest of the experimental setup are decoupled.

All specimens used in these experiments are made from steel 42CrMo4. The fatigue crack growth is observed on two specimen geometries (plain and circular specimen). The cyclic fatigue load is applied only in the tension range, in the form of haversine with the stress ratios 0.05 and 0.25. The load is force and displacement controlled. In the case of displacement controlled experiments, system of three external displacement transducers is used to overcome the influence of additional rotational degrees of freedom from the applied universal joints. The experiments are executed either with the constant amplitude for the whole duration of the test, or as a block-test with the amplitude which is constant inside the block and differs between the blocks. In addition, the experiments with the load applied in two different directions are performed. Hence, the growth of kinked cracks is investigated. To perform this group of experiments, a completely new specimen geometry (circular specimen) with appropriate clamping jaw device is developed. The applied load amplitude levels are chosen in the range that leads to the high cycle fatigue with the brittle damage. This damage behaviour is in agreement with the material model used for the material parameter identification.

Acoustic emission is detected using two types of acoustic emission transducers with appropriate preamplifiers. The wideband transducers and resonant piezoelectric transducers are applied in the investigation of frequency range at which acoustic emission occurs.

The electrical resistance is measured in three directions in the experiments with

circular specimen. To perform these measurements, an additional control process engaging an automatic gauge head selector switch is developed. For the purpose of correction of the temperature influence on the electrical resistance and for the numerical calculation of the distribution of electrical potential, the specific electrical resistance and temperature coefficient of specific electrical resistance are experimentally determined.

The high resolution CCD camera is used for the documentation of macroscopic crack propagation. The photographs from this camera enabled the measurement of the crack length with maximum resolution of 12.5 μm. These results are used to establish the relationship between the evolution of electrical resistance and the crack propagation.

The calculation of global specimen stiffness, based on the recorded data of the force measurement and averaged elongation of the specimen, is used for the comparison with the measured values from nondestructive testing methods.

The relationship between the evolution of electrical resistance and the crack length is validated using the numerical calculation of the distribution of electrical potential across the damaged specimen with different crack lengths. After this validation, the determination of material parameters for the brittle damage material model is performed, using the results of evolution of global specimen stiffness during service life and the relationship between the evolution of electrical resistance and the crack propagation.

The following conclusions can be made based on the experimental results obtained using the proposed measurement methods.

It is possible to observe the decrease of specimen stiffness in a relatively late phase of the service life from the results of the evolution of global specimen stiffness. This indicates that the change of specimen stiffness is related to the macroscopic crack initiation and propagation, and the changes on the microscale level, such as microcrack initiation and propagation, cannot be detected based on the change of the global specimen stiffness.

The investigation of the frequency range at which damage evolution occurs shows that most of acoustic emission event counts have the frequency between 50 and 250 kHz. For given experimental conditions, a huge part of acoustic emission from the damage evolution occurs with an amplitude between 40 and 70 dB. The time difference measurement method enables the determination of origin of acoustic emission. The experimental results show that most events are located at the position where the crack is present, confirming that the acoustic emission is from the crack growth. Measurements of acoustic emission indicate that acoustic waves are emitted during the whole damage process. The low acoustic emission output is evident during the initial cycles. This is followed by a period with almost no acoustic emission, when damage accumulation gives rise to the long crack-initiation lifetime. With the macrocrack initiation and propagation, the significant increase in the acoustic emission output is detected. Based on the results of the measurement of acoustic emission, it can be concluded that this method is suitable for the qualitative identification of the fatigue damage which

includes recognition of the macrocrack initiation and its propagation. However, the implementation of some alternative methods, such as measurement of electrical resistance, is recommended for the quantitative analysis of the fatigue damage.

The evolution of electrical resistance has a similar form to the evolution of the specimen stiffness. However, it is shown that the electrical resistance indicates changes in the microstructure of the specimen significantly earlier. It can be concluded that the method of measurement of the electrical resistance is capable of detecting the damage evolution in the early phase of the service life and it enables the formulation of the damage evolution on the basis of the microcrack growth. Furthermore, the investigation of the electrical resistance evolution in different directions shows that the direction of the fastest increase of electrical resistance is the direction perpendicular to the crack propagation. With the inclination from this direction, the rate of change of electrical resistance decreases. Nevertheless, measuring in other directions does not lead to any loss of valuable information about the crack propagation.

The relationship between the evolution of electrical resistance and the crack propagation during the service life of the specimen is evaluated from the measured data. Subsequently, this relationship is confirmed with the numerical calculations using a finite element analysis software. Furthermore, based on these results and the evolution of global specimen stiffness, the material parameters from brittle damage material model are identified. The achieved material parameters are used for the recalculation of experiments. The results obtained from the numerical analysis are in good agreement with the experimental results of evolution of global specimen stiffness and crack propagation.

The presented work may be extended in a number of ways. In the case of measurement of acoustic emission, the implementation of miniature acoustic emission transducers could lead to the better detection of acoustic emission sources during damage evolution on small specimens. Measurement of electrical resistance can be performed between more points, which can lead to the better understanding of the change of electrical potential field during damage evolution. Further experiments with the loading in different directions can be performed, in order to get better overlook of the crack propagation under mixed-mode loading. To investigate the application of these two nondestructive methods in the process of detection of fatigue damage in structures with complex geometry, the experiments could be extended to the cyclic loaded beams and frames.

A Investigation of sample rate by data acquisition

The comparative investigation with different sample rates is performed in order to get the optimal combination of the qualitative acquisition of wave form signals according to the applied cyclic load frequency and the amount of recorded data. The analysis is applied on both specimen forms and for both displacement and force controlled loading. The results for plain and circular specimen are presented in Figures A.1 and A.2, respectively. The figures represent the plots of applied load amplitude and load amplitude ratio, which is calculated as the ratio between the measured and the applied load amplitude.
The measured data are recorded with sample rates 100, 150 and 200 Hz in the case of plain specimen, and with sample rates 75, 100, 150 and 200 Hz in the case of circular specimen. The results show a significantly better quality of the recorded data for sample rates 150 and 200 Hz than for other tested sample rates. Since the difference between quality of recorded data for sample rates 150 Hz and 200 Hz is relatively small, the sample rate of 150 Hz is adopted in all experiments due to the significantly larger amount of recorded data in the case of sample rate of 200 Hz.

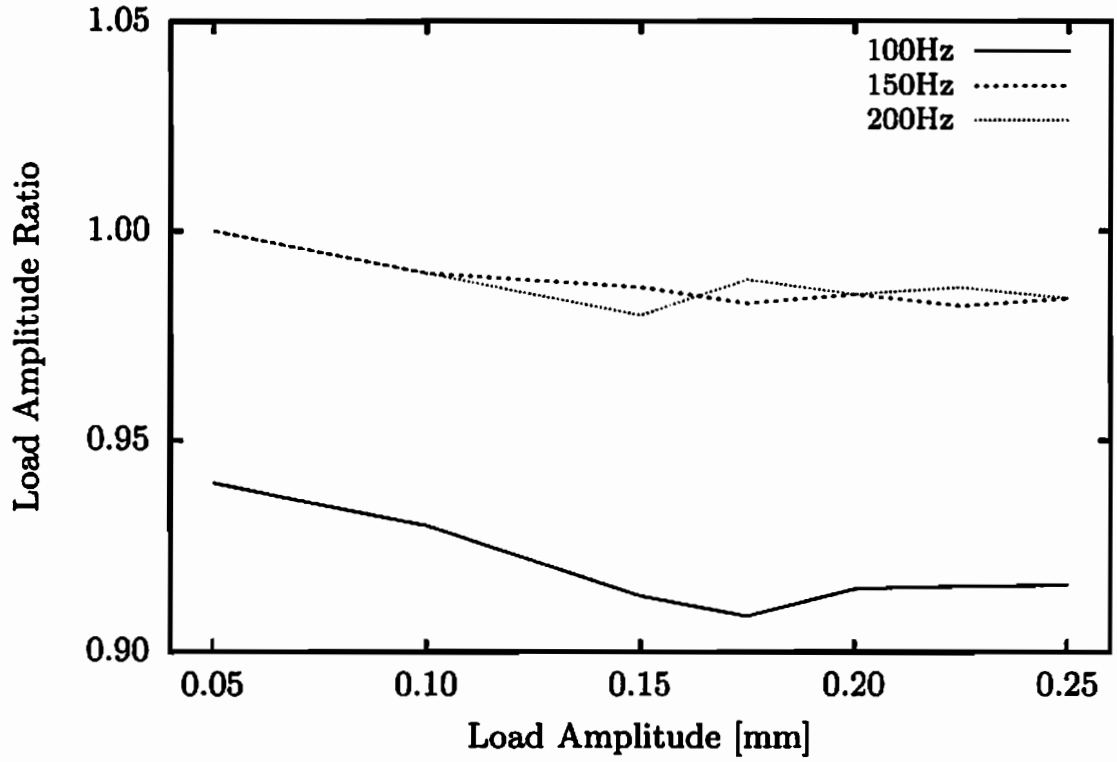

(a) Displacement controlled loading

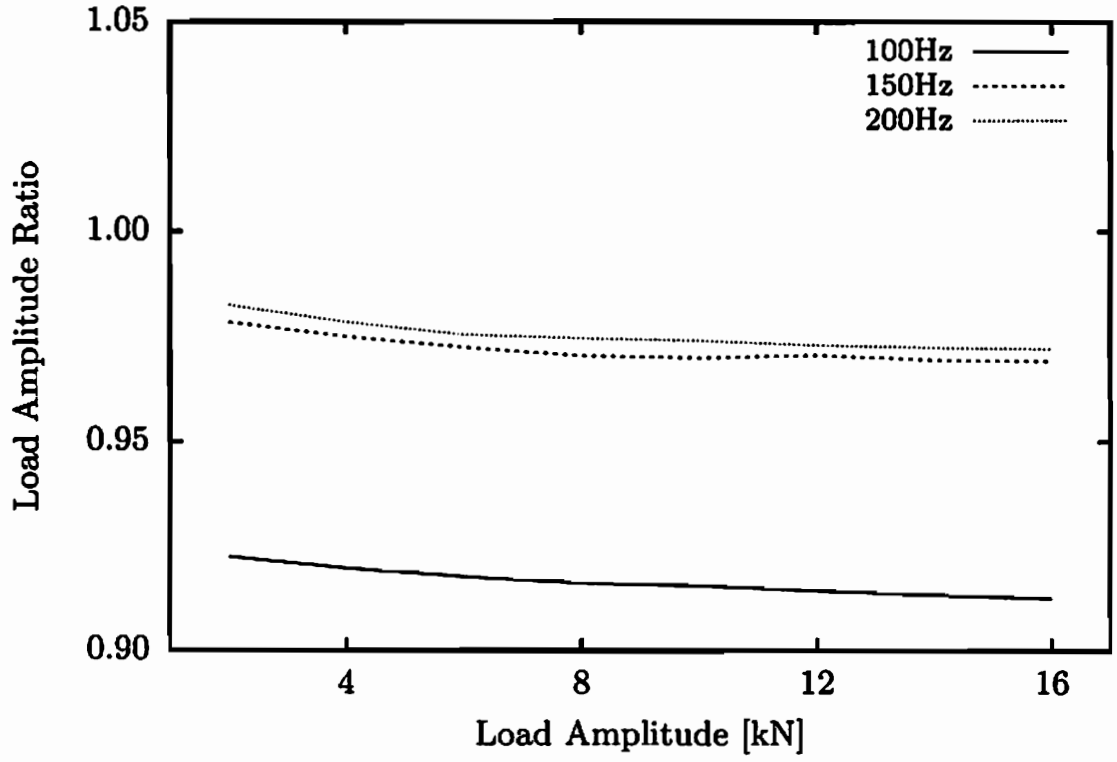

(b) Force controlled loading

Figure A.1: Plain specimen - sample rate

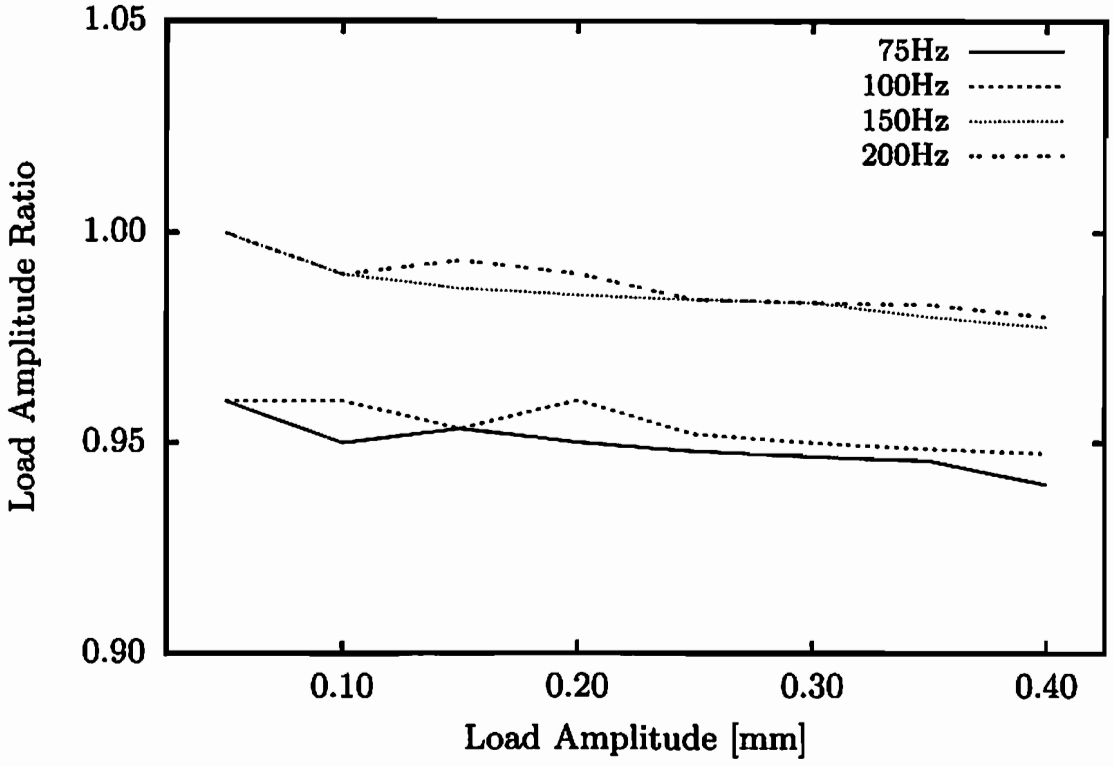

(a) Displacement controlled loading

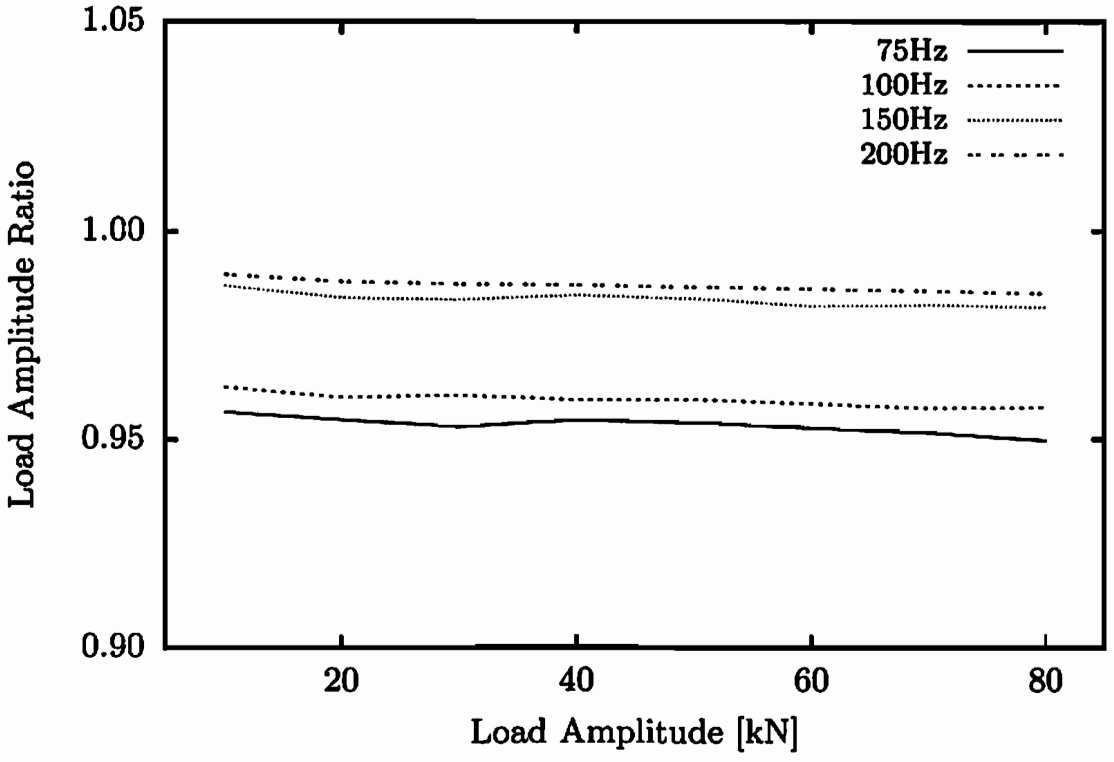

(b) Force controlled loading

Figure A.2: Circular specimen - sample rate

Bibliography

AMESTOY, M. & LEBLOND, J. B. (1992): *Crack paths in plane situations II. Detailed form of the expansion of the stress intensity factors*, in: International Journal of Solids and Structures, Volume 29, 465–501.

ANDERSON, R. (1925): *An Investigation on the Constitution, Heat Treatment, and Microstructure of Duralumin* 1925, Ph. D. thesis, Massachusetts Institute of Technology.

ASARO, R. & RICE, J. (1977): *Strain localization in ductile single crystals*, in: Journal of the Mechanics and Physics of Solids, Volume 25(5), 309–338.

BARNETT, W. J. & TROIONO, A. R. (1957): *Crack propagation in the hydrogen-induced brittle fracture of steel*, in: Journal of Metals, Volume 9, 486–494.

BARON, J. & YING, S. (1987): *Acoustic emission source location*, in: MCINTIRE, P. & MILLER, R. K. (Eds.): *Nondestructive Testing Handbook, Acoustic Emission Testing (second ed.)*, American Society for Nondestructive Testing 1987, Volume 5, Chapter 6, pp. 135–154.

BASQUIN, O. H. (1910): *The exponential law of endurance tests*, in: Proceedings of the American Society for Testing and Materials, Volume 10, 625–630.

BASSIM, M. N. (1987): *Macroscopic origins of acoustic emission*, in: MCINTIRE, P. & MILLER, R. K. (Eds.): *Nondestructive Testing Handbook, Acoustic Emission Testing (second ed.)*, American Society for Nondestructive Testing 1987, Volume 5, Chapter 2, pp. 46–61.

BAUSCHKE, H. M. & SCHWALBE, K. H. (1985): *Measurement of the depth of surface cracks using the Direct Current Potential Drop Method*, in: Materialwissenschaft und Werkstofftechnik, Volume 16(5), 156–165.

BELYTSCHKO, T., LIU, W. K. & MORAN, B. (2000): *Nonlinear finite elements for continua and structures*, John Wiley & Sons, Ltd. 2000.

BERKOVITS, A. & FANG, D. (1993): *Acoustic emission during fatigue of a nickel base superalloy*, in: Journal of Acoustic Emission, Volume 11(2), 85–94.

BERKOVITS, A. & FANG, D. (1995): *Study of fatigue crack characteristics by acoustic emission*, in: Engineering Fracture Mechanics, Volume 51(3), 401–416.

BETTEN, J. (1986): *Applications of tensor functions to the formulation of constitutive equations involving damage and initial anisotropy*, in: Engineering fracture mechanics, Volume 25(5-6), 573–584.

BILBY, B. & CARDEW, G. (1975): *The crack with a kinked tip*, in: International Journal of Fracture, Volume 11, 708–712.

BLUMENAUER, H. & PUSCH, G. (1993): *Technische Bruchmechanik (3 ed.)*, Deutscher Verlag für Grundstoffindustrie, Leipzig - Stuttgart 1993.

BROEK, D. (1991): *The practical use of fracture mechanics*, Kluwer Academic Publishers 1991.

BRUHNS, O. T., XIAO, H. & MEYERS, A. (1999): *Self-consistent Eulerian rate type elasto-plasticity models based upon the logarithmic rate*, in: International Journal of Plasticity, Volume 15, 479–520.

BRUHNS, O. T., XIAO, H. & MEYERS, A. (2003): *Some basic issues in traditional Eulerian formulation of finite elastoplasticity*, in: International Journal of Plasticity, Volume 19, 2007–2026.

CHABOCHE, J. L. (1981): *Continuous damage mechanics - A tool to describe phenomena before crack initiation*, in: Nuclear Engineering and Design, Volume 64(2), 233–247.

CHABOCHE, J. L. (1984): *Anisotropic creep damage in the framework of continuum damage mechanics*, in: Nuclear Engineering and Design, Volume 79(3), 309–319.

CHABOCHE, J. L. (1988): *Continuum damage mechanics: Part I: General concepts, Part II: Damage growth, crack initiation, and crack growth*, in: Journal of Applied Mechanics, Volume 55(3), 59–71.

CHOW, C. L. & LU, T. J. (1990): *A unified approach to fatigue crack propagation in metals and polymers*, in: Journal of Materials Science Letters, Volume 9(12), 1427–1430.

CHOW, C. L. & LU, T. J. (1992): *An analytical and experimental study of mixed-mode ductile fracture under monproportional loading*, in: International Journal of Damage Mechanics, Volume 1(2), 191–236.

CHOW, C. L. & WANG, J. (1987): *An anisotropic theory of elasticity for continuum damage mechanics*, in: International Journal of Fracture, Volume 33(1), 3–16.

CLASSEN-NEKLUDOWA, M. (1929): *Über die sprungartige Deformation*, in: Zeitschrift für Physik, Volume 55, 555–558.

COFFIN, L. F. (1954): *A study of the effects of cyclic thermal stresses on a ductile metal*, in: Transactions of the American Society of Mechanical Engineers, Volume 76, 931–950.

CORDEBOIS, J. P. & SIDOROFF, F. (1979): *Damage induced elastic anisotropy*, in: BOEHLER, J. P. (Ed.): *Proceedings of the 115th European Mechanics Colloquium on Mechanical Behavior of Anisotropic Solids*, 1979, pp. 761–774.

CORDEBOIS, J. P. & SIDOROFF, F. (1982): *Endommagement anisotrope en élasticité et plasticité*, in: Journal de mécanique théorique et appliquée, Volume Numéro spécial, 45–60.

CZOCHRALSKI, J. (1917): *Fortschritte der Metallographie: Einfluss der Formänderung*, in: Stahl und Eisen, Volume 37(21), 502–504.

DIN 43722 (1994): *Thermopaare – Teil 3: Thermoleitungen und Ausgleichsleitungen, Grenzabweichungen und Kennzeichnungssystem (IEC 60584-3: 1989, modifiziert), Deutsche Fassung HD 446.3 S1: 1989*, DIN Deutsches Institut für Normung e.V.

DIN EN 10083-3 (2007): *Vergütungsstähle - Teil 3: Technische Lieferbedingungen für legierte Stähle; Deutsche Fassung EN 10083-3:2006*, DIN Deutsches Institut für Normung e.V.

DIN EN 60584-2 (1994): *Thermopaare – Teil 2: Grenzabweichungen der Thermospannungen (IEC 584-2: 1982 + A1: 1989), Deutsche Fassung EN 60584-2: 1993*, DIN Deutsches Institut für Normung e.V.

DONAHUE, R. J., CLARK, H. M. I., ATANMO, P., KUMBLE, R. & MCEVILY, A. J. (1972): *Crack opening displacement and the rate of fatigue crack growth*, in: International Journal of Fracture, Volume 8, 209–219.

DOWLING, N. E. & BEGLEY, J. A. (1976): *Fatigue Crack Growth During Gross Plasticity and the J-Integral*, in: ASTM STP 590. American Society for Testing and Materials, , 82–106.

DROUILLARD, T. F. (1987): *Introduction to acoustic emission technology*, in: MCINTIRE, P. & MILLER, R. K. (Eds.): *Nondestructive Testing Handbook, Acoustic Emission Testing (second ed.)*, American Society for Nondestructive Testing 1987, Volume 5, pp. 1–10.

DRUCKER, D. C. & PRAGER, W. (1952): *Soil mechanics and plastic analysis or limit design*, in: Quarterly of Applied Mathematics, Volume 10, 157–165.

DUFAILLY, J. & LEMAITRE, J. (1995): *Modeling very low cycle fatigue*, in: International Journal of Damage Mechanics, Volume 4, 153–170.

DUNEGAN, H. & HARRIS, D. (1969): *Acoustic emission - a new nondestructive testing tool*, in: Ultrasonics, Volume 7(3), 160–166.

DUNEGAN, H., HARRIS, D. & TATRO, C. (1968): *Fracture analysis by use of acoustic emission*, in: Engineering Fracture Mechanics, Volume 1(1), 105–110.

EGLE, D. (1987): *Wave propagation*, in: MCINTIRE, P. & MILLER, R. K. (Eds.): *Nondestructive Testing Handbook, Acoustic Emission Testing (second ed.)*, American Society for Nondestructive Testing 1987, Volume 5, Chapter 2, pp. 46–61.

ERDOGAN, F. & RATWANI, M. (1970): *Fatigue and fracture of cylindrical shells containing a circumferential crack*, in: International Journal of Fracture, Volume 6(4), 379–392.

FANG, D. & BERKOVITS, A. (1994): *Evaluation of fatigue damage accumulation by acoustic emission*, in: Fatigue Fracture of Engineering Materials Structures, Volume 17(9), 1057–1067.

FANG, D. & BERKOVITS, A. (1995): *Fatigue design model based on damage mechanisms revealed by acoustic emission measurements.*, in: Journal of Engineering Materials and Technology, Volume 117, 200–208.

FORMAN, R., KEARNEY, V. & ENGLE, R. (1967): *Numerical analysis of crack propagation in a cyclic-load structure*, in: Journal of Basic Engineering, Volume 89D, 459–464.

GANGLOFF, R. P. (1981): *Electrical potential monitoring of crack formation and subcritical growth from small defects*, in: Fatigue and Fracture of Engineering Materials and Structures, Volume 4(1), 15–31.

GDOUTOS, E. E. (1993): *Fracture mechanics: an introduction*, Kluwer Academic Publishers 1993.

GERBER, H. (1874): *Bestimmung der Zulässigen Spannungen in Eisenkonstruktionen*, in: Zeitschrift des Bayerischen Architeckten und Ingenieur-Vereins, Volume 6, 101–110.

GOODMAN, J. (1899): *Mechanics applied to engineering*, London: Longmans Green 1899.

GRABE, C. (2007): *Experimental testing and parameter identification on the multidimensional material behavior of shape memory alloys* 2007, Ph. D. thesis, Mitteilung aus dem Institut für Mechanik, Ruhr-Universität Bochum, Nr. 142.

GREEN, A., BLACKBURN, P., CRAIG, B., CROSS, N., FERDINAND, M., FOWLER, T. & ROBINSON, D. (1987): *Acoustic emission applications in the petroleum and chemical industries*, in: MCINTIRE, P. & MILLER, R. K. (Eds.): *Nondestructive Testing Handbook, Acoustic Emission Testing (second ed.)*, American Society for Nondestructive Testing 1987, Volume 5, Chapter 7, pp. 155–223.

GRIFFITH, A. A. (1921): *The phenomena of rupture and flow in solids*, in: Philosophical Transactions of Royal Society of London, Volume A221, 163–198.

GRIFFITH, A. A. (1924): *Theory of rupture*, in: *Proceedings of the First International Congress for Applied Mechanics*, 1924, Volume 1, pp. 55–63.

GROSS, D. & SEELIG, T. (2006): *Fracture Mechanics: With an Introduction to Micromechanics*, Springer-Verlag 2006.

GURSON, A. (1977): *Continuum thery of ductile rupture by void nucleation and growth: Part I - Yield criteria and flow rules for porous ductile media*, in: Journal of Engineering Materials and Technology, Volume 99, 2–15.

HAIBACH, E. (1970): *Modifizierte lineare Schadensakkumulations-Hypothese zur Berücksichtigung des Dauerfestigkeitsabfalls mit fortschreitender Schädigung*, Technical report, Technische Mitteilung Nr.50/70 des Laboratoriums für Betriebsfestigkeit, 1970.

HAIBACH, E. (2002): *Betriebsfestigkeit*, Springer 2002.

HAIBACH, E. & LEHRKE, H. (1976): *Das Verfahren der Amplitudentransformation zur Lebensdauerberechnung bei Schwingbeanspruchung*, in: Archiv für Eisenhüttenwesen, Volume 47(10), 623–628.

HAIGH, J. R., SKELTON, R. P. & RICHARDS, C. E. (1976): *Oxidation-assisted crack growth during high cycle fatigue of a 1%Cr-Mo-V steel at 550° C*, in: Materials Science and Engineering, Volume 26(2), 167–174.

HALFORD, G. R. (1997): *Cumulative fatigue damage modeling - crack nucleation and early growth*, in: International Journal of Fatigue, Volume 19(93), S253–S260.

HEIDERICH, M. (2004): *Ein Beitrag zur zerstörungsfreien Schädigungsanalyse* 2004, Ph. D. thesis, Mitteilung aus dem Institut für Mechanik, Ruhr-Universität Bochum, Nr. 133.

HICKS, M. & PICKARD, A. (1982): *A comparison of theoretical and experimental methods of calibrating the electrical potential drop technique for crack length determination*, in: International Journal of Fracture, Volume 20, 91–101.

HILL, R. (1968): *On constitutive inequalities for simple materials-I*, in: Journal of the Mechanics and Physics of Solids, Volume 16(4), 229–242.

HOLMYARD., E. & LITT, D. (1928): *The Works of Gerber, Englished by Richard Russel, A New Edition with Introduction*, J.M. Dent and Sons Ltd., London and E.P. Dutton and Company, New York N.Y. 1928.

HOPWOOD, T. & MCGOGNEY, C. (1987): *Acoustic emission application in civil engineering*, in: MCINTIRE, P. & MILLER, R. K. (Eds.): *Nondestructive Testing Handbook, Acoustic Emission Testing (second ed.)*, American Society for Nondestructive Testing 1987, Volume 5, Chapter 10, pp. 312–345.

HSU, N. N. & BRECKENBRIDGE, F. R. (1979): *Characterization and Calibration of Acoustic Emission Sensors*, in: Materials evaluation, Volume 39, 60–68.

HUANG, M., JIANG, L., LIAW, P., BROOKS, C., SEELEY, R. & KLARSTROM, D. (1998): *Using acoustic emission in fatigue and fracture materials research*, in: JOM: The Journal of the Minerals, Metals & Materials Society, Volume 50(11), online.

HUTCHINSON, J. W. (1968): *Singular behaviour at the end of a tensile crack in a hardening material*, in: Journal of the Mechanics and Physics of Solids, Volume 16(1), 13–31.

IKEDA, K., YOSHIMI, M. & MIKI, C. (1991): *Electrical potential drop method for evaluating crack depth*, in: International Journal of Fracture, Volume 47, 25–38.

IRWIN, G. (1957): *Analysis of stress and strain states near the end of a crack transversing a plate*, in: Journal of Applied Mechanics, Volume 24, 361–364.

JOHNSON, H. H. (1965): *Calibrating the electric potential method for studying slow crack growth*, in: Materials Research and Standards, Volume 5, 442–445.

KACHANOV, L. M. (1958): *Rupture time under creep conditions*, in: Izvestia akademii nauk SSSR, Otd. Tekhn. Nauk,, Volume 8, 26–31.

KACHANOV, M. (1992): *Effective elastic properties of cracked solids*, in: Applied Mechanics Reviews, Volume 45(8), 304–335.

KAISER, J. (1950): *Untersuchungen über das Auftreten von Geräuschen beim Zugversuch* 1950, Ph. D. thesis, Technische Hochschule München.

KAISER, J. (1953): *Erkenntnisse und Folgerungen aus der Messung von Geräuschen bei Zugbeanspruchung von metallischen Werkstoffen*, in: Archiv für Eisenhüttenwesen, Volume 24(1-2), 43–45.

KLESNIL, M. & LUKAŠ, P. (1972): *Effect of stress cycle asymmetry on fatigue crack growth*, in: Materials Science and Engineering, Volume 9, 231–240.

KÖRTVÉLYESSY, L. (1998): *Thermoelement Praxis: neue theoretische Grundlagen und deren Umsetzung*, 3. Edition, Vulkan-Verlag Essen 1998.

LE, K. C. (1989): *Equilibrium criterion for a nonlinear elastic slitted body*, in: SALAMA, K. & RAVI-CHANDAR, K. (Eds.): *Advances in Fracture Research*, Oxford: Pergamon Press 1989, pp. 49–53.

LE, K. C. (1990): *Variational principles of non-linear theory of brittle fracture*, in: Journal of Applied Mathematics and Mechanics, Volume 54, 543–549.

LE, K. C., SCHÜTTE, H. & STUMPF, H. (1998): *Dissipative driving force in ductile crystals and the strain localization phenomenon*, in: International Journal of Plasticity, Volume 14(10-11), 1109–1131.

LE, K. C., SCHÜTTE, H. & STUMPF, H. (1999): *Determination of the driving force acting on a kinked crack*, in: Archive of Applied Mechanics, Volume 69, 337–344.

LEBLOND, J. (1993): *Crack kinking and curving in three-dimensional elastic solids application to the study of crack path stability in hydraulic fracturing*, in: ROSSMANITH, H. P. & MILLER, K. J. (Eds.): *Mixed-Mode Fatigue and Fracture*, Professional Engineering Publishing 1993, pp. 219–243.

LECKIE, F. A. & ONAT, F. T. (1981): *Tensorial Nature of Damage Measuring Internal Variables*, in: IUTAM Colloquium on Physical Nonlinearities in Structural Analysis, , 140–155.

LEMAITRE, J. (1996): *A course of damage mechanics*, Springer-Verlag Berlin Heiderberg 1996.

LEMAITRE, J. & CHABOCHE, J. L. (1990): *Mechanics of solid mateterials*, Cambridge university press 1990.

LOWES, J. M. & FEATNEHOUGH, G. D. (1971): *The detection of slow crack growth in crack opening displacement specimens using an electrical potential method*, in: Engineering Fracture Mechanics, Volume 3(2), 103–108.

MALVERN, L. E. (1969): *Introduction to the mechanics of a continuous medium*, Prentice-Hall, Inc., Englewood Cliffs, New Jersey 1969.

MANSON, S. S. (1953): *Behavior of materials under conditions of thermal stress*, in: *Proceedings of Heat Transfer Symposium*, University of Michigan Press 1953, pp. 9–76.

MANSON, S. S. (1966): *Interfaces between fatigue, creep, and fracture*, in: International Journal of Fracture, Volume 2(1), 327–363.

MANSON, S. S. & HALFORD, G. R. (1981a): *Practical implementation of the double linear damage rule and damage curve approach for treating cumulative fatigue damage*, in: International Journal of Fracture, Volume 17(2), 169–192.

MANSON, S. S. & HALFORD, G. R. (1981b): *Practical implementation of the double linear damage rule and damage curve approach for treating cumulative fatigue damage*, in: International Journal of Fracture, Volume 17(4), R35–R42.

MANSON, S. S. & HALFORD, G. R. (1986): *Re-examination of cumulative fatigue damage analysis - an engineering perspective*, in: Engineering fracture mechanics, Volume Volume 25, Issues 5-6, 539–571.

MARSDEN, J. E. & HUGHES, T. J. R. (1983): *Mathematical formulations of elasticity*, Dover Publications, Inc., Mineola, New York 1983.

MAUGE, C. & KACHANOV, M. (1994): *Effective elastic properties of an anisotropic material with arbitrarily oriented interacting cracks*, in: Journal of the Mechanics and Physics of Solids, Volume 42(4), 561–584.

MCKEIGHAN, P. C., ZHU, W. X. & SMITH, D. J. (1995): *A full field DC potential drop calibration for an asymmetrically cracked M(T) specimen*, in: Journal of Testing and Evaluation, Volume 23, 102–110.

MINER, M. (1945): *Cumulative damage in fatigue*, in: Journal of Applied Mechanics, Volume 12(3), A159–A164.

MOHR, O. (1900): *Welche umstände bedingen die elastizitätsgrenze und den bruch eines materials?*, in: Zeitschrift des Vereins Deutscher Ingenieure, Volume 24, 1524–1530.

MURAKAMI, S. (1988): *Mechanical modeling of material damage*, in: Journal of Applied Mechanics, Volume 55, 280–286.

MURAKAMI, S., HAYAKAWA, K. & LIU, Y. (1998): *Damage evolution and damage surface of elastic-plastic-damage materials under multiaxial loading*, in: International Journal of Damage Mechanics, Volume 7, 103–128.

MURAKAMI, S. & OHNO, N. (1981): *A continuum theory of creep and creep damage*, in: *A. R. S. Ponter und D. R. Hayhurst (Eds.) - Creep in Structures*, Springer-Verlag 1981, pp. 422–443.

MURAV'EV, V., STEPANOV, L., CHAPLYGIN, V., LEBEDEV, E., KOZHEMYAKIN, V., KAREEV, A. & KATARUSHKIN, S. (2002): *Study of growth of fatigue cracks in metallic samples using methods of acoustic emission and strain measurement*, in: The Russian Journal of Nondestructive Testing, Volume 38(11), 857–864.

MURAV'EV, V., STEPANOVA, L. & KAREEV, A. (2003): *Evaluation of the danger degree of fatigue cracks in the acoustic emission testing of cast pieces of a freight-car truck*, in: The Russian Journal of Nondestructive Testing, Volume 39(1), 54–59.

NAM, K. (1999): *Acoustic emission from surface fatigue cracks in SS41 steel*, in: Fatigue Fracture of Engineering Materials Structures, Volume 22, 1103–1109.

OGDEN, R. W. (1997): *Non-linear elastic deformations*, Dover Publications, Inc., Mineola, New York 1997.

PALMGREN, A. (1924): *Die Lebensdauer von Kugellagern*, in: VDI Zeitschrift, Volume 68, 339–341.

PARIS, P. C. (1962): *The growth of fatigue cracks due to variations in load* 1962, Ph. D. thesis, Lehigh University.

PARIS, P. C. & ERDOGAN, F. (1963): *A Critical Analysis of Crack Propagation Laws*, in: Journal of Basic Engineering, Volume 85, 528–534.

PARIS, P. C., GOMES, M. P. & ANDERSON, W. E. (1961): *A rational analytic theory of fatigue*, in: The Trend in Engineering, Volume 13, 9–14.

POLLOCK, A. A. (1968): *Stress-wave emission - a new tool for industry*, in: Ultrasonics, Volume 6(2), 88–92.

POLLOCK, A. A. (1989): *Acoustic emission inspection*, Volume 17, 9 Edition, ASM International 1989.

PORTEVIN., A. & LECHATELIER, F. (1923): *Sur un phénoméne observé lors de l´Essai de traction d´Alliges en cours de transformation*, in: Comptes Rendus Hebdomadaires des Seances de l´Academie des Siences, Volume 176, 507–510.

PROSSER, W. H. (1996): *Applications of Advanced, Waveform Based AE Techniques for Testing Composite Materials*, in: *Proceedings of the SPIE Conference on Nondestructive Evaluation Techniques for Aging Infrastructure and Manufacturing: Materials and Composites*, Scottsdale, Arizona 1996, pp. 146–153.

PROSSER, W. H. (1998): *Waveform Analysis of AE in Composites*, in: *Proceedings of the Sixth International Symposium on Acoustic Emission From Composite Materials*, San Antonio 1998, pp. 61–70.

PROSSER, W. H., JACKSON, K. E., KELLAS, S., SMITH, B. T., MCKEON, J. & FRIEDMAN, A. (1995): *Advanced, Waveform Based Acoustic Emission Detection of Matrix Cracking in Composites*, in: Materials Evaluation, Volume 53(9), 1052–1058.

RABOTNOV, Y. N. (1968): *Creep rupture*, in: *Proceedings of the 12th International Congress of Applied Mechanics*, 1968, pp. 342–349.

READ, D. T. & PFUFF, M. (1991): *Potential drop in the center-cracked panel with asymmetric crack extension*, in: International Journal of Fracture, Volume 48, 219–229.

RICE, J. R. (1968a): *Mathematical analysis in the mechanics of fracture*, in: LIEBOWITZ, H. (Ed.): *Fracture: An Advanced Treatise*, Academic Press, New York 1968, Volume 2, pp. 191–311.

RICE, J. R. (1968b): *A path independent integral and the aproximate analysis of strain concetration by notches and cracks*, in: Journal of Applied Mechanics, Volume 35, 379–386.

RICE, J. R. (1974): *Limitations to the small scale yielding approximation for crack tip plasticity*, in: Journal of the Mechanics and Physics of Solids, Volume 22, 17–26.

RICE, J. R. & ROSENGREN, G. F. (1968): *Plane strain deformation near a crack tip in a power-law hardening material*, in: Journal of the Mechanics and Physics of Solids, Volume 16(1), 1–12.

RITCHIE, R. O. (1977): *Influence of microstructure on near - threshold fatigue crack propagation in ultra-high strength steel*, in: Metal Science, Volume 11, 368–381.

RITCHIE, R. O. (1999): *Mechanisms of fatigue-crack propagation in ductile and brittle solids*, in: International Journal of Fracture, Volume 100, 55–83.

RITCHIE, R. O. & BATHE, K. J. (1979): *On the calibration of the electrical potential technique for monitoring crack growth using finite element methods*, in: International Journal of Fracture, Volume 15(1), 47–55.

RITCHIE, R. O., GARRETT, G. G. & KNOTT, J. F. (1971): *Crack-Growth monitoring: Optimisation of the electrical potential technique using an analogue method*, in: International Journal of Fracture, Volume 7, 462–467.

RITCHIE, R. O. & KNOTT, J. F. (1973): *Mechanisms of fatigue crack growth in low alloy steel*, in: Acta Metallurgica, Volume 21(5), 639–648.

SAXENA, A. (1980): *Electrical potential technique for monitoring subcritical crack growth at elevated temperatures*, in: Engineering Fracture Mechanics, Volume 13(4), 741–750.

SCHEIL, E. (1929): *Über die Umwandlung des Austenits in Martensit in gehärtetem Stahl*, in: Zeitschrift für Anorganische und Allgemeine Chemie, Volume 183, 98–120.

SCHOFIELD, B. H., BAREISS, R. A. & KYRALA, A. A. (1958): *Acoustic emission under applied stress*, Technical report, WADC Technical Report58-194. Boston, MA:Lessells and Associates, 1958.

SCHÜTTE, H. (2001): *Ein finites Modell für spröde Schädigung basierend auf der Ausbreitung von Mikrorissen* 2001, Ph. D. thesis, Mitteilung aus dem Institut für Mechanik, Ruhr-Universität Bochum, Nr. 128.

SCHÜTTE, H. & BRUHNS, O. T. (2002a): *On a geometrically nonlinear damage model based on a multiplicative decomposition of the deformation gradient and the propagation of microcracks*, in: Journal of the Mechanics and Physics of Solids, Volume 50, 827–853.

SCHÜTTE, H. & BRUHNS, O. T. (2002b): *On the prediction of lifetime with a microcrack growth based continuum damage model*, in: *International Symposium Anisotropic Behaviour of Damaged Materials 2002*, 2002.

SEVOSTIANOV, I., BOGARAPU, M. & TABAKOV, P. (2002a): *Correlation between elastic and electric properties for cyclically loaded metals*, in: International Journal of Fracture, Volume 118(4), L77–L82.

SEVOSTIANOV, I., KOVÁIK, J. & SIMANÍK, F. (2002b): *Correlation between elastic and electric properties for metal foams: Theory and Experiment*, in: International Journal of Fracture, Volume 114(4), L23–L28.

SIMO, J. C. & JU, J. W. (1987): *Strain- and stress-based continuum damage models - I Formulation*, in: International Journal of Solids and Structures, Volume 23(7), 821–840.

SKRZYPEK, J. & GANCZARSKI, A. (1999): *Modeling of material damage and failure of structures*, Berlin: Springer-Verlag 1999.

SMITH, K., WATSON, P. & TOPER, T. (1970): *A stress-strain function for fatigue of metals*, in: Journal of Materials, Volume 5(4), 767–778.

SOBOYEJO, W. & RAMASUNDARAM, P. (1996): *Damage in a* $[0/90]_{2s}$ *nicalon-reinforced CAS glass ceramic composite*, in: International Journal of Damage Mechanics, Volume 5, 278–291.

SÖDERBERG, C. R. (1939): *Factor of safety and working stress*, in: Transactions of the American Society of Mechanical Engineers, Volume 52, 13–28.

SPANNER, J. C., BROWN, A., HAY, D. R., MUSTAFA, V., NOTVEST, K. & POLLOCK, A. (1987): *Fundamentals of acoustic emission testing*, in: MCINTIRE, P. & MILLER, R. K. (Eds.): *Nondestructive Testing Handbook, Acoustic Emission Testing (second ed.)*, American Society for Nondestructive Testing 1987, Volume 5, Chapter 1, pp. 11–44.

STANKOVIĆ, Z. & BRUHNS, O. T. (2007): *Fatigue life investigation using non-destructive testing methods*, in: PAMM, Volume 7, 4030027–4030028.

STANKOVIĆ, Z., BRUHNS, O. T. & SCHÜTTE, H. (2007): *Detection of fatigue crack growth using acoustic emission and electrical resistance*, in: STANGENBERG, F., BRUHNS, O. T., HARTMANN, D. & MESCHKE, G. (Eds.): *ICLODC 2007*, Ruhr Universität Bochum: SFB 398 2007, pp. 417–426.

STEIN, E. & BARTHOLD, F.-J. (1996): *Elastizitätstheorie*, in: MEHLHORN, G. (Ed.): *Der Ingenieurbau, Grundwissen: Werkstoffe, Elastizitätstheorie*, Ernst & Sohn, Berlin 1996.

STUMPF, H. & HOPPE, U. (1997): *The application of tensor algebra on manifolds to nonlinear continuum mechanics*, in: Zeitschrift für Angewandte Mathematik und Mechanik, Volume 77(5), 327–339.

SURESH, S. (1991): *Fatigue of materials*, Cambridge university press 1991.

SUTTON, S. A. (1974): *Fatigue crack propagation in an epoxy polymer*, in: Engineering fracture mechanics, Volume 6(3), 587–595.

TADA, N. (1992): *Monitoring of a surface crack in a finite body by means of electrical potential technique*, in: International Journal of Fracture, Volume 57, 199–220.

TOBIAS, A. (1976): *Acoustic emission source location in two dimensions by an array of three sensors*, in: Non-destructive Testing, Volume 9(1), 9–12.

TRESCA, H. (1872): *Mémoire sur l'écoulement des corps solides*, in: Académie des Sciences, Paris, Volume 20, 73–135.

TROST, A. (1944): *Ermittlung von Rissen und Messung der Rißtiefen in metallischen Werkstoffen durch elektrische Spannungsmessung*, in: Metallwirtschaft, Volume 23, 308–309.

TRUESDELL, C. & NOLL, W. (2003): *The non-linear field theories of mechanics*, Springer-Verlag Berlin Heidelberg New York 2003.

UNANGST, K. D., SHIH, T. T. & WEI, R. P. (1977): *Crack closure in 2219-T851 aluminum alloy*, in: Engineering Fracture Mechanics, Volume 9(3), 725–734.

VAHAVIOLOS, S., CULP, J., KLEIN, R. F., MCGONEY, C., MILLER, R. K., MITCHELL, J., SAIFI, M. & SCHWENK, E. B. (1987): *Acoustic emission applications in welding*, in: MCINTIRE, P. & MILLER, R. K. (Eds.): *Nondestructive Testing Handbook, Acoustic Emission Testing (second ed.)*, American Society for Nondestructive Testing 1987, Volume 5, Chapter 9, pp. 275–310.

VOGELSANG, H. (2001): *Parameteridentifikation für ein selbstkonsistentes Stoffmodell unter Berücksichtigung von Phasentransformationen* 2001, Ph. D. thesis, Mitteilung aus dem Institut für Mechanik, Ruhr-Universität Bochum, Nr. 129.

VON MISES, R. (1913): *Mechanic der festen Körper in Plastisch deformablem Zustand*, in: Nachrichten von der Gesellschaft der Wissenschaten zu Göttingen (Mathematisch-Physikalische Klasse), , 582–592.

VORMWALD, M. & HEULER, P. (1993): *Examination of short-crack measurement and modelling under cyclic inelastic conditions*, in: Fatigue and Fracture of Engineering Materials and Structures, Volume 16(7), 693–706.

WADLEY, H. N. G. & SIMMONS, J. A. (1987): *Microscopic origins of acoustic emission*, in: MCINTIRE, P. & MILLER, R. K. (Eds.): *Nondestructive Testing Handbook, Acoustic Emission Testing (second ed.)*, American Society for Nondestructive Testing 1987, Volume 5, Chapter 3, pp. 63–90.

WEGST, C. W. (1992): *Stahlschlüssel*, Volume 16, Stahlschlüssel Wegst GmBH 1992.

WESTERGAARD, H. (1939): *Bearing pressures and cracks.*, in: Journal of Applied Mechanics, Volume 6, A49–A53.

WHEELER, O. E. (1972): *Spectrum loading and crack growth*, in: Journal of Basic Engineering, Volume 94, 181–186.

WILLIAMS, M. L. (1957): *On the stress distribution at the base of a stationary crack*, in: Journal of Applied Mechanics, Volume 24, 109–114.

WÖHLER, A. (1858/70): *Über die Festigkeits-Versuche mit Eisen and Stahl*, in: Zeitschrift für Bauwesen, Volume 8,10,13,16,20.

WOO, C. W. & CHOW, C. L. (1984): *Fatigue crack propagation in aluminium and PMMA*, in: International Journal of Fracture, Volume 26(2), R37–R42.

WU, C. H. (1978a): *Elasticity problems of a slender Z-crack*, in: Journal of Elasticity, Volume 8(2), 183–205.

WU, C. H. (1978b): *Maximum-energy-release-rate criterion applied to a tension-compression specimen with crack*, in: Journal of Elasticity, Volume 8(3), 235–257.

XIAO, H., BRUHNS, O. T. & MEYERS, A. (1997a): *Hypo-elasticity model based upon the logarithmic stress rate*, in: Journal of Elasticity, Volume 47, 51–68.

XIAO, H., BRUHNS, O. T. & MEYERS, A. (1997b): *Logarithmic strain, logarithmic spin and logarithmic rate*, in: Acta Mechanica, Volume 124, 89–105.

XIAO, H., BRUHNS, O. T. & MEYERS, A. (2000a): *The choice of objective rates in finite elastoplasticity: general results on the uniqueness of the logarithmic rate*, in: Proceedings of the Royal Society London A, Volume 456, 1865–1882.

XIAO, H., BRUHNS, O. T. & MEYERS, A. (2000b): *A consistent finite elastoplasticity theory combining additive and multiplicative decomposition of the stretching and the deformation gradient*, in: International Journal of Plasticity, Volume 16, 143–177.

XIAO, H., BRUHNS, O. T. & MEYERS, A. (2006): *Elastoplasticity beyond small deformations*, in: Acta Mechanica, Volume 182, 31–111.

XIAO, H., BRUHNS, O. T. & MEYERS, A. (2007): *Thermodynamic laws and consistent Eulerian formulation of finite elastoplasticity with thermal effects*, in: Journal of the Mechanics and Physics of Solids, Volume 55(2), 338–365.

ZHENG, Q. S. & BETTEN, J. (1996): *On damage effective stress and equivalence hypothesis*, in: International Journal of Damage Mechanics, Volume 5(3), 219–240.

Mitteilungen aus dem Institut für Mechanik

Nr. 1 Theodor Lehmann: Dezember 1976
Große elasto-plastische Formänderungen

Nr. 2 Bogdan Raniecki/Klaus Thermann: Juni 1978
Infinitesimal Thermoplasticity and Kinematics of Finite Elastic-Plastic Deformations. Basic Concepts

Nr. 3 Wolfgang Krings: Januar 1976
Beitrag zur Finiten Element Methode bei linearem, viskoelastischem Stoffverhalten Stoffverhalten

Nr. 4 Burkhard Lücke: Januar 1976
Theoretische und experimentelle Untersuchen der zyklischen elastoplastischen Blechbiegung bei endlichen Verzerrungen

Nr. 5 Knut Schwarze: Februar 1976
Einfluß von Querschnittsverformungen bei dünnwandigen Stäben mit stetig gekrümmter Profilmittellinie

Nr. 6 Hubert Sommer: Januar 1977
Ein Beitrag zur Theorie des ebenen elastischen Verzerrungszustandes bei endlichen Formänderungen

Nr. 7 H. Stumpf/F. J. Biehl: März 1977
Die Methode der orthogonalen Projektionen und ihre Anwendungen zur Berechnung orthotroper Platten

Nr. 8 Albert Meyers: April 1977
Ein Beitrag zum optimalen Entwurf von schnellaufenden Zentrifugenschalen

Nr. 9 Berend Fischer: April 1977
Zur zyklischen, elastoplastischen Beanspruchen eines dickwandigen Zylinders bei endlichen Verzerrungen

Nr. 10 Wojciech Pietraszkiewicz: Mai 1977
Introduction to the Non-Linear Theory of Shells

Nr. 11 Wilfried Ullenboom: Juni 1977
Optimierung von Stäben unter nichtperiodischer dynamischer Belastung

Nr. 12 Jürgen Güldenpfennig: Juli 1977
Anwendung eines Modells der Vielkristallplastizität auf ein Problem gekoppelter elastoplastischer Wellen

Nr. 13 Pawel Rafalski: März 1978
Minimum Principles in Plasticity

Nr. 14 Peter Hilgers: Juli 1978
Der Einsatz eines Mikrorechners zur hybriden Optimierung und Schwingungsanalyse

Nr. 15 Hans-Albert Lauert: August 1979
Optimierung von Stäben unter dynamischer periodischer Beanspruchung bei Beachtung von Spannungsrestriktionen

Nr. 16 Martin Fritz: Juli 1979
Berechnund der Auflagerkräfte und der Muskelkräfte des Menschen bei ebenen Bewegungen aufgrund von kinematographischen Aufnahmen

Nr. 17 H. Stumpf/F. J. Biehl: Dezember 1979
Approximations and Error Estimates in Eigenvalue Problems of Elastic Systems with Application to Eigenvibrations of Orthotropic Plates

Nr. 18 Uwe Kohlberg: Juli 1979
Variational Principles and theirNumerical Application to Geometrically Nonlinear v. Karman Plates

Nr. 19 Heinz Antes: Januar 1980
Über Fehler und Möglichkeiten ihrer Abschätzung bei numerischen Berechnungen von Schalentragwerken

Nr. 20 Czeslaw Wozniak: März 1980
Large Deformations of Elastic and Non-Elastic Plates, Shells and Rods

Nr. 21 Maria K. Duszek: Juni 1980
Problems of Geometrically Non-Linear Theory of Plasticity

Nr. 22 Burkhard von Bredow: Dezember 1980
Optimierung von Stäben unter stochastischer Erregung

Nr. 23 Jürgen Preuss: Februar 1981
Optimaler Entwurf von Tragwerken mit Hilfe der Mehrzielmethode

Nr. 24 Ekkehard Großmann: Februar 1981
Kovarianzanalyse mechanischer Zufallsschwingungen bei Darstellung der mehrfachkorrelierten Erregungen durch stochastische Differentialgleichungen

Nr. 25 Dieter Weichert: März 1981
Variational Formulation and Solution of Boundary-Value Problems in the Theory of Plasticity and Application to Plate Problems

Nr. 26 Wojciech Pietraszkiewicz: Juni 1981
On Consistent Approximations in the Geometrically Non-Linear Theory of Shells

Nr. 27 Georg Zander: September 1981
Zur Bestimmung von Verzweigungslasten dünnwandiger Kreiszylinder unter kombinierter Längs- und Torsionslast

Nr. 28 Pawel Rafalski: September 1981
An Alternative Approach to the Elastic-Viscoplastic Initial-Boundary Value Problem

Nr. 29 Heinrich Oeynhausen: November 1981
Verzweigungslasten elastoplastisch deformierter, dickwandiger Kreiszylinder unter Innendruck und Axialkraft

Nr. 30 F.-J. Biehl: Dezember 1981
Zweiseitige Eingrenzung von Feldgrößen beim einseitigen Kontaktproblem

Nr. 31 Maria K. Duszek: Juni 1982
Foundations of the Non-Linear Plastic Shell Theory

Nr. 32 Reinhard Piltner: Juli 1982
Spezielle finite Elemente mit Löchern, Ecken und Rissen unter Verwendung von analytischen Teillösungen

Nr. 33 Petrisor Mazilu: Dezember 1982
Variationsprinzipe der Thermoplastizität I. Wärmeausbreitung und Plastizität

Nr. 34 Helmut Stumpf: Dezember 1982
Unified Operator Description, Nonlinear Buckling and Post-Buckling Analysis of Thin Elastic Shells

Nr. 35 Bernd Kaempf: März 1983
Ein Exremal-Variationsprinzip für die instationäre Wärmeleitung mit einer Anwendung auf thermoelastische Probleme unter Verwendung der finiten Elemente

Nr. 36 Alfred Kraft: Juli 1983
Zum methodischen Entwurf mechanischer Systeme im Hinblick auf optimales Schwingungsverhalten

Nr. 37 Petrisor Mazilu: August 1983
Variationsprinzipe der Thermoplastizität II. Gekoppelte thermmomechanische Prozesse

Nr. 38 Klaus-Detlef Mickley: November 1983
Punktweise Eingrenzung von Feldgrößen in der Elastomechanik und ihre numerische Realisierung mit Fundamental-Splinefuntionen

Nr. 39 Lutz-Peter Nolte: Dezember 1983
Beitrag zur Herleitung und vergleichende Untersuchung geometrisch nichtlinearer Schalentheorien unter Berücksichtigung großer Rotationen

Nr. 40 Ulrich Blix: Dezember 1983
Zur Berechnung der Einschnürung von Zugstäben unter Berücksichtigung thermischer Einflüsse mit Hilfe der Finite-Element-Methode

Nr. 41 Peter Becker: Februar 1984
Zur Berechnung von Schallfeldern mit Elemtmethoden

Nr. 42 Diemar Bouchard: Februar 1984
Entwicklung und Anwendung eines an die Diskrete-Fourier-Transformation angepaßten direkten Algorithmus zur Bestimmung der modalen Parameter linearer Schwingungssysteme

Nr. 43 Uwe Zdebel: Dezember 1984
Theoretische und experimentelle Untersuchungen zu einem thermo-plastischen Stoffgesetz

Nr. 44 Jan Kubik: April 1985
Thermodiffusion Flows in a Solid with a Dominant Constituent

Nr. 45 Horst J. Klepp: Juni 1985
Über die Gleichgewichtslagen und Gleichgewichtsbereiche nichtlinearer autonomer Systeme

Nr. 46 J. Makowski/L.-P. Nolte/H. Stumpf: Juli 1985
Finite In-Plane Deformations of Flexible Rods - Insight into Nonlinar Shell Problems

Nr. 47 Franz Karl Labisch: August 1985
Grundlagen einer Analyse mehrdeutiger Lösungen nichtlinearer Randwertprobleme der Elastostatik mit Hilfe von Variationsverfahren

Nr. 48 J. Chroscielewski/L.-P. Nolte: Oktober 1985
Strategien zur Lösung nichtlinearer Probleme der Strukturmechanik und ihre modulare Aufbereitung im Konzept MESY

Nr. 49 Karl-Heinz Bürger: Dezember 1985
Gewichtsoptimierung rotationssymmetrischer Platten unter instationärer Erregung

Nr. 50 Ulrich Schmid: Februar 1987
Zur Berechnung des plastischen Setzens von Schraubenfedern

Nr. 51 Jörg Frischbier: März 1987
Theorie der Stoßbelastung ortotroper Platten und ihr experimentelle Überprüfung am Beispiel einer unidirektional verstärkten CFK-Verbundplatte

Nr. 52 W. Tampczynski: Juli 1987
Strain history effect in cyclic plasticity

Nr. 53 Dieter Weichert: Dezember 1987
Zum Problem geometrischer Nichtlinearitäten in der Plastizitätstheorie

Nr. 54 Heinz Antes/Thomas Meise/Thomas Wiebe: Januar 1988
Wellenausbreitung in akustischen Medien Randelement-Prozeduren im 2-D Frequenzraum und im 3-D Zeitbereich

Nr. 55 Wojciech Pietraszkiewicz: März 1988
Geometrically non-linear theories of thin elastic shells

Nr. 56 Jerzy Makowski/Helmut Stumpf: April 1988
Finite strain theory of rods

Nr. 57 Andreas Pape: Mai 1988
Zur Beschreibung des transienten und stationären Verfestigungsverhaltens von Stahl mit Hilfe eines nichtlinearen Grenzflächenmodells

Nr. 58 Johannes Groß-Weege: Juni 1988
Zum Einspielverhalten von Flächentragwerken

Nr. 59 Peihua LIU: Juli 1988
Optimierung von Kreisplatten unter dynamischer nicht rotationssymmetrischer Last

Nr. 60 Reinhard Schmidt: August 1988
Die Anwendung von Zustandsbeobachtern zur Schwingungsüberwachung und Schadensfrüherkennung auf mechanische Konstruktionen

Nr. 61 Martin Pitzer: Juli 1988
Vergleich einiger FE-Formulierungen auf der Basis eines inelastischen Stoffgesetzes

Nr. 62 Jerzy Makowski/Helmut Stumpf: Dezember 1988
Geometric structure of fully nonlinear and linearized Cosserat type shell theory

Nr. 63 O. T. Bruhns: Januar 1989
Große plastische Formänderungen - Bad Honnef 1988

Nr. 64 Khanh Chau Le/Helmut Stumpf/Dieter Weichert: Juli 1989
Variational principles of fracture mechanics

Nr. 65 Guido Obermüller: Juni 1989
Ein Beitrag zur Strukturoptimierung unter stochastischen Lasten

Nr. 66 Herbert Diehl: Juni 1989
Ein Materialmodell zur Berechnung von Hochgeschwindigkeitsdeformationen metallischer Werkstoffe unter besonderer Berücksichtigung der Schädigung durch Scherbänder

Nr. 67 Michael Geis: November 1989
Zur Berechnund ebener, elastodynamischer Rißprobleme mit der Randelementmethode

Nr. 68 Günter Renker: November 1989
Zur Identifikation nichtlinearer strukturmechanischer Systeme

Nr. 69 Berthold Schieck: November 1989
Große elastische Dehnungen in Schalen aus hyperelastischen inkompressiblen Materialien

Nr. 70 Frank Szepan: Dezember 1989
Ein elastisch-viskoplastisches Stoffgesetz zur Beschreibung großer Formänderungen unter Berücksichtigung der thermomechanischen Kopplung

Nr. 71 Christian Scholz: Dezember 1989
Ein Beitrag zur Gestaltsoptimierung druckbelasteter Rotationsschalen

Nr. 72 J. Badur/H. Stumpf: Dezember 1989
On the influence of E. and F. Cosserat on modern continuum mechanics and field theory

Nr. 73 Werner Fornefeld: Januar 1990
Zur Parameteridentifikation und Berechnung von Hochgeschwindigkeitsdeformationen metallischer Werkstoffe anhand eines Kontinuums-Damage-Modells

Nr. 74 J. Saczuk/H. Stumpf: April 1990
On statical shakedown theorems for non-linear problems

Nr. 75 Andreas Feldmüller: April 1991
Ein thermoplastisches Stoffgesetz isotrop geschädigter Kontinua

Nr. 76 Ulfert Rott: April 1991
Ein neues Konzept zur Berechnung viskoplastischer Strukturen

Nr. 77 Thomas Heinrich Pingel: Juli 1991
Beitrag zur Herleitung und numerischen Realisierung eines mathematischen Modells der menschlichen Wirbelsäule

Nr. 78 O. T. Bruhns: Dezember 1991
Große plastische Formänderungen - Bad Honnef 1991

Nr. 79 J. Makowski/J. Chroscielewski/H. Stumpf:
Computational Analysis of Shells Undergoing Large Elastic Deformation Part I:Theoretical Foundations

Nr. 80 J. Chroscielewski/J. Makowski/H. Stumpf:
Computational Analysis of Shells Undergoing Large Elastic Deformation Part II: Finite Element Implementation

Nr. 81 R. H. Frania/H. Waller: Mai 1992
Entwicklung und Anwendung spezieller finiter Elemente für Kerbspannungsprobleme im Maschienebau

Nr. 82 B. Bischoff-Beiermann: Juli 1992
Zur selbstkonsistenten Berechnung von Eigenspannungen in polykristallinem Eis unter Berücksichtigung der Monokristallanisotropie

Nr. 83 J. Pohé: Februar 1993
Ein Beitrag zur Stoffgesetzentwicklung für polykristallines Eis

Nr. 84 U. Kikillus: Mai 1993
Ein Beitrag zum zyklischen Kiechverhalten von Ck 15

Nr. 85 T. Guo: Juni 1993
Untersuchung des singulären Rißspitzenfeldes bei stationärem Rißwachstum in verfestigendem Material

Nr. 86 Achim Menne: Januar 1994
Identifikation der dynamischen Eigenschaften von hydrodynamischen Wandlern

Nr. 87 Uwe Folchert: Januar 1994
Identifikation der dynamischen Eigenschaften Hydrodynamischer Kopplungen

Nr. 88 Jörg Körber: April 1994
Ein verallgemeinertes Finite-Element-Verfahren mit asymptotischer Stabilisierung angewendet auf viskoplastische Materialmodelle

Nr. 89 Peer Schieße: April 1994
Ein Beitag zur Berechnung des Deformationsverhaltens anisotrop geschädigter Kontinua unter Berücksichtigung der thermoplastischen Kopplung

Nr. 90 Egbert Schopphoff: Juli 1994
Dreidimensionale mechanische Analyse der menschlichen Wirbelsäule

Nr. 91 Christoph Beerens: Juli 1994
Zur Modellierung nichtlinearer Dämpfungsphänomene in der Strukturmechanik

Nr. 92 K. C. Le/H. Stumpf: November 1994
Finte elastoplasticity with microstructure

Nr. 93 O. T. Bruhns: Dezember 1994
Große plastische Formänderungen - Bad Honnef 1994

Nr. 94 Armin Lenzen: Dezember 1994
Untersuchung von dynamischen Systemen mit der Singulärwertzerlegung - Erfassung von Strukturveränderungen

Nr. 95 J. Makowski/H. Stumpf: Dezember 1994
Mechanics of Irregular Shell Structures

Nr. 96 J. Chroscielewski/J. Makowski/H. Stumpf: Dezember 1994
Finte Elements for Irregular Nonlinear Shells

Nr. 97 W. Krings/A. Lenzen/u. a.: Februar 1995
Festschrift zum 60. Geburtstag von Heinz Waller

Nr. 98 Ralf Podleschny: April 1995
Untersuchung zum Instabilitätsverhalten scherbeanspruchter Risse

Nr. 99 Bernd Westerhoff: Juli 1995
Eine Untersuchung zum geschwindigkeitsabhängigen Verhalten von Stahl

Nr. 100 Marc Mittelbach: Dezember 1995
Simulation des Deformations- und Schädigungsverhaltens beim Stoßversuch mit einem Kontinuums-Damage-Modell

Nr. 101 Ulrich Hoppe: Mai 1996
Über grundlegende Konzepte der nichtlinearen Kontinuumsmechanik und Schalentheorie

Nr. 102 Marcus Otto: Juni 1996
Erweiterung des Kaustikenverfahrens zur Analyse räumlicher Spannungskonzentrationen

Nr. 103 Horst Lanzerath: Juli 1996
Zur Modalanalyse unter Verwendung der Randelementemethode

Nr. 104 Andreas Wichtmann: August 1996
Entwicklung eines thermodynamisch konsistenten Stoffgesetzes zur Beschreibung der Reckalterung

Nr. 105 Bjarne Fossa: Oktober 1996
Ein Beitrag zur Fließflächenmessung bei vorgedehnten Stoffen

Nr. 106 Khanh Chau Le: Dezember 1996
Kontinuumsmechanisches Modellieren von Medien mit veränderlicher Mikrostruktur

Nr. 107 Holger Behrens: Januar 1997
Nichtlineare Modellierung und Identifikation hydrodynamischer Kupplungen mit allgemeinen diskreten Modellansätzen

Nr. 108 Johannes Moosheimer: Juli 1997
Gesteuerte Schwingungsdämpfung mit Elektrorheologischen Fluiden

Nr. 109 Dirk Klaus Anding: Oktober 1997
Zur simultanen Bestimmung materialabhängiger Koeffizienten inelastischer Stoffgesetze

Nr. 110 Stephan Weng: Dezember 1997
Ein Evolutionsmodell zur mechanischen Analyse biologischer Strukturen

Nr. 111 Michael Straßberger: Dezember 1997
Aktive Schallreduktion durch digitale Zustandsregelung der Strukturschwingungen mit Hilfe piezo-keramischer Aktoren

Nr. 112 Hans-Jörg Becker: Dezember 1997
Simultation des Deformationsverhaltens polykristallinen Eises auf der Basis eines monokristallinen Stoffgesetzes

Nr. 113 Thomas Nerzak: Dezember 1997
Modellierung und Simulation der Ausbreitung adiabatischer Scherbänder in metallischen Werkstoffen bei Hochgeschwindigkeitsdeformationen

Nr. 114 O. T. Bruhns: März 1998
Große plastische Formänderungen

Nr. 115 Jan Steinhausen: August 1998
Die Beschreibung der Dynamik von Antriebssträngen durch Black-Box-Modelle hydrodynamischer Kupplungen

Nr. 116 Thomas Pandorf: August 1998
Experimentelle und numerische Untersuchungen zur Kerbspitzenbeanspruchung bei schlagbelasteten Biegeproben

Nr. 117 Claus Oberste-Brandenburg: Juni 1999
Ein Materialmodell zur Beschreibung der Austenit-Martensit Phasentransformation unter Berücksichtigung der transformationsinduzierten Plastizität

Nr. 118 Michael Märtens: Dezember 1999
Regelung mechanischer Strukturen mit Hilfe piezokeramischer Stapelaktoren

Nr. 119 Dirk Kamarys: Dezember 1999
Detektion von Systemveränderungen durch neue Identifikationsverfahren in der experimentellen Modalanalyse

Nr. 120 Wolfgang Hiese: Januar 2000
Gültigkeitskriterien zur Bestimmung von Scherbruchzähigkeiten

Nr. 121 Peter Jaschke: Februar 2000
Mathematische Modellierung des Betriebsverhaltens hydrodynamischer Kupplungen mit hybriden Modellansätzen

Nr. 122 Stefan Müller: Februar 2000
Zum Einsatz von semi-aktiven Aktoren zur optimalen Schwingungsreduktion in Tragwerken

Nr. 123 Dirk Eichel: Juni 2000
Zur Kondensation strukturdynamischer Aufgaben mit Hilfe von Polynommatrizen

Nr. 124 Andreas Bürgel: August 2000
Bruchmechanische Kennwerte beim Wechsel im Versagensverhalten dynamisch scherbeanspruchter Risse

Nr. 125 Daniela Lürding: März 2001
Modellierung großer Deformationen in orthotropen, hyperelastischen Schalenstrukturen

Nr. 126 Thorsten Quent: Mai 2001
Ein mikromechanisch begründetes Modell zur Beschreibung des duktilen Verhaltens metallischer Werkstoffe bei endlichen Deformationen unter Berücksichtigung von Porenschädigung

Nr. 127 Ndzi C. Bongmba: Mai 2001
Ein finites anisotropes Materialmodell auf der Basis der Hencky-Dehnung und der logarithmischen Rate zur Beschreibung duktiler Schädigung

Nr. 128 Henning Schütte: August 2001
Ein finites Modell für spröde Schädigung basierend auf der Ausbreitung von Mikrorissen

Nr. 129 Henner Vogelsang: Dezember 2001
Parameteridentifikation für ein selbstkonsistentes Stoffmodell unter Berücksichtigung von Phasentransformationen

Nr. 130 Jörn Mosler: Dezember 2002
Finite Elemente mit sprungstetigen Abbildungen des Verschiebungsfeldes für numerische Analysen lokalisierter Versagenszustände

Nr. 131 Karin Preusch: Mai 2003
Hierarchische Schalenmodelle für nichtlineare Kontinua mit der p-Version der Finite-Element Methode

Nr. 132 Christoph Müller: August 2003
Thermodynamic modeling of polycrystalline shape memory alloys at finite strains

Nr. 133 Martin Heiderich: Juni 2004
Ein Beitrag zur zerstörungsfreien Schädigungsanalyse

Nr. 134 Raoul Costamagna: Juli 2004
Globale Materialbeziehungen für das geklüftete Gebirge

Nr. 135 Markus Böl: Januar 2005
Numerische Simulation von Polymernetzwerken mit Hilfe der Finite-Elemente-Methode

Nr. 136 Gregor Kotucha: August 2005
Regularisierung von Problemen der Topologieoptimierung unter Einbeziehung von Dichtegradienten

Nr. 137 Michael Steiner: Februar 2006
Deformations- und Versagensverhalten innendruckbeanspruchter Stahlrohre durch Stoßbelastung

Nr. 138 Dirk Bergmannshoff: Dezember 2006
Das Instabilitätsverhalten zug-/scherbeanspruchter Risse bei Variation des Belastungspfades

Nr. 139 Olaf Schilling: Januar 2007
Über eine implizite Partikelmethode zur Simulation von Umformprozessen

Nr. 140 Jörn Mosler: Mai 2007
On the numerical modeling of localized material failure at finite strains by means of variational mesh adaption and cohesive elements

Nr. 141 Rainer Fechte-Heinen: Juni 2007
Mikromechanische Modellierung von Formgedächtnismaterialien

Nr. 142 Christian Grabe: Juni 2007
Experimental testing and parameter identification on the multidimensional material behavior of shape memory alloys

Nr. 143 Markus Peters: Juli 2007
Modellierung von Rissausbreitung unter Verwendung der p-Version der XFEM mit einer adaptiven Integrationsmethode

Nr. 144 Claus Oberste-Brandenburg: Juli 2007
Thermomechanical modeling of shape memory alloys at different length scales

Nr. 145 Stefan Reichling: Juli 2007
Das inverse Problem der quantitativen Ultraschallelastografie unter Berücksichtigung großer Deformationen

Nr. 146 Kianoush Molla-Abbasi: Januar 2008
A Consistent Anisotropic Brittle Damage Model Based on the Concept of Growing Elliptical Cracks

Nr. 147 Sandra Ilic: August 2008
Application of the multiscale FEM to the modeling of composite materials

Nr. 148 Patrick Luig: Oktober 2008
A consistent Eulerian rate model for shape memory alloys

Nr. 149 Lidija Stanković: Februar 2009
Describing multiple surface localised failure by means of strong discontinuities at finite strains

Nr. 150 Thorsten Bartel: März 2009
Multiskalenmodellierung martensitischer Phasentransformationen in Formgedächtnislegierungen unter Verwendung relaxierter Energiepotenziale

Nr. 151 Zoran Stanković: April 2009
Detection of fatigue crack growth using nondestructive testing methods

Mitteilungen aus dem Institut für Mechanik
RUHR-UNIVERSITÄT BOCHUM
Nr. 151

978-3-935892-29-2